

**MOLECULAR SIMULATION STUDY OF DIVERTING MATERIALS USED IN
MATRIX ACIDIZING**

A Dissertation

by

ABDULLAH SULTAN

Submitted to the Office of Graduate Studies of
Texas A&M University
in partial fulfillment of the requirements for the degree of

DOCTOR OF PHILOSOPHY

August 2009

Major Subject: Petroleum Engineering

**MOLECULAR SIMULATION STUDY OF DIVERTING MATERIALS USED IN
MATRIX ACIDIZING**

A Dissertation

by

ABDULLAH SULTAN

Submitted to the Office of Graduate Studies of
Texas A&M University
in partial fulfillment of the requirements for the degree of

DOCTOR OF PHILOSOPHY

Approved by:

Chair of Committee,	A. D. Hill
Committee Members,	P. B. Balbuena
	H. A. Nasr-El-Din
	J. M. Seminario
	B. T. Connell
Head of Department,	S. A. Holditch

August 2009

Major Subject: Petroleum Engineering

ABSTRACT

Molecular Simulation Study of Diverting Materials Used in Matrix Acidizing.

(August 2009)

Abdullah Sultan, B.Sc.; M.Sc., King Fahd University of Petroleum & Minerals

Chair of Advisory Committee: Dr. A. Daniel Hill

Recently there has been a great deal of attention in the oilfield industry focused on the phenomenal properties of viscoelastic surfactants (VES). The interest is motivated by their applications as switchable smart fluids, their surface tension, and their thickening and rheology enhancement in aqueous solution. Surfactant molecules in solution are known for their ability to assemble spontaneously into complex structures. Under certain thermodynamic conditions, temperature and electrolyte concentrations, wormlike micelles are formed. These micelles share similar equilibrium and dynamic properties with polymer solutions. However, micellar chains can break and recombine spontaneously which make them part of the more general class of living polymers. It is vital to understand the properties of viscoelastic wormlike micelles with regard to their flow in porous media.

The overall objective of this study is to establish a better understanding of counterion effect on behavior of VES. The dependence of macroscopic properties on intermolecular interactions of complex fluid systems such as VES is an enormous challenge. To achieve our objective, we use first-principle calculations and molecular dynamics (MD) simulations to resolve the full chemical details in order to study how the structure of the micellar and solution properties depends on the chemical structure of the surfactant head group (HG) and type of counterion. In particular, we run simulations for different structures in gas-phase and aqueous solutions together with their salt counterions at

room temperature and atmospheric pressure. For this purpose, we consider four types of surfactant HG (anionic, cationic, betaine and amidoamine oxide) together with the most common ions present in the acidizing fluid of a carbonate reservoir such as Ca^{2+} , Mg^{2+} , Fe^{2+} , Fe^{3+} , Mn^{2+} and Zn^{2+} , Cl^- , OH^- and HS^- . Hydration of ions as well as interactions with surfactant the HG are studied using density functional theory (DFT). The results give important insight into the links between molecular details of VES HG structure and observed solution properties. This study proposes for the first time the possible mechanisms that explain the exotic behavior of VES at high Fe(III) concentration. Also, our MD simulation suggests that distribution of chloride ion around surfactant molecules is responsible for their viscosity behavior in HCl solution. We believe that our results are an important step to develop more systematic procedures for the molecular design and formulation of more effective and efficient VES systems.

DEDICATION

To my parents

ACKNOWLEDGEMENTS

All praises and thanks are for Allah (Subhanau-wa-Talla), the Lord of the entire creation that exists (in earth and in the Heavens). May his peace and blessings be upon all His messengers, prophets, and all humankind (alive or dead) Amen. I am extremely grateful to Almighty Allah who alone made this accomplishment possible.

I am most thankful to my advisor, Dr. Dan Hill, for his invaluable support, guidance and, more importantly, for giving me the freedom to pursue my own ideas and think independently. He would always push me towards challenging tasks that could make a difference at the most fundamental level. He would continuously ask me questions which made me reflect on my course of thought and organize myself. Working with him has been a great learning experience, and I thank him for sharing his knowledge of engineering and other aspects of life, and for being a mentor as well as a good friend.

With a deep sense of gratitude and appreciation, I would like to express my sincere thanks to Dr. Perla B. Balbuena for her inspiring guidance, help and excellent cooperation in co-supervising this research work. It was her keen interest which made this research work presentable in this format. I thoroughly enjoyed discussions with her new results in our bimonthly meetings which gave me a whole new perspective of my research and were most enlightening. She was very encouraging and inspiring, and I have been most fortunate to work with her.

I'm very thankful to Dr. Hisham Nasr-El-Din, a committee member, who introduced me to the world of viscoelastic surfactant when I worked in his lab during my internship, summer 2006, and was always willing to provide insightful comments on my research before and after I joined Texas A&M University. I personally learned a lot of ethical and technical values by interacting with him. He is simply a model to be followed. Also, I would like to extend my thanks to Dr. J. M. Seminario, who helped me a lot before

becoming a member of my committee as I learned the fundamentals of nanotechnology and computational chemistry in his classes. He always inspired my knowledge and reshaped my way of thinking with his frequent saying “we can do it.” Last but not least, I appreciate the time dedicated by Dr. B. T. Connell, a committee member, a great help all the times I dropped by his office to talk about molecular formulation or mechanisms.

My PhD program would not have been possible without the generous support of my sponsor, King Fahd University of Petroleum & Minerals, Dhahran, Saudi Arabia, to which I owe much. I’m a proud graduate of this institution and will serve upon my return, with great honor, as a faculty member at KFUPM for many years to come. All thanks and gratitude are extended to the Saudi Arabian Cultural Mission in Washington D.C. and the sponsored students office at TAMU for their unlimited logistical support and help that made my time much easier.

I’m very thankful to Dr. Lisa Peres of the molecular simulation lab in the Chemistry Department at Texas A&M University for her support while running my simulations. She was the first person to contact when unable to resolve a “termination error” in my simulation. With her excellent personality, strong knowledge of science and good experience, she easily manages to help a number of students at the same time. I would like to thank Dr. M. Hall, a professor of inorganic chemistry at TAMU for the many useful discussions we had. I would like to thank other research groups and professors from outside TAMU with whom I joined good discussions through e-mails and in particular, those who provided me with good hints on the first guess of molecular structures. They include: Pamela Hill and Edwin Schauble of the Earth and Science Department at University of California, Los Angeles, C. W. Bock, and J. P. Glusker of the Institute for Cancer Research, Philadelphia University, Todor Dudev and Carmay Lim from the Institute of Biomedical Science at National Tsing Hua University, Taiwan. I also appreciate the many good discussions I had during the early stages of my research with E. S. Boek of Schlumberger Cambridge Research Center, J. T. Padding and W. J.

Briels from the Computational Dispersion Rheology Group at the University of Twente, The Netherlands.

I would like to thank all the Dr. Hills' group members whom I had a chance to interact with over the years. This includes the ones who have left and the ones still here: Saleh, Wahby, Maysam, Manabu, Jassim, Omer, Mohammed, Mou, Jiayao, Nerwing, Jason, Ben, Rashad, Nimish, and Qi. They made it enjoyable and fun to be part of the group, especially those with whom I'm sharing the office. I thank Zhu's group members for being our office mates and all the students, faculty and staff of the Petroleum Engineering Department who made my graduate life an enjoyable experience.

I thank the Middle East Carbonate Research Consortium for providing the financial support required to carry out this research. I thank the Supercomputing facilities at Texas A&M University in College Station, and Doha, Qatar for providing the necessary supercomputing time and support. Finally, I thank all my innumerable friends in College Station, who made my stay here the most memorable experience. I thank my parents for their belief in me and for providing all the help and support throughout my life. I thank them for all the hardships they went through to make me reach this point of my career. I am forever indebted to them. I submit that all my successes and achievements drew that inspiration from their blessings, encouragement and support. Hence it is to them, to whom now and ever I owe my very self, that I dedicate this work of mine.

NOMENCLATURE

<i>ab initio</i>	First principle quantum mechanical approach for obtaining the electronic properties of a molecule based on the approximate solution to the many-electron Schrodinger equation, using only fundamental concepts, the mass and charge of the nuclear particles; literally: “from the beginning”.
Basis function	function describing the atomic orbitals that when linearly combined make up the set of molecular orbitals in a quantum mechanics calculation, Gaussian basis sets and Slater type orbitals are example of basis functions.
Density functional theory	Class of quantum methods in which the total energy is expressed as a function of the electron density, and which the exchange correlation contribution are based on the solution of the Schrodinger equation for an electron gas.
Energy minimization	Computational procedure for altering the configuration of a molecular model until the minimum energy arrangement has been attained. Approach is used for molecular dynamic, Monte Carlo simulation, and quantum mechanics methods.
Forcefield	A set of parameterized analytical expressions used in molecular mechanic for evaluating the contributions to the total potential energy of molecular system; forcefield typically, but not always, include contributions for bond stretching, angle bending, dihedral torsion, van der Waals, and columbic interaction.
12-2-12	12-2-12(dimethylene-1,2-bis(dodecyldimethylammonium bromide))

2,1-NHC	2,1-hydroxy-1-naphtoic
AA	Acetic acid
AAMCDEEA	<i>N</i> -[(acetylamino)methyl]-2-carboxy- <i>N,N</i> -dimethylethanaminium
AAPhdMA	[3-(acetylamino)propyl](hydroxy) dimethylammonium
AAPhP	1-[3-(acetylamino)propyl]-1-hydroxypyrrolidinium
APhMA	[3-(acetylamino)propyl] (hydroxy)bis(hydroxymethyl) ammonium
ATAC	Erucyl trimethylammonium chloride
BA	Butanoic acid
bAETMedA	<i>N,N'</i> -bis[2-(acetyloxy)ethyl]- <i>N,N,N',N'</i> -tetramethylethane-1,2-diaminium
BdMEA	<i>N</i> -benzyl- <i>N,N</i> -dimethylethanaminium
C-14TMAB	Tetradecyltrimethylammonium
C ₁₆ SE	Sucrose hexadecanoate
C ₁₆ SO ₃ Na	1-hexadecane sulfonic acid
CMDMEA	<i>N</i> -(carboxymethyl)- <i>N,N</i> -dimethylethanaminium

C _m E _n	Polyoxyethylene alkyl ether
CMPMBdA	<i>N</i> -carboxy- <i>N,N,N',N',N'</i> -pentamethylbutane-1,4-diaminium
CTAB	Cetyltrimethylammonium bromide
CTAC	Cetyltrimethylammonium chloride
CTAT	Cetyltrimethylammonium tosilate
CTEEA	2-carboxy- <i>N,N,N</i> -trimethylethanaminium
CTMMA	Carboxy- <i>N,N,N</i> -trimethylmethanaminium
dETMedA	<i>N,N'</i> -diethyl- <i>N,N,N',N'</i> -tetramethylethane-1,2-diaminium
dMNPA	<i>N</i> -[3-(dimethylnitro)propyl]acetamide
DTAC	Dodecyltrimethylammonium chloride
EHAC	Erucyl bis(hydroxyethyl)-methylammonium chloride
EhhMEA	<i>N</i> -ethyl-2-hydroxy- <i>N</i> -(2-hydroxyethyl)- <i>N</i> -methylethanaminium
Et3NHC	Triethylammonium chloride or <i>N,N</i> -diethylethanaminium

HMB14dA	<i>N,N,N,N,N',N'</i> -hexamethylbutane-1,4-diaminium
HME12dA	<i>N,N,N,N,N',N'</i> -hexamethylethane-1,2-diaminium
HMMEA	<i>N,N</i> -bis(hydroxymethyl)- <i>N</i> -methylethanaminium
NaOA	Sodium oleate
NaSal	Sodium 2-hydroxybenzoate
PB	potassium butanoate
PTHC	p-toluidine hydrochloride or 4-methylanilinium
S1BS	Sodium butane-1-sulfonate
SDES	Sodium trioxethylene sulfate
SHNC	Sodium 3-hydroxynaphthalene-2-carboxylate
SPS	Sodium propyl sulfate
TMA	<i>N,N,N</i> -trimethylmethanaminium or Tetramethylammonium
TMEA	<i>N,N,N</i> -trimethylethanaminium
TmoEA	2-methoxy- <i>N,N,N</i> -trimethyl-2-oxoethanaminium

TABLE OF CONTENTS

	Page
ABSTRACT	iii
DEDICATION	v
ACKNOWLEDGEMENTS	vi
NOMENCLATURE	ix
TABLE OF CONTENTS	xiii
LIST OF FIGURES	xvi
LIST OF TABLES	xxx
 CHAPTER	
I INTRODUCTION	1
1.1 Formation Damage	2
1.2 Well Stimulation	4
1.3 Statement of the Problem and Approach	7
1.4 Research Objectives	8
II ROLE OF MOLECULAR SIMULATION IN THE ADVANCEMENT OF NANOTECHNOLOGY APPLICATIONS IN THE OILFIELD INDUSTRY	11
2.1 Nanotechnology	12
2.2 Quantum Chemistry	14
2.3 Molecular Modeling	19
2.4 Nanotechnology in Oilfield Industry	24
III CHEMISTRY OF VISCOELASTIC SURFACTANTS USED AS DIVERTING MATERIALS IN WELL STIMULATION	27
3.1 Introduction	28
3.2 Chemistry of Matrix Acidizing	31
3.3. Acid Additives	34
3.4 Surfactants	35
3.5 Dynamic Properties of WLM in Solution	51
IV <i>AB INITIO</i> STUDY OF HYDRATION AND BINDING ENERGIES FOR $M^x(H_2O)_n.mH_2O$ CLUSTERS ($M=Ca^{2+}, Mg^{2+}, Na^+$) IN CARBONATE RESERVOIRS	57

CHAPTER	Page
4.1 Introduction	57
4.2 Computational Method.....	60
4.3 Results and Discussion.....	61
V THEORETICAL STUDY OF FERRIC AND FERROUS HYDRO- CLUSTERS AND COMPLEXES WITH CHLORIDE AND SULFUR IONS.....	85
5.1 Introduction	85
5.2 Definition of the System	88
5.3 Simulation	89
5.4 Results and Discussion.....	90
VI <i>AB INITIO</i> AND MOLECULAR SIMULATION STUDIES OF INTERACTION BETWEEN INORGANIC COUNTERIONS AND ANIONIC VISCOELASTIC SURFACTANTS	123
6.1 Introduction	124
6.2 Simulation	127
6.3 Results and Discussion.....	128
VII THEORETICAL STUDY OF CATIONIC AND GEMINI SURFACTANTS IN ACID SOLUTION	158
7.1 Introduction	159
7.2 Simulation	161
7.3 Results and Discussion.....	162
7.4 Molecular Simulation.....	182
VIII GEOMETRY OPTIMIZATION AND MOLECULAR SIMULATION OF BETAINES AND AMIDOAMINE OXIDE SURFACTANTS	183
8.1 Introduction	184
8.2 Simulation	186
8.3 Results and Discussion.....	187
IX CONCLUSIONS AND RECOMMENDATIONS.....	195
9.1 Summary and Conclusions.....	195
9.2 Recommendations	203
REFERENCES.....	206
APPENDIX A	226
APPENDIX B	234
APPENDIX C	242

	Page
APPENDIX D	252
APPENDIX E.....	258
VITA	264

LIST OF FIGURES

	Page
Figure 1.1 Schematic overview of various surfactant HGs and counterions with corresponding chapter included in this study	9
Figure 2.1 Schematic view of an atom. The dense, positively charged nucleus contains most of the atom mass and is surrounded by negatively charged electrons	13
Figure 2.2 Reaction field models of solvation: (a) Onsager model (Dipole), (b) Tomasi's model (PCM), (c) Isodensity model (IPCM) and (d) Self-Consistent Isodensity model (SCIPCM)	19
Figure 2.3 (a) Schematic representation of a wormlike micelle showing characteristic length-scales: the overall radius of gyration R_g , the contour length L , the persistence length l_p and the cross-section radius R_{cs} . (b) schematic of simulation scale.....	21
Figure 3.1 Amines "latent" gelator forms hard gel after ammonium carbamate formation by uptake of CO_2 from solution. The gelation procedure offers a convenient, rapid, and efficient method to sequester (reversibly) and sense the presence of CO_2 . Options test for R_1 and R_2 groups are shown	30
Figure 3.2 Smart fluid (surfactant) triggered by (a) temperature, and (b) light	30
Figure 3.3 Schematic representation of different types of surfactants: (a) single-tailed, (b) doubletailed, (c) gemini, (d) bolaform and (e) oligomer	36
Figure 3.4 General chemical structure of anionic surfactant: (a) ethoxylate (b) sulfate and (c) dimer-(poley) amide succinate)	39
Figure 3.5 General chemical structure of tetra-coordinated ammonium salts. (a) quaternary ammonium (b) tertiary amine (c) 9-octadecen-1-aminium, N,N-bis (2-hydroxyethyl)-N-methyl-chloride	41

	Page
Figure 3.6 Schematic of quaternary ammonium salt preparation starting with primary, secondary or tertiary amine.....	42
Figure 3.7 General molecular structure of (a) alkyl-betaine, examples of this class are: BET-O-30 and BTE-E-40 with $R_1=C_{16}H_{30}$ and $R_1=C_{16}H_{30}$, respectively, numbers in the name refer to percentage of active surfactant, (b) Alkyl-amidopropylbetaine.	43
Figure 3.8 (a) General molecular structure of amidoamine oxide (AO) with R_1 is fatty aliphatic (C_{14} - C_{21}), R_2 alkyl group (C_2 - C_4), R_3 and R_4 are hydroxyl ethyl or heterocyclic ring, and R_5 is H (b) pyrrolidine ring for R_3 and R_4 , (c) piperidine ring, and (d) morpholine ring	44
Figure 3.9 Schematic representation of gemini surfactant, (a) dimertic with the spacer group connecting the two heads groups (HG), (b) bolaform where the spacer connect the two moieties at points on the alkyl tail somewhere close to the end, and (c) cross structure, where the two tails connect to single or double benzene rings, R, and the extension, E, can be the same or different	46
Figure 3.10 Examples of gemini surfactants, (a) sulfonate (b) sulfate (c, d) cationic	47
Figure 3.11 General molecular structure of (a) <i>monoesterquat</i> , (b) <i>diesterquat</i> of dimethyl-diethanol ammonium, (c) <i>diesterquat</i> of triethanol ammonium, (d) <i>diesterquat</i> of 2,3,-dihydroxypropyl ammonium and (e) hydrolysis of esterquat. R can be oleyl or erucyl chain	49
Figure 3.12 Examples of oxygen scavengers from IRGANOX [®] family that can be used to delay internal breakers: (a) Irganox [®] L 565, (b) Irganox [®] L 1010, and (c) Irganox [®] L 1076	50
Figure 3.13 Aggregation morphologies of VES in aqueous solution (a) bilayer micelle, (b) vesicle, (c) spherical (d,e) wormlike micelle, and (f) inverted micelle	52
Figure 3.14 Acid placement techniques in matrix acidizing.....	56

	Page
Figure 3.15 Selection of type of surfactant based on pH range	56
Figure 4.1 Optimized parameters and geometrical structure for $n \leq 7$ water clusters (a) $\text{H}_2\text{O}(\text{H}_2\text{O})$, (b) $\text{H}_2\text{O}(\text{H}_2\text{O})_2$, (c) $\text{H}_2\text{O}(\text{H}_2\text{O})_3$, (d) $\text{H}_2\text{O}(\text{H}_2\text{O})_4$, (e) $\text{H}_2\text{O}(\text{H}_2\text{O})_5$, (f) $\text{H}_2\text{O}(\text{H}_2\text{O})_6$. Shown in these diagrams are hydrogen bond length, HB, (\AA), bond angle ($^\circ$), binding energy, ΔE , (kcal/mol) and number of imaginary frequency in square brackets. Color code: red for O atoms, light gray for H atoms	64
Figure 4.2 Optimized parameters and geometrical structure for $n > 7$ water clusters (a) $\text{H}_2\text{O}(\text{H}_2\text{O})_7$, (b) $\text{H}_2\text{O}(\text{H}_2\text{O})_9$, (c) $\text{H}_2\text{O}(\text{H}_2\text{O})_{17}$. Shown in these diagrams are hydrogen bond length, HB, (\AA), bond angle ($^\circ$), binding energy, ΔE , (kcal/mol) and number of imaginary frequency in square brackets. Color code: red for O atoms, light gray for H atoms	67
Figure 4.3: Optimized parameters and geometrical structure from <i>ab initio</i> molecular orbital calculations for first shell hydro-Na (a) $[\text{Na}(\text{H}_2\text{O})]^+$, (b) $[\text{Na}(\text{H}_2\text{O})_2]^+$, (c) $[\text{Na}(\text{H}_2\text{O})_3]^+$, (d) $[\text{Na}(\text{H}_2\text{O})_4]^+$, (e) $[\text{Na}(\text{H}_2\text{O})_5]^+$, (f) $[\text{Na}(\text{H}_2\text{O})_6]^+$. Shown in these diagrams are bond length (\AA), bond angle ($^\circ$) and APT charges (electronic units). Color code: yellow for Na atoms, red for O atoms, light gray for H atoms	70
Figure 4. 4 Optimized parameters and geometrical structure for second shell hydration of Na-clusters: (a) $\text{Na}[(\text{H}_2\text{O})_4.\text{H}_2\text{O}]^+$, (b) $\text{Na}[(\text{H}_2\text{O})_4.2\text{H}_2\text{O}]^+$, (c) $\text{Na}[(\text{H}_2\text{O})_6.\text{H}_2\text{O}]^+$, (d) $\text{Na}[(\text{H}_2\text{O})_6.2\text{H}_2\text{O}]^+$, (e) $\text{Na}[(\text{H}_2\text{O})_6.12\text{H}_2\text{O}]^+$. Shown in these diagrams are bond length (\AA), bond angle ($^\circ$), binding energy, ΔE , (kcal/mol) and APT charges, q, (electronic units). Number of imaginary frequency is given in square brackets. Color code: dark violet for Na atoms, red for O atoms, light gray for H atoms	72
Figure 4.5 Optimized parameters and geometrical structure from <i>ab initio</i> molecular orbital calculations (a) $\text{Mg}[\text{H}_2\text{O}]^{2+}$, (b) $\text{Mg}[\text{H}_2\text{O}]_2^{2+}$, (c) $\text{Mg}[\text{H}_2\text{O}]_3^{2+}$, (d) $\text{Mg}[\text{H}_2\text{O}]_4^{2+}$, (e) $\text{Mg}[\text{H}_2\text{O}]_5^{2+}$, (f) $\text{Mg}[\text{H}_2\text{O}]_6^{2+}$. Shown in these diagrams are bond length (\AA), bond angle ($^\circ$) and APT charges (electronic units). Color code: yellow for Na atoms, red for O atoms, light gray for H atoms.....	75

Figure 4.6	Optimized parameters and geometrical structure from <i>ab initio</i> molecular orbital calculations (a) $\text{Mg}[(\text{H}_2\text{O})_6.\text{H}_2\text{O}]^{2+}$, (b) $\text{Mg}[(\text{H}_2\text{O})_6.2\text{H}_2\text{O}]^{2+}$, (c) $\text{Mg}[(\text{H}_2\text{O})_6.12\text{H}_2\text{O}]^{2+}$. Shown in these diagrams are bond length (Å), bond angle (°), binding energy, ΔE , (kcal/mol) and APT charges, q, (electronic units). Number of imaginary frequency is given in square brackets. Color code: dark violet for Na atoms, red for O atoms, light gray for H atoms.....	76
Figure 4.7	Optimized parameters and geometrical structure from <i>ab initio</i> molecular orbital calculations (a) $\text{Ca}[\text{H}_2\text{O}]^{2+}$, (b) $\text{Ca}[\text{H}_2\text{O}]_2^{2+}$, (c) $\text{Ca}[\text{H}_2\text{O}]_3^{2+}$, (d) $\text{Ca}[\text{H}_2\text{O}]_4^{2+}$, (e) $\text{Ca}[\text{H}_2\text{O}]_5^{2+}$, (f) $\text{Ca}[\text{H}_2\text{O}]_6^{2+}$. Shown in these diagrams are bond length (Å), bond angle (°), binding energy, ΔE , (kcal/mol) and APT charges, q, (electronic units). Number of imaginary frequency is given in square brackets. Color code: yellow for Ca atoms, red for O atoms, light gray for H atoms	80
Figure 4.8	Optimized parameters and geometrical structure from <i>ab initio</i> molecular orbital calculations (a) $\text{Ca}[\text{H}_2\text{O}]_7^{2+}$, (b) $\text{Ca}[\text{H}_2\text{O}]_8^{2+}$. Shown in these diagrams are bond length (Å), bond angle (°), binding energy, ΔE , (kcal/mol) and APT charges, q, (electronic units). Number of imaginary frequency is given in square brackets. Color code: yellow for Ca atoms, red for O atoms, light gray for H atoms	82
Figure 4.9	Optimized parameters and geometrical structure from <i>ab initio</i> molecular orbital calculations (a) $\text{Ca}[\text{H}_2\text{O}]^{2+}$, (b) $\text{Ca}[\text{H}_2\text{O}]_2^{2+}$, (c) $\text{Ca}[\text{H}_2\text{O}]_3^{2+}$, (d) $\text{Mg}[\text{H}_2\text{O}]_4^{2+}$, (e) $\text{Mg}[\text{H}_2\text{O}]_5^{2+}$, (f) $\text{Mg}[\text{H}_2\text{O}]_6^{2+}$, (g) $\text{Mg}[\text{H}_2\text{O}]_6^{2+}.\text{H}_2\text{O}$, (h) $\text{Mg}[\text{H}_2\text{O}]_6^{2+}.2\text{H}_2\text{O}$. shown in these diagrams are bond length (Å), bond angle (°), binding energy, ΔE , (kcal/mol) and Mulliken charges, q, (electronic units). Color code: yellow for Ca atoms, red for O atoms, light gray for H atoms	83
Figure 5.1	Schematic presentation of the problem, (a) type of ions present in tubing system before reaction with carbonate rocks, and after acid reactions. Iron is a major player in both cases. (b) acid-channeling (wormhole) around the wellbore divided into three zones: fresh acid, partially spent acid and spent acid front	88

- Figure 5.2 Optimized structures with geometrical parameters from *ab initio* calculations using B3LYP/6-311g** (H,O) and B3LYP/SDD (Fe) for hydro-ferrous, Fe(II), complexes, (a) $[\text{Fe}(\text{H}_2\text{O})_2]^{2+}$, (b) $[\text{Fe}(\text{H}_2\text{O})_3]^{2+}$, (c) $[\text{Fe}(\text{H}_2\text{O})_4]^{2+}$ (d) $[\text{Fe}(\text{H}_2\text{O})_5]^{2+}$ (e) $[\text{Fe}(\text{H}_2\text{O})_6]^{2+}$. Shown in these diagrams are bond length (Å), bond angles (°), binding energy (kcal mol^{-1}) and Fe-charge (electron unit). Values in square brackets are APT charges and in parentheses for Mulliken charges both with hydrogen summed into heavy atoms. Color code for atoms is: red for O, slate blue for Fe, and light gray for H 93
- Figure 5.3 Optimized structures with geometrical parameters from DFT calculations using B3LYP/6-311g** (H,O) and B3LYP/SDD (Fe) for hydro-ferric, Fe(III), complexes, (a) $[\text{Fe}(\text{H}_2\text{O})_2]^{3+}$, (b) $[\text{Fe}(\text{H}_2\text{O})_3]^{3+}$, (c) $[\text{Fe}(\text{H}_2\text{O})_4]^{3+}$ (d) $[\text{Fe}(\text{H}_2\text{O})_5]^{3+}$ (e) $[\text{Fe}(\text{H}_2\text{O})_6]^{3+}$. Shown in these diagrams are bond length (Å), bond angles (°), binding energy (kcal mol^{-1}) and Fe-charge (electron unit). Values in square brackets are APT charges and in parentheses for Mulliken charges both with hydrogen summed into heavy atoms. Color code for atoms is: red for O, slate blue for Fe, and light gray for H 96
- Figure 5.4 Optimized structures with geometrical parameters from DFT calculations using B3LYP/6-311g** (H,O) and B3LYP/SDD (Fe) for hydro-ferric, Fe(III), complexes, (a) 24-HB $[\text{Fe}(\text{H}_2\text{O})_{2.12}\text{H}_2\text{O}]^{3+}$, (b) 20-HB $[\text{Fe}(\text{H}_2\text{O})_{2.12}\text{H}_2\text{O}]^{3+}$. Shown in these diagrams are bond length (Å), bond angles (°), binding energy (kcal mol^{-1}) and Fe-charge (electron unit). Color code for atoms is: red for O, slate blue for Fe, and light gray for H 99
- Figure 5.5 Binding energy as a function of water molecules in first shell (n) and second shell (m). (●) for $[\text{Fe}(\text{H}_2\text{O})_n.m\text{H}_2\text{O}]^{2+}$, and (○) $[\text{Fe}(\text{H}_2\text{O})_n.m\text{H}_2\text{O}]^{3+}$. The first 7-points are calculated using B3LYP/6-311++g**/SDD and the last 2-points are at B3LYP/LanL2DZ 100
- Figure 5.6 Optimized structures with geometrical parameters from *ab initio* calculations using B3LYP/6-311g** (H,O) and B3LYP/SDD (Cl) for hydro-chloride clusters: (a) $[\text{Cl}.\text{H}_2\text{O}]^-$, (b) $[\text{Cl}.2\text{H}_2\text{O}]^-$, (c) $[\text{Cl}.3\text{H}_2\text{O}]^-$ with no HB, (d) $[\text{Cl}.3\text{H}_2\text{O}]^-$ with HB between trimer H_2O , (e) $\text{Cl}(\text{H}_3\text{O}).2\text{H}_2\text{O}$, (f) $[\text{Cl}.9\text{H}_2\text{O}]^-$, Shown in these diagrams

are bond length (Å), bond angles (°), binding energy (kcal/mol) and Fe-charge (electron unit). Color code for atoms is: red for O, slate blue for Fe, and light gray for H..... 104

Figure 5.7 Optimized structures with geometrical parameters from *ab initio* calculations using B3LYP/6-311g** (H,O) and B3LYP/SDD (Fe) for ferricchloride complexes: (a) $[\text{FeCl}_5\text{H}_2\text{O}]^{2+}$, (b) $[\text{Fe-transCl}_2\text{H}_2\text{O}]^+$, (c) $[\text{Fe-cisCl}_2\text{H}_2\text{O}]^+$, (d) $[\text{FeCl}_3\text{H}_2\text{O}]$. Shown in these diagrams are bond length (Å), bond angles (°), binding energy (kcal mol^{-1}) and Fe-charge (electron unit). Values in square brackets are APT charges and in parentheses for Mulliken charges both with hydrogen summed into heavy atoms. Color code for atoms is: red for O, slate blue for Fe, and light gray for H..... 107

Figure 5.8 Optimized structures with geometrical parameters from *ab initio* calculations using B3LYP/6-311g** (H,O) and B3LYP/SDD (Fe) for ferricchloride complexes: (a) $[\text{FeCl}_4\text{H}_2\text{O}]^-$, (b) $[\text{FeCl}_4]^-$, (c) $[\text{FeCl}_5\text{H}_2\text{O}]^{2-}$, (d) $[\text{FeCl}_6]^{3-}$. Shown in these diagrams are bond length (Å), bond angles (°), binding energy (kcal mol^{-1}) and Fe-charge (electron unit). Values in square brackets are APT charges and in parentheses for Mulliken charges both with hydrogen summed into heavy atoms. Color code for atoms is: red for O, slate blue for Fe, and light gray for H..... 110

Figure 5.9 Optimized structures with geometrical parameters from *ab initio* calculations using B3LYP/6-311g** (H,O) and B3LYP/SDD (Fe, Cl) for ferricchloride complexes: (a) tetrachloroferrate $[\text{FeCl}_4\text{H}_2\text{O}]^-$, (b) shows hydrogen and Cl-H bonds, (c) shows hydrogen bonds only. Shown in these diagrams are bond length (Å), bond angles (°), binding energy (kcal mol^{-1}) and Fe-charge (electron unit). Values in square brackets are APT charges and in parentheses for Mulliken charges both with hydrogen summed into heavy atoms. Color code for atoms is: red for O, slate blue for Fe, and light gray for H..... 111

Figure 5.10 Optimized structures with geometrical parameters from DFT calculations using B3LYP/6-311g** (H,O) and B3LYP/SDD (Fe) for iron-hydroxide: (a) $[\text{Fe}(\text{OH})_2\text{H}_2\text{O}]$, (b) $[\text{Fe}(\text{OH})_3\text{H}_2\text{O}]$. Shown in these diagrams are bond length (Å), bond angles (°), binding energy (kcal mol^{-1}) and Fe-charge (electron unit). Values in square brackets are APT charges and in parentheses for Mulliken charges both with

	hydrogen summed into heavy atoms. Color code for atoms is: red for O, slate blue for Fe, and light gray for H.....	115
Figure 5.11	Optimized geometrical structure in gas-phase of hydrated hydrogen sulfide using B3LYP/6-311++g**. (a) $\text{H}_2\text{S}(\text{H}_2\text{O})$, (b) $\text{H}_2\text{S}(\text{H}_2\text{O})_2$, (c) $\text{H}_2\text{S}(\text{H}_2\text{O})_3$, (d) $\text{H}_2\text{S}(\text{H}_2\text{O})_4$, (e) $\text{H}_2\text{S}(\text{H}_2\text{O})_5$, (f) $\text{H}_2\text{S}(\text{H}_2\text{O})_6$, (g) $\text{H}_2\text{S}(\text{H}_2\text{O})_7$, and (h) $\text{H}_2\text{S}(\text{H}_2\text{O})_8$. Color code: red for O, light gray for H and yellow for S.....	119
Figure 5.12	Binding energy and average bond length of $\text{H}_2\text{O}(\text{H}_2\text{O})_n$ and $\text{H}_2\text{S}(\text{H}_2\text{O})_n$ ($n=1-8$) clusters. (■) for w- H_2O energy (left-y-axis) (□) for $\langle\text{HB}\rangle$ of w- H_2O cluster (right-y-axis), (▲) for w- H_2S energy (left-y-axis) and (△) for $\langle\text{SH}-\text{O}\rangle$ of w- H_2O cluster (right-y-axis). $\Delta E_{w_H_2O} = -9.666(n) + 5.81$, ($R^2 = 0.994$) and $\Delta E_{w_H_2S} = -8.9352(n) + 9.17$, ($R^2 = 0.992$)	120
Figure 5.13	Optimized structure of Fe-S. (a) FeS_3 , (b) FeS_4 , (c) FeS_5 , and (d) $\text{Fe}_4\text{S}_4.4\text{H}_2\text{O}$	122
Figure 6.1	Optimized geometrical structure of acetic acid (AA) head group with localized HOMO, LUMO molecular orbitals, and electron density. (a) AA in gas-phase, (b) anionic $[\text{AA}]^-$ in gas-phase and (c) AA in water solution, with second row for LUMO, third for HOMO, and forth row for electron density potential, respectively. Isosurface value = $0.02 \text{ e}/\text{\AA}^3$, $0.0004 \text{ e}/\text{\AA}^3$ for MO and density, respectively	131
Figure 6.2	Optimized structures for acetic acid (AA) and acetate (^-OAc) in gas-phase calculated using B3LYP/6-311++G**: (a) dimers $(\text{AA})_2$, (b) dimers $(\text{AA})_2$, (c) $\text{AA}.\text{H}_2\text{O}$, (d) $^-\text{OAc}.\text{H}_2\text{O}$, (e) $\text{AA}(\text{HS})^-$, (f) $\text{AA}(\text{OH})^-$, (g) $\text{AA}(\text{H}_3\text{O})^+$, and (h) $^-\text{OAc}(\text{H}_3\text{O})$. Shown in this graphs binding energy, ΔE_i , and average hydrogen bond, $\langle\text{HB}\rangle$. Color code: red for O, light gray for H, dark gray for C and yellow for S	131
Figure 6.3	Optimized structures for acetate (^-OAc) HG complexation in gas-phase with Ca^{2+} ion calculated using B3LYP/6-311++G**: (a) $\text{Ca}(^-\text{OAc})_2$, (b) $\text{Ca}(^-\text{OAc})_2.2\text{H}_2\text{O}$, and (c) $\text{Ca}(^-\text{OAc})_2.4\text{H}_2\text{O}$. Shown in	

	this graphs bond distance (\AA), binding energy, ΔE_i , and average hydrogen bond, $\langle \text{HB} \rangle$. Color code: red for O, light gray for H, dark gray for C, and for Ca	138
Figure 6.4	Optimized structures for <i>di</i> -, <i>tri</i> - and <i>tetra</i> acetate (OAc) HG complexation in gas-phase with Ca^{2+} ion calculated using B3LYP/6-311++G**. (a) $\text{Ca-cis}(\text{OAc})_2\cdot\text{H}_2\text{O}$ (b) $\text{Ca}(\text{OAc})_4\cdot 2\text{H}_2\text{O}$, (c) $\text{Ca}(\text{OAc})_3\cdot 3\text{H}_2\text{O}$, (d) 3D view of $\text{Ca}(\text{OAc})_4\cdot 2\text{H}_2\text{O}$, (e) $\text{Ca}(\text{OAc})_3\cdot 4\text{H}_2\text{O}$ and (e) $\text{Ca}(\text{OAc})_4\cdot 3\text{H}_2\text{O}$. Shown in this graphs bond distance (\AA), binding energy, ΔE_i , and average hydrogen bond, $\langle \text{HB} \rangle$	140
Figure 6.5	Optimized structures for acetate (OAc) HG complexation in gas-phase with metal ions calculated using B3LYP/6-311++G**: (a) $\text{Na}(\text{OAc})_2\cdot 4\text{H}_2\text{O}$, (b) $\text{Mg}(\text{OAc})_2\cdot 4\text{H}_2\text{O}$, and (c) $\text{Fe}(\text{OAc})_2\cdot 4\text{H}_2\text{O}$, (d) $\text{Fe}(\text{OAc})_3\cdot 3\text{H}_2\text{O}$, (e,e') $\text{Al}(\text{OAc})_3\cdot 3\text{H}_2\text{O}$ Shown in this graphs binding energy, ΔE_i , and average hydrogen bond, $\langle \text{HB} \rangle$. Color code: red for O, light gray for H, and dark gray for C.	143
Figure 6.6	Binding energy of metal cations with water molecules, $[\text{M}(\text{H}_2\text{O})_6]^{x+}$ (\square) and with acetate, $\text{M}(\text{OAc})_x\cdot (n-x)\text{H}_2\text{O}$ (\blacksquare). Replacement of x -water molecules with corresponding number of acetate anions is favorable (exothermic process)	146
Figure 6.7	Bond length in octahedral metal acetate complex $\text{M}(\text{OAc})_x\cdot (n-x)\text{H}_2\text{O}$. (\square) for metal ion with water oxygen, and (\blacksquare) for metal with carboxylate oxygen of HG.....	147
Figure 6.8	Optimized structures for acetate (OAc) HG interaction with organic salts in gas-phase calculated using B3LYP/6-311++G**: (a) NaHNC-OAc , (b) NaSal-OAc , (c) CaSal-OAc and (d) PTH-OAc . Shown in this graphs binding energy, ΔE_i , and average hydrogen bond, $\langle \text{HB} \rangle$. Color code: red for O, light gray for H, dark gray for C	148
Figure 6.9	Molecular simulation snapshot for a system of 32 erucate anionic surfactants ($4\times 4\times 2$) with 2839 water molecules and 8 counterions (Ca^{2+}). (a) Initial geometry of 0.5 wt% and (b) final structure after 100,000 time steps (1 ns)	151

Figure 6.10	Optimized geometrical structure of potassium butanoate (PB) head group with localized HOMO and LUMO molecular orbitals. (a) PB in gas-phase, and (b) anionic $[PB]^-$ in gas-phase with second row for HOMO, and third for LUMO and forth row for electron density potential, respectively. Isosurface value= $0.02 \text{ e}/\text{\AA}^3$, $0.004 \text{ e}/\text{\AA}^3$ for MO and density, respectively	153
Figure 6.11	Complexation of potassium butanoate (PB) head group with calcium (Ca^{2+}) in gas-phase. Optimized structure at B3LYP/6-311++G**	154
Figure 6.12	Calculated relaxed potential energy scanning for the dihedral angle, ϕ , C–C–C–C (1-2-6-11 in Figure C.1) using 6-31+g* at (●) HF and (○) B3LYP. ΔE is calculated as relative energy to the minimum value at $\phi=180^\circ$	154
Figure 6.13	Optimized geometrical structure of sodium butane-1-sulfonate (S1BS) head group with localized HOMO and LUMO molecular orbitals. (a) S1BS in gas-phase, (b) anionic $[S1BS]^-$ in gas-phase and (c) S1BS in water solution, with second row for HOMO, and third for LUMO, respectively	156
Figure 6.14	Potential density of sodium butane-1-sulfonate (S1BS) (a) S1BS in gas-phase, (b) anionic $[S1BS]^-$ in gas-phase.....	157
Figure 6.15	Complexation of sodium butane-1-sulfonate (S1BS) head group with (a) Ca^{2+} , and (b) Mg^{2+} in gas-phase using B3LYP level of theory and 6-311++G** basis set. Binding energy for $Mg(S1BS)_2$ is 103.03 kcal/mol higher than that for $Ca(S1BS)_2$	157
Figure 7.1	Optimized geometrical structure of selected cationic head groups (HGs) with localized HOMO and LUMO molecular orbitals in the second and third column, respectively. (a) BdMEA, (b) TMA, (c) EhhMEA, (d) HMMEA and (e) TMEA . Color code: red for O, blue for N, dark gray for C and light grey for H	164
Figure 7.2	Optimized molecular structure for TMA interaction with Cl and 4-water molecules calculated at B3LYP/LAnL2DZ. (a) $TMA[Cl.4H_2O]$, (b) $TMA[Cl.4H_2O]$, (c) $TMA[Cl.4H_2O]$, (d)	

	TMA[Cl ₄ H ₂ O], (e) TMA-Cl and (f) [TMA-Cl ₄] ³⁻ . Shown in the picture the total binding energy, kcal/mol, average hydrogen bond, Å and Cl-H bond distance Å. color code: red for O, green for Cl, dark gray for C and light gray for H	168
Figure 7.3	Initial (first column) and final optimized structure (second column) of TMEA cationic HG with Cl ⁻ as a counterion.....	170
Figure 7.4	Initial (first column) and final optimized structure (second column) of HMMEA cationic HG with Cl ⁻ as a counterion.....	173
Figure 7.5	Optimized structures of cationic HG complexes with tetrachloroferrate. (a) TMA-FeCl ₄ , (b) TMA-FeCl ₄ .H ₂ O, (c) TMA-FeCl ₄ .H ₂ O, and (d) HMMA-FeCl ₄ .2H ₂ O. shown on the right-hand side binding energy, kcal/mol, and bond length, Å. color code: green for Cl, red for O, dark blue for Fe, dark gray for C and light gray for H.....	176
Figure 7.6	Optimized geometrical structure in gas-phase calculated using B3LYP/LanL2DZ for (a) [Cl ₃ Fe-O-FeCl ₃] ²⁻ , (b) [Fe ₂ Cl ₉] ³⁻ , (c) TMA) ₂ -Fe ₂ OCl ₆ , (d) (TAM)-Fe ₂ Cl ₉	178
Figure 7.7	Optimized structures of TMA ⁺ complexes with di- and trianionic compounds in gas-phase using B3LYP/LanL2DZ. (a,b) (TMA) ₂ -Fe ₂ OCl ₆ , (c,d) (TAM)-Fe ₂ Cl ₉	179
Figure 7.8	General structure of (a) symmetrical <i>bis</i> -quaternary ammonium salt with <i>s</i> and <i>R</i> groups are specified for each gemini HG considered in this study, and molecular orbital (HOMO, LUMO) of (b) bAETMedA, and (c) dETMedA.....	180
Figure 7.9	Optimized structures of gemini surfactant HGs. (a) dETMedA ²⁺ , (b) dETMedA-Cl ₂ , (c) bAETMedA ²⁺ , (d) bAETMedA-Cl ₂ , (e) HMB14dA, and (f) HME12dA.....	181
Figure 7.9	MD simulation snapshot after 1 ns	182

Figure 8.1	Optimized geometrical structure of selected betaine head groups (HGs) with localized HOMO and LUMO molecular orbitals in the second and third columns, respectively. (a) AAMCDEEA, (b) CMDMEA, (c) CMPMBdA (d) CtMMA, and (e) TMoEA. Color code: red for O, blue for N, dark gray for C and light grey for H 189	189
Figure 8.2	Optimized structure of Betaine HG with chloride ion. (a) AAMCEDEEA, (b) AAMCEDEEA, (c) CMDMEA, (d) TMoA, (e) CMPMBdA, and (f) CTMMA 191	191
Figure 8.3	Optimized structures of betaine HG complexes with tetrachloroferrate. (a) AAMCDEEA, and (b) CTEEA 192	192
Figure 8.4	Optimized geometrical structure of AAMCDEEA with cationic metals 193	193
Figure 8.5	MD simulation snapshot after 1 ns of C22 AAMCDEEA with (a) 284(H ₂ O)_5Cl (3.1wt%), (b) 289(H ₂ O)_15Cl (8.5 wt%), (c) 285(H ₂ O)_30Cl (15.9wt%) and (d) 287(H ₂ O)_40Cl (20.0 wt%) 194	194
Figure A.1	Schematic diagram of the problem 226	226
Figure A.2	Schematic representation of the most stable water-cluster, H ₂ O(H ₂ O) _n , (n=1-9,18) calculated at B3LYP/6-311++G(d,p) 227	227
Figure A.3	Binding energy of water cluster as function of water monomers for (H ₂ O) _n , (n=1-9) calculated at: (♦) B3LYP/6-311++G(d,p) from this study, (■) HF/6-311++G (2d,2p), (▲) B3LYP/6-311++G(2d,2p) and (×) MP2/6-311++G(2d,2p). The last three are taking from Ref.(Maheshwary et al., 2001). The dotted line shows a linear fitting of $\Delta E_i, b=A+B/n$, with B = 12.89 and A = -9.278 228	228
Figure A.4	Average hydrogen bond for water clusters, (H ₂ O) _n , (n=1-9) calculated at: B3LYP/6-311++G(d,p) 228	228
Figure A.5	Reorganization energy for the clusters, [M(H ₂ O) _n] ^{x+} , (n=1-9) calculated at: B3LYP/6-311++G(d,p). As the size of metal ion	

	Page
increases, the reorganization energy decreases	229
Figure A.5 Reorganization energy for the clusters, $[M(H_2O)_n]^{x+}$, ($n=1-9$) calculated at: B3LYP/6-311++G(d,p) . As the size of metal ion increases, the reorganization energy decreases	229
Figure A.6 Binding energy for the clusters, $[M(H_2O)_n]^{x+}$, ($n=1-18$) calculated at: B3LYP/6-311++G(d,p)	
Figure B.1 Formations of the Fe(III) species in HCl solutions. The mole fractions were calculated from the reported stability constants.....	235
Figure B.2 Change of Binding energy as function of water molecules in hydro iron complex calculated at B3LYP/6-311++G(d,p)/SDD.....	236
Figure B.3 Binding energy as a function of water molecules in first shell (n) and second shell (m). (●) for $[Fe(H_2O)_n.mH_2O]^{2+}$, and (○) $[Fe(H_2O)_n.mH_2O]^{3+}$. The first 7-points are calculated using B3LYP/6-311++g**/SDD and the last 2-points are at B3LYP/LanL2DZ.....	237
Figure B.4 3D geometrical structure of $[Cl(H_2O)_9]^-$ with (a) all hydrogen bonding (HB) and Cl–H are connected and (b) all three H_2O trimers around Cl^- ion calculated at B3LYP/6-311++G(d,p)/SDD.....	237
Figure B.5 Optimized geometrical structure in gas-phase of hydrated hydrogen sulfide using B3LYP/6-311++g**. (a) $[H_3O(H_2S)]^+$, (b) $[H_3O(H_2S)_2]^+$, (c) $[H_3O(H_2S)_3]^+$, (d) $[H_3O(H_2S)_4]^+$, (e) $[H_3O(H_2S)_5]^+$, (f) $[H_3O(H_2S)_6]^+$, (g) $[H_3O(H_2S)_7]^+$, and (h) $[H_3O(H_2S)_8]^+$. Color code: red for O, light gray for H and yellow for S.....	239
Figure C.1 : Fundamental interactions in VES solution (a) For polar solvents, hydrophobic interaction use to dominate, (b) while in the case of non polar solvent Van der Waals is specially relevant, (c) electrostatic and (d) hydrogen bonds.....	243

Figure C.2	Optimized molecular structure for (a) $\text{AA}(\text{H}_3\text{O})^+$ in gas-phase, (b) dimer $(\text{AA})_2$ in water solvent, PCM model. All calculated using B3LYP/6-311++G**, and color code is: red for O, dark gray for C, light gray for H and yellow for S.....	224
Figure C.3	Relation between binding energy of metal acetate, metal hydrate and square valency divided by ionic radius of the cation.....	224
Figure C.4	3D optimized molecular structure with Ca–O and hydrogen bond (OH–O) are connected for All calculated using B3LYP/6-311++G**, and color code is: red for O, dark gray for C, light gray for H and yellow for Ca, Al	245
Figure C.5	Proposed schematic structure for $\text{Ca}(\text{AA})_3 \cdot 2\text{H}_2\text{O}$, $[\text{R}=(\text{CH}_3\text{CH}_2)_n]$	246
Figure C.6	Effect of coordination number, water molecules, n, and number of acetate HGs, m, on the binding energy (top) and bond length (bottom) for calcium acetate complex, $[\text{Ca}(\text{OAc})_n \cdot m\text{H}_2\text{O}]^{2-n}$	247
Figure C.7	Optimized geometry of metal acetate at B3LYP/6-311++g**(H,O,C,Al)/ SDD(Mn,Zn). (a) $\text{Mn}(-\text{OAc})2.4\text{H}_2\text{O}$, (b) $\text{Mn}(-\text{OAc})3.3\text{H}_2\text{O}$, (d) $\text{Zn}(-\text{OAc})2.4\text{H}_2\text{O}$, and (e) $\text{Al}(\text{OAc})_3$. Shown below each structure, binding energy (kcal/mol), bond length (Å), and number of imaginary frequencies in square brackets	248
Figure C.8	Optimized structure of organic salts at B3LYP/6-311++g**. (a) NaSal, (b) NaHNC, (c) PTHC, and (d) Et3NHCl.....	248
Figure C.9	MD simulation for 1 ns of C22(OAc) with (a) 5, (b) 10 and (c) 15 wt%.....	250
Figure D.1	Optimized molecular structure of $[\text{Cl}(\text{H}_2\text{O})_4]^-$ at B3LYP/6-311++g**(H,O)/SDD(Cl). (a) $[\text{Cl}(\text{H}_2\text{O})_4]^-$, and (b) top view. Shown in the figure binding energy, kcal/mol, average hydrogen bond between water molecules. The average $\langle \text{H}—\text{Cl} \rangle = 2.3929$ Å. color code: green for Cl, red for O, light gray for H.....	252

Figure D.2	Optimized structure in gas-phase of (a) HMMAEA, and (b) HMMAEA—Cl(S3)	252
Figure D.3	Initial structures for interaction between TMA^+ and $[\text{Cl}(\text{H}_2\text{O})_4]^-$ with final optimized geometries are shown in Figure 7.2. Shown in the picture bond distances, Å. color code: red for O, green for Cl, dark gray for C and light gray for H	253
Figure D.4	Optimized structure in gas-phase of (a) BdMEA—Cl (S1), and (b) BdMEA—Cl (S2).....	253
Figure D.5	Optimized structure in gas-phase of (a) EhhMEA (b) EhhMEA—Cl (S1), (c) EhhMEA—Cl (S2), and (d) EhhMEA—Cl (S3)	255
Figure D.6	Optimized structure of TMA with organic salt (Sal^-) in gas-phase	256
Figure D.7	Optimized structure of TMA^+ with $[\text{FeCl}_4]^-$ in gas-phase	256
Figure D.8	Optimized structures of TMA complexes with (a) $\text{Fe}_2\text{Cl}_6\text{O}$, and (b) Fe_2Cl_9 . Shown in the Figure all bonds Cl—H <3.0 Å, are connected.....	257
Figure D.9	MD simulation of C22 BdMEA in water solution at various Cl concentrations	257
Figure E.1	Optimized structure for AAMCDEEA with two water molecules calculated at B3LYP/6-311++g**	259
Figure E.2	Optimized geometrical structure of selected amidoamine-oxide head groups (HGs) with localized HOMO and LUMO molecular orbitals in the second and third column, respectively. (a) APhdMA, (b) APhP, (c) AphMA, and (d) dMNPA. Color code: red for O, blue for N, dark gray for C and light grey for H	260
Figure E.3	Optimized structure of Amidoamine Oxide with water molecules	264

LIST OF TABLES

	Page
Table 1.1 Summary of all QM calculations included in the study	10
Table 1.2 Summary of all MD simulations included in the study	10
Table 2.1 Statistical ensembles	21
Table 2.2 Summary of molecular simulation studies reported on surfactant systems	24
Table 3.1 List of major acid additives with their concentration	34
Table 3.2 Comparison between polymeric and surfactant diversion systems	38
Table 3.3 Dependence of gemini surfactant properties on molecular structure, some reported physical properties including Krafft temperature, T_k , critical micelle concentration, cmc, for the general structure in Figure 7(c)	47
Table 3.4 Summary of common surfactants used in oilfield industry as diverting fluid.....	55
Table 4.1 Thermodynamic properties of carbonate minerals.....	59
Table 4.2 Calculated zero-point vibrational energy, ZPVE, bond distance, bond angle, and total binding energy for $[\text{Na}(\text{H}_2\text{O})_n.m\text{H}_2\text{O}]^{2+}$ using B3LYP/6-311++G**	73
Table 4.3 Thermodynamic properties of $[\text{Mg}(\text{H}_2\text{O})_n.m\text{H}_2\text{O}]^{2+}$ using B3LYP/6- 311++G**	78
Table 4.4 Thermodynamic properties of $[\text{Ca}(\text{H}_2\text{O})_n.m\text{H}_2\text{O}]^{2+}$ using B3LYP	84

	Page
Table 5.1 Calculated average bond length, average bond angle, and equilibrium binding energy for $[\text{Fe}(\text{H}_2\text{O})_n]^{x+}$, $\Delta E_i = E_{\text{cluster}} - (E_{\text{Fe}} + nE_{\text{H}_2\text{O}})$ at $T=298.15$ K and $p=1$ atm using B3LYP/6-311g**/SDD.....	94
Table 5.2 Calculated average bond length, average bond angle, and equilibrium binding energy for $[\text{Fe}(\text{H}_2\text{O})_6.12\text{H}_2\text{O}]^{x+}$, $\Delta E_i = E_{\text{cluster}} - (E_{\text{Fe}} + 18E_{\text{H}_2\text{O}})$ at $T=298.15$ K and $p=1$ atm using B3LYP.....	100
Table 5.3 Calculated average bond length, equilibrium binding energy (gas-phase and water solvent) for $[\text{FeCl}_x(\text{H}_2\text{O})_n]^{3-x}$, $\Delta E_i = E_{\text{complex}} - (E_{\text{Fe}} + nE_{\text{H}_2\text{O}} + xE_{\text{Cl}})$ at $T=298.15$ K and $p=1$ atm using B3LYP/6-311g**/SDD.....	112
Table 5.4 Binding energy and geometrical properties of $\text{H}_2\text{O}(\text{H}_2\text{O})_n$, $\text{H}_2\text{S}(\text{H}_2\text{O})_n$ and $\text{H}_3\text{O}(\text{H}_2\text{S})_n$	120
Table 5.5 Equilibrium reactions of Fe(III), Fe(II) with various anions in solution and their precipitation conditions.....	238
Table 5.6 Thermodynamic properties of aquoiron complexes, $[\text{Fe}(\text{H}_2\text{O})_n.m\text{H}_2\text{O}]^{2,3+}$	238
Table 6.1 Thermodynamic property of the complex $\text{Ca}(\text{OAc})_n.m\text{H}_2\text{O}$, with binding energy, $\Delta E_i = E_{\text{complex}} - (E_{\text{Ca}^{2+}} + nE_{\text{H}_2\text{O}} + mE_{\text{OAc}})$	137
Table 6.2 Thermodynamic property of the complex $\text{M}^{x+}(\text{OAc})_n.(6-n)\text{H}_2\text{O}$	154
Table 6.3 Geometrical and binding properties of $\text{Ca}(\text{Bu})_n.m\text{H}_2\text{O}$	154
Table 6.4 Binding energy, bond length and atomic charge calculated at B3LYP/6-311++G** for $\text{M}(\text{HG}).4\text{H}_2\text{O}$, ($\text{M} = \text{Ca}^{2+}$, Mg^{2+} ; $\text{HG} = \text{H}_2\text{O}$, S1BS, SPS)	156
Table A.1 Thermodynamic properties for water clusters, $\text{H}_2\text{O}.n\text{H}_2\text{O}$ using B3LYP/6-311++G**.....	231

	Page
Table A.2 Thermodynamic properties of $[\text{Na}(\text{H}_2\text{O})_n.m\text{H}_2\text{O}]^+$ using B3LYP/6-311++G**	231
Table A.3 Thermodynamic properties of $[\text{M}(\text{H}_2\text{O})_n.m\text{H}_2\text{O}]^{2+}$ using B3LYP/6-311++G**	232
Table A.4 Total sequential binding energy, $\Delta E_s = E_{\text{M}(\text{H}_2\text{O})_n} + [1 - E_{\text{M}(\text{H}_2\text{O})_n} + E_{\text{H}_2\text{O}}]$, (kcal/mol) for $[\text{M}(\text{H}_2\text{O})_n.m\text{H}_2\text{O}]^{x+}$ Complexes at Various Level of Theory. Values in the table are for $-\Delta E_s$	233
Table B. 1 Solubility of iron oxides and green rust at $T=298.15$ K, $p=1$ bar	234
Table B. 2 Thermodynamic properties	234
Table B.3 Effect of multiplicity on thermodynamic properties of Ions and complexes using DFT in gas-phase. All calculations performed using B3LYP level of theory and 6-311++G** (for H, O, S), SDD (for Fe, Cl) basis sets. Minimum spin state is in parenthesis	235
Table B.4 Effect of theory level and basis on the thermodynamic properties of Fe^{x+} ($x=2,3$). Spin Sates are: 5 for Fe^{2+} and 6 for Fe^{3+}	236
Table B.5 Equilibrium reactions of Fe(III), Fe(II) with various anions in solution and their precipitation conditions	
Table B.6 Thermodynamic properties of aquoiron complexes, $[\text{Fe}(\text{H}_2\text{O})_n.m\text{H}_2\text{O}]^{2,3+}$	
Table B.7 List of most common Fe–S systems with their properties and natural abundance	240
Table B.8 Geometrical properties of first shell, $\text{Fe}(\text{H}_2\text{O})_n$, hydration	241
Table B.9 Thermodynamic properties and hydrogen bond in the structure $[\text{Fe}(\text{H}_2\text{O})_6.12\text{H}_2\text{O}]^{2,3+}$	241

	Page
Table C.1	Fundamental interactions in VES solution (a) For polar solvents, hydrophobic interaction use to dominate, (b) while in the case of non polar solvent Van der Waals is specially relevant, (c) electrostatic and (d) hydrogen bonds 249
Table C.2	Geometrical parameters of optimized structure: $[M(H_2O)_6]$ at B3LYP..... 249
Table C.3	Thermodynamic properties of Acetate (OAc) HG complexation with metal ions calculated at B3LYP/6-311++G**. Binding energy is calculated by: $\Delta E_i = [M(OAc)_n.mH_2O] - [nOAc + M^{x+} + mH_2O]$ 251
Table C.4	Thermodynamic properties of Acetate (OAc) HG complexation with metal ions calculated at B3LYP/6-311++G**. Binding energy is calculated by: $\Delta E_i = [Ca(OAc)_n.mH_2O] - [nOAc + Ca^{2+} + mH_2O]$ 251
Table D.1	Binding energy and structural properties of cationic HGs with counterions calculated at B3LYP/6-311++g**(N,C,H)/SDD(Cl) 256

CHAPTER I

INTRODUCTION

Once an oil well has been constructed, its production can be limited by low natural reservoir permeability or by permeability reductions induced by particulate damage to the rock pore space during either drilling or production. Matrix acidizing and creation of hydraulic fractures are major stimulation processes commonly used to overcome these limitations. The oil and gas industry has been acidizing oil and/or gas bearing formations since the 1930s (Economides and Nolte, 2000). The primary acid used in the early days was hydrochloric acid. It is interesting to note that hydrochloric acid is still the primary acid used today for oil and gas well damage removal and stimulation. Since the early days, various other acid types have been developed along with additives to help make acidizing more effective.

In attempt to achieve uniform placement of acid across all layer various placement techniques have been used in the industry. Production log data can be utilized to identify high-permeability zones or thief zones, enabling the design of an efficient placement technique. Diversion techniques can be either mechanical, or chemical. Although mechanical techniques are very effective, they are more expensive and time consuming than chemical techniques and they are not applicable in open-hole or gravel packed completion. Mechanical control of treating fluid placement can be accomplished by coiled tubing with an inflatable packer, or with conventional straddle packers or ball sealers. On the other hand, chemical diverters can be achieved through placing viscous fluid into the matrix to decrease injectivity or to create a filter resistance. This filter cake results in temporary resistance (skin) which alters the injection profile. Gelled and foamed acids are being used increasingly as a mean of improving acid placement. The most common diverting fluids used are polymers such as polyacrylamide.

This dissertation follows the style of Journal of Petroleum Science and Engineering.

This polymer can be cross-linked by borate or transition metal complexes to form viscoelastic gels. A serious limitation for many of these polymeric fluids is that, the in-situ gelled acids caused loss of core permeability in tight carbonate cores (Nasr-El-Din and Samuel, 2007). Precipitation of the cross-linker (iron) at high temperature and in sour environment is common. Also, H₂S scavengers may interact with the polymer and loss their ability to remove hydrogen sulfide. In addition, it could form external filter cake that reducing injectivity and large volume normally needed. A new generation of diverting fluids based upon viscoelastic surfactant (VES) has been introduced (Chang et al., 1999) with attempts to address this problem. The gel rheology of VES is caused by wormlike cylindrical micelles once they come into contact with hydrocarbon.

The major concerns with matrix acidizing in carbonates include the following: effective diversion, limiting wormholing and excessive fluid leak off, high and low temperature applications, acid concentration. A better understanding of the chemical diversion is needed to explain difference in data reported by various laboratories especially on VES. This introduction chapter will address formation damage causes as a mitigation step to design an effective and efficient stimulation treatment. In addition, statement of the problem, objectives and approach are presented.

1.1 Formation Damage

One of the most common reasons for a decline in oil production is "damage" to the formation that plugs the rock pores and therefore impedes the flow of oil. Sources of formation damage include: spent drilling fluid, fines migration, paraffin, mineral precipitation (scale). This damage generally arises from another fluid deliberately injected into the wellbore, for instance, drilling fluid. Even after drilling, some drilling fluid remains in the region of the formation near the wellbore, which may dehydrate and form a coating on the wellbore (Chang et al. 2002). The natural effect of this coating is to decrease permeability to oil moving from the formation in the direction of the wellbore. Another reason for lower-than-expected production is that the formation is

naturally "tight," (low permeability formations) that is, the pores are sufficiently small that the oil migrates toward the wellbore only very slowly. The common denominator in both cases (damage and naturally tight reservoirs) is low permeability.

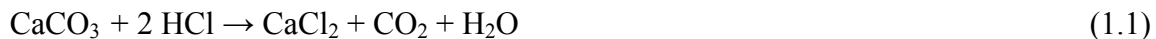
The reservoir zone where permeability has been affected by formation damage is referred to as skin. The extent of this permeability reduction depends on the amount of damage and the depth to which it occurs. Formation damage is typically categorized by the mechanism of its creation as either natural or induced (Sengul and Remisio, 2002). Natural damages are those occur primarily as a result of producing the reservoir fluid. Induced damages are the result of an external operation that was performed on the well such as a drilling, well completion, repair, stimulation treatment or injection operation. In addition, some completion operations, induced damages or design problems may trigger natural damage mechanisms. Damage identification is a prerequisite to the proper design of a carbonate acidizing treatment (Abou-Sayed et al., 2005). In formations that are highly sensitive to acid, nonacidic formulations should be used, and the choice of the treating fluid is usually determined by the type of damage. Furthermore, the volume of treating fluid depends on the extent and location of the damage. In addition, poorly cemented chinks can be permanently impaired by acidic water-base fluids, which can easily dissolve the calcitic cement material, resulting in formation compaction from a loss of mechanical strength.

Formation damage tends to receive less attention in horizontal completions than in vertical wells (Sengul and Remisio, 2002). This is largely due to the significantly higher production rates that are often achieved in these wells. However, few horizontal wells perform as well as theoretically possible, and many do not produce any more than vertical wells under the same conditions. This is probably because formation damage in horizontal wells is often greater than in vertical wells.

1.2 Well Stimulation

Hydrocarbons are obtained from a reservoir by drilling a well that penetrates the hydrocarbon-bearing formation. This provides a partial flow path for the oil to reach the surface. In order for oil to be produced, that is, travel from the formation to the wellbore (and ultimately to the surface) there must be a sufficiently unimpeded flowpath from the formation to the wellbore. This flowpath is depends on porosity and permeability of the formation, mainly. Techniques performed by hydrocarbon producers to increase the net permeability of the reservoir are referred to as "stimulation techniques." Essentially, one can perform a stimulation technique by: injecting chemicals into the wellbore to react with and dissolve the damage (filter cake removal), injecting chemicals through the wellbore and into the formation to react with and dissolve small portions of the formation to create alternative flowpaths for the hydrocarbon (thus rather than removing the damage, redirecting the migrating oil around the damage) or injecting chemicals through the wellbore and into the formation at pressures sufficient to actually fracture the formation and creating a large flow channel.

Carbonate rocks, by definition, contain more than 50% carbonate minerals (Economides and Nolte, 2000). The most common carbonate minerals are calcite (calcium carbonate, CaCO_3) and dolomite, MgCO_3). Carbonate rocks are typically classified by the calcite:dolomite ratio, and those with a ratio higher than 50% are generally called limestones. Carbonate rocks present singular physical characteristics, such as double porosity or high permeability contrasts. When stimulating carbonate reservoir, HCl reacts with carbonate (calcite and dolomite) as shown in the following equations:



At present, matrix acidizing treatments are plagued primarily by three very serious limitations: (1) radial penetration; (2) axial distribution; and (3) corrosion of the pumping and well bore tubing. The first two limitations are strongly related to acid placement (Chang et al., 2002). The problem of proper placement is a particularly

vexing one since the injected fluid will preferentially migrate to higher permeability zones (the path of least resistance) rather than to the lower permeability zones, yet it is those latter zones which require the acid treatment (i.e., because they are low permeability zones). In response to this problem, numerous, disparate techniques have evolved to achieve more controlled placement of the fluid i.e., to divert the acid away from naturally high permeability zones and zones already treated, and towards the regions of interest. Various materials and methods have been applied to enhance acid diversion across vertical and long treatment intervals. Each technique has some merits, and the basic goal of all of them is to temporary shut-off higher permeability sections in order to force the stimulation fluids into the lower permeability section.

Well stimulation refers to the various techniques employed to improve the permeability of hydrocarbon-bearing formation (Economides and Nolte, 2000). Yet, this relatively simple technique certainly represents one of the most cost-effective methods to enhance well productivity and improve hydrocarbon recovery. The science of acidizing has its origins over 100 years ago when hydrochloric acid was used to stimulate carbonate formations (Frasch et al. 1896). The acidizing technique was not applied in widespread basis until the 1930's when Dow Chemical Company developed an effective acid corrosion inhibitor for mineral acid. The results from the first commercial application of matrix acidizing by Pure Oil Company in one of their wells in Michigan was spectacular (Kalfayan, 2000). Through the 1970's and 80's, the number of catastrophic acid job tend to overshadow the successful treatments and as a consequence, acidizing treatments were decreased in many areas. New acid systems and better understanding of acidizing chemistry, thermodynamic and flow modeling have been introduced early 1980's and well stimulation since then have become a routine operation for many hydrocarbon producing fields. The purpose of an acid treatment is to remove formation damage along as much of the hydrocarbon flow path. Also, it is desirable to make the acid less aggressive to the well architecture and avoid undesirable reaction that could result in formation damage. Acid pump into the well will react with carbonate rocks according

(equations 1.1 and 1.2). Hydrochloric acid reacts immediately with the carbonate rock and tend to form a few large channels know as “wormholes” through the rock, rather than opening up the pore structure. The acid penetration distance is limited to a few feet at most. Conventionally, hydrocarbon wells in carbonate reservoirs are acidized immediately after drilling before production start and often the treatment is repeated every 2-3 years. In horizontal wells, the removal of drilling damage caused by accumulation of drilling mud and filtercake and fine rock particles is very costly process due to the need to use special techniques, such as injection of acid through coiled tubing to avoid corrosion of wellhead equipments and to prevent acid being spent before it reaches the far end of the horizontal well. The purpose of acidizing treatment is to remove formation damage along the hydrocarbon flow path as possible. An effective treatment must therefore remove as much damage as possible along the entire flow path.

Surfactant molecules when dissolve in water above a certain concentration, referred to as critical micellar concentration (CMC), self-aggregate into supramolecular structure. The shape of surfactant aggregates formed in dilute solution can be spherical, globular, rodlike or bilayer vesicle depending on geometrical and thermodynamic properties as will be seen in Chapter III. The self-aggregation of the molecules are arises because of the fact that the surfactant molecule consist of two parts, hydrophobic and hydrophilic, which are distinctly different in character. Surfactants differ from each other based on their head group, tail, net charge and chemical structure. They are broadly classified as ionic and nonionic depending on whether the head group has a net charge or not. Ionic surfactants are further classified as cationic, anionic, or zwitterionic. Study of viscoelastic surfactant was of particular interest in the last two decays as they posse interesting scientific and conceptual challenges, and show unusual surprising phenomena most of the time.

Molecular simulation, like any other basic scientific research, is complicated and expensive. Advances in instrumentation, methodology and theory are always sought

after their economical value and ability to make research proceed more efficiently and effectively. Experiments to learn the details of viscoelastic surfactant structure, to measure their properties and establish relationship between the two can be very time-consuming and expensive. The synthesis of a new surfactant structure in laboratory can require weeks of work by highly skilled scientist and technicians while tying up expensive equipment and using various chemical and catalysts. The analytical laboratory work needed to characterize the newly synthesized material is also expensive to obtain and the total cost of the work, including sample preparation, set-up time of equipment, the actual analytical procedure, and sample tracking and reporting, rapidly mount into many thousands of dollars. Giving these considerations, it is worth investigating other methods and approaches for properties prediction. Even if not perfectly accurate, such methods could reasonably indicate whether it might be worthwhile to synthesis the material and do the analytical work or not, and they could also suggest alternative molecular structure to consider. Although computational models may not be perfect, they are often good enough to rule out 90% of possible compounds as being unsuitable for their intended use.

1.3 Statement of the Problem and Approach

Viscoelastic surfactant (VES) materials are the choice now days for many applications in the oilfield industry. It serves as switchable “smart” fluid for acid diversion in well stimulation treatment. Though the systems do not require many additives, it is still expensive compared to polymer. It has critical limitations and thermal stability at high temperature. Higher corrosion inhibitor concentration can adversely affect the performance of viscoelastic surfactant used. Also, higher iron concentrations are negatively influence the performance of the VES and might result in complete precipitation. Therefore, there is a need in the petroleum industry to have better system that overcomes all, if not most, of the limitations listed above. We are expecting to better understanding of VES behavior in solution considering possible interaction with most influential ions. Changes in head group (HG) structures which are known through experiment to have a dramatic impact on phase stability and rheological behavior of

polymeric materials in general. That will lead to better understanding of the side groups' effect and will help in identifying the high potential materials that can be used. Typical MD simulations cover the motion of a few tens of thousands of atoms over a period of a few nanoseconds; on current computers such a run would take a week to complete. As usual atomistic models are limited to small length (10 nm) and time (10 ns) scale, whereas wormlike micelles have counter length in the range of micrometers and relation time of at least millisecond

1.4 Research Objectives

1. To study hydration and dehydration process of common metal cations present in carbonate reservoir at room temperature.
2. To investigate possible interaction between iron ions with chloride, hydroxide and bisulfate.
3. To evaluate the molecular structure effect of various surfactant head groups on the on their complexation with organic and inorganic counterions.
4. To verify theoretically the cause of cationic, and betaine surfactants precipitations at high concentration of ferric ions.
5. To set up the guidelines for oilfield industry to enhance or develop new “responsive” materials for controllable placement of fluids in well stimulation treatment.

The dissertation is organized in nine chapters and five appendixes. Chapter II layouts the theoretical background of quantum mechanics and molecular dynamic simulations and their role in the advancement of nanotechnology research in oilfield industry. Chapter III serves as a literature review of ionic surfactants, their classifications, applications, and synthesis. In Chapter IV, thermochemical properties of pure water clusters as well as the hydration of N^+ , Ca^{2+} , and Mg^{2+} metals are presented and discussed. Chapter V presents the iron chemistry its interactions with chloride and hydrogen sulfide. For Chapters VII–VIII, various surfactant HGs are evaluated theoretically as in Figure 1.1. Summary of all QM and MD simulation are shown in Tables 1.1 and 1.2, respectively.

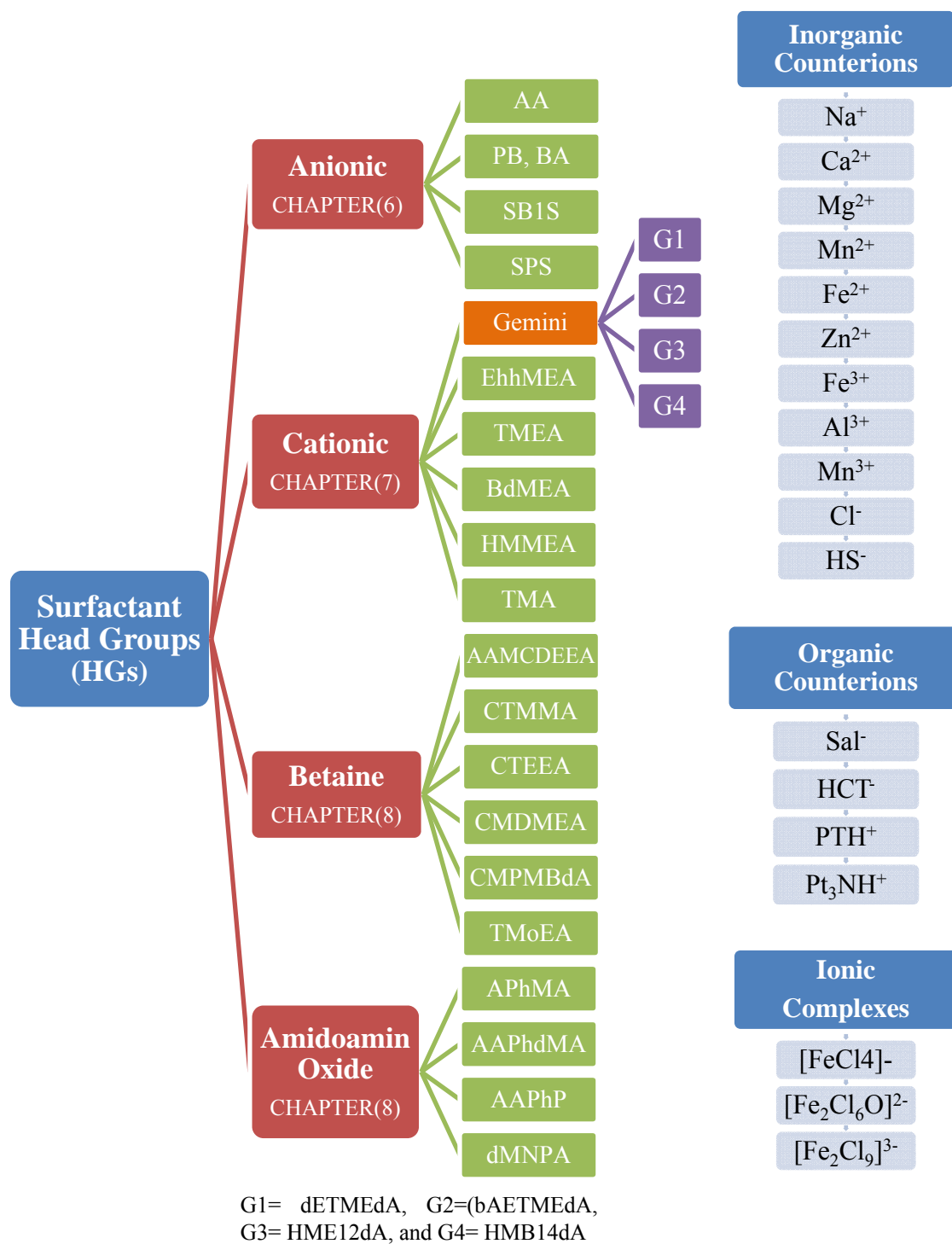


Figure 1.1: Schematic overview of various surfactant HGs and counterions with corresponding chapter included in this study.

Table 1.1: Summary of all QM calculations included in the study

Chapter No.	List of Calculations	Phase	Level of theory and basis sets
IV	$\text{H}_2\text{O}(\text{H}_2\text{O})_n$, where $n=1-8, 17$	Gas-phase	
	$[\text{Ca}(\text{H}_2\text{O})_{n-m}\text{H}_2\text{O}]^{2+}$, where $n=1-8, m=2,3,12$	Gas-phase	B3LYP
	$[\text{Mg}(\text{H}_2\text{O})_{n-m}\text{H}_2\text{O}]^{2+}$, where $n=1-6, m=2,3,12$	Gas-phase	6-311++g(d,p)
	$[\text{Na}(\text{H}_2\text{O})_{n-m}\text{H}_2\text{O}]^+$, where $n=1-6, m=2,3,12$	Gas-phase	
V	$[\text{Fe}(\text{H}_2\text{O})_{n-m}\text{H}_2\text{O}]^{2+}$, where $n=1-6, m=12$	Gas-phase	
	$[\text{Fe}(\text{H}_2\text{O})_{n-m}\text{H}_2\text{O}]^{3+}$, where $n=1-6, m=12$	Gas-phase	B3LYP
	$[\text{FeCl}_{n-(6-n)}\text{H}_2\text{O}]^{3-n}$, where $n=1-6$	Gas, PCM	6-311++g(d,p)
	$\text{Fe}(\text{OH})_2 \cdot 4\text{H}_2\text{O}$, $\text{Fe}(\text{OH})_3 \cdot 3\text{H}_2\text{O}$	Gas-phase	SDD, LanL2DZ
	$\text{H}_2\text{S}(\text{H}_2\text{O})_n$, $\text{H}_3\text{O}^+(\text{H}_2\text{S})_n$, $n=1-8$		
VI	$\text{M}(\text{HG})_{n-m}\text{H}_2\text{O}$, where $\text{M}=\text{Ca}^{2+}, \text{Mg}^{2+}, \text{Fe}^{2+}, \text{Mn}^{2+}, \text{Zn}^{2+}, \text{Fe}^{3+}, \text{Mn}^{3+}, \text{Al}^{3+}$	Gas-phase PCM	
VII	$(\text{HG})-\text{Cl}$, $(\text{TMA})(\text{IC})$, $\text{IC}=\text{FeCl}_4^-$, $\text{Fe}_2\text{Cl}_6\text{O}^{2-}$, $\text{Fe}_2\text{Cl}_9^{3-}$	Gas-phase	B3LYP, HF 6-311++g(d,p) SDD, LanL2DZ
VIII	$(\text{HG})-\text{Cl}$, $(\text{AAMCDEEA})-\text{M}$, $(\text{HG})-\text{FeCl}_4^-$, where $\text{M}=\text{Ca}^{2+}, \text{Mg}^{2+}, \text{Fe}^{2+}$	Gas-phase	

Table 1.2: Summary of all MD simulations included in the study

Chapter No.	Type of HG, tail	Ion	# H ₂ O	x_{ion} wt%	# surfactant	Total No. Molecules
VI	AA, Erucate (C22)	—	2843	0.0	4×4×2 (32)	2875
		Na^+	2726	1.2	4×4×2 (32)	2790
		Ca^{2+}	2839	0.5	4×4×2 (32)	2879
		Ca^{2+}	2663	1.1	4×4×2 (32)	2711
		Ca^{2+}	2695	2.1	4×4×2 (32)	2759
VII	BdMEA, Erucate (C22)	Cl^-	344	2.6	1	350
		Cl^-	303	8.2	1	319
		Cl^-	266	11.9	1	287
		Cl^-	264	16.9	1	295
		Cl^-	256	21.8	1	297
VIII	AAMDCEEA, Erucate (C22)	Cl^-	284	3.1	1	290
		Cl^-	289	8.5	1	305
		Cl^-	280	11.4	1	301
		Cl^-	285	15.9	1	316
		Cl^-	287	20.9	1	328

CHAPTER II

ROLE OF MOLECULAR SIMULATION IN THE ADVANCEMENT OF NANOTECHNOLOGY APPLICATIONS IN THE OILFIELD INDUSTRY

A theory is something nobody believes, except the person who made it...an experiment
is something everybody believes, except the person who made it.
— Albert Einstein

Molecular modeling has played a key role in the development of our understanding of many chemical and natural processes. It has a long history in advancement of nanotechnology from both designing prospective and explaining experimental data. Understanding the properties of fluids and materials is of great importance in the gas and oil industry (Ungerer et al., 2005). Over the last few decades, molecular simulation has emerged in the scientific community as a new corpus of theoretical methods which go far beyond the classical theories, and which may provide alternative ways of making predictions. Molecular simulation refers to computational methods in which molecular structure is explicitly taken into account. It is usually not realistic to predict the aqueous properties of materials as a function of temperature, pressure, and composition using quantum mechanics (QM) simply because any system large enough to define the system, which is greater than 100 atoms in many cases, has too many degrees of freedom for practical calculations (Sherman, 2001). Quantum mechanical calculations on small system can predict the thermodynamics with good accuracy using continuum model of solvation, and can also provide interatomic potential which can be then used to predict bulk properties using classical molecular dynamic calculations. Such calculation can be very useful in predicting general behavior of materials in solution.

The objective of this chapter is to review the general concept of nanotechnology and its possible applications in oilfield industry and to lay the background for molecular modeling approach in nano-scale research. It is not the attempt to present a comprehensive literature survey, rather to stir the imagination by considering various

examples that illustrate what molecular modeling has to offer. Also, this chapter serves as the theoretical background to all *ab initio*, DFT and molecular dynamic simulation results that are presented in later chapters of the dissertation.

2.1 Nanotechnology

Nanotechnology comprises technological developments on the nanometer scale. The *United States' National Nanotechnology Initiative* website (<http://www.nano.gov>) defines nanotechnology as: “the understanding and control of matter at dimensions of roughly 1 to 100 nm, where unique phenomena enable novel applications.” In the nano range, the physical, chemical, and biological properties of materials are unique. Therefore, nanotechnology provides us with tools to create functional and intelligent materials, devices, and systems by controlling materials in the nano scale, making use of their novel phenomena and associated properties (Goddard et al., 2002). The top-down approaches are those by which the bulk dimensions of a material are reduced until nanometer size features are produced. A well-known example of the top-down approach is the reduction in dimensions of the transistors on silicon chips which are fast approaching the nanoscale. By contrast, bottom-up approaches involve assembling structures molecule by molecule, or atom by atom, to fabricate structures with nano dimensions such as designing self-assembled monolayers. Nanotechnology has become more tangible since bottom-up and top-down approaches started to coincide. Atoms consist of a dense positively charged nucleus surrounded at a relatively large distance by negatively charged electrons (Figure 2.1). The nucleus consists of subatomic particles called neutrons, which are electrically neutral, and protons, which are positively charged. Although, the nucleus is extremely small (about 10^{-14} to 10^{-15} m) in diameter, it contains essentially all the mass of the atom. Electrons have negligible mass and circulate around the nucleus at a distance of approximately 10^{-10} m.

The preparation (*via* molecular self assembly) of materials with ultimate properties defined in advance has been understandably identified as a high priority research need.

Gels (and, in principle, also worm micelles) may take part in the attempt to satisfy this genuine need. Many properties of assembled materials, such as chemical functionality, material morphology and mechanical and dynamic properties can be engineered at the molecular level by careful design of the individual assembling molecules. This underlies, for example, the preparation of sensors based on the detection of specific functionalities by donor–acceptor interactions or the detection of morphologies which utilize spatial recognition by channels, grooves and cavities of the host materials. Smart fluids have genuine need to be designed atom-by-atom to resolve some problems in oilfield chemistry.

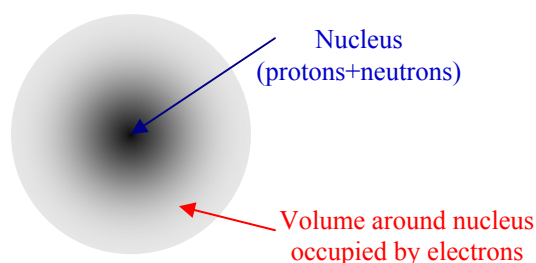


Figure 2.1: Schematic view of an atom. The dense, positively charged nucleus contains most of the atom mass and is surrounded by negatively charged electrons.

The nanoscale concept has introduced a new scenario where physicochemical principles, laws and properties are quite different from those of the macro and micro worlds. Two especially significant differences have been observed: the surface/volume ratios and the chemical reactivities of nanostructured matter and nanoparticles are much greater than those of macro- or microscale matter. Also, quantum effects are enhanced by effect of the configuration of molecular orbitals, which is similar to that of atomic orbitals; as a consequence, the optical, electrical, thermal, magnetic and various other properties of nanoscale matter are very different to those at the macro and microscale. Nanoscience and nanotechnology unarguably have promising prospects. A recent report of the US

National Science Foundation (Roco and Bainbridge, 2001) predicts that a new revolution based on the bio–nano–info triangle will shortly surpass the present evolution of the computer–info binomial. Moving from macro → micro to nano is the current technical trend in science and engineering. We are now in a transition era where major opportunities for both science and technology abound. It is not late for oilfield industry to be more adaptive of recent advancement in basic science to help solving one of the long-term humanity problems, energy. As computational chemistry played a key role in the development of our present understanding of the details of many chemical process and molecular structures, the next two sections of this chapter will cover both electronic structure theory (QM) and molecular mechanics.

2.2 Quantum Chemistry

Quantum mechanics gives a mathematical description of the behavior of electrons that has never been found to be wrong (Young, 2001). In theory, it can predict any property of an individual atom or molecule exactly, however, the quantum mechanical equations have never been solved exactly for any chemical system other than the hydrogen atom. *Ab initio* is a Latin word means “from the beginning”, which refers to calculations that are driven from theoretical principle with no inclusion of experimental data (Young, 2001). By first principle calculations we mean solving the Schrödinger equation: $\mathbf{H}\Psi = \mathbf{E}\Psi$, where \mathbf{H} is the Hamiltonian operator, Ψ is the wavefunction and E is the total energy of the system. With the value of E known, we can use statistical mechanics to predict thermodynamic properties of the system. *Ab initio* computations are based on iterative calculations of self-consistent electronic field (SCF), as the case for the semiempirical methods, but do not use experimental data to calibrate quantities that appear in the calculations. These methods are much more computationally demanding than semiempirical methods, but their reliability and range of applicability has improved greatly as more powerful computers have permitted more sophisticated approaches and have enable handling of more complex molecules. The computations are carried out by successive series of calculations minimizing the energy of the electron distribution and

the molecular geometry. The calculation is repeated until convergence criteria are met. *Ab initio* Hartree–Fock calculations with simplified ligands gave more-or-less useless results bond lengths were wrong by tenths of angstroms, the relative energies of isomers were often wrong, the relative energies of possible spin multiplicities were wrong, etc. This was quite unlike the situation for organic chemistry where Hartree–Fock methods generally provided at least a reasonable starting point to gain insight into reaction mechanisms, structure, and spectra for small molecules (up to about six carbon atoms) in the gas phase. More advanced methods, such as Møller–Plesset perturbation theory, configuration interaction, or coupled cluster theory, were then routinely used to provide semiquantitative agreement with experiment and proof of the basic reasonableness of the results.

2.2.1 Selection of Theoretical Method and Basis Set

A critical step in the computation of electronic structure is the selection of the basis set. A basis set is a mathematical description of the orbitals within a system used to perform the theoretical calculation (Foresman and Frisch, 1993). Larger basis sets approximate more accurately the orbitals by imposing fewer restrictions on the locations of the electrons in space. These basis functions themselves are composed of a linear combination of Gaussian functions; such basis functions are referred to as contracted functions, and the component gaussian functions are referred to as primitives.

The most common type of *ab initio* calculation is called a Hartree-Fock calculation (abbreviated HF), in which the primary approximation is the central field approximation. The energies are calculated in units called Hartrees (1 Hartree = 27.2116 eV). Because of the central field approximation, the energies from HF calculations are always greater than the exact energy and tend to a limiting value called the Hartree-Fock limit as the basis set is improved (Seminario, 1999). The steps in a Hartree-Fock calculation start with an initial guess for the orbital coefficients, usually using a semiempirical method. This function is used to calculate energy and a new set of orbital coefficients, which can then be used to obtain a new set, and so on. This procedure continues iteratively until the

energies and orbital coefficients remain constant from one iteration to the next. This is called having the calculation converge. There is no guarantee the calculation will converge. HF theory is very useful for providing initial, first-level prediction for organic systems. It is also reasonably good at computing the structure and vibrational frequencies of stable molecules and some transition state metals (Seminario, 1999). However, its neglect of electron correlation makes it unsuitable for some calculations involving reaction and bond dissociation (Foresman and Frisch, 19993). This means that HF takes into account the average affect of electron repulsion, but not the explicit electron-electron interaction. Higher level of *ab initio* theory has overcome some limitation of HF. Those include: Møller-Plesset (MP) perturbation theory, Configuration interaction (CI), multi-configurational self-consistent field (MCSCF), multi-reference configuration interaction (MRCI), Coupled cluster (CC). Full description of these theories is beyond the objective of this chapter and can be found in other well documented work (Young, 2001; Foresman and Frisch, 1993).

Ab initio calculations give very good qualitative results and can yield increasingly accurate quantitative results as the molecules in question become smaller. The advantage of *ab initio* methods is that they eventually converge to the exact solution once all the approximations are made sufficiently small in magnitude. In general, the relative accuracy of results is: $HF \ll MP2 < CISDG \approx MP4 \approx GCCSD < CCSD(T) < CCSDT < Full\ CI$. The disadvantage of *ab initio* methods is that they are expensive. These methods often take enormous amounts of computer CPU time, memory, and disk space. The HF method scales as N^4 , where N is the number of basis functions (Seminario, 1999).

Semiempirical calculations are set up with the same general structure as a HF calculation in that they have a Hamiltonian and a wave function. They are characterized by their use of parameters derived from experimental data or *ab initio* calculations in order to simplify the approximation to Schrödinger equation (Young, 2001). Usually, the core electrons are not included in the calculation and only a minimal basis set is used. They are relatively inexpensive and can be practically applied to very, very large molecules

(Foresman and Frisch, 1993). There are a variety of Semiempirical models, among the best known are: Austin Model 1 (AM1), Parameterization method 3 (PM3), Huckel, Pariser-Parr-Pople (PPP), complete neglect of differential overlap (CNDO), modified intermediate neglect of differential overlap (MINDO), Zerner's INDO (ZINDO), symmetrically orthogonalized intermediate neglect of differential overlap method (SINDO1), (Young, 2001). The advantage of semiempirical calculations is that they are much faster than *ab initio* calculations.

Density functional theory (DFT) has become very popular in recent years (Seminario, 1999). The premise behind DFT is that the energy of a molecule can be determined from the electron density instead of a wave function (Young, 2001). DFT methods achieved significantly greater accuracy than HF theory at a modest increase in cost. They compute electron correlation by general function of the electron density. DFT tends to be classified either as an *ab initio* method or in a class by itself.

Geometry optimization is one of the most important steps in the theoretical treatment of molecular simulation. Also, accurate application of molecular orbital theory and reliable determination of the reaction and activation energies require reasonable molecular geometries of reactants, transition states (TS), intermediates, and products. With the development of efficient analytical energy gradient and second-derivative (Hessian matrix) methods, complete optimization of geometric parameters for minima and saddle points has become more common. A minimum with all positive eigenvalues in Hessian matrix corresponds to an equilibrium structure, while a saddle point with one negative eigenvalue in a Hessian matrix corresponds to a transition-state structure usually connecting two stationary structures (Foresman and Frisch, 19993). The nature of stationary points on the potential energy surface can be characterized by the number of imaginary frequencies: zero for a minima, one for a TS (first-order saddle point), and two or more (x) for a “maximum” (x -order saddle point). Currently, the most common geometry optimizations for studies of molecular interaction are performed at the HF, MP2, and DFT levels of theory. A poor description of the electronic state by HF or MP2

may lead to incorrect results for the geometry optimization. Recent progress in DFT has shown clearly that the new generation of gradient-corrected DFT methods such as Becke's three-parameter hybrid exchange potential (B3) with the Lee–Yang–Parr (LYP), Perdue (P86), or Perdue–Wang (PW91) correlation functional are efficient and accurate computational methods in studies of reactions, especially for transition-metal systems and complexes containing metals.

2.2.2 Simulation of Solvent Effect

Most molecular systems are associated with solvent. There is an energy of interaction between solute and solvent. Because of this, the solute properties dependent on energy, such as geometry, vibrational frequencies, total energy, and electronic spectrum, depend on the solvent. The presence of a solvent, particularly a polar solvent, can also stabilize charge separation within the molecule. This not only changes the energy, but also results in a shift in the electron density and associated properties. In reality, this is the result of the quantum mechanical interaction between solute and solvent, which must be averaged over all possible arrangements of solvent molecules according to the principles of statistical mechanics. Gas-phase calculations do not give reliable energies of aqueous complexes. Therefore, we need to include the long-range solvation of the molecular system under consideration. This can be done explicitly by surrounding the complex or molecular structure with 100-1000 water molecules together with whatever other species are needed to define the solution composition. This calculation is not practical if not possible by traditional quantum mechanical calculations. The other way is to include this effect implicitly by making a cavity around atoms in which to place a solute molecule which is referred to as self-consistent reaction field (SCRF). The simplest SCRF model is the Onsager reaction field model (Figure 2.2(a)). In this model, the solute occupies a fixed spherical cavity of radius a_0 within the solvent field. A dipole in the molecule will induce a dipole in the medium, and the electric field applied by the solvent dipole will in turn interact with molecular dipole leading to net stabilization (Foresman and Frisch, 1993). Tomasi's Polarized Continuum Model (PCM) define the cavity as the union of a

series of interlocking atomic sphere. We have used this model throughout this study. The most rigorously correct way of modeling chemistry in solution would be to insert all the solvent molecules explicitly and then run molecular dynamics (MD) or Monte Carlo calculations to give a time-averaged, ensemble average of the property of interest. This can be done using molecular-mechanics-style force fields, but even that is not a trivial amount of computational work. The primary problem with explicit solvent calculations is the significant amount of computer resources necessary (Young, 2001). This may also require a significant amount of work for the researcher.

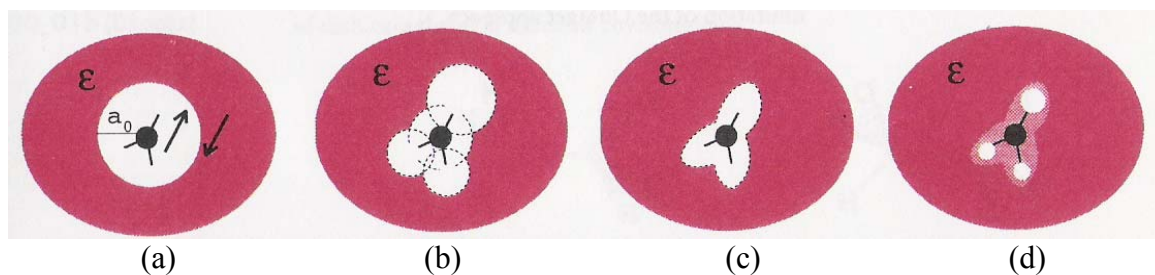


Figure 2.2: Reaction field models of solvation: (a) Onsager model (Dipole), (b) Tomasi's model (PCM), (c) Isodensity model (IPCM) and (d) Self-Consistent Isodensity model (SCIPCM).

2.3 Molecular Modeling

Molecular dynamics is a simulation of the time-dependent behavior of a molecular system, such as vibrational motion or Brownian motion. It requires a way to compute the energy of the system, most often using a molecular mechanics calculation. This energy expression is used to compute the forces on the atoms for any given geometry. Molecular dynamic simulation solves the classical equation of motion for a system of N atoms interacting according to optional energy forcefield. It is useful to study time evolution of variety of systems at nonzero temperatures, for example biological molecules, polymers, catalytic materials in solution or gas phase. Molecular dynamics solves Newton's familiar equation of motion: $F_i(t) = m_i a_i(t)$, where F_i is the force, m_i is

the mass, and a_i is the acceleration of atoms i . the force on atom i can be computed directly from the derivative of the potential V with respect to the coordinates r_i as:

$$\frac{\partial V}{\partial r_i} = m_i \left(\frac{\partial^2 r_i}{\partial t^2} \right) \quad (2.1)$$

Regular solution theory and the pseudophase approximation were used to predict pH dependence of critical micelle concentration (cmc) for mixture of amine-oxide and betaine surfactants. The method provided reasonable estimation of (cmc) values; however, a significant experimental effort was required to obtain certain input parameters (Zimmerman and Schnaare, 1999). Recently molecular thermodynamic (MT) theory was developed by Blankschtein and Goldsipe to overcome the shortcoming of the empirical nature of available models (Goldsipe and Blankschtein, 2007). The new model requires only knowledge of the surfactant structure, solution conditions, deprotonation constant (pK1), and any additives to the solution. The size and shape of the supramolecular structures depends on the geometry of the surfactant, its charge, concentration, as well as physicochemical conditions such as temperature, ionic strength, shear rate and salt concentration (Dreiss, 2007). Understanding how micellar structure is connected to the chemical composition and geometry of the surfactants, and in turn, how the structural features of the aggregates can be tuned by specific control parameters, and how these dictate the bulk properties, offers a considerable challenge.

Numerous theoretical approaches and simulations have been proposed to predict structure–property relationships. Simulation methods in which each atom is explicitly represented are well established but have difficulty addressing many cooperative effects of experimental and theoretical interest (Table 2.1). There is simply too large a gap between the timescale and spatial scale that govern typical intramolecular events and those which are relevant for collective motions as shown in Figure 2.3 (b). In order to increase the time and length scales accessible in the simulation of surfactants, details atomistic models are replaced by coarse-grained (CG) models in which each particle represent a collection of atomic particles.

Table 2.1: Statistical ensembles

Statistical ensemble	Imposed Variables	Associated thermodynamic potential	Application
Canonical ensemble	N, V, T	$A = E - TS$ (Helmholtz free energy)	Phase properties (P, H, C_v, μ, \dots)
Grand Canonical ensemble	μ_i, V, T	PV ($E - TS - \sum \mu_i N_i$)	Adsorption isotherms, selectivity
Isothermal-isobaric ensemble	N, P, T	$G = H - TS$ (Gibbs free energy)	Phase properties (H, C_p, ρ, m, \dots)
Gibbs ensemble at imposed global volume	$N = \sum N_i, V = \sum V_i, T$	$A = E - TS$ (Helmholtz free energy of the whole system)	Phase equilibrium of pure components and mixtures
Gibbs ensemble at imposed global volume	$N = \sum N_i, P, T$	$G = H - TS$ (Gibbs free energy of the whole system)	Phase equilibrium of mixtures

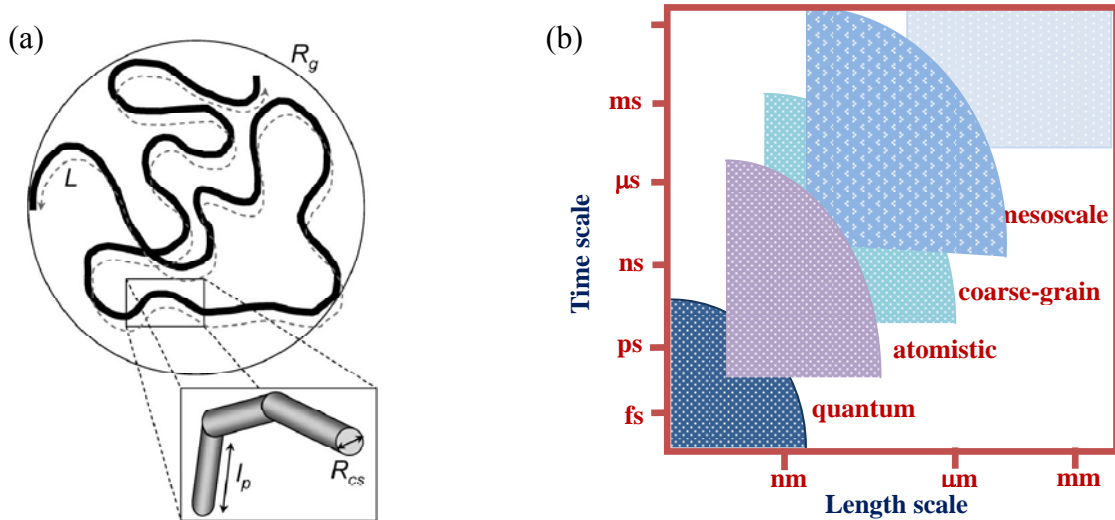


Figure 2.3: (a) Schematic representation of a wormlike micelle showing characteristic length-scales: the overall radius of gyration R_g , the contour length L , the persistence length l_p and the cross-section radius R_{cs} . (b) schematic of simulation scale.

Mesoworm model was introduced for the first time by Padding and others (Padding et al., 2005) were the length scale and, more particularly, the material properties of individual wormlike micelles can in principle be measured from detailed simulations or targeted experiments. Relevant properties include the solvent viscosity, worm diameter, bending rigidity (persistence length), compressibility and free energy associated with breaking and fusion process of wormlike micelles. Allowing the model to have these parameters as input from, the macroscopic properties such as rheology can be predicted from realistic input. This coarse-graining approach is neither unique nor trivial and careful treatment of relative length and energy scale can lead to quantitative agreement of simulation with experimental results (Zana, 2007). A typical coarse-grained box contains 4000-32,000 persistence length units, at a box size of 300-600 nm. The computational speed is typically of the order 0.1-1 ms per week on a single PC processor. Although a lot of theoretical and experimental work has been aimed at elucidating the behavior of charged surfactants, many questions remain unanswered and we are still far from a complete understanding (Hansen and Löwen, 2000; Levin 2002). The reasons for this are many:

1. Charged systems are typically aqueous systems, and the behaviour of water at surfaces is complicated in itself and not fully understood.
2. Oppositely charged groups or ions are pushed together by Coulombic attraction; as a result of the small separations, quantum effects come into play and make the interaction between oppositely charged ions highly specific.
3. Collective behaviour of charged ions at an oppositely charged surface arises since the degrees of freedom of all ions are coupled via the long-ranged Coulomb interaction and leads to large-wavelength correlations.

It is the mixture of all these effects, each operative at a different length scale, that makes the problem of charged surfaces intractable on the *ab initio* level with present computer power. Nevertheless, progress has been made in the last few years by concentrating on certain aspects at a time, leaving aside the other complications. As examples of such

approaches, we briefly review four different simulations which are concerned with very different length scales and aspects of charged surfaces (Table 2.2):

1. Recently, coarse grained Monte Carlo simulations were performed for charged ions at oppositely charged, smooth surfaces within the so-called primitive model (which leaves aside effects such as water structure and specific ion interactions). Here the large lengthscale properties can be analysed and, more specifically, deviations from the classical Poisson–Boltzmann equation can be quantified.
2. More detailed Brownian dynamics simulations take into account the substrate surface structure and also allow one to estimate mobilities of ions.
3. Molecular dynamics simulations of water at hydrophobic substrates reveal that such substrates induce formation of a thin layer within which the water is depleted from the wall. Many charged surfaces are of hydrophobic nature, and it is suggested that these water structuring effects at surfaces are important since they will influence the degree of surface-group dissociation and the interactions with counterions.
4. Finally, at the smallest length scale, the interaction between oppositely charged ions has been studied using *ab initio* quantum chemistry calculations.

As mentioned before, each of these four simulation techniques is capable of dealing with one aspect of charged surfaces, but necessarily leaves aside other aspects. Quantum chemistry techniques can be used for calculations for molecules or small clusters of molecules on a basically *ab initio* level, but are not suited for looking at counterion density distributions or other large-length-scale effects. Molecular dynamics simulations yield structural and dynamic properties of larger systems, assuming a fixed set of heuristically determined force fields, but the maximal system size and the maximal simulation time are smaller than one would need for many applications. Finally, Monte Carlo methods and Brownian dynamics simulations allow one to go to large system sizes and also large timescales; the price one pays for this is simplistic models which neglect most of microscopic details, and a neglect of the shorttimescale behaviour. The future challenges will be allowing for cross-fertilization between these various approaches and

designing reliable hybrid simulation techniques which combine the strengths of more than one of them.

Table 2.2: Summary of Molecular Simulation studies reported on Surfactant systems

Surfactant	Sal/co-surfactant	Type of simulation	Number of atoms and scale	Ref.
C ₉ TAC, EHAC	Water	MD, using LAMMPS	50 surfactants	[1]
3-2-3	Polyion	MD (effect of chain length)	$n=12, 24, 36, 60$	[2]
DSB	NaCl	MD, CG, using GTOMACS, T=300 K, V=8.89×8.89×8.89 nm	DSB=50, NaCl=50, H ₂ O=5500	[3]
12-s-12	-	MD, NAMD, CHARM M, T=300 K, V= 40×40×120 Å	64 surfactants	[4]
C ₁₂ E ₁₂	decane	PINY-MD	119 surfactants	[5]
SDS, CTAB, DPC, C ₁₂ E ₈	Octane, water	MD, using GTOMACS, T=300 K		[6]
SDS	Water	MD	8-9 μs	[7]
EHAC	Water	MD, DL_POLY	128 surfactants	[8,9]
SDS	Water, TEC	MD, using GTOMACS, T=300 K	20 ns	[10]

Data are taken from reference: [1] (Maillet et al., 1999). [2] (Xu et al., 2007). [3] (Jun et al., 2007). [4] (Khurana et al., 2006). [5] (Allen et al., 2000). [6] (Abel et al., 2006). [7] (Michel and Cleaver, 2007). [8] (Boek et al., 2002). [9] (Padding et al., 2005). [10] (Luo and Dai, 2007).

2.4 Nanotechnology in Oilfield Industry

Over the next 30 years, global energy demand is projected to rise as high as almost 60%, a challenging trend that may be met only by revolutionary breakthroughs in energy science and technology. The oilfield industry needs stunning discoveries in underlying core science and engineering. Breakthroughs in nanotechnology open up the possibility of moving beyond the current alternatives for energy supply by introducing technologies that are more efficient and environmentally sound. Nanotechnology is characterized by collaboration among diverse disciplines, making it inherently innovative and more precise than other technologies. Such a technology may be the cornerstone of any future energy technology that offers the greatest potential for innovative solutions.

Nanotechnology is exciting because the science and engineering behind it are largely unknown. In fact, most scientists are aware that the laws that govern materials at nanoscale are very different from those that have been widely accepted in larger scales. Recent work by Nobel Prize physicist Richard Smalley of Rice U. supports this hypothesis. He discovered that carbon nanotubes and fullerenes (buckyballs), nanoparticles of carbon, which are conventionally characterized as graphite, behaved in ways unlike graphite (Smalley and Yakobsonb, 1998).

Nanotechnology could be used to enhance the possibilities of developing unconventional and stranded gas resources. Near-term challenges focus on liquefied-natural-gas (LNG) infrastructure and efficiency, and developing gas-to-liquids (GTL) technology. Long-term issues to be addressed are production of methane hydrates and gas by wire—producing electricity at the location of the gas source and carrying the electricity by wire to market rather than the gas to market by pipeline. Nanotechnology can address the problems associated with accessing stranded natural-gas resources by developing nanocatalysts and nanoscale membranes for GTL production and creating nanostructured materials for compressed-natural-gas transport or long-distance electricity transmission (Satyanarayana et al., 2003). Nanotechnology could help improve oil and gas production by making it easier to separate oil and gas in the reservoir—for instance, through improved understanding of processes at the molecular level. There are many other potential clean energy sources that could be enhanced through the use of nanotechnology. The practical application of nanotechnology in the oil sector is, fortunately, less frightening. It opens interesting prospects for improved oil recovery, not least through better understanding of processes at the interface between liquids and solids. The aim is to understand how oil and water can be separated more effectively. Nanotechnology could be applied to improved oil recovery in the form of tailoring surfactants. These can then be added to the reservoir in a more controlled way than with existing substances, thereby releasing more oil. It could also help develop new metering techniques with tiny sensors to provide improved information about the reservoir.

Gels can be designed to respond to electrical and magnetic fields. This property underlies the use of contractible gels in the development of artificial muscles for robotic actuators or prosthetic limbs — the swelling and shrinkage of these gels enable the conversion of electrical (or chemical) energy to mechanical work. For example, a gel made out of an elastic poly(dimethylsiloxane), an electrorheological fluid and a suspension of cross-linked poly(ethylene oxide) particles in silicone oil containing salt and other additives has been prepared. The gel contracts in less than 100 ms (the response time of human skeletal muscles to an electrical signal from the brain) when a 1 Hz ac electrical field is applied to it and then expands when the current reversed. Magnetic response may be implemented by embedding a ferromagnetic Ni-based material inside an appropriate gel. A magnetic field warms the ferromagnetic material up and thus the surrounding gel is also heated. Consequently, the gel expands and contracts. Such gels could be adapted to implanted drug delivery systems, for instance. Another imaginative strategy is to use a ferrofluid (an aqueous suspension of ferromagnetic nanoparticles) instead of water. The viscosity variations in line with the compression and stretching of the gel could be utilized in vibration damping, molding systems and remotely activated clutching mechanisms. In recent years, the development of sensors has become increasingly important. Sensor technology has flourished as the need for physical, chemical, and biological recognition systems and transducing platforms grow. Nowadays sensors are used in applications ranging from environmental monitoring, medical diagnostics and health care, in automotive and industrial manufacturing, as well as defense and security. Sensors are finding a more prominent role in today's world, as we place strong emphasis on devices aimed at making our lives better, easier, and safer. Sensor technology is quite possibly the area in which nanotechnology has had one of the greatest impacts.

In summary, molecular simulation has been useful tool for researchers to model a molecular system prior to synthesizing that molecule in the laboratory and achieved better understanding of many problems which cannot be obtained from any experimental method.

CHAPTER III

CHEMISTRY OF VISCOELASTIC SURFACTANTS USED AS DIVERTING MATERIALS IN WELL STIMULATION

Energy will be one of defining issues of this century, and one thing is clear: the era of easy oil is over ...we need your help
—Chevron

Matrix acidizing has been used in oilfield industry to remove formation damage caused by drilling-mud invasion, clay swelling and clay migration and production impairment from inorganic scaling. When acid is injected into the reservoir below the fracturing rate and pressure, acid will typically enter the region with the highest permeability. Proper diversion is required to direct the treatment fluid into the damage zone to achieve maximum benefit of the acid stimulation. Effective diversion is the key for successful matrix treatment in carbonate reservoir. Viscoelastic surfactant-based acid systems have been used as acid diverter for many fields worldwide including oil wells, seawater injectors, horizontal, water disposal wells and deep sour-gas wells. However, there are few problems associated with this system when used in sour (H_2S) reservoir. Stable oil-in-water emulsion can be formed at low surfactant viscosity (i.e. when interact with reservoir hydrocarbon), which can add another complication to clean the wellbore. Precipitation of cationic and zwitterionic surfactant at high concentration of ferric ions (Fe^{3+}) is another problem associated with VES system. By looking at literature related to oilfield industry, we observe a lack of general knowledge with regard to the chemistry of viscoelastic surfactants used as diverting materials. Therefore, this chapter intends to explain the necessary chemical background, thermodynamic behavior and to present general understanding of chemical structure influence on dynamic properties of VES systems which may be useful for many scientists and engineers working in this field. This chapter will also present general review of what is called “responsive” or smart fluids and their possible applications in upstream industry.

3.1 Introduction

Responsive materials or what is known as “smart” or “switchable” fluids are characterized by a change in their properties in response to a specific physical or chemical stimulus (deJong et al., 2006). In many cases, those responsive materials are similar to gel and they combine the elastic behavior of solids with micro-viscous properties of fluids. Chemical gels, can react with physical or chemical stimulus by changing their size, shape, optical, dielectric, viscoelastic characteristic, or their chemical properties such as the affinity for guest molecules, and maintained three dimensional network of structure by covalent bonds. It has many applications in oilfield industry, drug delivery, optical, nanosensors, etc. The response behavior of chemical gels depends on their viscoelastic properties as well as on the sensitivity of the interaction potential between the three dimensional network of the structure and solution. Typical stimuli that we might consider for smart fluid applications in oilfield industry include temperature, pH, electric field, light, magnetic field, concentration, ionic strength, presence of chemical or biological agent, and mechanical stress. The responses can also be manifold: precipitation, degradation, change in hydration state, swelling, change in shape or structure, conformational alternation, and micellisation. In contrast to the chemical gel, the network structures of physical gel are built from smaller subunits, which are held together by noncovalent interaction. Physical gel is formed, in most cases, by low molecular-mass organic materials that convert liquid into a gel (deJong et al., 2006).

There are many mechanisms by which we can design responsive smart-fluids. Host-guest complex formation represents a very interesting type of trigger because it relies on complementary intermolecular interactions. Hydrogen bonding groups are particularly useful in the design of selective host-guest interactions because of their strength and directionality (deJong et al., 2006). Also, donor-acceptor interactions have been used frequently to stabilize host-guest complexes. Metal-ion responsive gels are another attractive mechanism for responsive materials because of the prominent role of metal

ions in many enzymes, catalysts, molecular electronic devices etc. The presence of a metal ion in a particular compound may have a large impact on its solubility, conductivity, and spectroscopic properties, for example. The use of reactive gases to develop responsive gel systems is an attractive concept especially in oilfield industry, because it allows the addition and withdrawal of reactants via the gas-phase, leaving all other components in the liquid or gel phase. As a result, gas responsive gels are attractive to sensor technology, in general. Moreover, the uptake and release of gaseous substances can be repeated many times without significant dilution of the system. In matrix acidizing treatment, for example, acid reacts with carbonate rock to produce chloride-salt, water and CO_2 gas. This gas can be used as a trigger to design a responsive fluid. George and Weiss (2002) introduced a system based on primary and secondary amines that can form gel within 30 second after adding CO_2 . The in situ chemical transformation of amine solutions and formation of gel is based on instantaneous conversion of “latent” to ammonium carbamates (Figure 3.1). Chemical reversibility is demonstrated by removal of CO_2 from gels upon gentle heating while N_2 is used as a displacing gas. The use of pH-sensitive groups to effect gel-to-solution transitions or to modify the three dimensional molecular networking has been addressed thoroughly in the literature with more insight into the importance of electrostatic interactions in aqueous and non-aqueous environments, and their relevance for applications in colloidal chemistry, drug delivery and biomedical systems and devices.

Smart fluid systems that act upon application of a physical trigger are particularly attractive because they can be useful for many applications. For instance, cross-linked polymeric gels that swell, shrink or change their shape under the influence of an electric field have been used to construct microporous valves, actuators, and smart drug release systems. Temperature is another physical trigger that can alter behavior of fluid and form gel. This was achieved recently using wormlike micellar solutions based on ionic surfactants and the rheological properties of unusual observation of an increasing viscosity with temperature in certain cationic wormlike micellar solutions was reported

by Kalur group (Kalur et al., 2005). The solutions contain a cationic surfactant with an erucyl (C_{22} , mono-unsaturated) tail namely erucyl bis(hydroxyethyl) methylammonium chloride (EHAC) and an organic salt, sodium hydroxynaphthalene carboxylate (SHNC). Figure 3.2(a) shows structure transformation when these solutions are heated resulting in high zero-shear viscosity. Erucyl dimethylamidopropyl betaine (EDAB) is a zwitterionic surfactant which also demonstrated change in viscosity as function of temperature. At low temperatures ($25^{\circ} - 60^{\circ}$), the solution of EDAB/SHNC respond like permanent elastic gels, whereas at high temperatures the same solutions show viscoelastic behavior (Kumar et al., 2007). Light can activate the growth of wormlike with sustainable (10,000 folds) increase in viscosity (Kumar and Raghavan, 2009). The system shown in Figure 3.2(b) composed of zwitterionic surfactant, (EDAB), and photoresponsive molecule, *trans*-ortho-methoxy-cinnamic acid (OMCA). One of the most prominent features of gels is their viscoelastic properties.

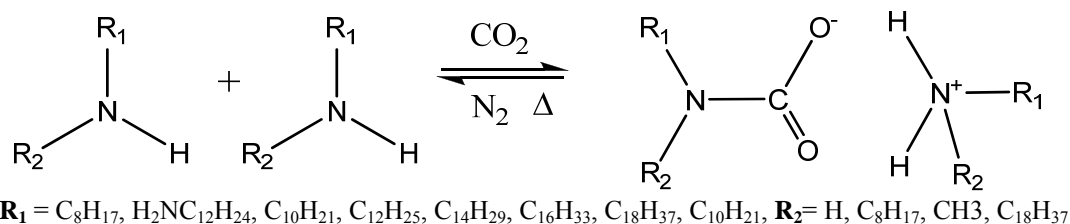


Figure 3.1: Amines “latent” gelator forms hard gel after ammonium carbamate formation by uptake of CO_2 from solution. The gelation procedure offers a convenient, rapid, and efficient method to sequester (reversibly) and sense the presence of CO_2 . Options test for R_1 and R_2 groups are shown.

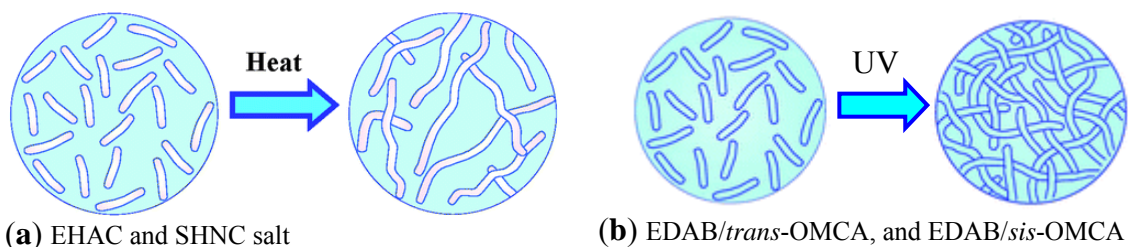


Figure 3.2: Smart fluid (surfactant) triggered by (a) temperature, and (b) light.

3.2 Chemistry of Matrix Acidizing

Carbonate acidizing is generally conducted with hydrochloric acid, except, perhaps in situations where temperatures are very high and corrosion is an issue. In such situations, organic acids like acetic or formic acids are used. To have deeper penetration of live acid and create large wormholes, retarded acid are occasionally preferred. The selection of an appropriate acid formulation is crucial decision considering the influence of chemical structure, temperature, pressure, pore size distribution, and reservoir fluid composition on the interaction between many chemical species in the system. Over the last two decades, many research centers have run thousands of experiments and mathematical modeling to establish some ground rules on which acid can successfully be applied in well stimulation treatment.

Once a hydrocarbon well has been constructed, its production can be limited by low natural reservoir permeability or by permeability reductions induced by particulate damage to the rock pore space either during drilling or production. The creation of hydraulic fractures is one major stimulation process commonly used to overcome these limitations. This treatment involves injecting high volume of fracturing fluid (“pads”) through a wellbore into the subterranean formation at extremely high pressures, high enough to overcome the *in situ* principal rock stress and to cause material failure of the porous medium. As the breakdown pressure of the formation is exceeded, deep-penetrating fractures or drainage ditches are initiated and propagated (Economides and Nolte, 2000). These induced fractures extend outwardly from the producing wellbore and provide conduits for expediting oil drainage. In 1998, about 70% of oil wells drilled worldwide were hydraulically fractured to stimulate and enhance oil production and to improve sweep efficiency in secondary and tertiary recovery processes (Economides and Nolte, 2000). However, when the production begins and the pressure decreases, the fractures may close or heal completely in, for instance, sandstone formations. Therefore, propping agents (proppants), such as naturally occurring (silica) sand and resin (epoxy)-coated sand and high-strength ceramics are needed. Other examples of proppants are

glass beads, walnut shell fragments and aluminium or nylon pellets (Kelly et al., 1995). These porous proppant packs keep the newly created fractures open. The pad is, therefore, followed by a second fluid designed primarily to suspend and transport as much of the intended volume of proppant as possible *via* a commonly tortuous path into the induced fracture. In order to transmit pressures and carry the proppant, the pad and fracturing packing fluids have to be viscosified. However, when the fracturing operation is finished, the carrier fluid should lose viscosity to allow the proppant to settle in place and then this low-viscosity fluid should efficiently flow back to the well and up to the surface, leaving behind the proppant grains. These conflicting demands have been commonly met, when the injected fluid is water or brine, by using polysaccharides such as algin, galactomannan gums (Kelly et al., 1995), guar, hydroxypropylguar (HPG) and hydroxyethylcellulose (HEC) often cross-linked by borate, transition metals (zirconium, titanium) complexes (Maitland, 2000) or compounds of aluminium or antimony (Kelly et al., 1995) to form viscoelastic gels which provide the required viscosity to carry the proppant (Maitland, 2000) and keep it within the fluid during the fracturing operation. Once the proppant is in place, the fracture closes around it, the water is squeezed out of the proppant and the water-soluble polymer forms a compacted cake that can hinder oil flow if not removed (Kelly et al., 1995). To solve this problem, delayed oxidative (using, for example, calcium or magnesium peroxide) or enzymatic breakers are included in the fracture fluid (Maitland, 2000). They are activated as a function of time or temperature to degrade the gel retained within the proppant pack in order to achieve good cleanup of the fracture. In contrast to oxidative breakers, enzyme breakers are true catalysts; their leaking off into the surrounding formation is prevented due to the high molecular weight of the enzymes, and they are less susceptible to the detrimental effect of trace contaminants (Kelly et al., 1995). Yet, enzyme breakers are inactive at higher temperatures limiting their use to shallow wells (Kelly et al., 1995), and, moreover, the long-chain polymers that effectively thicken the fracture fluid, do not degrade efficiently. Only 30–45% of the polymer pumped during the treatment return from the well during the flow-back period. Thus, small cross-linked fragments are inevitably left

in the pore spaces of the proppant and reduce the hydraulic conductivity of the pack significantly. Varying the polymer concentration is one of the attempts to address this problem, but another tack, taken relatively recently, is the use of viscoelastic surfactants (VES) functioning in the form of worm micelles. They have two obvious advantages:

1. Due to their micellar network structure they can transport solids regardless of low apparent viscosity so that no cross-linkers are needed.
2. Once the worm micelles come into contact with oil produced from the fracture, they transform to small spherical micelles or microemulsions (Maitland, 2000) and that have viscosity lower by orders of magnitude, thereby greatly facilitating the flow of residues out of the pack and fracture. The use of gel breakers is then spared and fracture flowback efficiencies are close to 100% (Maitland, 2000).

The surfactant microstructure and consequently the length and stiffness of its worm micelles can be tuned by altering control parameters (such as ionic strength, temperature, chemical composition, etc.) (Magid et al., 2000), and thereby modifying the rheological properties of these micelles (Hassan et al., 1998) and the capability of fracturing fluids (containing such thread-like micelles) to flow *via* porous media (Maitland, 2000). Furthermore, the recent trend to drill and complete wells in highly demanding areas has entailed the utilizing of such tailor-made surfactant systems. For example, stricter environmental standards have limited the exploiting of certain surfactants in environmentally sensitive areas. Thus, cationic surfactants that operate successfully, are cost effective and even environmentally acceptable in most land-based locations, are not always dischargable in marine environments. An anionic surfactant that meets these discharge needs has been developed for wells in Lake Maracaibo, Venezuela (Kefi et al., 2004/2005). Another surfactant system has been designed to address challenges in the shallow gas development areas in southern Alberta, Canada, where to the stringent environmental regulations marginal economics and low wellbore temperatures have been added as constraints (Kefi et al., 2004/2005) .

3.3 Acid Additives

Acidizing fluid include formulation based on hydrochloric acid (HCl), organic acids or chelating agents with the objective to remove damage by dissolving scale and stimulate the near wellbore area. Various additives may be added to the solution to enhance injectivity, protect equipments, place the acid and help returning the fluid. The additives commonly added include surfactants, chelating agent, corrosion inhibitors, H₂S scavenger. Table 3.1 provides a list of the typical concentration range of some major additives to acid systems. Stimulation fluids can also include other additives for specific applications to optimize the performance of the treatment. Examples include but not limited to: scale inhibitor, fluid loss control additives, gas, emulsifiers, paraffin inhibitor, iron control agent, and clay control agent. There is increasing concern and laboratory evidence that some additives adsorb into the formation, form scale, or may cause damage in presence of other fluids. Additives have great influence on rheological properties of acidizing fluid. Recent work by the group of Nasr-El-Din investigated experimentally the effect of corrosion inhibitor, iron control agent, H₂S scavenger, anti-slug agents, and mutual solvents on the viscoelastic properties of betaine type of surfactant (Al-Ghamdi et al., 2004). Mutual solvent is based on alcohol or ether and often used with crudes that might form emulsion. It has polar character between water and oil and miscible in both phases (Rae and di-Lillo, 2003). Friction reducers are generally used in coiled tubing operation. Nitrogen can be added to the system when the treatment desire foaming fluid.

Table 3.1: List of major acid additives with their concentration

Additive name	Temperature range (°F)	Typical concentration
Corrosion inhibitor	< 350	1-25 gal/tank
Iron control	< 350	10-20 gal/tank
Clay stabilizer	< 350	2-10 gal/tank
Diversion	< 350	1-2 lb/gal
Friction reducer	< 300	0.125-2 gal/tank
Solvent	< 250	50-100 gal/tank
Sulfide scavenger	< 250	3-20 al/tank

3.4 Surfactants

The most common fluids used in well stimulation are based on natural polymers, such as guar (Maitland, 2000), cross-linked by borate or transition metal (Zr, Ti) complexes to form viscoelastic gels. These fluids transmit hydraulic pressure to the rock to induce fractures in the formation, into which sand or other ceramic particles ('proppant') are transported by the gel to give a porous proppant pack which keeps the fractures open on removal of the fluid pressure. For the most common cross-linker, borate, (Maitland, 2000) have shown that gel rheology scales with pH and temperature in accordance with theories of associating polymers. Harry et al. (Harry et al., 1999) have given more insight into the nature of other Group 4 metal alkoxides and complexes which act as cross-linkers and the factors which control the rate of gel formation. Harris et al. (Harris and Batenburg, 1999) have examined the effect of salt on guar hydration, cross-linker equilibria and gel breaking to give a better understanding of how sea-water may be used to formulate guar fluids.

Conventional gels consisting of partially hydrolysed polyacrylamides cross-linked with Cr^{3+} ions suffer from a number of disadvantages: relatively poor thermal stability, hydrolytic instability of Cr^{3+} above pH 6, fast cross-linking rates, syneresis of the gel in place. The recent introduction (Hardy et al., 1999) of controlled hydrolysis acrylamide/acrylic copolymers in combination with organic cross-linkers like the diamine polyethyleneimine seems to overcome many of these problems. These enable incubation times for deep placement of many hours to be achieved by control of cross-linker concentration alone and give gels stable up to 150°C. These gels represent a significant advance in that they have been customised to reservoir conditions and process constraints, rather than trying to modify materials transferred from other (usually less demanding) applications using increasingly complex cocktails of chemical additives. However, the current level of understanding is unsatisfactory and this is an area where more scientific insight will definitely pay dividends in devising improved field systems.

Despite the advantages of using polymer as gelling agents in acid treatment, such a fluid system may be problematic. Conventional polymeric gelling fluid may leave an undesirable residue in the near wellbore area. To overcome some problems associated with polymeric system (Table 3.2), surfactant has been introduced as alternative gelling agent. The name surfactant is derived from the phrase: surface active agents. With surface we mean the region between two phases, which is also called the interface. The surface activity of surfactants arises from the fact that these molecules are amphiphilic. An amphiphilic molecule consists of two parts: a polar (hydrophilic) head group that likes water and nonpolar (hydrophobic) tail group that dislike water. The widespread applications of surfactants originate from the intrinsic duality in their molecular characteristics. In addition to conventional single-tailed or double-tailed connected to single head group surfactants, other types of surfactants displaying interesting properties have been developed. Figure 3.3 shows schematically different types of amphiphiles. Gemini surfactants (type c) are a relatively new type of surfactants. The name gemini was introduced in 1991 by Menger indicating a surfactant that consists of two hydrocarbon tails each attached to a hydrophilic head group, which is connected by variable length a rigid spacer (Zana, 2002). Amongst them, bis(quaternary ammonium) surfactants with the structure $C_sH_{2s-\alpha,\pi}-(Me_2N + C_mH_{2m+1}Br-)_2$, referred to as m-s-m, have been found to form wormlike micelles at relatively low concentrations (1% or less) when the spacer is short (Buhler et al., 1997).

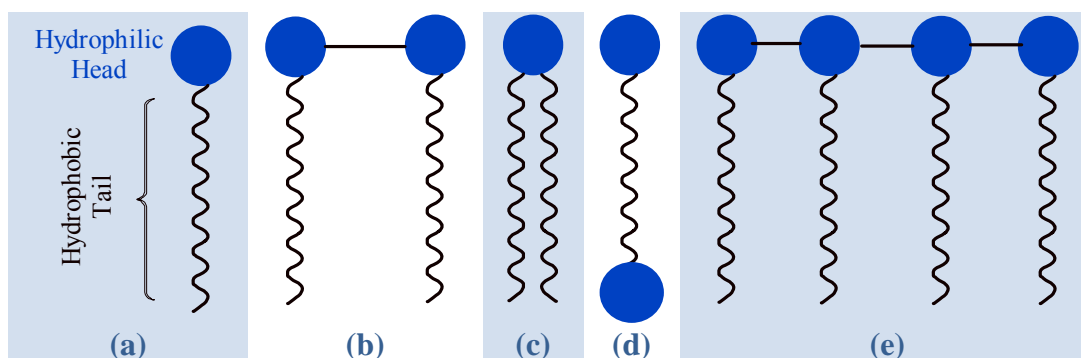


Figure 3.3: Schematic representation of different types of surfactants: (a) single-tailed, (b) doubletailed, (c) gemini, (d) bolaform and (e) oligomer.

Above a critical concentration c^* , wormlike micelles entangle into a transient network, similar to a solution of flexible polymers, which display remarkable viscoelastic properties (Dreiss, 2007). The most well-known and studied wormlike micelles systems are cationic surfactants with a long aliphatic chain, such as CTAB or CPBr, for which micellar growth takes place at relatively high concentration or in the presence of salt (Dreiss, 2007). Wormlike micelles have drawn considerable interest over the past two decades, both from a theoretical viewpoint as well as for industrial and technological applications, the range of which keeps expanding. Their unique viscoelastic behaviour is exploited to tune the rheology in numerous applications without the use of polymers or additives. In 1983, the Dow Chemical company introduced a family of surfactants as thickeners in consumer products later known as VES (Chase, 1997). Their outstanding performance led engineers at the Dowell Tulsa Technology Center, now Schlumberger, to explore ways of applying VES in oil and gas industry (Kefi et al., 2004/2005). Three classes of VES are useful in oilfield applications: cationic, anionic and zwitterionic (Zana, 2007). Each has advantages and disadvantages that influence the manner in which they are used.

Over the past 15-years, there has been a great deal of interest in the aqueous self-assembly of surfactants into threadlike or wormlike micelles. These micelles are long, flexible, cylindrical chains with contour lengths on the order of a few micrometers. The entanglement of these wormlike chains into a transient network imparts viscoelastic properties to the solution. Wormlike micelles are much like polymers with the important exception that the micelles are in thermal equilibrium with their monomers. Their gel rheology is caused by worm-like cylindrical micelles. Once these come into contact with hydrocarbon produced from the fracture or wormhole, they revert to small spherical micelles or microemulsions, the fluid viscosity/elasticity falls by orders of magnitude, the fluid residues flow easily out of the pack and fracture flowback efficiencies of close to 100% are achieved. Viscoelastic surfactant means the elastic or storage modulus, G' , of the solution is equal or greater than the loss modulus, G'' , when measured using

oscillatory shear viscometer. There are few problems associated with viscoelastic surfactant when used in well treatment. Stable oil-in-water emulsion can be formed at low surfactant viscosity (i.e. when interact with reservoir hydrocarbon), which can add another complication to clean the wellbore. Table 3.2 summarizes main characteristics of polymer-based and surfactant based acid diversion systems.

Table 3.2: Comparison between polymeric and surfactant diversion systems

Surfactant-Based Acid	<ul style="list-style-type: none"> • Simple system required minimum additives. • Can be placed using bullheading or CT • Ability to break when gets contact with hydrocarbons. • High level of ferric iron can adversely affect the apparent viscosity. • Required less stages compared with other acid systems. • Reduces friction loss in CT resulting in high pumping rate ~2.3 bpm. • More economical where it can save an average of two days of rig time. • Volume needed for the same treatment is less than PBS. • Doesn't tolerate hydrocarbons. • Shorter time is needed to lift spent acid due to reduction in surface tension. 	Polymer-Based Acid <ul style="list-style-type: none"> • The in-situ gelled acids caused loss of core permeability in tight carbonate cores. • Precipitation of the cross-linker (iron) at high temperature and in sour environment. • H₂S scavengers may interact with the polymer and loss their ability to remove hydrogen sulfide. • Large volume normally needed. • It could form external filter cake that reducing injectivity.
-----------------------	--	---

3.4.1 Anionic

Anionic surfactant is the oldest class of surfactants. They have been known from the first day humankind start using soaps. The term soap is mainly applied to the water-soluble alkali metal salt of fatty acid (with at least 8-carbon atoms) (Behler et al., 2001). The main application of soap is in personal care and detergent industries. It has also wide applications in oilfield industry including drag reduction and enhanced oil recovery. It is well known that carboxylate surfactants are more sensitive to the presence of polyvalent cations such as Ca^{2+} , Mg^{2+} than the corresponding phosphate, sulfates or sulfonate

(Porter, 1994). Thus, sulfonate VES are compatible with higher concentration of divalent cations present in formation water compared to carboxylate. Sulfonate based on amide such as N-oleyl or N-tallowyl N-methyl taurate has the advantage of inhibiting scale formation (Christanti et al., 2008). Figure 3.4 shows general structure of anionic surfactant based on natural fatty acid which makes them less expensive compared to other classes of surfactant. Recently, the oligomeric or dimer anionic surfactants with two head groups (Figure 3.4(c)) are of great interest in oilfield industry (Hughes et al., 2002).

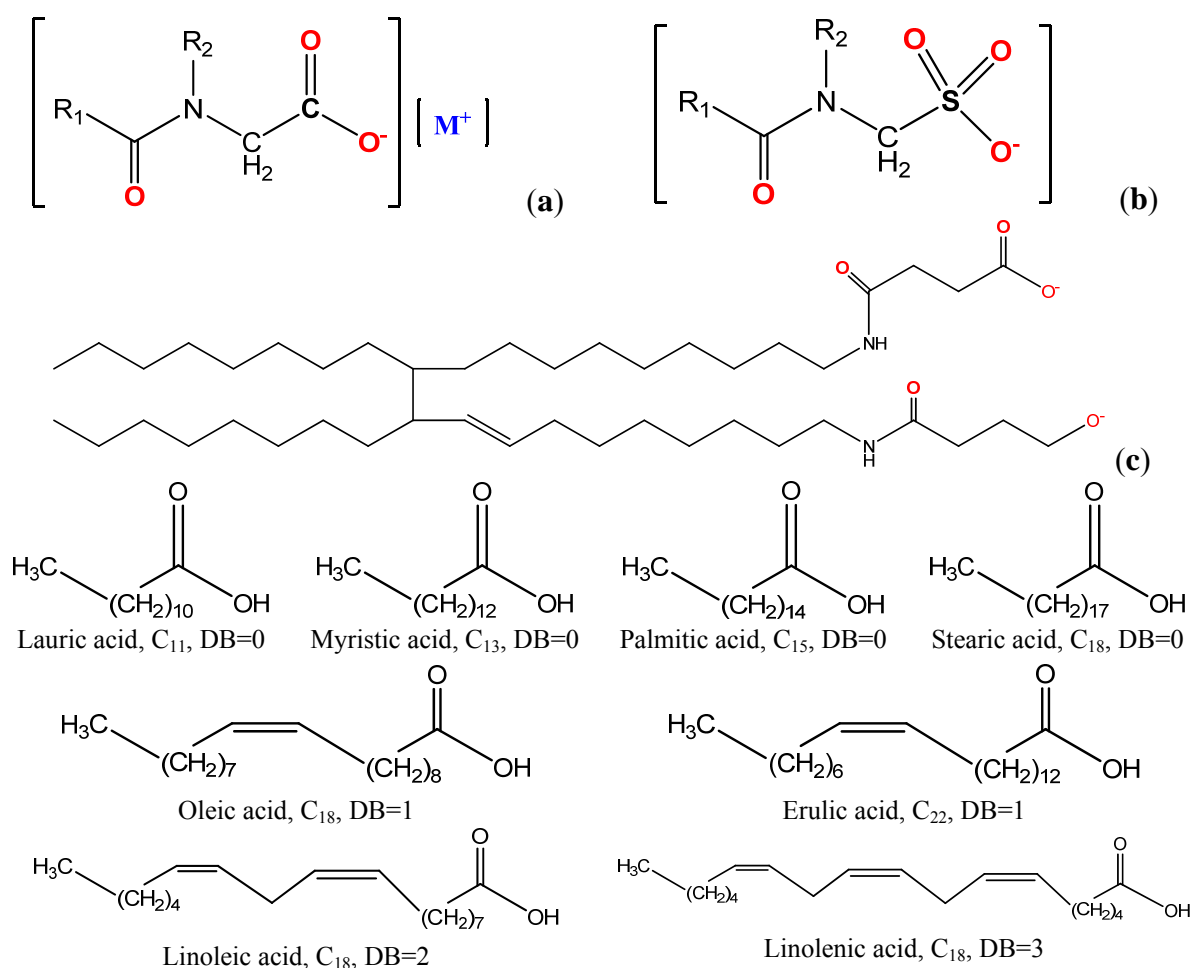


Figure 3.4: General chemical structure of anionic surfactant: (a) ethoxylate (b) sulfate and (c) dimer-(poley) amide succinate).

3.4.2 Cationic

The simple salt of long-chain amines are often called quaternaries or pseudo cationic amine salts is formed when R_4 in Figure 3.5 (a) is replaced by H atom. These pseudocationics are formed by neutralization with acids and thus represents protonated amines. The bonding in amines is similar to the bonding in ammonia (NH_3 , $pK_a=9.26$). Nitrogen atom is sp^3 -hybridized with three substituent occupying three corners of a tetrahedron and the lone pair of electron occupying the forth corner as shown in Figure 3.5(b). The R-N-R bond angles are close to the 109° tetrahedral value. A common example of cationic surfactant used as viscosifying agent is erucyl bis(2-hydroxyethyl)methyl ammonium chloride which is also known as (Z)-13 docosenyl-N-N-bis(2-hydroxyethyl) methyl ammonium chloride. For successful application of cationic surfactant in well stimulation, the hydrophobe chains are preferably to be greater than 18 carbon atoms in length. An example of one such commercially available material is ClearFRAC[®], commercially available from Schlumberger-Doll Research, namely erucyl-N,N-di-(2-hydroxyethyl)-N-methylammonium chloride (EHMAC), which is asserted to provide performance at the highest application temperatures ($\sim 250^\circ F$ ($\sim 121^\circ C$)) of any currently commercially available viscoelastic fluid. This product reportedly contains less than 3% hydrophobe carbon chains of 18 carbons or less. Because the intermediate used to make EHMAC must be purified to remove the components with alkyl chains of 18 carbons or less, EHMAC costs substantially more to produce than other alkyl amine cationic materials. The high cost of EHMAC limits the number of stimulation processes for which it is used on a repeated basis. A commercially available alternative to ClearFRAC[®] is AquaClear[®] surfactant fluid, commercially available from BJ Services Company. It also uses a quaternary alkylamine, but is less costly because an extensively purified intermediate is not required. However, the maximum application temperature for AquaClear[®] is about $170^\circ F$ ($\sim 76.7^\circ C$), which is substantially lower than ClearFRAC[®].

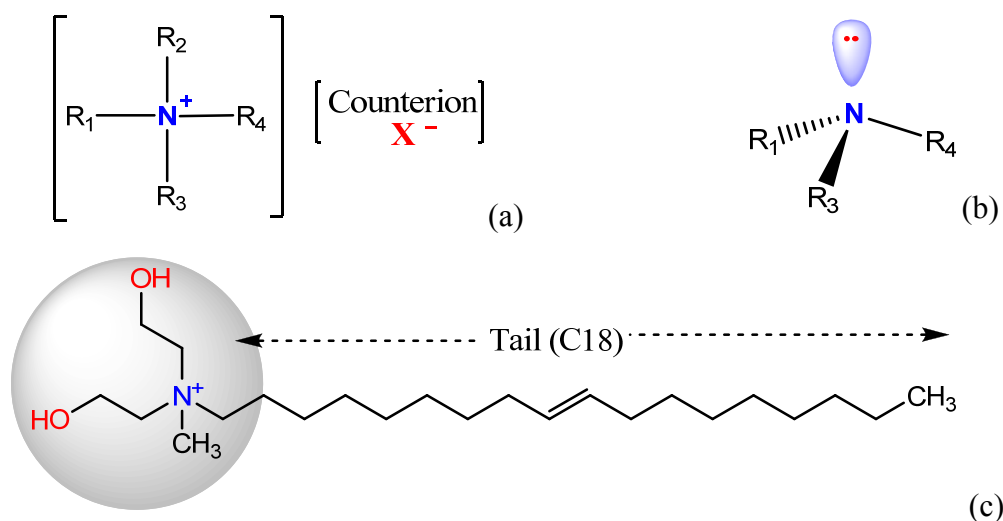


Figure 3.5: General chemical structure of tetra-coordinated ammonium salts. (a) quaternary ammonium (b) tertiary amine (c) 9-Octadecen-1-aminium, N,N-bis (2-hydroxyethyl)-N-methyl-chloride

Quaternary surfactants are mainly obtained by reaction of tertiary amines with classical alkylating agents such as methyl chloride, dimethyl sulfate or benzyl chloride, Figure 3.6, (Behler et al., 2001). The quaternization reaction is carried normally at temperature between 80 and 100 °C depending on type of solvent. Primary or secondary amines may also serve as raw materials but they need to be converted to tertiary amines before quaternization reaction. Esterification of alkanamines with fatty acid followed by quaternization or starting with ester quat can be another alternative. The chemical and physical properties of cationic surfactant vary depend on length of the tail, functional group in the head and kind of the counterion (anion). The main feature of all quaternary compounds is the attractiveness to almost any surfaces that are negatively charged. Their salts are considerably stable at ambient conditions and start decomposing above 100°C though a dealkylation reaction. The esterquat and betaine esters that may present in the quaternary ammonium structure are sensitive to hydrolysis, which makes them decomposable and feature for number of applications in oilfield industry. With the variety of cationic surfactant types, it is impossible to make solid statements about toxicity within the scope of short review.

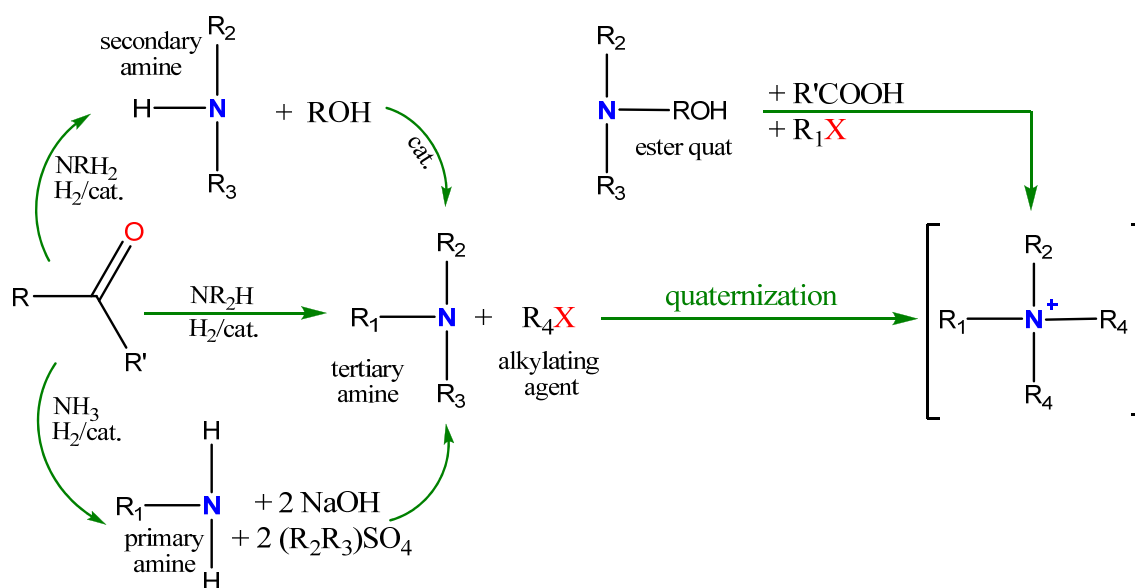


Figure 3.6: Schematic of quaternary ammonium salt preparation starting with primary, secondary or tertiary amine.

3.4.3 Betaines

The name “betaine” was proposed by Bruhl in 1876 after the discovery of the natural product trimethylammonium acetate, and subsequently the term has been used to describe compounds with similar structure or derivatives. It is a special class of what is called “amphoteric” surfactants. Figure 3.7(a) shows a general structure of the simplest betaine, where R_1 is a hydrophobic chain in the range of 16 to 25 carbon atoms. The methyl group can be replaced by other substituents, for example an alkyl aryl group or fatty alkylamino-alkyle group. Most of the amphoteric surfactants are derived from coconut or palm kernel oil or their corresponding fatty acid. The unique behavior of Betaine surfactants is due to their zwitterionic character. Weak acid are only partially dissociated in water because the anion of the acid has a strong affinity for hydrogen ions. When a salt of a weak acid is dissolved in water, it releases anions into solution that have the same strong affinity for hydrogen ions. Therefore, these anions immediately bond to hydrogen ions and thereby form the parental acid. Irrespective of the pH value, betaines permanently represent a four bonded nitrogen atom. At very low pH value, the

anionic group is protonated and cationic character become dominant. Betaines represent a separate type of structure compared to other classes of surfactants. The preparation procedure is relatively simple as shown in Figure 3.7 (a). The process involves quaternization reaction of tertiary amine with monochloroacetate as alkylation reagent. The reaction must be carried out in an aqueous solution to achieve high yield, and the final concentration of betaine should be in the range of 30% to avoid any tendency to gelatinize (Uphues, 1998). Alkylamino betaines are very common as diverting material [slb], and can be prepared in two steps process. First fatty acid or their esters are condensed with usually dimethylaminopropyl amine followed by reaction with sodium chloroacetate as shown in Figure 3.7 (b). The reaction temperature for alkyl betaine is in the range 70-90°C depending on the type of tertiary amine used, while it limited by the boiling point of amine (~140°C) in the case of alkylamidopropyl betaine. The reaction can be carried out in an alcoholic solution with subsequent filtration to remove sodium chloride as some applications required salt-free product.

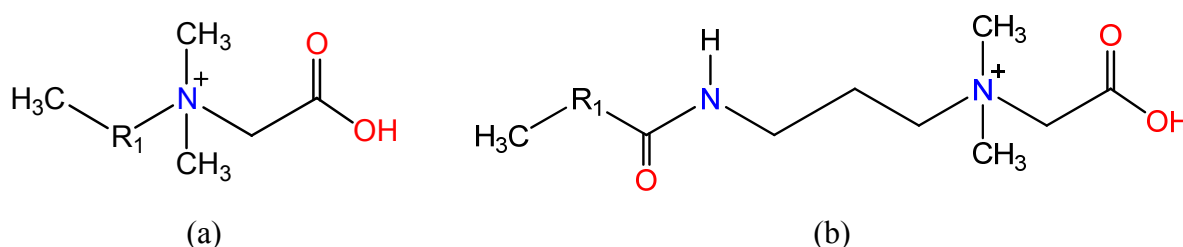


Figure 3.7: General molecular structure of (a) alkyl-betaine, examples of this class are: BET-O-30 and BTE-E-40 with $R_1 = C_{16}H_{33}$ and $R_1 = C_{16}H_{33}$, respectively, numbers in the name refer to percentage of active surfactant, (b) Alkyl-amidopropylbetaine.

3.4.4 Amidoamine Oxide

Amidoamine oxide, also known as amine oxide, has been introduced lately to oilfield industry as another class of surfactant that can be used effectively in well stimulation treatments. It provides gels that do not undergo phase separation over extended period of time and exhibit high heat stability (Dobson et al., 2003). It has been reported that the

3% and 15% gel of Aromox[®] are stable up to 5-6 weeks at room temperature (Dobson et al., 2003). The general formula of this class of surfactant is shown in Figure 3.8, where R_1 is saturated or unsaturated, straight or branched chain aliphatic group with 13 to 22 carbon atoms. R_2 is divalent alkylene group of 2-6 carbon atoms, R_3 and R_4 are independently C_1 - C_4 alkyl or hydroxyalkyl groups or together they form a heterocyclic ring of up to six members, and R_5 is hydrogen or a C_1 - C_4 alkyl or hydroxyalkyl group. The concentration of gelling agent in the aqueous solution is generally in the range of from about 4% to 6% by weight. Examples of Amidoamine-oxide surfactants are: tallowamidopropylamine oxide known commercially as Aromox[®] APA-T, tallow amidopropyl dimethylamine oxide, coco amidoalkylamine oxide, oleyl amidoalkylamine oxide, and erucyl amidopropyl dimethylamine oxide. The amine oxide gelling agent can be prepared by reacting a tertiary amine with concentrated hydrogen peroxide in a miscible glycol or alcohol solvent. However, if alcohols are used as a solvent, it has to be removed from the final product because alcohol solvents such as isopropanol modifies the structure of surfactant aggregates, and hence negatively affect the ability of the amine-oxide solution to thicken (Dobson et al., 2003). To achieve high viscosity, the molecular structure of Amidoamine oxide should have less than 1% free fatty acid and between 6-8% free amine. Results showed that Amidoamine oxide are effectively thickening (3-15%) HCl acid solution

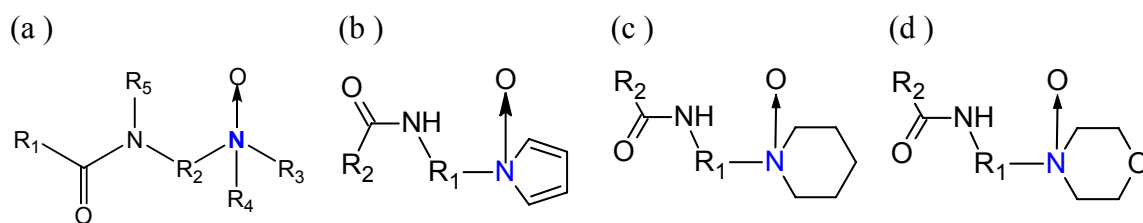


Figure 3.8: (a) General molecular structure of amidoamine oxide (AO) with R_1 is fatty aliphatic (C_{14} - C_{21}), R_2 alkyl group (C_2 - C_4), R_3 and R_4 are hydroxyl ethyl or heterocyclic ring, and R_5 is H (b) pyrrolidine ring for R_3 and R_4 , (c) piperidine ring, and (d) morpholine ring.

3.4.5 Gemini

Gemini or dimeric surfactants represent a new class of molecules that have attracted the attention of many industrial and academic researchers in the last few years. These surfactants are made up at least of two hydrophobic chains and two ionic or polar groups connected at the level of the head groups (HG), or very close to the head groups, by a spacer which can be flexible, or rigid, hydrophobic or hydrophilic as shown in Figure 3.9. The gemini surfactants behave as normal surfactants, however, they have three interesting properties: (1) the critical micelle concentration (CMC) is 1~2 order of magnitude lower than the conventional monomeric surfactant; (2) more efficient in decreasing the surface tension at water compared with other classes; (3) they have remarkable rheological properties at relatively low surfactant concentration; (4) they have better solubilizing, wetting, foaming than the conventional surfactants (Zana and Alami, 2003). Several reviews on gemini surfactants have recently been published following the synthesis of gemini surfactant in a great variety of chemical structures in the early 1990s (Zana and Xia, 2004). Gemini surfactants containing identical head groups and identical hydrophobic tails are called “symmetrical” and those with nonidentical heads have been referred to as “asymmetrical” or “hetero-gemini”. The bis(quaternary ammonium bromide) surfactant with the structure $C_sH_{2s}-\alpha,\omega-(Me_2N^+C_mH_{2m+1}Br^-)_2$, referred to as (*m-s-m*, $X^-=Br^-$) have been by far the most investigated gemini surfactants because of their synthesis and purification are relatively easy (Dreiss, 2007). The *m* stands for the number of carbons in the alkyl chain, and *s* for the carbon atoms in the spacer group. The same symbols are used for asymmetric type as (*m-s-m'*, $2X^-$) and to oligomers class as (*m-s-m-s-m*, $3X^-$). It was generally observed that CMC decreases with increasing number of carbons in the tail, *m*, and goes through a maximum upon increasing spacer carbon, *s*, irrespective of the value of *m* (Zana and Alami, 2003).

Gemini surfactants can be nonionic, anionic, cationic, zwitterionic or any combination of them as shown in Figure 3.10. In solution, gemini surfactants with short alkyl tail group (*m*<8) found to behave similarly to their monomeric counterparts (Frindi et al., 1994).

As mentioned earlier, surfactants are dynamic in solution and the association and disassociation of gemini surfactants from their micelles are a single step process (i.e. the formation/breakup proceeds via one surfactant at a time into/from its micelles). The association reaction is diffusion controlled, whereas the rate of disassociation depends strongly on the surfactant hydrophobicity (Zana and Alami, 2003). Results showed that the residence time of 12-s-12 gemini surfactant in its micelles as well as the life time of the micelles are much longer, (0.1-10 s), than that for the corresponding monomeric surfactant, Table 3.3, (Sein et al., 1993). The interesting rheological properties exhibited by gemini surfactants worth further investigation and study for applications such as a diverting agent in oilfield industry. Many gemini surfactants presented in the literature up to date, to the best of our knowledge, have been made by elaborate syntheses in laboratories not in a realistic scaled up process. The available commercial gemini product is Ceralution[®] by Sasol company (Marl, Germany) based on anionic (Coco fatty acid ethylenediamide) dimeric surfactant (2005). Number of cationic gemini surfactants including stearamidopropyldimethyl-ammonium di-chloride (Figure 3.10(d)), and soyamidopropyl-dimethylammonium-stearamidopropyl-dimethylammonium chloride toluene sulfonate have been synthesized and evaluated for oilfield application (Knox, 2008).

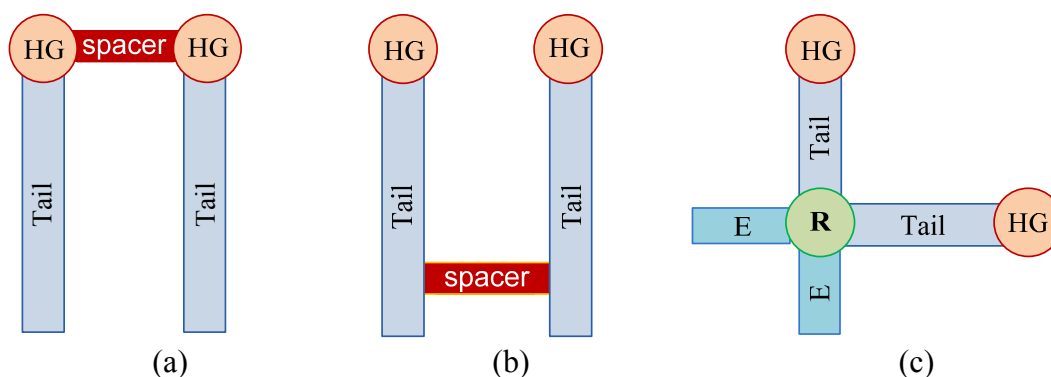


Figure 3.9: Schematic representation of gemini surfactant, (a) dimertic with the spacer group connecting the two heads groups (HG), (b) bolaform where the spacer connect the two moieties at points on the alkyl tail somewhere close to the end, and (c) cross structure, where the two tails connect to single or double benzene rings, R, and the extension, E, can be the same or different.

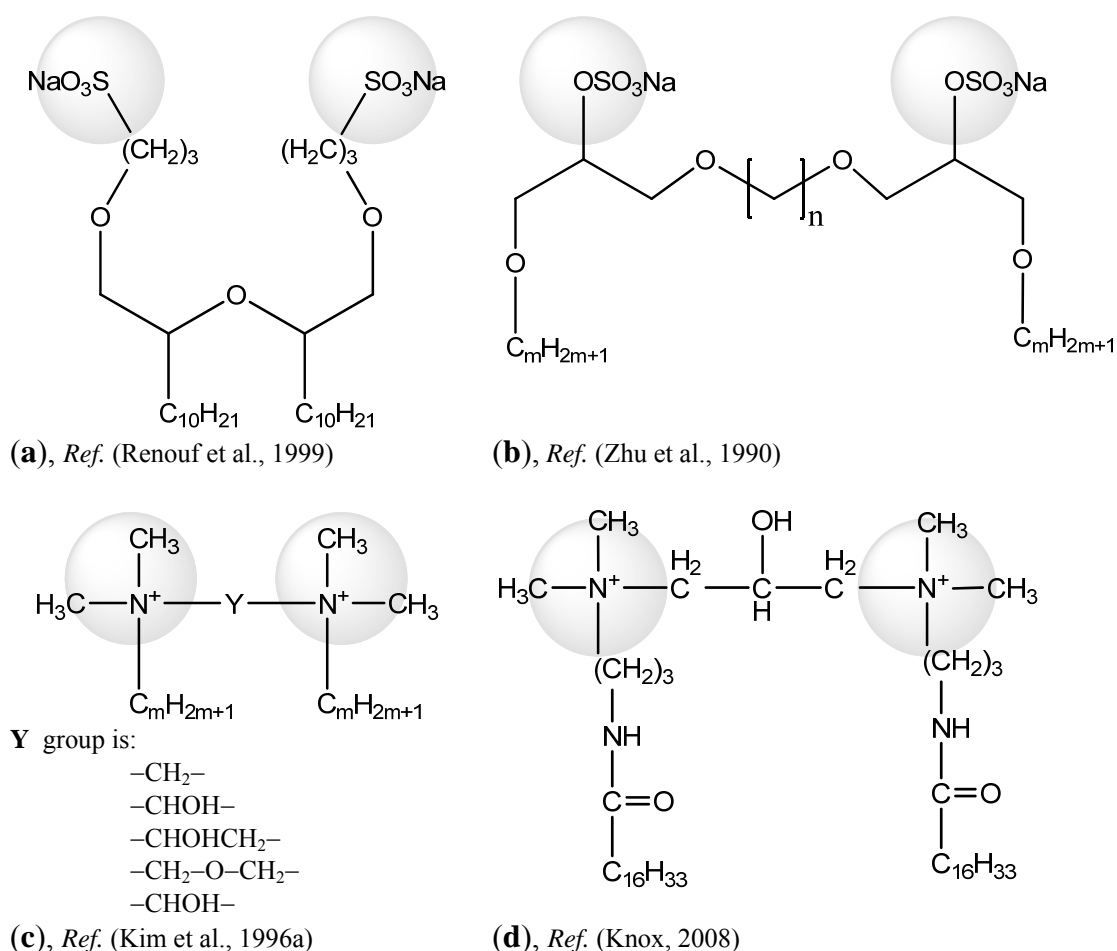


Figure 3.10: Examples of gemini surfactants, (a) sulfonate (b) sulfate (c, d) cationic.

Table 3.3: Dependence of gemini surfactant properties on molecular structure, some reported physical properties including Krafft temperature, T_k , critical micelle concentration, cmc, for the general structure in Figure 7(c).

Counterion	m	Spacer (Y)	T_k (°C)	cmc (mM)
Cl ⁻	12	-(CH ₂) ₃ -	< 0 ¹	0.980 ¹
Cl ⁻	16	-(CH ₂) ₃ -	< 0 ¹	0.015 ¹
Br ⁻	16	-(CH ₂) ₃ -	42 ²	0.025 ³
Cl ⁻	12	-CH ₂ CHOHCH ₂ -	< 0 ¹	0.780 ¹
Cl ⁻	18	-CH ₂ CHOHCH ₂ -	~40 ¹	-
Cl ⁻	12	-CH ₂ C≡CCH ₂ -	< 23 ⁴	1.57 ⁴

¹ data are taken from (Kim et al., 1996b), ² from (Zana, 2002). ³ from (Zana et al., 1991). ⁴ from (Menger et al., 2000).

3.4.6 Esterquat

Esterquat is a class of quaternary ammonium surfactant with general formula shown in Figure 3.11 where the hydrophobic part is linked to the charged head group via ester bond. The alkyl chain between R and cationic nitrogen is less than 4 carbon atoms in length. Esterquat upon hydrolysis, decompose into fatty acid soap in addition to a highly water-soluble quaternary ammonium diol. This type of surfactant is commonly referred to as “cleavable surfactants” and usually biodegrade rapidly more than alkylquats. They are stable in aqueous solution only in a narrow range of pH range and for a certain period of time. Esterquat is generally prepared by reaction of an acid with an alcohol in presence of a catalytic agent at high temperature ($\sim 250^{\circ}\text{C}$). The most common esterquat surfactants are those derived from alkanolamines and fatty acids. They can be classified as mono- di- and triesterquat depending on structure of alkanolamine and stoichiometry of the reaction as shown in Figure 3.11. Most esterquat are solid materials that do not have defined melting point but decompose upon heating (Kruger et al., 2003). Most esterquats have good water solubility. However, the di- and triesterquats are usually less soluble (Kruger et al., 2003). Due to their ester group, they have more possibility to react and thermally decompose at high temperature. In acidic medium such as the case of matrix acidizing, the protonation of ester carbonyl is slow and hindered by the positively charged nitrogen. Thus, they are more stable at acidic pH. Once the pH of solution increases (neutral-to-alkaline), the ester bond hydrolyzes quickly to yield fatty acid and small hydrophilic quaternary (Figure 3.11(e)). The diesterquat hydrolyzes in the same way with two fatty acid molecules are released. The stability of esterquat is influenced by temperature, pH, and chemical structure. This type of surfactant has been introduced recently to oilfield industry (Zhou and Trevor, 2002) as a fracturing fluid; however, results reported based on field treatment are below expectations (Nasr-El-Din et al., 2009). Esterquat generally have the ability to form rodlike micelles over a broad range of concentration (Zhou and Trevor, 2002). Sugar esters are another example of cleavable surfactants that have been receiving considerable attention, mainly because of advancement in synthesis process.

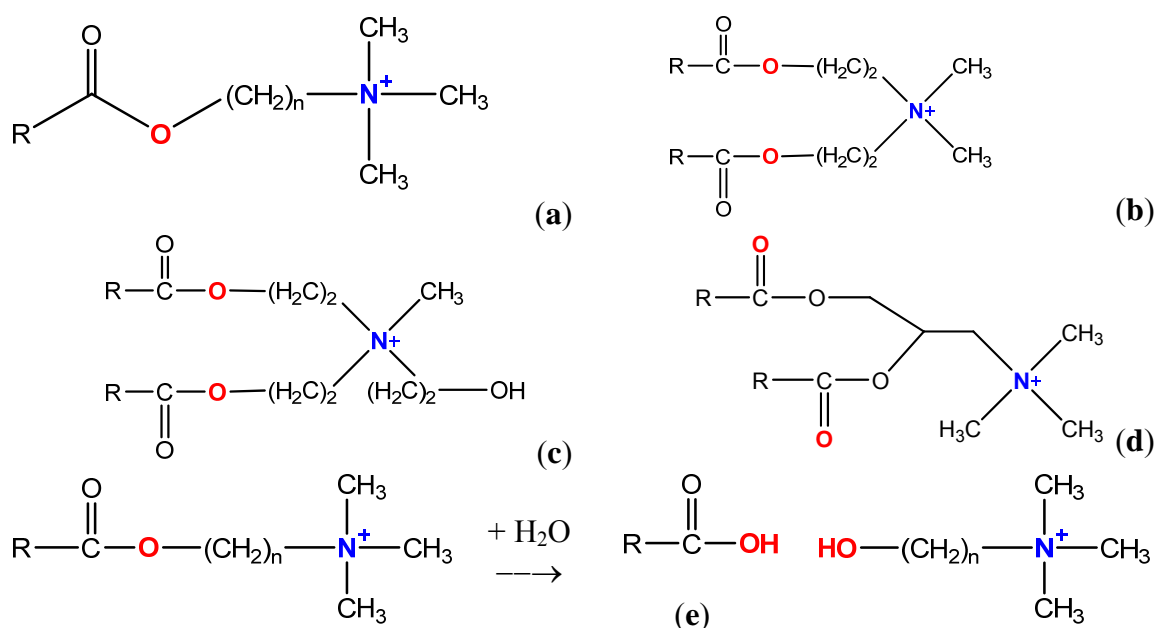


Figure 3.11: General molecular structure of (a) *monoesterquat*, (b) *diesterquat* of dimethyl-diethanol ammonium, (c) *diesterquat* of triethanol ammonium, (d) *diesterquat* of 2,3,-dihydroxypropyl ammonium and (e) hydrolysis of esterquat. R can be oleyl or erucyl chain.

3.4.7 Internal breaker

In some oilfield treatments such as acid diversion in matrix acidizing of gas wells, gravel packing, fracturing, lost circulation treatment, or scale squeezes, we need ultimately to break viscosity build up after the fluid has performed its function with pre-selectable breaking time. It has been recognized that the very high viscosity of viscoelastic surfactant fluids at very low shear rates might cause incomplete cleanup. Which raised the question do we need internal breaker? (Huang and Crews, 2008). Recent review of VES application in matrix acidizing and acid fracturing has shown formation damage due to longer flow back and cleanup period, particularly for low permeability and gas reservoir (Nasr-El-Din and Samuel, 2007). To break the high viscosity wormlike into small spherical micelles required contact with hydrocarbon. The unbroken VES fluids require high reservoir pressure in order to initiate flow during the cleanup process. It has been the practical exercise in matrix acidizing and fracturing treatment to depend upon reservoir conditions to break surfactant micelles after the completion of treatment.

Relying on external breaker has been a point of contention and discussion between scientists in oilfield industry in the last two year. I still remember my first argument in the international formation damage conference, which held in Lafayette (2008), with the idea that we do not need internal breaker, as reservoir hydrocarbon (external) will completely break the wormlike micelles and decrease viscosity of the gel to near zero based on rheological data reported in the literature (Molchanov et al., 2007). However, my view has changed lately and internal breaker may be required in some field treatments based on reservoir pressure, type of fluid and permeability. Internal breakers are compounds placed within the VES fluid during surface mixing and will break the gelled fluid after certain time without the need for contact with reservoir hydrocarbons. Suitable acids such as sulfuric, nitric, or acetic acid are useful breakers (Li et al., 2008). It is believed that the internal breaker slowly disrupt *inter*- and *intramicelles* binding forces that enable the formation of viscoelastic fluid. The breaking time may be controlled by selections of the amount and type of acid internal breaker to be added to the stimulation fluid. Temperature can also effect the time required for the fluid to completely break to water-like viscosity. it has been suggested to coat the breakers to delay breaking time (Li et al., 2008). The breaking time may optionally be accelerated using redox activator such as sodium metabisulfite or be delayed by addition of oxygen scavengers such as those shown in Figure 3.12. Unsaturated fatty acid mineral oil when used together result in efecient internal breakers to reduce the viscosity of VES-gelled (Crews and Huang, 2008).

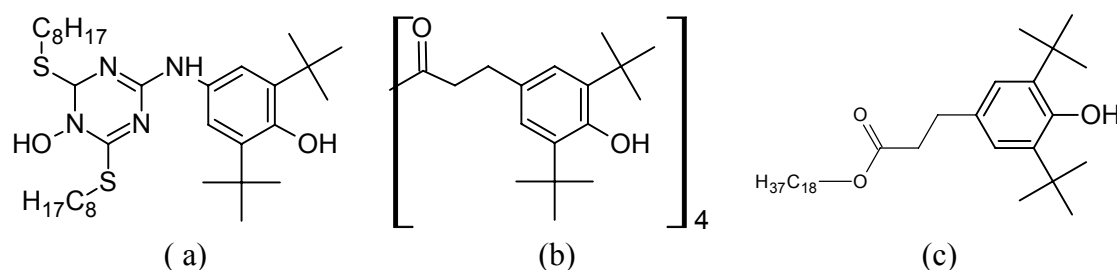


Figure 3.12: Examples of oxygen scavengers from IRGANOX® family that can be used to delay internal breakers: (a) Irganox® L 565, (b) Irganox® L 1010, and (c) Irganox® L 1076.

3.5 Dynamic Properties of WLM in Solution

Surfactants in solution tend to form long flexible cylindrical micelles with a large spread in length and properties resembling those of polymer solution. The dynamic properties of these systems are complex. This is due to the self-assembling nature of the micelles that can be considered as equilibrium polymer undergoing reversible breakdown process. At very low salt concentration, the micelles are stiffer, smaller and linear until the amount of salt is sufficient to screen out the electrostatic interaction. Their growth can be described by the mean field model and the couple reputation-reaction theory. In presence of an excess salt, several sets of experiment data suggest that intermicellar branching occurs, that can eventually lead at very high salt content to the formation of saturated network, stable only at sufficiently high surfactant concentrations (Lequeux and Candau, 1994).

Morphologies of aggregates formed by surfactants in aqueous solution are micelles, vesicles, bicontinuous, or inverted structures as shown in Figure 3.13. Aggregate morphology is mainly determined by a delicate balance between attractive hydrophobic interactions of surfactant alkyl tails and electrostatic repulsions of surfactant head groups. In addition to repulsive interactions of electrostatic origin, repulsions due to hydration of the head groups must be taken into account. An opposing effect is exerted by the interfacial tension that tends to decrease the effective head group area. The molecular architecture of a given surfactant determines the type of aggregate into which a surfactant associates in aqueous solution. The relationship between the shape of the surfactant monomer and the aggregate morphology can be represented by the packing parameter approach. The packing parameter (P) is calculated from equation: $P=V/(l \cdot a_0)$. In this equation, V is the volume of the hydrocarbon part of the surfactant, l its chain length of the extended all-trans alkyl tail, and a_0 the mean cross-sectional (effective) head group surface area. Surfactants where $0 < P < 1/3$ form micelles in aqueous solution. If $1/3 < P < 1/2$ wormlike micelles are formed whereas surfactants with $1/2 < P < 1$ form vesicles. Inverted structures are formed when $P > 1$.

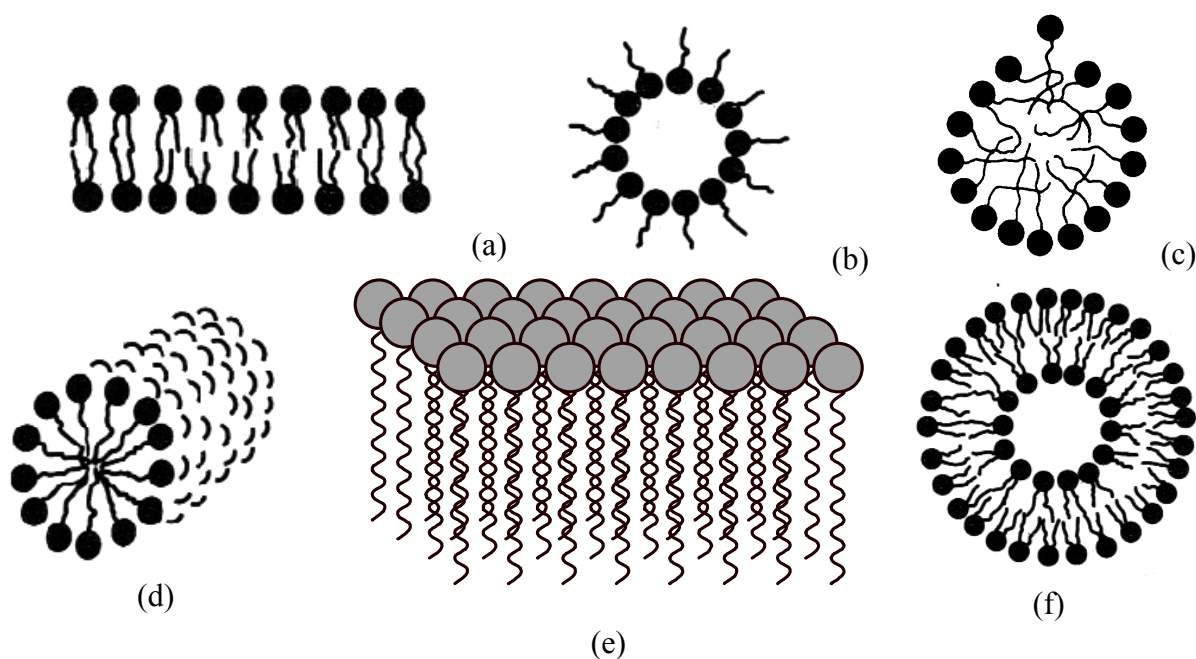


Figure 3.13: Aggregation morphologies of VES in aqueous solution (a) bilayer micelle, (b) vesicle, (c) spherical (d,e) wormlike micelle, and (f) inverted micelle.

Generally, unbranched single-tailed surfactants possess a conical shape and aggregate to form spherical micelles in aqueous solution above their critical micelle concentration (cmc). The interior of micelles consisting for the most part of methylene groups of alkyl tails of the surfactants is alkane-like and it contains almost no water. Only the first two methylene groups of the surfactant (counted from the head group) have considerable contact with water in the aqueous solution. The lifetime of a spherical micelle is of the order of milliseconds and the residence time of a monomer in a micelle is of the order of microseconds. Monomer exchange is diffusion controlled. Spherical micelles usually consist of 40-100 monomers and are approximately 5 nm in diameter.

Wormlike micelles are formed by surfactants whose monomer shape resembles a truncated cone. Both theoretical and experimental studies show that wormlike micelles are long (several tens of micrometers) and flexible and that they undergo transformations on relatively short timescales. The presence of wormlike micelles in aqueous solution is

often reflected by an increase in relative viscosity. Viscoelastic solutions are formed upon increasing the surfactant concentration; viscoelasticity indicates that an entangled network of wormlike micelles has been formed. Formation of wormlike micelles can often be induced by addition of strongly binding counter ions to ionic surfactants in aqueous solution. Counterions have a large influence on the morphology that surfactant aggregates adopt in aqueous solution. Changing the counter ion of ionic surfactants for a more strongly bound one leads to a decrease of the effective head group area. Especially aromatic counter ions like tosylate, benzoate, or salicylate are effective in inducing micellar growth (Raghavan, 2001). In addition to a decrease of a_0 , penetration of the aromatic ring of a counter ion between the surfactant molecules leads to an increase in the volume of the surfactant monomer. A combination of both effects results in an increase in P and consequently the surfactants self-assemble into a less curved aggregate. This case corresponds to a change from spherical to wormlike micelles (Zana and Kaler, 2007). Upon growing, wormlike micelles may form a three dimensional network that shows viscoelasticity. The orientation of substituents on the aromatic ring appears to be extremely important for inducing viscoelasticity. Recent studies of microstructure and rheology for model worm-like micelle forming systems such as CTAB provide the underpinning understanding of molecular-bulk property relationships to guide fluid design (Zana and Kaler, 2007). Of particular significance for controlling applications is the strong coupling between shear flow and structure/phase behaviour for these systems. Molecular and mesoscopic simulations are also proving successful at probing these relationships. The general rheological behaviour of viscoelastic surfactants comprising wormlike micelles can be rationalised within the now classical framework of Cates (Cates and Candau, 1990), their near Maxwell-like behaviour in the linear viscoelastic regime and their non-monotonic stress-strain curve giving rise to double valued shear-rates for a given shear stress (Zana and Kaler, 2007), implying unstable flow behaviour in certain flow regimes. A recent comprehensive study by Hu et al. (Hu et al., 1998) has characterised this behaviour in some detail in transparent Couette cells using laser light scattering to image the shear-induced fluid microstructure changes

simultaneously. Studies of worm-like micelle systems in elongational flow are also beginning to emerge. Chen and Warr (Chen and Warr, 1997) have used light scattering to measure the micelle radius of gyration in the elongation direction and show that this follows apparent elongational viscosity closely, increasing initially as the micelles align and extend in the flow but then decreasing markedly above a critical extension rate, possibly due to micelle chain scission. The implications for the flow of these fluids through porous media, where rapidly changing elongational flows play a major role, could be extremely significant. While having some obvious advantages over polymeric gels, conventional non-polymer gels (surfactants) also have some disadvantages. One is the temperature limitation of surfactant gels. As well depth increases, well bore hole temperature usually also increases, and may frequently exceed 250° F. (about 121° C.). Currently, conventional surfactant technology fails under these conditions, while polysaccharide gels continue to perform. Another disadvantage is cost, in that the material cost for polysaccharide gels is substantially lower than that for surfactant gels. Yet another disadvantage of conventional surfactants is their toxicity to the environment and their poor biodegradability. Because cationic alkylamines do not breakdown readily in the environment, they tend to accumulate. Alkylamine quaternary compounds are also toxic to many life forms, so they can have a destructive impact, particularly on environments in which they accumulate. Some areas of the world have imposed regulatory restrictions on chemicals based on their being hazardous to the environment. For example, in the North Sea, chemicals such as cationic alkylamine are either restricted or banned entirely. Thus, there is a need for gellants, in particular, viscoelastic gellants, that can provide all or most of the advantages of the surfactant technology, and that (1) can provide viscoelastic properties at higher temperatures (greater than 110°C. or 230°F.); (2) are more eco-friendly; and/or (3) are more cost effective. The presently described technology addresses these needs. Summary of common VES commercial systems are shown in Table 3.4. Figure 3.14 shows various diversion systems that might be used in matrix acidizing with functionality according to pH range as in Figure 3.15.

Table 3.4: Summary of common surfactants used in oilfield industry as diverting fluid

<i>Class</i>	<i>Name</i>	<i>Manufacturer</i>	<i>Description</i>
Anionic	pOly	Segma-Aldrich	Potassium oleate
	Empol ⁽¹⁾	Henkel Corp.	Oleic oligomer
	EFS-4 ⁽²⁾	Halliburton	Methyl ester sulfonate (MES) surfactant
	Miranate LEC ⁽³⁾ Edenor TM ⁽⁴⁾	Rhodia Inc. Oleo solutions	Sodium laureth-13 carboxylate Mixture of linoleic and oleic acids
Cationic	EHMAC ⁽⁵⁾ or (ClearFRAC [®])	Schlumberger	erucyl-N,N-di-(2-hydroxyethyl)-N-methylammonium chloride
	Ethoquad O/12 ⁽⁶⁾	Akzo Nobel	Oleyl methyl bishydroxyethyl ammonium chloride
	Alkaquat DMB-451 ⁽⁷⁾	Rhodia Inc.	Benzyl triammonium chloride
Gemini	SAPDMA GQ ⁽⁸⁾	McAndrews, Held & Malloy	stearamidopropyldimethylammonium di-chloride (18APDMA-3(OH)-18-APDMA)
	SoyAPDMA-3-(OH)-18APDMA ⁽⁸⁾	McAndrews, Held & Malloy	soyamidopropyldimethylammonium-stearamidopropyl-dimethylammonium chloride toluene sulfonate
Betaine	BET-O ⁽⁹⁾	Rhodia Inc. Schlumberger	C ₁₇ H ₃₃ alkene tail group, dissolve in water, NaCl and propylene glycol
	BET-E ⁽⁹⁾	Rhodia Inc. Schlumberger	C ₂₁ H ₄₁ alkene tail group, dissolve in water, NaCl and isopropanol
	EDAB ⁽⁹⁾	Rhodia Inc.	Erucyl dimethyl amidopropyl betaine
	Rewoteric AM TEG TM ⁽¹¹⁾	Degussa Corp.	Tallow dihydroxyethyl betaine
Amidoamine-oxide	APA-T ⁽¹²⁾ (Aromox [®])	Akzo Nobel	Tallowalkylamidopropyl dimethylamine oxide
	Ethomeen T/12, S/12 ⁽¹¹⁾	Akzo Nobel	Fatty amine ethoxylate surfactant.
Esterquat	Erucyl-SD ⁽¹³⁾	Schlumberger	N,N-dimethyl N-ethyl glycine erucyl ester
	MOS-SD ⁽¹³⁾	Schlumberger	Monooleyl succinic acid

Data are taken from reference: ⁽¹⁾ (Hughes et al., 2002). ⁽²⁾ (Welton et al., 2007). ⁽³⁾ (Christanti et al., 2008). ⁽⁴⁾ (Hartshorne et al., 2007). ⁽⁵⁾ (Morris, 2008). ⁽⁶⁾ (Lin et al., 2001). ⁽⁶⁾ (Colaco et al., 2006). ⁽⁷⁾ (Knox, 2008). ⁽⁸⁾ (Zhou and Hughes, 2006). ⁽⁸⁾ (Chang et al., 2002). ⁽¹⁰⁾ (Welton, 2008). ⁽¹¹⁾ (Doboson et al., 2003). ⁽¹²⁾ (Zhou and Trevor, 2002).

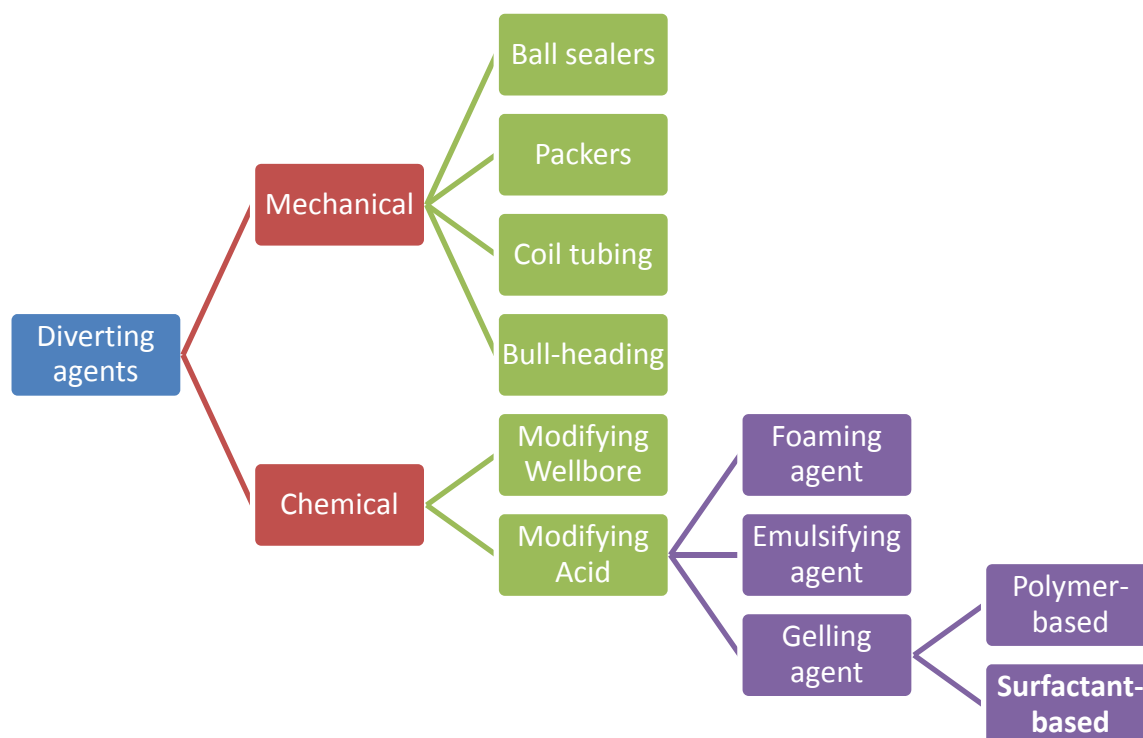


Figure 3.14: Acid placement techniques in matrix acidizing.

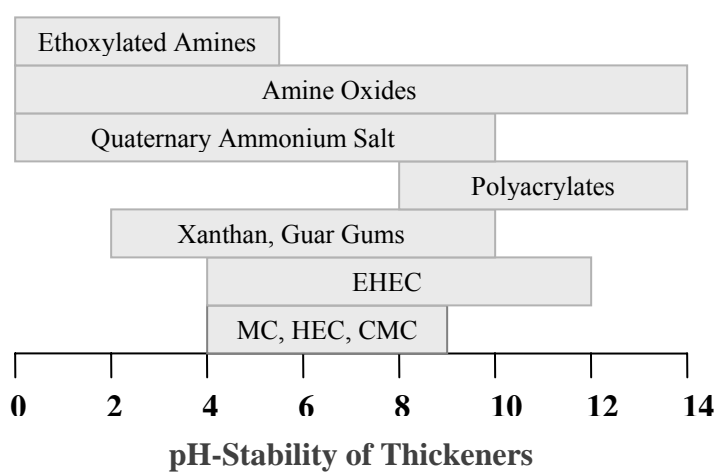


Figure 3.15: Selection of type of surfactant based on pH range.

CHAPTER IV

***AB INITIO* STUDY OF HYDRATION AND BINDING ENERGIES FOR M^+ (H_2O)_n.*m* H_2O CLUSTERS ($M=Ca^{2+}$, Mg^{2+} , Na^+) IN CARBONATE RESERVOIRS**

Because of recent improvements in the accuracy of theoretical predictions meaningful comparisons between theoretical and experimental findings have become possible

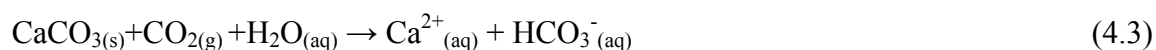
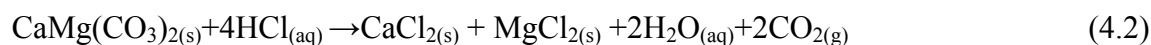
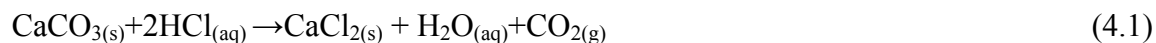
— Yuan T. Lee

The importance of metal ions and their diverse occurrences in oilfield chemistry is indubitable. Hydration of mono- and divalent metal ions (Na^+ , Ca^{2+} , and Mg^{2+}) is presented in this chapter using DFT (B3LYP). The study of hydrated gas-phase metal ions provides a link between intrinsic chemistry of the isolated ion and its chemistry in solution. Solvation of metal ions can lead to an understanding of the structures and functions of many surfactants in well stimulation treatment where metal ions play a role. The structures and binding enthalpies of gas-phase mono- and divalent ion hydrates containing up to 18 water molecules have been studied computationally. *Ab initio* molecular orbital calculations was employed to study hydrated structures of the form $[M(H_2O)_n]^{2+}.mH_2O$ for calcium and magnesium and $[M(H_2O)_n]^+.mH_2O$ for sodium, in which there are n water molecules in the first coordination shell and m water molecules in the second coordination shell. An understanding of the energetic contribution of individual structural characteristics as well as the energetic trends in binding energy is developed, which will help in better design of field treatments in carbonate reservoirs.

4.1 Introduction

Hydrocarbons (oil and gas) are obtained from a subterranean geologic reservoir by drilling a well that penetrate the bearing formation. In order for hydrocarbon to be produced, there must be sufficiently unimpeded flow path from the reservoir to the bottom of the well. Formation rocks (sandstone or carbonate) are the main medium of transport and having conduits (pores) of sufficient size and number play a crucial role in hydrocarbons flow. Carbonate geology represents around 50% of hydrocarbon-bearing

reservoirs in the world and more 70% in some areas such as the Middle East. The basic minerals in carbonate sediments include aragonite or calcite (CaCO_3), low-Mg calcite (0-4 mol % MgCO_3), high-Mg magnesite (10-25 mol % MgCO_3), and dolomite ($\text{MgCa}(\text{CO}_3)_2$) (Table 4.1). Acidizing a hydrocarbon formation is the process of reacting an acid with geological rock to enhance flow of hydrocarbons to the wellbore. This stimulation treatment helps to open up new channels around the wellbore especially for low permeability reservoir and in many cases remove any damage caused by spent drilling fluid, fine migration, paraffin, or mineral precipitation (scale). To ensure effective coverage of all zones in a single hydrocarbon well, controllable acid delivery mechanism is needed. Chemical delivery or what is known in oilfield industry as “chemical diversion” is the method of choice in many cases. Hydrochloric acid (HCl) is mainly used in matrix acidizing, however, various forms of weak acids such as formic, citric, acetic and chelating agents are preferable in some cases based on geological chemistry, well completion, and flowing fluid. Injecting acid into carbonate reservoir will result in reactions with the rocks according to Equations (4.1) and (4.2). This result in the following ions and molecules (Mg^{2+} , Ca^{2+} , CO_3^{2-} , HCO_3^- , H_2CO_3 , CO_2 , H_3O^+ , OH^- , Cl^-) to be presented in solution when calcite or dolomite are in equilibrium with their ions in pure water after the reaction with strong acid is completed. A deep understanding of metal ion interactions with water at the atomistic and molecular levels, and how these interactions are affected by collective effect of pressure and temperature are of great interest for achieving an adequate selection of viscoelastic surfactant and designing more effective and efficient stimulation treatment.



Direct experimental determination of metal speciation in aqueous solution and on mineral surfaces can be determined using different techniques such as spectroscopy, Raman spectra and neutron scattering (Sherman, 2001). However, with the advancement

in theoretical chemistry and high computational speed, the structures, thermodynamic properties and spectroscopic of metal complexes can be predicated from first principle quantum mechanical calculation. Molecular properties of the alkaline-earth and alkaline metals cations are of great interest for many applications including geochemistry, biological systems (Periole et al., 1997), hydrogen storage (Page and Nagy-Felsobuki, 2008; Shang et al., 2004). They have a wide range of bonding characteristics ranging from weak van der Waals interaction to the formation of strong covalent or ionic bonds.

Table 4.1: Thermodynamic properties of carbonate Minerals

Mineral	Formula	Molecular weight	Density (g cm ⁻³)	Crystal system	$\Delta G_{f,298}$ (J mole ⁻¹)
Calcite	CaCO ₃	100.09	2.71	Trigonal	-1128842
Aragonite	CaCO ₃	100.09	2.93	Orthogonal	-1127793
Veterite	CaCO ₃	100.09	2.54	Hexagonal	-1125540
Monohydrocalcite	CaCO ₃ .H ₂ O	118.10	2.43	Hexagonal	-1361600
Ikaite	CaCO ₃ .6H ₂ O	208.18	1.77	Mono	-
Magnesite	MgCO ₃	84.32	2.96	Trigonal	-1723746
Nesquehonite	CaCO ₃ .3H ₂ O	138.36	1.83	Trigonal	-1723746
Artinite	Mg ₂ CO ₃ (OH) ₂ .3H ₂ O	196.68	2.04	Mono	-2568346
Dolomite	CaMg(CO ₃) ₂	184.40	2.87	Trigonal	-2161672
Huntite	CaMg ₃ (CO ₃) ₄	353.03	2.88	Trigonal	-4203425

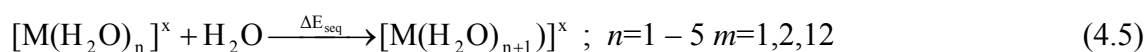
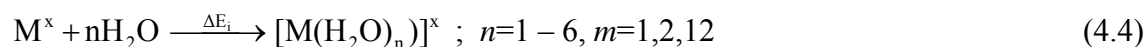
Divalent cations hydrolysis and interaction with other small molecules have been studied in the literature ranging from *ab initio* to molecular dynamic simulation. Mg²⁺ and Ca²⁺ in methanol solution were investigated using Car-Parrinello molecular dynamic (CPMD) simulation (Faralli et al., 2008). Studying interaction between cations and other chemicals in a “realistic” water environment is the main concern for many researchers. Whereas experimental data using X-ray and neutron diffraction shows the water molecules in the first hydration shell of Mg²⁺ and Ca²⁺ ranging from 6 to 10 (Ohtaki and Radnai, 1993), Monte Carlo and molecular dynamics studies observe values ranging from 7 (Bernal-Uruchurtu and Ortega-Blake, 1995) to 9 (Floris et al., 1994). It was shown as a result of *ab initio* calculations that Ca²⁺ and Mg²⁺ with 8 water molecules in

its first shell is slightly more stable than that with 9. The number of water molecules in the second hydration shell of Na^+ , Ca^{2+} , and Mg^{2+} are 12 or greater (Clementi and Barsotti, 1978; Ohtaki and Radnai, 1993). Hydration is typically described according to the nature of the inner and outer shells (first and second coordination sphere). Number of water molecules in the first shell is determined to a large extent by the chemical and physical properties of the central metal ion (e.g., size, charge, electronic state, etc.). Additional shells of water result from hydrogen bonding with the inner-shell water molecules, as well as from long-range electrostatic effects from the metal ion. These additional shells begin the interface between the immediate metal ion environment and that of bulk water. Apart from this work, we have come across many several molecular dynamic simulations on the solvation of alkali, alkaline earth and first row transition metal cations. The objective of this chapter is to predict the nature of metal complexes and the chemistry of aqueous fluids using first principle theory that is not dependent upon any extrapolations or predicting model as in the equation of states (Helgeson and Kirkham, 1974; Helgeson et al., 1981). *Ab initio* molecular orbital calculations for a variety of hydrated monovalent and divalent ions of the form $\text{M}[\text{H}_2\text{O}]_n^{x+} \cdot m\text{H}_2\text{O}$ (where the n and m denote the number of water molecules in the first and second coordination shells, respectively) were performed using density functional theory.

4.2 Computational Method

All hydro-metal complexes considered in the present study $[\text{M}(\text{H}_2\text{O})_n \cdot m\text{H}_2\text{O}]$; $\text{M}=\text{Na}^+$, Ca^{2+} , Mg^{2+} , $n = 1-6$, $m=1,2,12$] were explored by density functional theory (DFT). The choice of the basis set represents a compromise between accuracy and our desire to include a significant number of water molecules in the system. Rao *et al.* (Rao et al., 2008) have evaluated recently the importance of the method and basis set for the accurate prediction of sequential binding energies of mono- and divalent cations. An increase in the quality of the basis set for double- ξ to triple- ξ has a significant effect on thermodynamic properties irrespective of the geometry. It was concluded that the B3LYP functional performs slightly the same as the wave function based methods like

MP2. In recent years, density functional theory, especially the B3LYP (Becke, 1993) functional emerged as a method of choice compared to MP2, due to its computational economy. Thus, it is the method of choice in this study with 6-311++G(d,p) basis set. This basis set gave the best value of calculated binding enthalpy compared to experimental one for $[\text{Na}(\text{H}_2\text{O})]^+$ cluster using DFT (B3PW91) (Balbuena and Seminario, 1999). This basis set includes a diffuse function on the heavy atoms and polarization functions on all atoms. All calculation are obtained at 298 K and performed by the Gaussian (G03) package (Frisch et al., 2004). Total and sequential binding energies were calculated using the following equations.



$$\Delta E_i = E_{\text{M}^x(\text{H}_2\text{O})_m} - (E_{\text{M}^x} + mE_{\text{H}_2\text{O}}) \quad (4.6)$$

$$\Delta E_{\text{seq}} = E_{\text{M}^x(\text{H}_2\text{O})_{n+1}} - (E_{[\text{M}(\text{H}_2\text{O})_n]^x} + E_{\text{H}_2\text{O}}) \quad (4.7)$$

4.3 Results and Discussion

Results in this chapter are presented according to coordination number of metal ion. First, pure water clusters of the form $\text{H}_2\text{O}(\text{H}_2\text{O})_n$, where $n=1-8,17$, are optimized at B3LYP/6-311++G(d,p). Although, cluster of the size 2–8 have been the subject of a number of earlier studies, we have repeated some of them for consistent analysis and comparison. Then, conformational analysis of metal-water clusters obtained by the B3LYP/6-311++G(d,p), variation of M–O distances, hydrogen bond, total binding energy, and charge analysis are presented. Both inner and outer shells are explored for the three metal ions ($\text{M}=\text{Na}^+$, Mg^{2+} , and Ca^{2+}). Previous studies have shown that including basis set superposition error for such complexes do not necessarily improve the accuracy of the results (Markham et al., 2002), and therefore, this correction is not incorporated into the binding energies reported in this chapter.

4.3.1 $H_2O.nH_2O$

Water is an essential part in well stimulation and oilfield reservoirs. We will present first the *ab initio* results for pure water cluster before going further and studying complexation with various metal ions. There is a general consensus among researchers that water is a highly structured liquid due to an extensive network of hydrogen bonding between molecules. Increasing temperature causes expansion of molecules, weakening the hydrogen bonds, and hence decreases density, whereas increasing pressure will result in density increase. Therefore, the structure of pure water is highly dependant on temperature and pressure. Ions dissolved in water as a result of electrolytes dissociation, will form ion-hydrate. Since most ions have large electric field around them, the dipolar water molecules will rearrange themselves in hydration shells around the ions with structure different from that in bulk water as we will see in the next sections of this chapter. Water cluster offer a paradigmatic case for bulk properties and substantial progress has been made in recent years in studying its structures. A number of *ab initio* calculations have been carried out to investigate the strength of hydrogen bond and understand their characteristics (Marcus, 2009). The water dimer, the smallest water cluster which constitutes the fundamental step in the study of water clusters, has been studied in great detail experimentally (Pribble and Zwier, 1994b) as well as theoretically (Maheshwary et al., 2001). It has been established that the most stable structure of a water dimer is of the C_s symmetry. The optimized structure calculated in this study using B3LYP/6-311++G** has a single hydrogen bond ($R_{OH}=1.93 \text{ \AA}$) with binding energy of -4.1 kcal/mol compared to $-5.5 \pm 0.7 \text{ kcal/mol}$ found experimentally. Figure 4.1 shows the optimized structures for $H_2O(H_2O)$ with corresponding binding energy and average hydrogen bond. For $n=3$, vibrational spectroscopic studies (Bentwood et al., 1980) as well as some of the early *ab initio* studies (Bene and Pople, 1970) suggested an open-chain conformer with nearly linear hydrogen bonds as the most stable structure of a water trimer. Some of the other experimental (Pugliano and Saykally, 1992) and theoretical studies (Maheshwary et al., 2001) show a cyclic structure with C_1 symmetry, with two external hydrogen atoms on one side of the O–O–O plane and a third one on

the other side of the plane, to be the most stable. The other conformational structure of trimer H_2O cluster with three external hydrogen atoms are in one side of the O–O–O plane (uuu) is less stable (Ugalde et al., 2000). The calculated binding energy for trimer water cluster is -13.5 kcal/mol with an average hydrogen bond length of 1.90 Å, which are in a good agreement with what have been reported in literature (Maheshwary et al., 2001). In such a structure, each monomer behaves as a donor as well as an acceptor. For $n=4$, the tetramer, the optimized structure corresponding to the global minimum is cyclic structure with S_4 symmetry. In this case, the free hydrogen (i.e. external) atoms alternate in their arrangement above and below the plane of the O–O–O–O ring. Other structures with two or three external hydrogen atoms in one side of the O-ring are less stable (Ugalde et al., 2000). There are four hydrogen bonds in the tetramer H_2O cluster with average length of 1.77 Å, and total binding energy of -22.2 kcal/mol. Pentagonal rings of water molecules, $n=5$, appear to follow the same cyclic ring pattern as that observed for the tri- and tetramer. The most stable structure for the pentamer it is monocyclic puckered with five external hydrogen atoms and five hydrogen bonds (Ugalde et al., 2000). *Ab initio* calculation also predicted such a ring structure and previous studies examined various structures of pentamers at the Hartree–Fock (HF) level and found that the ring was more stable than the bipyramidal forms by at least 1 kcal/mol (Burke et al., 1993). The calculated binding energy for pentamer H_2O cluster is -30.0 kcal/mol with average hydrogen bond of 1.74 Å. For hexamer water cluster, $n=6$, the structure of $(\text{H}_2\text{O})_6$ represents a transition from cyclic to three-dimensional geometries (Muller-Dethlefs and Hobza, 2000), and it has been studied extensively by theory and experiments. Although some of the *ab initio* calculations (Tsai and Jordan, 1993) suggested the cyclic and the prismatic structures to be the most stable, it has recently become clear (Maheshwary et al., 2001) that a large number of alternative three-dimensional structures, such as chair or book, boat, and cage, are likely to be of comparable energies. Zero-point vibrational energy (ZPE) seems to play an important role in deciding the preferred geometry of the hexamer.

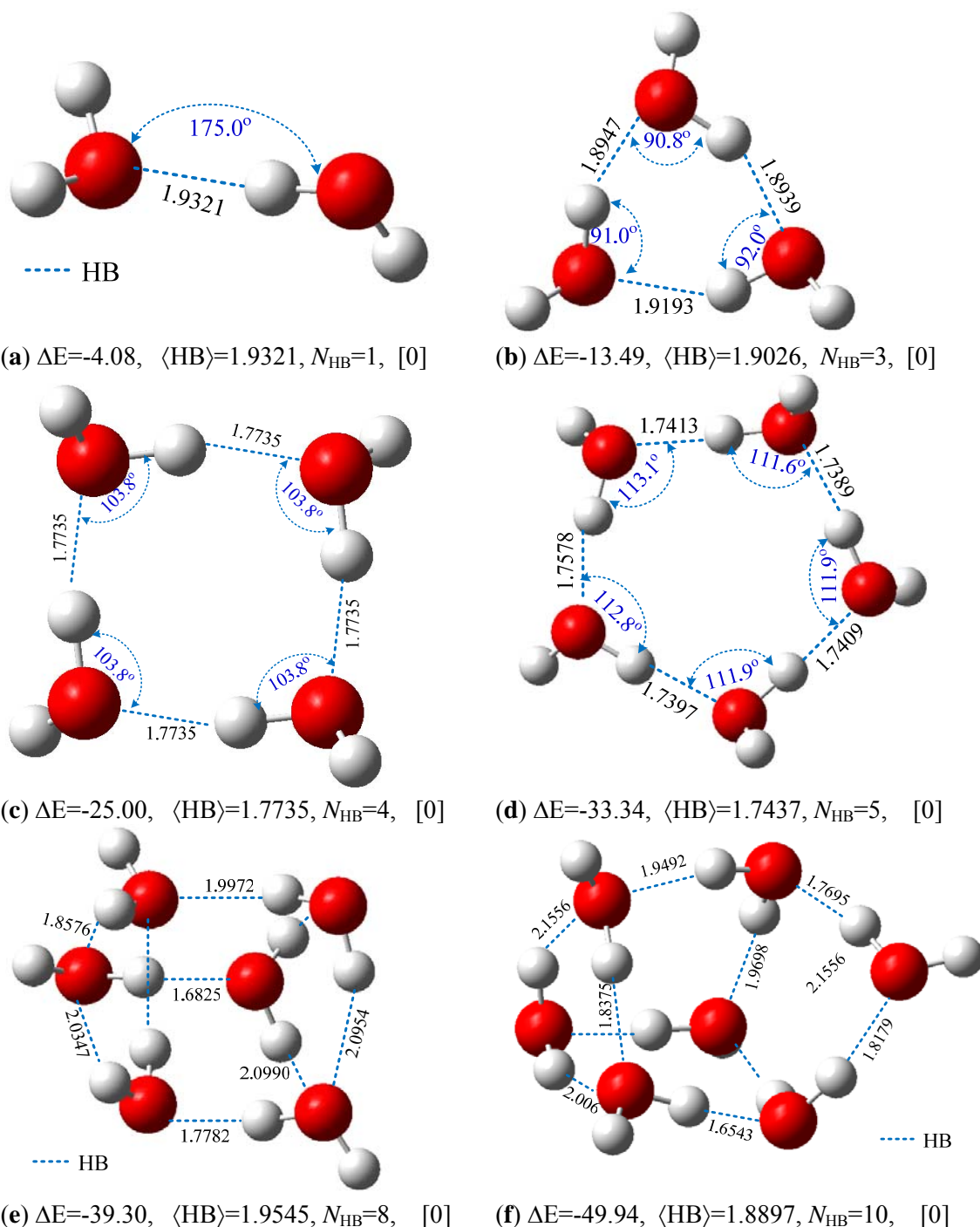


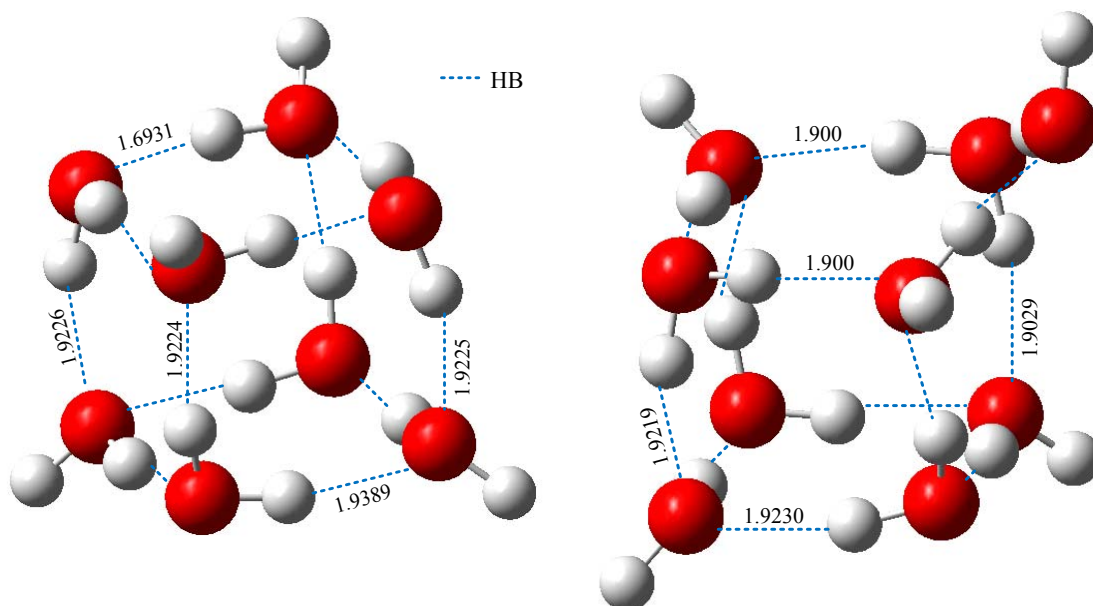
Figure 4.1: Optimized parameters and geometrical structure for $n \leq 7$ water clusters (a) $H_2O(H_2O)$, (b) $H_2O(H_2O)_2$, (c) $H_2O(H_2O)_3$, (d) $H_2O(H_2O)_4$, (e) $H_2O(H_2O)_5$, (f) $H_2O(H_2O)_6$. Shown in these diagrams are hydrogen bond length, HB, (Å), bond angle ($^\circ$), binding energy, ΔE , (kcal/mol) and number of imaginary frequency in square brackets. Color code: red for O atoms, light gray for H atoms.

A detailed study on water hexamer cages at the semiempirical (PM3) level has been carried out recently by Coe et al. (Tissandier et al., 2000). Though the cage structure with four external H atoms and eight hydrogen bonds has been reported to be the most stable (Ugalde et al., 2000), recent studies showed that the prism structure with three external H atoms and nine hydrogen bonds is more stable (Maheshwary et al., 2001). Therefore, the calculation presented in this chapter is for prism hexamer water cluster which has a binding energy of -43.7 kcal/mol and average hydrogen bond of 1.95 Å. The average hydrogen bond length decreases as the number of water molecules increases in the clusters ($n=1-5$) and hence the binding energy increases, however, it increases at $n=6$. This can be explained by the number hydrogen bond donors in both cases. For $n<6$, there are only one hydrogen bond donor, whereas for $n=6$ there are three single donor with $\langle\text{HB}\rangle=1.77$ Å and five double donors with $\langle\text{HB}\rangle=2.04$ Å.

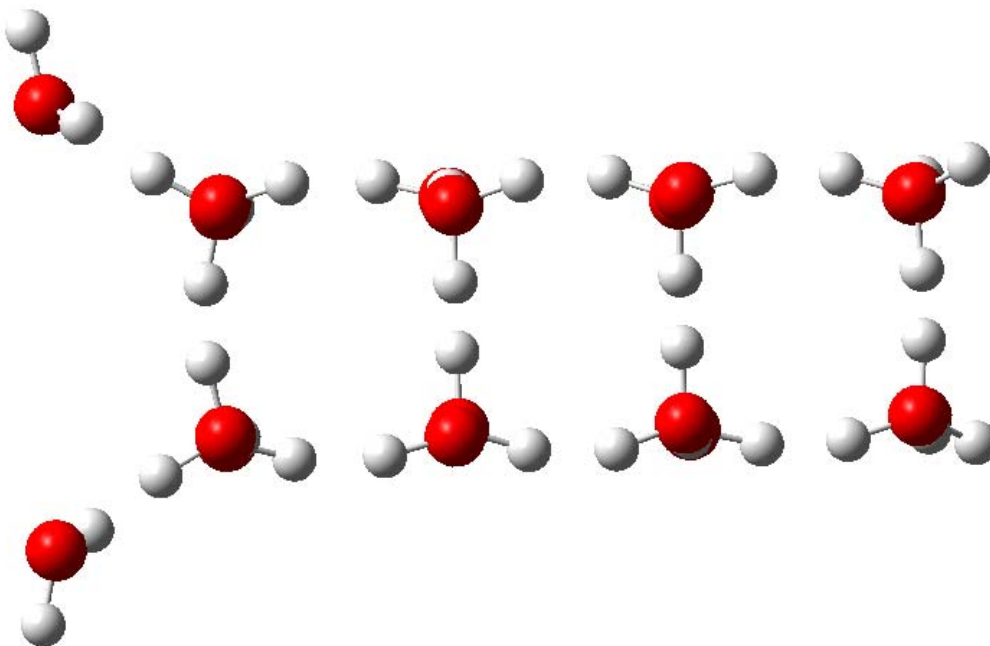
Experimental IR spectra of benzene-(H₂O)₇ (Pribble and Zwier, 1994a) and phenol-(H₂O)₇ (Janzen et al., 1999) clusters suggest a compact noncyclic and a cuboid structure, respectively for the heptamer. The vibrational O-H spectra of pure (H₂O)₇ (Brudermann et al., 1999) indicate the existence of two isomers derived from the S₄ octamer cube by the removal of either a double-donor or a double-acceptor water molecule. With the increase in the size of the cluster, the number of possible structures increases rapidly, and it becomes difficult to probe all of the conformers. Therefore, theoretical studies until recently (Maheshwary et al., 2001) have tended to focus on a few of them: seven-membered cyclic structures as well as cages made up of different cyclic n -mers fused together. The consensus seems to be that there are several cage structures lying close to each other, with the cuboidal geometry (with a corner missing) being the lowest in energy as shown in Figure 4.1 (f). The calculated binding energy for this cubelike structure is -44.4 kcal/mol, and it has ten-hydrogen bonds with average bond length of 1.89 Å. the optimized structure for heptamer H₂O cluster has three free hydrogen, two of them are in the 3-corner base and the third is in the 4-corner base. Also, we observe that most hydrogen bonds are not exactly linear, and hence the angle

$\angle\text{OHO}$ is in the range of $160\text{--}170^\circ$ and the average O–O distance between neighboring oxygen atoms involved in a hydrogen bond is around 2.80 \AA .

Extensive *ab initio* calculations (Kim et al., 1994) suggest that, at low temperatures, $(\text{H}_2\text{O})_8$ would stabilize into a cube with D_{2d} or S_4 symmetry and that, at higher temperatures, entropy considerations could favor the other geometries. HF/6-31G(d,p) was used in recent study to optimize energy for seven different possible structures of octamer water cluster (Maheshwary et al., 2001). The cubic geometry with D_{2d} symmetry found to be the most stable with 12 hydrogen bonds as shown in Figure 4.2 (a). the binding energy for this structure was calculated to be -56.6 kcal/mol with average hydrogen bond distance of 1.82 \AA . The higher binding energy and lower hydrogen bond length for $(\text{H}_2\text{O})_8$ compared to $(\text{H}_2\text{O})_7$ and $(\text{H}_2\text{O})_6$, indicate that the octamer cluster is more stable as a 3D structure. For $n=9$, Jensen et al. (Jensen et al., 1996) considered 44 possible structures for the nonamer in their extensive HF calculations using the 6-311G(d) and 6-311G(d,p) basis sets and concluded that the most stable structure consisted of a four-membered ring stacked over a five-membered ring that could be thought of as an extended cube. The only available experimental result for $(\text{H}_2\text{O})_9$ (Buck et al., 1998) seems to be in qualitative agreement with the predicted structure. *Ab initio* computations at the DFT/B3LYP/6-311G(d,p) and MP2/DZP levels were carried out to determine the structure, energies, vibrational spectra, and electronic properties of the clusters for $(\text{H}_2\text{O})_n$, $n = 1\text{--}10$ with less focus on structures for $n \geq 7$ (Lee et al., 1995). Recently, Sathyamurthy et al. (Maheshwary et al., 2001) has used HF/6-31G(d,p) and DFT/B3LYP/6-31G(d,p) to optimize five possible nonamer structures based on experimental studies of Buck et al. (Buck et al., 1998). The binding energy for the most stable nonamer H_2O cluster with one water molecule bonded to the cubic octamer is -65.1 kcal/mol and its average hydrogen bond calculated to be 1.45 \AA . the relation between binding energy and size of water cluster is linear as shown in Figure B2. The binding energy per water molecule can be expressed in terms of a simple function: $\Delta E_i = A + B/n$ as shown by previous study (Lee et al., 1995).



(a) $\Delta E = -63.67$, $\langle \text{HB} \rangle = 1.8227$, $N_{\text{HB}} = 12$, [0] (b) $\Delta E = -72.70$, $\langle \text{HB} \rangle = 1.8547$, $N_{\text{HB}} = 13$, [1]



(c) $\Delta E =$, $\langle \text{HB} \rangle =$, N_{HB} (**Notice:** the structure in (c) is the initial geometry).

Figure 4.2: Optimized parameters and geometrical structure for $n > 7$ water clusters (a) $\text{H}_2\text{O}(\text{H}_2\text{O})_7$, (b) $\text{H}_2\text{O}(\text{H}_2\text{O})_9$, (c) $\text{H}_2\text{O}(\text{H}_2\text{O})_{17}$. Shown in these diagrams are hydrogen bond length, HB, (Å), bond angle ($^\circ$), binding energy, ΔE , (kcal/mol) and number of imaginary frequency in square brackets. Color code: red for O atoms, light gray for H atoms.

4.3.2 $[Na(H_2O)_n]^+$

Sodium has an ionic radius of 0.95 Å and can be found in most reservoirs. We choose it as an example of monovalent ion in studying well simulation of carbonate reservoir because it is the major cation in oilfield brines (Schechter, 1992). Experimental results based on X-ray diffraction shows the hydration number of Na^+ is distributed over the range 4-8 with 6 as the most probable (>95%) (Ohtaki and Radnai, 1993). The nonadditive contribution in the first hydration shell of Na^+ , K^+ , and Mg^{2+} based on *ab initio* QM/MM approach has been studied. Also, molecular dynamic simulation (Periole et al., 1997) was used to investigate the two-body interaction potential model for water distribution around selected cations, and showed that the first hydration shell for Na^+ , and K^+ is not well defined as for divalent ions. Optimized geometrical structures of $Na[H_2O]_n^+.mH_2O$ ($n=1-6$, $m=1-2$) are shown in Figure 4.3. All structures presented here are not at local minima on their respective potential energy surface and the numbers of imaginary frequency are shown in square brackets in Figure 4.3. The optimized structure for $n=1$, $[Na(H_2O)]^+$, is linear with $\angle O-Na^+-H$ equal to 127° . The Na^+-O bond length is 2.22 Å with 7% absolute error from the experimental value which was determined by diffraction method to be in the range of 2.40–2.50 Å (Ohtaki and Radnai, 1993). Conformational symmetry of C_{2v} is a local minimum with calculated total binding energy of $\Delta E_i = -25.0 \text{ kcal mol}^{-1}$. The binding energy was calculated as the difference in enthalpy between the cluster and individual molecules of water and metal ion as in equation (6) at the same level of theory and basis set. The two conformations D_{2d} and C_{2v} (W-Na-W and Na-W-W, respectively; W=water) for $[Na(H_2O)_2]^+$ was examined in this research and recently published by other group (Rao et al., 2008). The structure $Na^+-H_2O-H_2O$ (M- Na^+ -W) is considerably less stable with binding energy of $\Delta E_i = -46.2 \text{ kcal mol}^{-1}$ compared to $\Delta E_i = -59.0 \text{ kcal mol}^{-1}$ for (W- Na^+ -W) calculated using B3LYP/6-31G(d). For $n=3$, there are three possible conformations in which water molecules are directly attached to the Na^+ ion, (Na^+-W_3), with D_3 , D_{3h} , and C_3 symmetry. The structure with D_3 point group is the minimum and predicted to be the lowest energy for all trihydrated Na^+ complexes. Other possible structures for

$[\text{Na}(\text{H}_2\text{O})_3]^+$ are with hydrogen bonding, where two water molecules are directly connected to Na^+ as in the case of $n=2$, and the third water molecule ($m=1$) interacts through hydrogen bonding with either of the former two. It has been reported recently (Rao et al., 2008) that $(n=2, m=1)$ structures are higher in energy than the one in which all three water molecules directly bind with the metal ion. For $n=4$, the possible combination of first shell, n , and the second shell, m , water molecules are: (4,0), (3,1) and (2,2). We performed our calculations only on the tetrahedral with all four water molecules are in the first shell, (4,0). It has been reported in previous theoretical studies (Pavlov et al., 1998; Carl et al., 2007) that the tetrahedral cluster (4,0) has the lowest energy structure. The binding energies for di-, tri- and tetra- penta- and hexhydrated Na^+ are $\Delta E_i = -47.1$, -64.2 and $-78.8 \text{ kcal mol}^{-1}$, respectively.

Figure 4.2 shows zero-point energy, ZPVE, average bond length, angle and binding energy for the most stable sodium ions with (m,n) water molecules. We observe that as the number of water molecules in the first shell increases, binding energy and bond length increases. Also, the average value of $\angle \text{O}-\text{Na}^+-\text{O}$ is not consistent with typical geometrical value shown in parenthesis in . This showed that the water molecules in the first hydration shell of Na^+ are not well defined suggesting continuous exchange with bulk water molecules which is in agreement with what has predicted using molecular simulation (Periole et al., 1997). For $n=5$, three different type of complexes are possible, (3,2), (4,1) and (5,0), for the pentahydrated Na ion. The complex of Na^+ with five water molecules in the first shell, (5,0), with C_{2v} symmetry is not the global minima as suggested in previous studies (Pavlov et al., 1998; Carl et al., 2007). Therefore, we optimized $(n=4, m=1)$ structure for the purpose of this study. Results show that the pentahydrate with four water molecules in the first shell and one in the second shell is 3.0 kcal/mol lower in energy compared to (5,0). Similar results have been reported for Li^+ and Be^{2+} (Rao et al., 2008). The possible complexes for $n=6$ are (3,3), (4,2), (5,1) and (6,0). It has generally been inferred that six water molecules are required to complete the first coordination shell surrounding Na^+ .

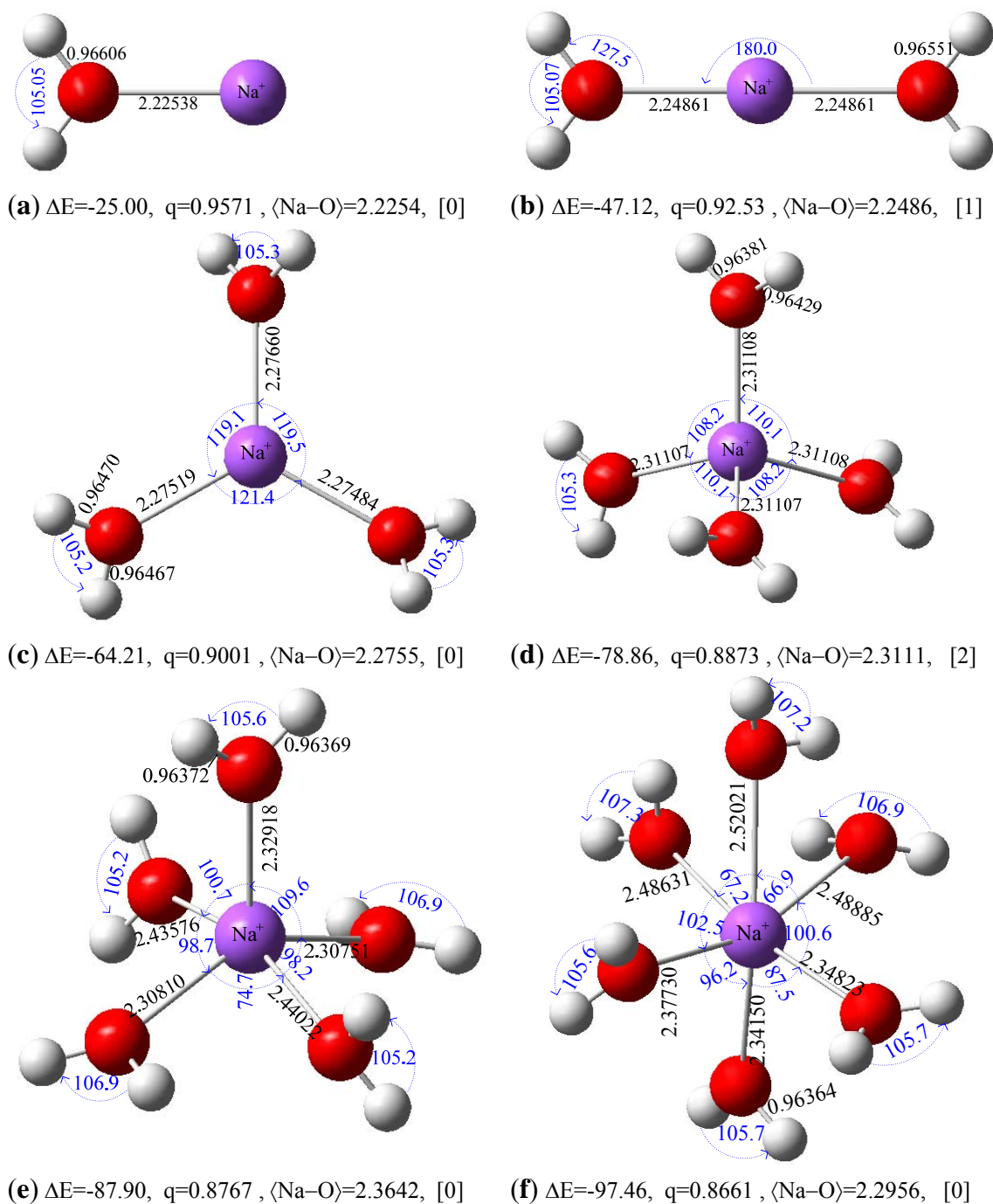


Figure 4.3: Optimized parameters and geometrical structure from *ab initio* molecular orbital calculations for first shell hydro-Na (a) $[\text{Na}(\text{H}_2\text{O})]^+$, (b) $[\text{Na}(\text{H}_2\text{O})_2]^+$, (c) $[\text{Na}(\text{H}_2\text{O})_3]^+$, (d) $[\text{Na}(\text{H}_2\text{O})_4]^+$, (e) $[\text{Na}(\text{H}_2\text{O})_5]^+$, (f) $[\text{Na}(\text{H}_2\text{O})_6]^+$. Shown in these diagrams are bond length (Å), bond angle (°) and APT charges (electronic units). Color code: yellow for Na atoms, red for O atoms, light gray for H atoms.

For many metal ions, the (6,0) is the most stable structure. However, for Na^+ , the (4,2) complex has the lowest energy with D_{2d} symmetry. It has a total binding energy of -103.2 kcal/mol which is 5.8 kcal/mol higher than that for (6,0). The average Na–O bond distance is 2.30 Å and the average hydrogen bond is 1.96 Å. Figure 4.4(b) shows that the Na^+ is sandwiched between two water molecules. We believe that the hydrogen covalent bond brings more stability to the complex. The (4,2) structure is apparently more favorable thermodynamically than (6,0) as a result of weak cation–water interactions which increase the significance of hydrogen bonding interaction. In a similar manner, the heptahydrated Na^+ has four possible complexes, (4,3), (5,2), (6,1) and (7,0). Result for (6,1) is included in this study. The total bonding energy for Octahedral cluster with one water molecule in the second shell, $[\text{Na}(\text{H}_2\text{O})_6 \cdot \text{H}_2\text{O}]^+$, is -108.0 kcal/mol. For $n=8$, the structure we optimized is (6,2) with water molecules in the second shell are hydrogen-bonded to two water molecules in the first shell. The average calculated hydrogen bond is 1.98 Å with total binding energy of -120.9 kcal/mol.

The charge on Na^+ ion calculated according to Analytic Perturbation Theory (APT) and shown in Figure 4.3 and 4.4 decreases as the number of water increases the cluster. For the case of $[\text{Na}(\text{H}_2\text{O})_6]^+$ and $[\text{Na}(\text{H}_2\text{O})_4 \cdot 2\text{H}_2\text{O}]^+$, we can conclude that the more electron density that is transfer to the sodium ion from water ligands, the lower binding energy. Recent QM, molecular dynamic simulation study of Na^+ with 199 water molecules (Tongraar and Rodeb, 2004) showed that the average coordination number in the first shell is 5.4 and water molecules in the first shell are quite strongly attached to the ion implying that Na^+ acts as a “structure making” (Marcus, 2009). However, relatively is known about the second hydration shell of Na^+ . Recently, the energy of two structures with 18 water molecules has been reposted (Bock et al., 2006). The first structure, $[\text{Na}(\text{H}_2\text{O})_4 \cdot 9\text{H}_2\text{O} \cdot 5\text{H}_2\text{O}]^+$, has 4,9 and 5-water molecules in the first, second and third shell, respectively, while the second one, $[\text{Na}(\text{H}_2\text{O})_6 \cdot 12\text{H}_2\text{O}]^+$, has 6-water molecules in the first shell and twelve in the second. Table 4.2 summarizes geometrical properties of first and second shell hydration of Na clusters.

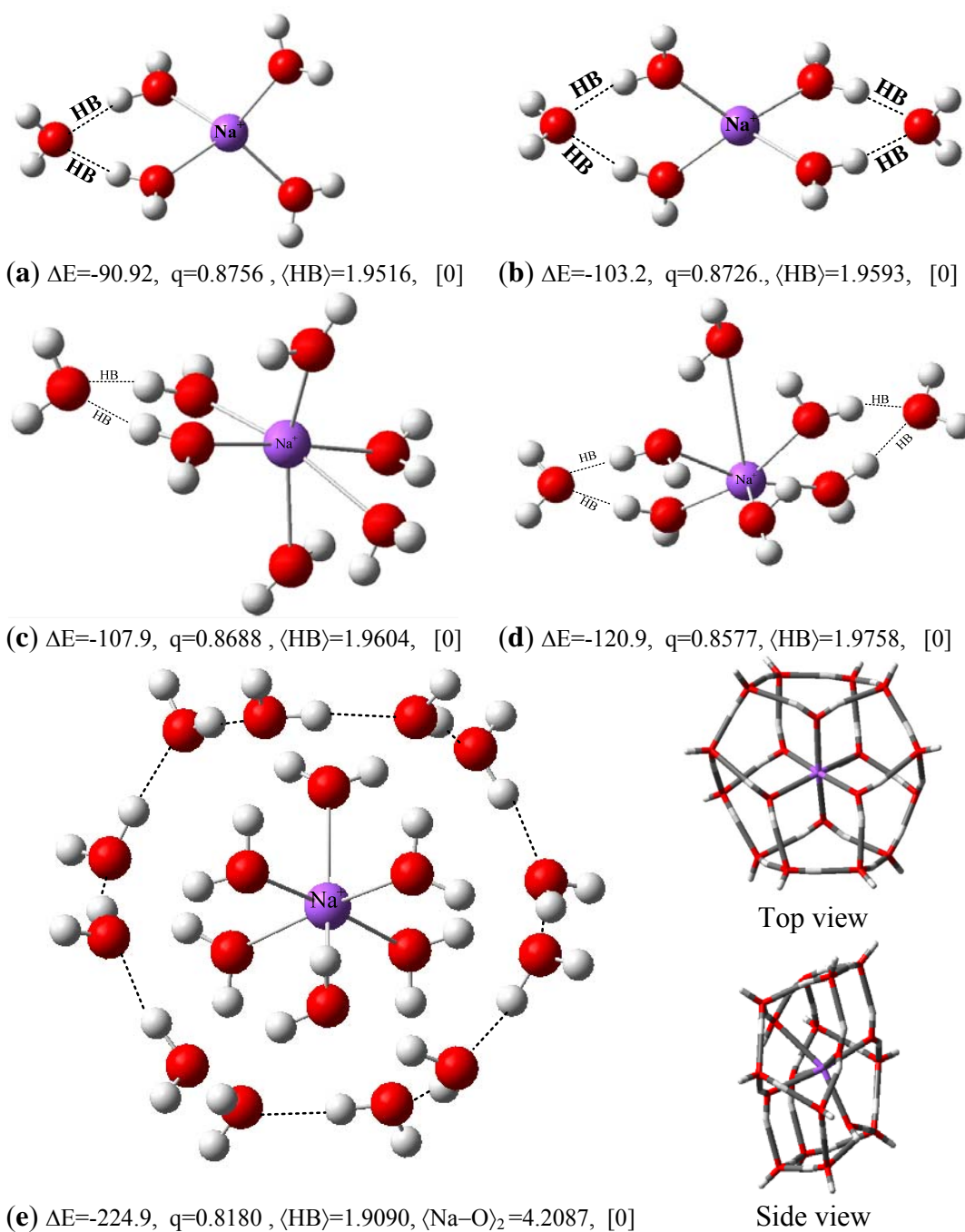


Figure 4.4: Optimized parameters and geometrical structure for second shell hydration of Na-clusters: (a) $Na[(H_2O)_4.H_2O]^+$, (b) $Na[(H_2O)_4.2H_2O]^+$, (c) $Na[(H_2O)_6.H_2O]^+$, (d) $Na[(H_2O)_6.2H_2O]^+$, (e) $Na[(H_2O)_6.12H_2O]^+$. Shown in these diagrams are bond length (\AA), bond angle ($^\circ$), binding energy, ΔE , (kcal/mol) and APT charges, q , (electronic units). Number of imaginary frequency is given in square brackets. Color code: dark violet for Na atoms, red for O atoms, light gray for H atoms.

Table 4.2: Calculated zero-point vibrational energy, ZPVE, bond distance, bond angle, and total binding energy for $[\text{Na}(\text{H}_2\text{O})_n.m\text{H}_2\text{O}]^{2+}$ using B3LYP/6-311++G**

# H ₂ O	n,m	ZPVE (kcal mol ⁻¹)	Na–O (°Å) [†]	∠O–Na ⁺ –O (°) [†]	ΔE _i ^c (kcal mol ⁻¹)	ΔE _{i, rearrg} (kcal mol ⁻¹)
1	1,0	15.0	2.22	127	-25.0	-25.0
2	2,0	30.0	2.25	180	-47.1	-43.0
3	3,0	45.2	2.28	120	-64.2	-50.7
4	4,0	59.6	2.31	109	-78.9	-53.9
5	5,0	75.6	2.36	92	-87.9	-54.6
5	4,1	76.4	2.30	103	-90.9	-57.6
6	6,0	92.7	2.43	109	-97.5	-58.2
6	4,2	92.8	2.30	104	-103.2	-63.9
7	6,1	107.9	2.44	90	-108.0	-58.0
8	6,2	125.3	2.62	83	-120.9	-57.2
18	6,12	286.7	2.59	87	-224.9	–

[†] Average value for first shell. ^b this value is for the angle ∠O–Na⁺–H. ^c based on enthalpy.

The total binding energy in the structure (4,9,5) is 0.4 kcal/mol higher than (6,12). Figure 4.4(e) shows a S₆ optimized geometry of $[\text{Na}(\text{H}_2\text{O})_6.12\text{H}_2\text{O}]^+$ with total binding energy of -224.9 kcal/mol estimated at B3LYP/6-311++g**. The average calculated bond length between Na and OH₂ in the first hydration shell is 2.59 Å which is less than (6,2) structure, while the ⟨Na–O⟩ for second shell is 4.21 Å. The interesting observation here is that the wide range in bond distance between Na and OH₂ in the second shell. The calculated range at B3LYP/6-3116++g** is 4.0319–4.37 Å. this suggest that the interaction between Na⁺ central ion and OH₂ in the second hydration shell is relatively weak. The (6,12) has 24 hydrogen bonds, 12 between each water molecule in the second shell and one in the inner shell, and other 12 between water molecules in the second shell leaving 12 hydrogen atom in the outer shell free. We also calculated the reorganization energy of water clusters by taking the energy difference between a pure water, (H₂O)_n, cluster and the complex of $[\text{Na}(\text{H}_2\text{O})_n]^+$. The results are available in Appendix A. the reorganization energy is an endothermic process as Na⁺ ion approach a cluster of water. This calculated energy for any water cluster of *n* water molecules is about the same of the one containing (*n*+1) molecules.

4.3.3 $[Mg(H_2O)_n]^{2+}$

Magnesium ions is one of the most widely investigated ions experimentally and computationally. The gas-phase studies provide a wealth of information on ion-logand and ion-solvent interactions. They are constitute a bridge between gas-phase and solution. *Ab initio* calculations on M^{2+} show that the first hydration shell consider completed when surrounded by six water molecules (Katz et al., 1996). The water molecules are generally regular with oxygen atoms at the corners of octahedron. The global minimum of the potential energy surface (PES) of $[Mg(H_2O)_6]^{2+}$ complex has T_h symmetry (Markham et al., 2002). The interaction between Mg^{2+} and water are primarily electrostatic in origin with the water dipoles directed toward the central cation. Calculations that have been carried out for $[Mg(H_2O)_n]^{2+}$ clusters are similar to that of $[Na(H_2O)_n]^+$ complexes. For $n=1$, the monoaquo is a planar with C_{2v} symmetry. The total binding energy for this complex is -81.8 kcal/mol which is almost three times higher than that for monovalent ion such as $[Na(H_2O)]^+$. The Mg-OH₂ bond length is evaluated to be 200-215 pm by X-ray diffraction method (Ohtaki and Radnai, 1993). The calculated value for monoaquo cluster is 1.94 Å as shown in Table 4.3. As we carried all calculation at the same level of theory, B3LYP, and with consistent basis set, 6-311++g**, we know for sure that Mg-O bond distance is sensitive to the inclusion of multiple polarization functions into the basis set. The binding energy, on the other hand, is not particularly sensitive to the choice of basis set (see Table 4.4) rather to the method employed. For $n=2$, the optimized structure shown in Figure 4.5 has one imaginary frequency with C_{2v} symmetry. The total binding energy for this complex is -154.2 kcal/mol with an average Mg-O bond distance of 1.96 Å. The reported binding energy of $[Mg(H_2O)_2]^{2+}$ are -152.6 and -14.0 kcal/mol at G3 and MP2(full)/6-311++G(3d,3p), respectively (Rao et al., 2008). We have also calculated the binding energy for bend structure; however, the linear is more stable. For $n=3$, the final optimized structure with C_s symmetry has one imaginary frequency too, and this could be at saddle point. The calculated binding energy is -210.7 kcal/mol and the average Mg-O bond distance is 1.99 Å.

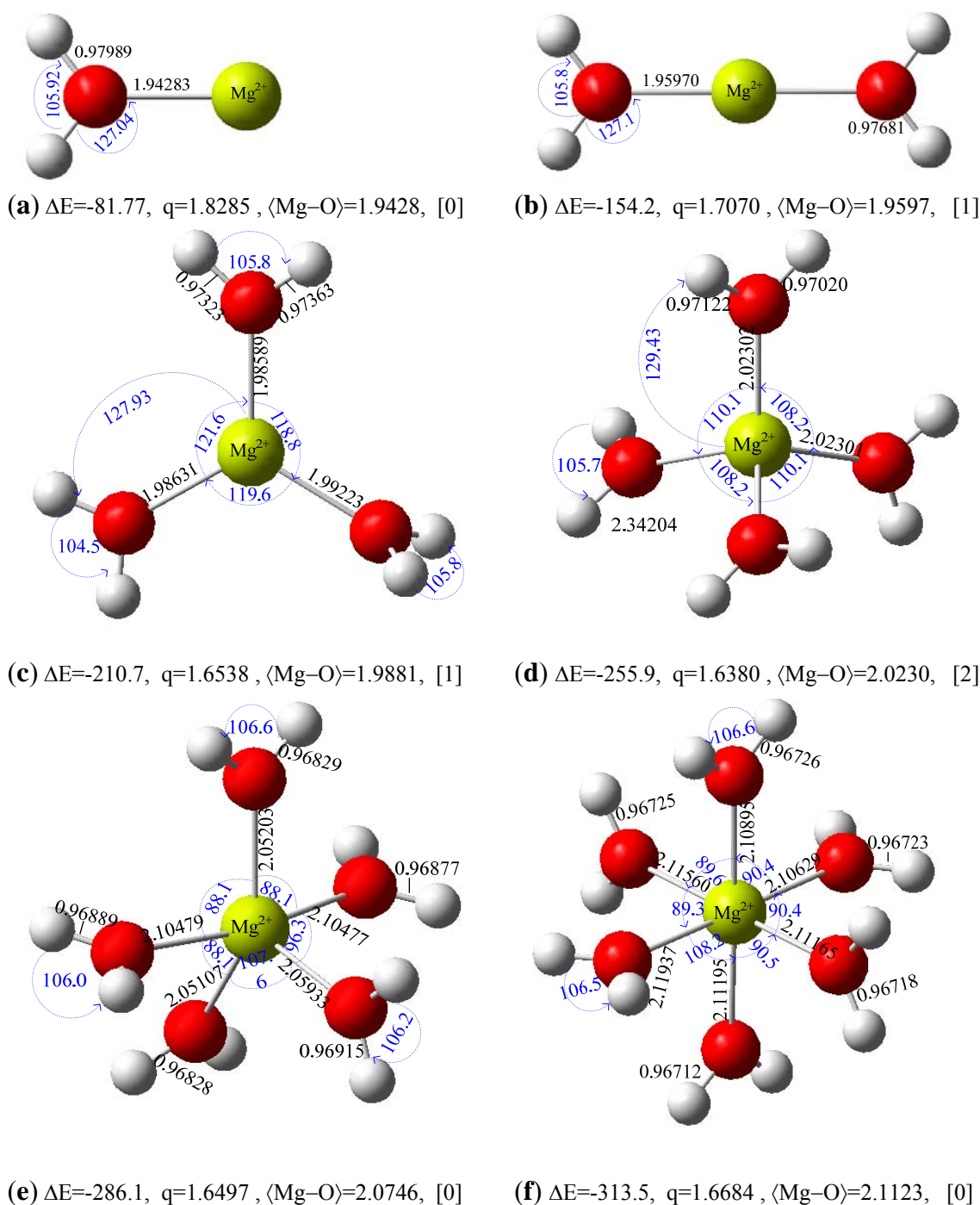
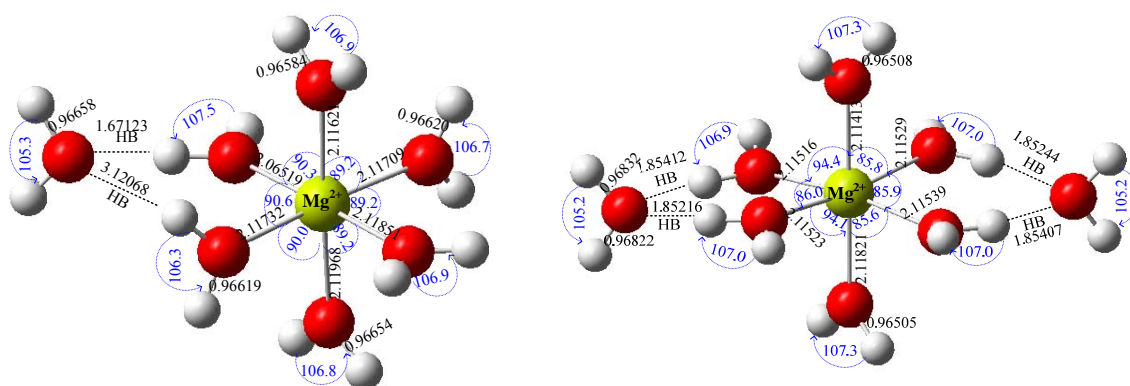
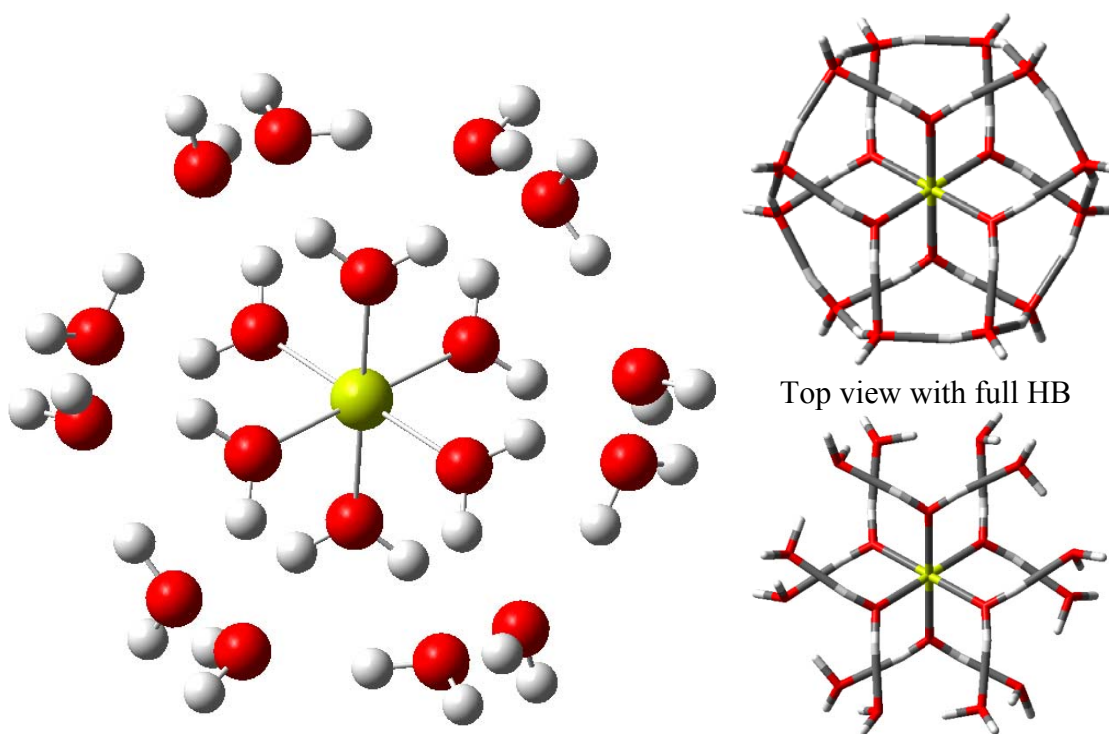


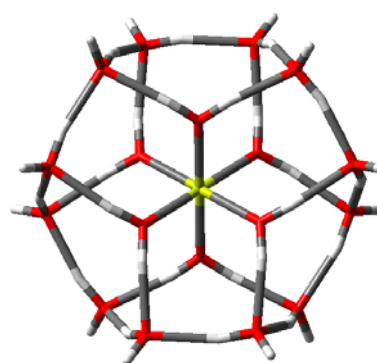
Figure 4.5: Optimized parameters and geometrical structure from *ab initio* molecular orbital calculations (a) $\text{Mg}[\text{H}_2\text{O}]^+$, (b) $\text{Mg}[\text{H}_2\text{O}]_2^+$, (c) $\text{Mg}[\text{H}_2\text{O}]_3^+$, (d) $\text{Mg}[\text{H}_2\text{O}]_4^+$, (e) $\text{Mg}[\text{H}_2\text{O}]_5^+$, (f) $\text{Mg}[\text{H}_2\text{O}]_6^+$. Shown in these diagrams are bond length (Å), bond angle ($^\circ$) and APT charges (electronic units). Color code: yellow for Na atoms, red for O atoms, light gray for H atoms.



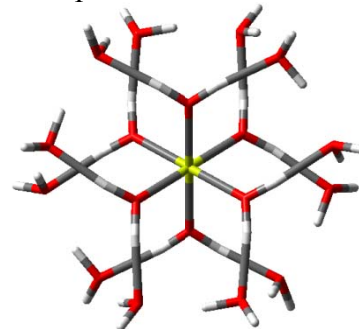
(a) $\Delta E = -333.3$, $q = 1.6586$, $\langle \text{HB} \rangle = 1.8500$, [1] (b) $\Delta E = -353.3$, $q = 1.6488$, $\langle \text{HB} \rangle = 1.8532$, [0]



(c) $\Delta E = -502.5$, $q = 0.8180$, $\langle \text{HB} \rangle = 1.8875$, [0]



Top view with full HB



Shell(1)-Shell(2) HB

Figure 4.6: Optimized parameters and geometrical structure from *ab initio* molecular orbital calculations. (a) $\text{Mg}[(\text{H}_2\text{O})_6.\text{H}_2\text{O}]^{2+}$, (b) $\text{Mg}[(\text{H}_2\text{O})_6.2\text{H}_2\text{O}]^{2+}$, (c) $\text{Mg}[(\text{H}_2\text{O})_6.12\text{H}_2\text{O}]^{2+}$. Shown in these diagrams are bond length (Å), bond angle (°), binding energy, ΔE , (kcal/mol) and APT charges, q , (electronic units). Number of imaginary frequency is given in square brackets. Color code: dark violet for Na atoms, red for O atoms, light gray for H atoms.

For $n=4$, the tetrahydrated structure has two imaginary frequencies with S_4 symmetry. The binding energy is calculated to be -255.9 kcal/mol which is 45.2 kcal/mol higher than that for triaquo complex. The (4,0) has already been confirmed to be the most stable compared to (3,1) or (2,2) (Pavlov et al., 1998). Though some studies suggested the pentahydrated structure $[\text{Mg}(\text{H}_2\text{O})_4.\text{H}_2\text{O}]^{2+}$ is more stable than $[\text{Mg}(\text{H}_2\text{O})_5]^{2+}$ at higher temperature, recent work by Glusker et al. showed the (5,0) is more stable calculated using B3LYP and MP2(full) (Markham et al., 2002). It has generally been a general consensus that the solvation of Mg^{2+} can accommodate six water molecules in the first coordination shell. The optimized structure shown in Figure 4.5(f) has a T_h symmetry and binding energy of -313.5 kcal/mol. The heptahydrate of Mg^{2+} with one water molecule in the second coordination shell has an average hydrogen bond of 1.85 Å and total binding energy of -333.3 kcal/mol. This value of binding energy is about the same (-325 kcal/mol) reported in previous study at B3LYP/6-311++G(3df,3dp) (Markham et al., 2002). For $n=8$, to our knowledge, no study reported the calculation at B3LYP/6-311++g**. This structure is optimized with six water molecules in the first coordination shell and two in the second sphere. The binding energy is calculated to be -353.3 kcal/mol with average hydrogen bond of 1.65 Å

The number of water molecules that complete the second hydration shell of Mg^{2+} has been estimated in variety of studies to be approximately 12 (Markham et al., 2002). The first structure for $[\text{Mg}(\text{H}_2\text{O})_6.12\text{H}_2\text{O}]^{2+}$ was reported by Pavlov et al. and optimized at B3LYP with the pseudopotential LanL2DZ basis set (Pavlov et al., 1998). We carried our calculations on the (6,12) structured using B3LYP/6-311++g** (Figure 4.6). The structure is similar to what we already optimized for $\text{Na}(\text{H}_2\text{O})_{18}^+$. It has six water molecules in the first shell with similar arrangement to $[\text{Mg}(\text{H}_2\text{O})_6]^{2+}$ and 12 water molecules in the second coordination sphere. The average Mg–O distance for first and second water shell are 2.10 and 4.14 Å, respectively. It is interesting to observe that range of bond distance between Mg and OH_2 in the second shell is 4.13-4.16 Å. this short range suggest strong interaction with the central Mg^{2+} ion. To our knowledge, there

is no experimental values available for the structure $[\text{Mg}(\text{H}_2\text{O})_6.12\text{H}_2\text{O}]^{2+}$. The binding energy of this complex is calculated to be -502.5 kcal/mol which is six times larger than that for $\text{Mg}(\text{H}_2\text{O})^{2+}$. The hydrogen atoms for all water molecules in the first shell are forming hydrogen bonding with oxygen from the second shell. The average calculated hydrogen bond is found to be 1.89 Å. whereas, hydrogen atoms in the second shell fall into two groups: 12 of them are free and 12 are involved in hydrogen bonding with oxygen from the same shell.

Table 4.3: Thermodynamic properties of $[\text{Mg}(\text{H}_2\text{O})_n.m\text{H}_2\text{O}]^{2+}$ using B3LYP/6-311++G**

# H ₂ O	n,m	ZPVE (kcal mol ⁻¹)	Mg–O (°Å) [†]	∠O–Mg ²⁺ –O (°) [†]	ΔE _i ^a (kcal mol ⁻¹)	ΔE _i ^{a'} (kcal mol ⁻¹)
1	1,0	15.4	1.94	180	-81.8	-80.3 ^b
2	2,0	31.1	1.96	180	-154.2	-151.3 ^b
3	3,0	47.2	1.99	120	-210.7	-208.0 ^b
4	4,0	62.6	2.02	109	-255.9	-254.9 ^b
5	5,0	79.2	2.07	93	-286.1	-287.1 ^b
6	6,0	95.1	2.11	90	-313.5	-313.7 ^b
7	6,1	110.4	2.11	89	-333.3	-337.4 ^c
8	6,2	127.1	2.11	88	-353.3	-337.2 ^d
18	6,12	291.0	2.10	88	-502.5	-501.4 ^c

[†] Average value, ^a this work. ^{a'} other work. ^b calculated at G3 from reference (Rao et al., 2008). ^c calculated at MP2(full)/6-311++g** taken from reference (Markham et al., 2002). ^d calculated at B3LYP/LanL2DZ taken from reference (Pavlov et al., 1998).

4.3.4 $[\text{Ca}(\text{H}_2\text{O})_n]^{2+}$

Calcium, with an ionic radius of 0.99 Å, is the fifth most abundant element on earth. Optimized geometrical structures of $[\text{Ca}(\text{H}_2\text{O})_n.m\text{H}_2\text{O}]^{2+}$ ($n=1-6$, $m=1-2$) are shown in Figure 4.7. All structures presented here have been verified to be at local minima on their respective potential energy surface by frequency analysis at the same theory level and basis set. Due to absence of any experimental data for individual species of hydrated Ca²⁺ ion under consideration, Ca–O distances, and O–Ca²⁺–O angles are compared to previously published theoretical work by Glusker et al. (Katz et al., 1996)

that used RHF/HUZSP*(p) and MP2-(Full)/HUZSP8(p) level of optimization. The initial structure for $n=2$, $[\text{Ca}(\text{H}_2\text{O})_2]^{2+}$, was linear with $\angle\text{O}-\text{Ca}^{2+}-\text{O}$ equal to 180° . We examined two conformations D_{2d} and C_{2v} for $\text{H}_2\text{O}-\text{Ca}^{2+}-\text{H}_2\text{O}$ (W-M-W; M=water, W=metal). The structure $\text{Ca}^{2+}-\text{H}_2\text{O}-\text{H}_2\text{O}$ (M-W-W) has been tested by Rao *et al.* (Rao *et al.*, 2008) and was considerably less stable compared to the first case. The binding energy was calculated as the difference in enthalpy between the cluster and individual molecules of water and metal ion as in equation (6) at the same level of theory and basis set. For $n=1$, $\Delta E_i = -57.8 \text{ kcal mol}^{-1}$, and bond length between Ca^{2+} and $-\text{OH}_2$ is 2.24 \AA . Table 4.4 shows average bond length, angle and binding energy for calcium ions with first shell water molecules. For $n=3$, there are three possible conformations in which water molecules are directly attached to the Ca^{2+} with D_3 , D_{3h} , and C_3 symmetry. The structure with D_3 point group is the minimum and predicted to be the lowest energy for all trihydrated Ca^{2+} complexes. Other possible structures for $[\text{Ca}(\text{H}_2\text{O})_3]^{2+}$ are with hydrogen bonding, where two water molecules are directly connected to Ca^{2+} as in the case of $n=2$, and the third water molecule ($m=1$) interacts through hydrogen bonding with either of the former two. It has been reported recently (Rao *et al.*, 2008) that ($n=2$, $m=1$) structures are higher in energy than the one in which all three water molecules directly bind with the metal ion. For $n=4$, the possible combination of first shell, n , and the second shell, m , water molecules are: (4,0), (3,1) and (2,2). We performed our calculations only on the tetrahedral with all four water molecules are in the first shell, (4,0), as it has been reported to be the lowest energy structure in previous theoretical studies (Pavlov *et al.*, 1998; Carl *et al.*, 2007). For $n=5$, three different type of complexes are possible, (3,2), (4,1) and (5,0), for the pentahydrated Calcium ion. The complex of Ca^{2+} with five water molecules in the first shell, (5,0), and C_{2v} symmetry is the global minima according to previous studies (Pavlov *et al.*, 1998; Carl *et al.*, 2007). Therefore, we optimized ($n=5$, $m=0$) structure for the purpose of this study. The possible complexes for $n=6$ are (3,3), (4,2), (5,1) and (6,0). Table 4.4 shows that the (6,0) octahedral geometry is the lowest energy for hexahydrated Ca^{2+} compared to (4,2).

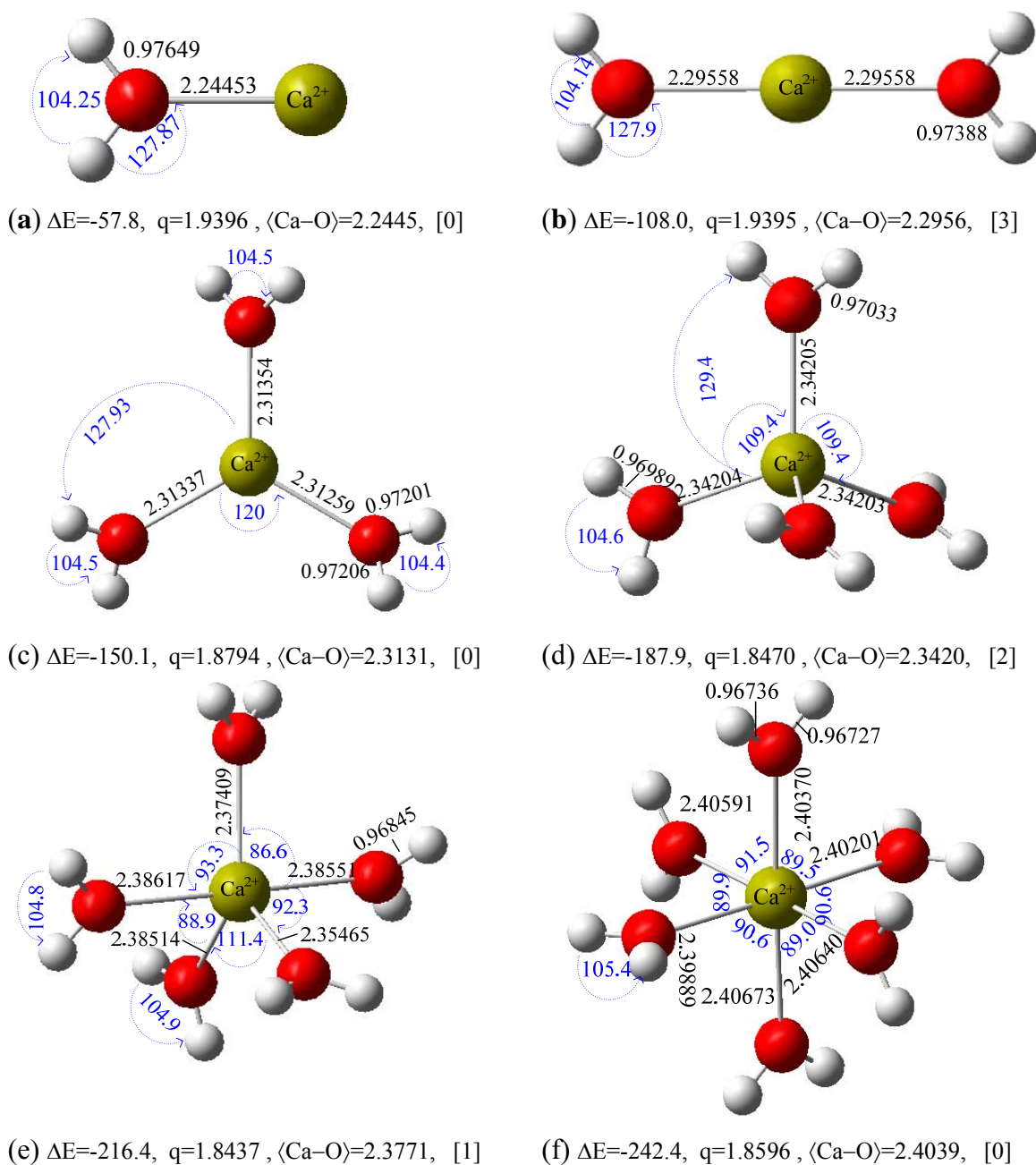
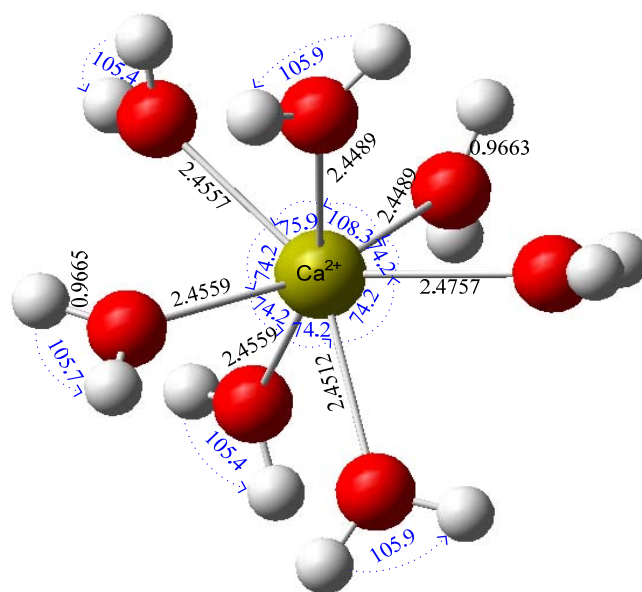


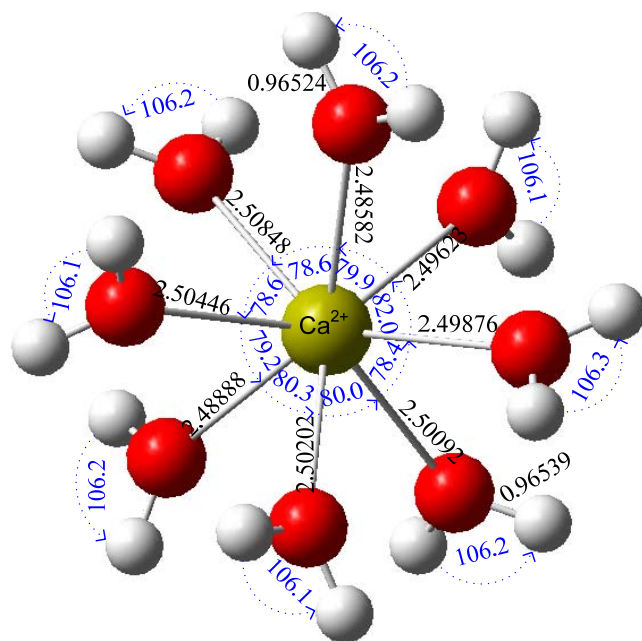
Figure 4.7: Optimized parameters and geometrical structure from *ab initio* molecular orbital calculations (a) $\text{Ca}[\text{H}_2\text{O}]^{2+}$, (b) $\text{Ca}[\text{H}_2\text{O}]_2^{2+}$, (c) $\text{Ca}[\text{H}_2\text{O}]_3^{2+}$, (d) $\text{Ca}[\text{H}_2\text{O}]_4^{2+}$, (e) $\text{Ca}[\text{H}_2\text{O}]_5^{2+}$, (f) $\text{Ca}[\text{H}_2\text{O}]_6^{2+}$. Shown in these diagrams are bond length (Å), bond angle (°), binding energy, ΔE , (kcal/mol) and APT charges, q , (electronic units). Number of imaginary frequency is given in square brackets. Color code: yellow for Ca atoms, red for O atoms, light gray for H atoms.

It has been shown in previous study that the complex $[\text{Ca}(\text{H}_2\text{O})_4.2\text{H}_2\text{O}]^{2+}$ is 11.9 kcal/mol higher in energy than $[\text{Ca}(\text{H}_2\text{O})_6]^{2+}$ at the MP2(full)/HUZSP*(p,d)/RHF/HUZSP*(p) (Katz et al., 1996). However, our result is consistent with recent finding by Sastary et. al. (Rao et al., 2008) with (6,0) is 7.4 kcal/mol higher in total binding energy compared to (4,2). This means that the hydrogen bonding between the inner and outer shell water molecules are not a large influence for the hexaaquo complex. In a similar manner, the heptahydrated Ca^{2+} has four possible complexes, (4,3), (5,2), (6,1) and (7,0). Results for the last three are included in this study. Octahedral cluster with one water molecule in the second shell, $[\text{Ca}(\text{H}_2\text{O})_6.\text{H}_2\text{O}]^{2+}$, is the lowest energy compared to the other two. The total binding energy for $[\text{Ca}(\text{H}_2\text{O})_6.\text{H}_2\text{O}]^{2+}$ and $[\text{Ca}(\text{H}_2\text{O})_5.2\text{H}_2\text{O}]^{2+}$ are 5.4 and 4.6 kcal/mol, respectively, higher than $[\text{Ca}(\text{H}_2\text{O})_7]^{2+}$. This suggests that for $n=7$, the Ca^{2+} does not accommodate seven water molecules in the first solvation shell and that could be due to “the crowding effect”. For $n=8$, the possible combination of inner and out shell water molecules are many: (4,4), (5,3), (6,2), (7,1) and (8,0). In this study, we are examining the geometrical structure and total energy of (6,2) and (8,0) as shown in Figure 4.9(d) and Figure 4.8(b), respectively. The calculated total binding energy for (6,2) is -281.4 kcal/mol which is 9.8 kcal/mol higher than that for (8,0), which means the octahedral structure with two water molecules in the outer shell more stable for this complex.

For $n=9$, the initial structure we started with is (9,0), however, the final optimized one is found to be (8,1) which explain the crowding effect for Ca^{2+} ion. The ground state for this complex is reported recently to be (6,3) (Carl et al., 2007), however, we are not including the result of this structure in our discussion as the calculation still running. The total binding energy for (8,1) is calculated to be -286.9 kcal/mol single hydrogen bond of 2.50 Å. Finally, the (6,12) Ca^{2+} complex is optimized as shown in Figure 4.9(f). The total binding energy for this complex is -423.2 kcal/mol and the average calculated Ca–O bond distance is 2.37 and 4.24 Å for inner and outer shell, respectively. The average hydrogen bond between the two shells is 1.91 Å.



(a) $\Delta E = -256.9$, $q = 1.9509$, $\langle \text{Ca-O} \rangle = 2.4594$, [1]



(b) $\Delta E = -271.6$, $q = 1.8652$, $\langle \text{Ca-O} \rangle = 2.4982$, [0]

Figure 4.8: Optimized parameters and geometrical structure from *ab initio* molecular orbital calculations (a) $\text{Ca}[\text{H}_2\text{O}]_7^{2+}$, (b) $\text{Ca}[\text{H}_2\text{O}]_8^{2+}$. Shown in these diagrams are bond length (Å), bond angle ($^\circ$), binding energy, ΔE , (kcal/mol) and APT charges, q , (electronic units). Number of imaginary frequency is given in square brackets. Color code: yellow for Ca atoms, red for O atoms, light gray for H atoms.

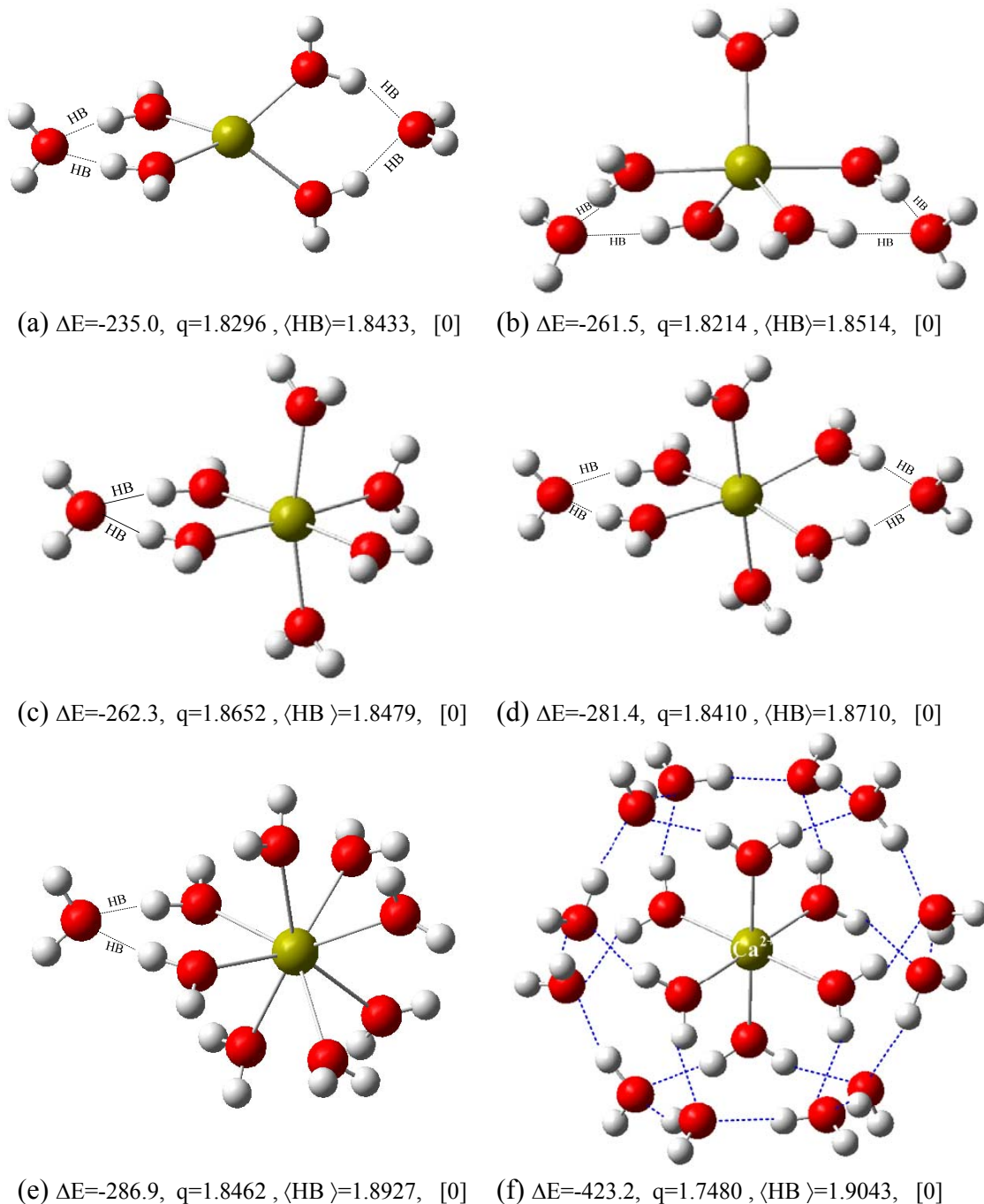


Figure 4.9: Optimized parameters and geometrical structure from *ab initio* molecular orbital calculations (a) $\text{Ca}[\text{H}_2\text{O}]^{2+}$, (b) $\text{Ca}[\text{H}_2\text{O}]_2^{2+}$, (c) $\text{Ca}[\text{H}_2\text{O}]_3^{2+}$, (d) $\text{Mg}[\text{H}_2\text{O}]_4^{2+}$, (e) $\text{Mg}[\text{H}_2\text{O}]_5^{2+}$, (f) $\text{Mg}[\text{H}_2\text{O}]_6^{2+}$, (g) $\text{Mg}[\text{H}_2\text{O}]_6^{2+} \cdot \text{H}_2\text{O}$, (h) $\text{Mg}[\text{H}_2\text{O}]_6^{2+} \cdot 2\text{H}_2\text{O}$. shown in these diagrams are bond length (Å), bond angle (°), binding energy, ΔE , (kcal/mol) and Mulliken charges, q , (electronic units). Color code: yellow for Ca atoms, red for O atoms, light gray for H atoms.

Table 4.4: Thermodynamic properties of $[\text{Ca}(\text{H}_2\text{O})_n.\text{mH}_2\text{O}]^{2+}$ using B3LYP/6-311++G**

# H ₂ O	n,m	ZPVE (kcal mol ⁻¹)	Ca–O (°Å) [†]	∠O–Ca ²⁺ –O (°) [†]	ΔE _i (kcal mol ⁻¹)	ΔE _i ^b (kcal mol ⁻¹)
1	1,0	15.3	2.24	180	-57.8	-57.8
2	2,0	30.5	2.30	180	-108.0	-50.2
2 ^a	2,0	30.7	2.28	127	-107.4	-49.6
3	3,0	46.2	2.31	120	-150.1	-42.6
4	4,0	61.2	2.34	109	-187.9	-37.8
5	5,0	77.1	2.38	94	-216.4	-28.5
6	6,0	92.9	2.40	90	-242.4	-26.0
6	4,2	95.4	2.32	104	-235.0	-18.6
7	7,0	109.2	2.46	82	-256.9	-14.5
7	5,2	109.1	2.36	93	-261.5	-19.1
7	6,1	109.2	2.40	88	-262.3	-19.8
8	8,0	123.6	2.50	80	-271.6	-14.7
8	6,2	125.5	2.40	87	-281.4	-19.1
9	8,1	140.2	2.51	77	-286.9	-15.3
18	6,12	289.2	2.37	88	-423.2	-

[†] Average value, ^a bend structure of $[\text{Ca}(\text{H}_2\text{O})_2]^{2+}$. ^b sequential energy defined by equation (2).

In summary, DFT was used to study the effective interaction between water molecules in the first and second hydration shell with alkaline and alkaline-earth cations. The stepwise hydration of Na^+ , Mg^{2+} and Ca^{2+} are studies with maximum of 18 water molecules in the first and second hydration shells. The geometrical properties and thermochemistry of all complexes with the reaction $\text{M}^{x+} + n\text{H}_2\text{O} \rightarrow [\text{M}(\text{H}_2\text{O})_n.\text{mH}_2\text{O}]^{x+}$ have been analyzed and compared with available experimental values. The hydration process of metal ion includes competitive effect of ion–water and water–water interactions. The ionic radius of metal ions is a key factor in the determination of coordination number (Vinogradov et al., 2003) as well as the M–OH₂ bond distance. The ionic radius of calcium (1.14 Å) and sodium (1.16 Å) are larger than magnesium (0.86 Å) which makes water molecules lie further from Na^+ , and Ca^{2+} compared to Mg^{2+} . With reference to bulk solvation, it should be noted that the calculations of first shell hydration do not include the effect of bulk water.

CHAPTER V
**THEORETICAL STUDY OF FERRIC AND FERROUS HYDRO-
CLUSTERS AND COMPLEXES WITH CHLORIDE AND SULFUR
IONS**

I could have done it in a much more complicated way
—Lewis Carroll, 1870

Iron is the one of the most abundant element in the earth's crust and it forms many ores including hematite (Fe_2O_3), magnetite (Fe_3O_4), limonite ($\text{FeO}(\text{OH})$), and siderite (FeCO_3). The importance of iron chemistry in geological, environmental, metallurgical, and biological contexts makes its understanding of fundamental significance. In oilfield industry, the primary source of iron in carbonate reservoir is tubing and well casing and it can reach to 100,000 ppm. During acid treatment (well stimulation), the iron dissolved can be presented in either ferric (Fe^{3+}) or ferrous (Fe^{2+}) form. Temperature, pressure, and pH of the solution important factors in the stability constants and precipitation range of iron complexes. Ferric and Ferrous ions play a crucial role in controlling many physicochemical and biochemical processes. Most of these processes take place in the solution and often require the desolvation of iron ions to form a metal-solvent cluster in solution. Therefore, understanding the hydration thermodynamics will not just resolve possible interaction in certain reservoir processes such as stimulation treatment, but will help modeling hydrothermal deposition, metal speciation in surface water as well as corrosion process in water systems. This chapter presents an extensive *ab initio* calculations for Fe(II) and Fe(III) chemistry in water solution, and their interactions with sulfur, chloride, and hydroxide ions that might be presented in stimulation fluid.

5.1 Introduction

Iron, the twenty-sixth element in the period table, is the second most abundant metal after Aluminum and the forth most abundant element on the earth's crust. The oxidation states of +2 and +3 correspond to the ferrous, Fe^{2+} , and ferric ions, Fe^{3+} , respectively.

The (II) and (III) oxidation states of iron are stable over broad region of pH (Baes and Mesmer, 1976). Both ions form numerous complexes with variety of ligands. The oxidizing (+6) state is stable in basic solutions but decomposes with evolution of oxygen and formation of Fe(III) in neutral or acidic solution. Metallic iron or free iron has a zero oxidation state and is represented as Fe^0 . The oxidation state of iron depends on the oxidizing or reducing characteristic of its solvent medium and the type of anion with which it is associated. In oxidation medium such as air, the ferric is more stable, whereas under reducing conditions (anaerobic medium), ferrous is more stable. Ferric ion is easily reduced by hydrogen while ferrous ion is slowly oxidized by air.

The primary source of iron in carbonate reservoir is tubing and well casing (Gougier et al., 1985). Nasr-El-Din et al. reported between 300 and 105,000 mg/l (ppm) of dissolved iron has been seen in acid used to clean the pipes. Iron products may also occur as a direct or indirect result of bacterial growth (Smith et al., 1969). During acid treatment the iron dissolved can be presented in either ferric (Fe^{3+}) or ferrous (Fe^{2+}) form. Iron or mile scale that made up of hematite (Fe^{3+}) or magnetite (Fe^{3+} , Fe^{2+}) is common in new tubular. This dissolved iron will remain in the acid solution until the pH begins to rise, then the iron loses its solubility and precipitate. Tubs used in oilfield industry are mainly Low-Carbon Steel (LCS) and can sustain HCl acid with concentration up to 20 wt% with proper corrosion inhibitor (Al-Mutairi and Nasr-El-Din, 2005). The precipitation of iron-complexes has been studied extensively in the literature. Temperature, pressure and pH of the solution play a crucial role in stability constant and precipitation range. Table 5.1 summarized the main complexes that may precipitate in well stimulation treatment in presence of iron. The precipitation of ferric hydroxide (pH~1.9) or other containing compounds can seriously damage the flow channels (wormholes) recently opened by acid reaction in carbonate rock formation. This precipitation can be minimized or eliminated by using reducing agent that convert Fe(III) to the more stable Fe(II) form. Despite the vast variety of experimental studies which can give great insight into the structural and dynamic properties of aqueous solution, they often require major

resources of research laboratory and often associated with errors, especially for very dilute systems due to technical limitations (Howell and Neilson, 1996). *Ab initio*, molecular dynamics (MD) and Monte Carlo (MC) simulations are well established and have proven a powerful theoretical tool for studying the solvation structure of ions (Allen, 1987). We believe that simulation may provide more understanding of iron ion complexation in atomistic level. This study gives new insight on the rate of exchange of coordinated water molecules around iron, and interaction energies between ions and water. Structural features of clusters involving an iron ion surrounded by up to 18 water molecules arranged in two shells have been studied using density functional theory (DFT). The gas-phase optimized structures and binding energies of $[\text{Fe}(\text{H}_2\text{O})_n.m\text{H}_2\text{O}]^{2+}$ and $[\text{Fe}(\text{H}_2\text{O})_n.m\text{H}_2\text{O}]^{3+}$ clusters with ($n=1-6$, $m=6$) are discussed. Bond distances (M–O) and angles ($\angle\text{O–M–O}$) for the first shell hydration are in good agreement with experimental values. Molecular level understanding of iron solvation will aid to attain correct mechanistic conclusions about iron ions control movements and their impact on oilfield treatment. The speciation and thermodynamic properties of ferric chloride complexes in acidic solution during well stimulation treatment is still poorly understood. Density functional theory was employed to determine the reaction thermodynamics of Fe(III) with chloride in a gas-phase using the B3LYP (Becke, 1993) level of theory with 6-311++g** basis sets for (H,O) atoms and SDD for (Fe,Cl) atoms. The study compares complex and binding energies for $[\text{Fe}(\text{H}_2\text{O})_6]^{3+}$, $[\text{FeCl}(\text{H}_2\text{O})_5]^{2+}$, $[\text{FeCl}_2(\text{H}_2\text{O})_4]^+$, $[\text{FeCl}_3(\text{H}_2\text{O})_3]$, $[\text{FeCl}_4(\text{H}_2\text{O})_2]^-$, $[\text{FeCl}_5(\text{H}_2\text{O})]^{2-}$, and $[\text{FeCl}_6]^{3-}$. We found that as chloride increases, higher ligand number complexes become important with FeCl_4^- predominating as the one with highest binding energy. The objective of this chapter is to study interaction between ferric and ferrous ions with other ions in acidic and base media. The main focus here is to study iron (Fe^{2+} , Fe^{3+}) ion complexation with OH^- , Cl^- , H_2S in acidic medium (H_3O^+) as well as at the spent acid front. This is very important in the development of good diverting fluid considering complexation products of iron in solution.

5.2 Definition of the System

In matrix acidizing and acid fracturing treatment, a high acid concentration ($> 15\text{wt}\%$) is injected in the well to clean filter cake, remove damage and open new flow channel in the near wellbore area to enhance hydrocarbon productivity. Tanks (T), well casing, tubing system, and surface equipments are potentially iron-rich resulting from corrosion or millscale. Acid can dissolve rust in storage, mixing tank, and tubing leading to a mixture of Fe^{2+} and Fe^{3+} in solution. However, dissolved oxygen in the acid will rapidly oxidize Fe^{2+} to Fe^{3+} . Once the acid interacts with the carbonate rocks (i.e. formation) more ions will be released into solution. To better understand the ion complexation and mechanisms of interaction taking place, the system is divided into two parts as shown in Figure 5.1.

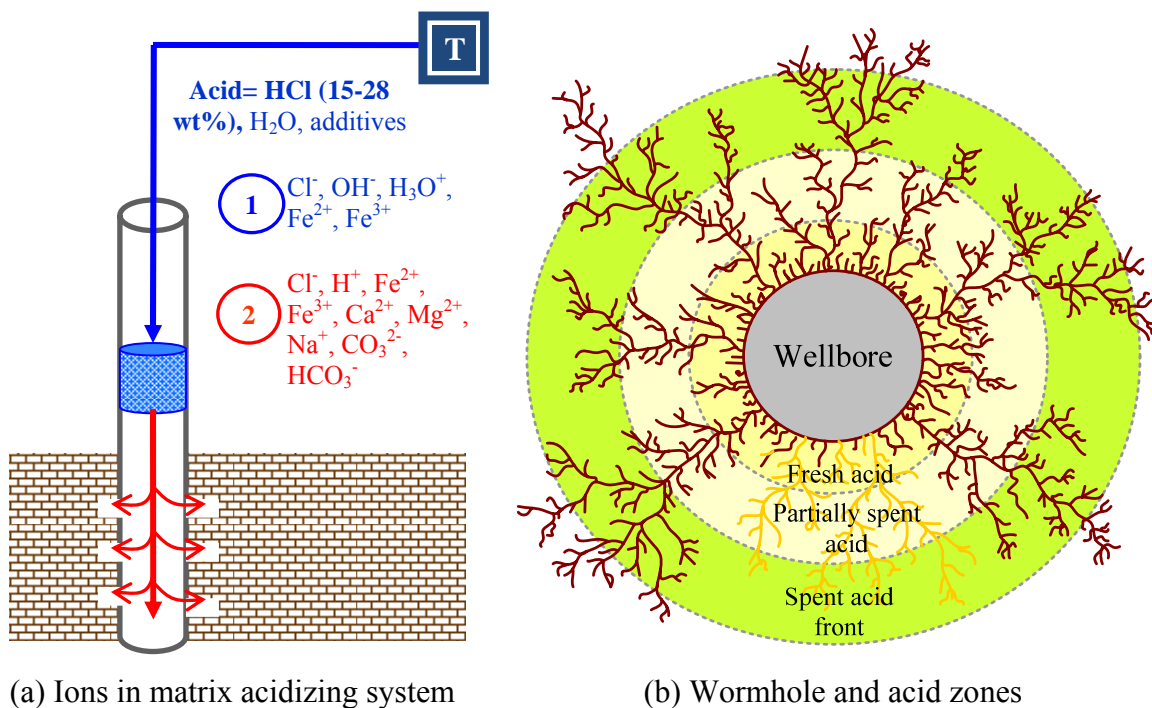


Figure 5.1: Schematic presentation of the problem, (a) type of ions present in tubing system before reaction with carbonate rocks, and after acid reactions. Iron is a major player in both cases. (b) acid-channeling (wormhole) around the wellbore divided into three zones: fresh acid, partially spent acid and spent acid front.

5.3 Simulation

In the last several years, the enormous progress in computational techniques is reflected in high applications of *ab initio* Hartree-Fock (HF), and density functional theory (DFT) to real reaction systems containing transition metals (Niu and Hall, 2000). This study employed density functional theory to calculate molecular properties of iron complexes in gas phase. The Becke gradient corrected exchange functional (Becke, 1988) in conjunction with the Lee–Yang–Parr correlation functional (Lee et al., 1988) with the three parameters (B3LYP) level of theory was used. The accuracy of the calculations, which ultimately affect the thermodynamic and kinetic data, depends on the combination of the theoretical method and basis set. For transition metals, the error in the *ab initio* Hartree–Fock energy usually called the “correlation energy” was just too large (Davidson, 2000). DFT has proven an effective method for the study of transition metal complexes. Computational transition metal chemistry today is almost synonymous with DFT for medium-sized molecules. Effective Core Potential (ECP) basis sets were tested for single iron atoms. ECP can represent the effect of the core electrons and decrease the computational effort by focusing on valence electrons only. The most recent form of ECP is Stuttgart-Dresden (SDD) which largely replaced the LANL2DZ and CEP-121. There is a fundamental difference between basis sets and effective core potentials (ECPs), which are in fact model Hamiltonians that replace the effect of the core electrons. The 6-311++G(d,p) basis sets are used for O, H, S atoms and SDD (Kaupp et al., 1991) pseudopotential and basis are used for Fe and Cl atom throughout this study to provide a consistent set of vibrational frequencies for the reaction products.

The total binding, sequential, and reorganization energies are calculated using the following equations:



5.4 Results and Discussion

Results in this chapter are arranged into two main parts. First, hydration of ferrous and ferric ions, $[\text{Fe}(\text{H}_2\text{O})_n]^{2,3+}$, are discussed with water in the inner shell ranging from 1 to 6. Outer hydration shell with 12 H_2O molecules are presented next for both iron ions. Complexation of ferric ion with chloride its thermodynamic properties in both gas-phase and solvent are studied as part of iron chemistry in high concentrated HCl acid. The second part gives general overview of hydrogen sulfide and sulfur-iron chemistry.

5.4.1 $\text{Fe}[(\text{H}_2\text{O})_n]^{2+}$

The principles underlying chemistry of iron in natural water have been presented by Stumm and Morgan (Stumm and Morgan, 1996). Books on environmental chemistry discussed complexes of iron, their presence in the underground (Appelo and Postma, 2005) and their kinetics (Stumm, 1990). The hydration of metal ions has been investigated by numerous experimental techniques and computer simulation for several decades because of its widespread and important role in many chemical, environmental, and biological processes.

MD simulation showed that six water molecules reside in the first hydration shell for both Fe^{2+} and Fe^{3+} ions with Fe–O bond length being 2.15 and 2.05 Å, respectively (Remsungnen and Rode, 2004). The second hydration shell of iron ions contains 12 water molecules according to experimental information (Ohtaki and Radnai, 1993) while MC simulation indicates 13 and 15 water molecules for Fe^{2+} and Fe^{3+} ions, respectively (Dégrève and Quintale, 1996). The number of water ligands in the second hydration shell is flexible and rapidly exchange with the bulk (Remsungnen and Rode, 2004). Cluster orientation and binding in this shell is dominantly but not exclusively determined by hydrogen bonding. Chemical and physical properties (size, charge, electronic state, etc.) of central iron ions determine the nature of the first coordination sphere (first shell), while additional shell of water result from hydrogen bonding. For $n=1$, the optimized monohydrate, $[\text{Fe}(\text{H}_2\text{O})]^{2+}$ is planar with C_{2v} symmetry and total binding energy $\Delta E_i = -$

90.5 kcal mol⁻¹. Such a structure is an indicative of a strong ion-dipole interaction which is common in mono- and divalent-metal ion monohydrate. Although some electron density (0.33 eV) is transferred from the water ligand to the ferrous ion, the bonding is predominantly electrostatic. The Fe–OH₂ bond length is 1.93 Å which is different from values estimated at MP2(full)/6-311++G* (R_{Fe–O}=1.94 Å) (Trachtman et al., 1998). This is expected, because for a given basis set, B3LYP calculations consistently yield shorter Fe–O distances than MP2(full). Optimized geometrical structures for Fe[(H₂O)_n]²⁺, (n=1–6), are shown in Figure 5.2 together with binding energy, Fe–O bond length and number of imaginary frequency. For n=2, the optimized diaquo ferrous structure has C_{2v} symmetry with one imaginary frequency. This structure is not at local minimum point on the potential energy surface (PES) and we are expecting the conformation D_{2d} to be the lowest energy structure as in the case of other divalent metal cations (Rao et al., 2008). The addition of second water molecules to the monoaquo ferrous cluster result in 75.9 kcal mol⁻¹ higher than that for [Fe(H₂O)]²⁺, and longer bond distance. To our knowledge, we did not come cross any experimental or higher level of calculation reporting the structural properties of the clusters [Fe(H₂O)_n]²⁺, with (n=1–5). Therefore, we are reporting our result using B3LYP theory with the intention to repeat them again at a higher level of theory in the next phase of this study.

The reorganization energy, (ΔE_a), needed to rearrange “pure” water cluster to form the corresponding water-iron complex is calculated at the same level of theory and basis set. Results are available in Appendix-B for both ferric- and ferrous-water clusters. As the metal ion approaches, all water molecules are reorganized in a different conformation to form iron-water cluster. The Values of ΔE_a are negative indicating that the hydration process is highly endothermic. For n=1, this energy has the same value as total binding energy according to equation (3). For diaquo ferrous, n=2, the energy needed for two water molecules to break their hydrogen bond in dimer water cluster and form aquo-complex with ferrous ion is -162.3 kcal/mol. The optimized structure for triaquo ferrous complex has D₃ symmetrical geometry with total binding energy of -225.3 kcal/mol that

is 59.0 kcal/mol higher than the diaquo complex. The calculated average bond distance $\langle\text{Fe-O}\rangle$ is 2.01 Å compared to 1.95 Å and 1.93 Å for mon- and diaquo complex, respectively. For $n=4$, the optimized geometry of tetraaquo ferrous complex has two imaginary frequencies, which means the structure shown in Figure 5.2(d) is not a minimum on potential energy surface (PES). Therefore, we will include results based on this geometrical in our discussion, though we believe that the calculation needs to be repeated to allocate more stable structure. We have not run the calculation again because of the high computational time (cost) that is required for iron complexes to converge. The total binding energy for tetraaquo ferrous complex is -268.2 kcal/mol which is 42.8 kcal/mol greater than that for $n=3$. As the number of water molecules increases around ferrous ion, the average bond distance $\langle\text{Fe-O}\rangle$ increases too. The rearranging energy also increases as the number of water molecules increases resulting in thermodynamically favorable transition to occur. For pentaquo ferrous complex, $n=5$, the optimized structure is stable with C_2 symmetry. It has a total binding energy of -296.88 kcal/mol and average bond distance $\langle\text{Fe-O}\rangle$ of 2.12 Å. For $n=6$, the hexaquo ferrous has local minimum clusters with T_h symmetry as shown in Figure 5.2(f). The total binding energy is 22.4 kcal/mol higher than that for pentaquo complex and the average bond distance $\langle\text{Fe-O}\rangle=2.17$ Å (in the range 2.15 –2.22 Å) is in good agreement with experiment, lying within the range of experimental values. The experimental value of Fe–O reported for Tutton salt (Cotton et al., 1993) is between 2.10 and 2.28 Å. level of theory and basis set has its effect on the value of Fe–O distance as the value calculated in this study is larger than what was predicated at DFT(NL) (2.13 Å) and lower than HF value (2.18 Å) (Li et al., 1996). The structure is approximately octahedral with average $\angle\text{OFeO}$ angle of 89°. Water molecules surrounding ferrous ion has average $\langle\text{O-H}\rangle=0.97$ Å and $\angle\text{HOH}=106.5^\circ$. We also observe that as the number of water molecules increase in the first hydration shell of ferrous ion, the calculated charge on Fe atom using APT analysis increases too. This is consistent with the increase in Fe–O bond distance which indicates less electron transfer from water oxygen to ferrous ion as the coordination number increases.

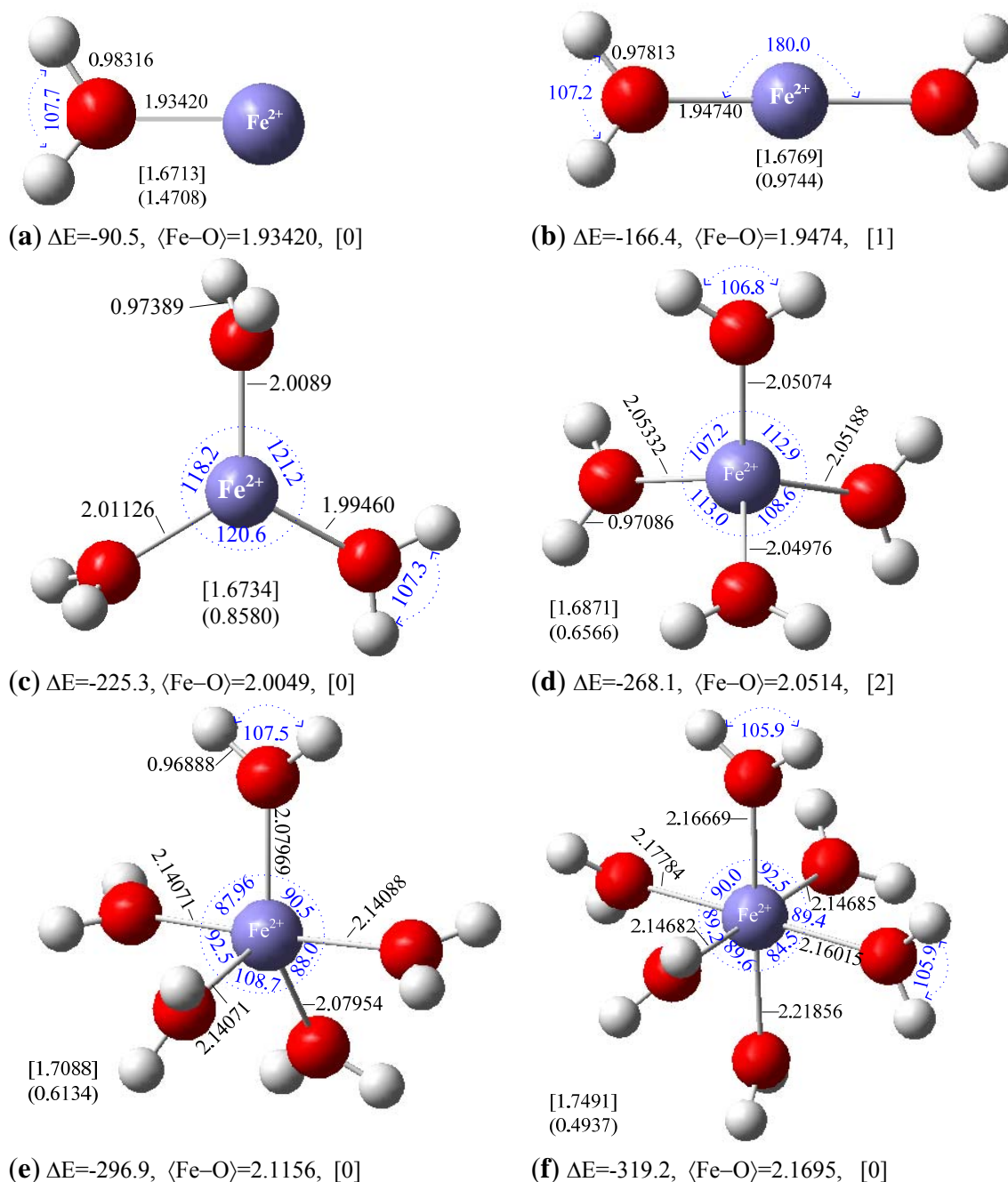


Figure 5.2: Optimized structures with geometrical parameters from *ab initio* calculations using B3LYP/6-311g** (H,O) and B3LYP/SDD (Fe) for hydro-ferrous, Fe(II), complexes, (a) $[\text{Fe}(\text{H}_2\text{O})_2]^{2+}$, (b) $[\text{Fe}(\text{H}_2\text{O})_3]^{2+}$, (c) $[\text{Fe}(\text{H}_2\text{O})_4]^{2+}$ (d) $[\text{Fe}(\text{H}_2\text{O})_5]^{2+}$ (e) $[\text{Fe}(\text{H}_2\text{O})_6]^{2+}$. Shown in these diagrams are bond length (Å), bond angles (°), binding energy (kcal mol^{-1}) and Fe-charge (electron unit). Values in square brackets are APT charges and in parentheses for Mulliken charges both with hydrogen summed into heavy atoms. Color code for atoms is: red for O, slate blue for Fe, and light gray for H.

Table 5.1: Calculated average bond length, average bond angle, and equilibrium binding energy for $[\text{Fe}(\text{H}_2\text{O})_n]^{x+}$, $\Delta E_i = E_{\text{cluster}} - (E_{\text{Fe}} + nE_{\text{H}_2\text{O}})$ at $T=298.15$ K and $p=1$ atm using B3LYP/6-311g**/SDD.

(Charge, Multi)	$n\text{H}_2\text{O}$	# img ^a	ΔE_i (kcal mol ⁻¹)	$\langle \text{Fe}-\text{O} \rangle$ (Å) [†]	$\angle \text{O}-\text{Fe}-\text{O}$ (°) [†]	$\langle \text{H}-\text{O} \rangle$ (Å) [†]	$\angle \text{H}-\text{O}-\text{H}$ (°) [†]
Fe (2,5)	1		-90.5	1.93	126 ^b	0.98	108
	2	0	-166.4	1.95	180	0.98	107
	3	0	-225.3	2.00	120	0.97	107
	4	0	-268.1	2.05	110	0.97	107
	5	1	-296.9	2.11	93	0.97	107
	6	0	-319.2	2.17	89	0.97	106
Fe (3,6)	1	—	—	—	—	—	—
	2	2	-364.2	1.96	180	1.00	106
	3	0	-470.2	1.93	120	1.00	106
	4	1	-554.6	1.96	110	0.99	107
	5	0	-608.8	2.02	93	0.98	107
	6	0	-653.3	2.07	90	0.98	106

[†] Average value, ^a number of imaginary frequencies in the final optimized structure. ^b value of $\angle \text{O}-\text{Fe}-\text{H}$.

5.4.2 $\text{Fe}[(\text{H}_2\text{O})_n]^{3+}$

Experimental techniques such as X-ray, NMR and neutron diffraction have been extensively applied to probe the structure of the first hydration shells of metal cations (Ohtaki and Radnai, 1993). The determination of hydration numbers shows that there are six water molecules in the first hydration shell of most di- or trivalent transition metal cations. The $[\text{Fe}(\text{H}_2\text{O})_6]^{3+}$ cluster is thus a reasonable static model for the first solvent coordination shell. Akesson *et al.* carried out a series of *ab initio* calculations on $[\text{M}(\text{H}_2\text{O})_6]^{m+}$ for first- and second-row transition metals at the HF-SCF level with medium-sized basis sets and effective core potentials (ECP) (Aakesson et al., 1992). Waizumi *et al.* also reported a local spin density functional calculation on these same clusters. As a constraint, the orientations of the water molecules were retained (Waizumi et al., 1992). DFT combined with continuum dielectric techniques was used in previous study (Li et al., 1996) to calculate redox and pK_a values for hydrated $[\text{M}(\text{H}_2\text{O})_6]^{x+}$ complex and optimize its geometry, (where $\text{M}=\text{Fe}, \text{Mn}$). More computational work has been carried out by Harria *et al.* (Harris et al., 1997) to optimize the structure

$[\text{Fe}(\text{H}_2\text{O})_6]^{3+}$ at various spin-states using UHF, MP2, BPW91 and BLYP and 6-31G* basis set. In this section, we report a more detail DFT calculation of ferric first-shell hydration.

For $n=1$, the initial structure with C_{2v} symmetry did not converge rather the single water molecule depart away from ferric ion as the simulation time increases. We have not reached to clear explanation on this observation. The molecular structure shown in Figure 5.3 (a) is for single point calculation of $[\text{Fe}(\text{H}_2\text{O})]^{3+}$ based on optimized structure of monoaquo ferrous, $[\text{Fe}(\text{H}_2\text{O})]^{2+}$. The binding energy of monoaquo ferric complex is -227.4 kcal/mol with equal Fe–O bond distance to monoaquo ferrous complex. The final optimized structure for diaquo ferric cluster has one imaginary frequency with linear C_{2v} symmetry. We believe the more stable structure of this complex has D_{2d} symmetry as in the case of mono- and divalent metal ions (Rao et al., 2008). The calculated binding energy is -364.2 kcal with average Fe–O bond distance of 1.96 Å. The energy needed for pure water molecules to rearrange and form stable complex with ferric ion are -227.4 and -364.2 kcal/mol for mono- and diaquo ferric complexes, respectively. The water molecules have higher affinity to break hydrogen bonds and rearrange around ferric ion. This affinity is consistently calculated to be double (~ 2.2) as compared to ferrous ions. For $n=3$, the optimized structure has -470.2 kcal/mol total binding energy which is 106 kcal/mol higher than that for diaquo complex. The geometrical structure has C_3 symmetry with average Fe–O bond distance of 1.93 Å. The three water molecules have an average $\angle\text{OHO}$ of 120° and $\langle\text{O–H}\rangle=1.00$ Å. The tetraaquo complex has two imaginary frequencies and is not at minimum point on the PES surface; however, we are reporting its optimized parameters. This saddle structure has total binding energy of -554.6 kcal/mol and average Fe–O distance of 1.96 Å. The average angle, $\angle\text{HOH}$, of water molecules surrounding ferric ions is 107° , and has $\langle\text{O–H}\rangle$ of 0.99 Å. The structure is approximately tetrahedral with $\angle\text{OFeO}$ angle of 110° .

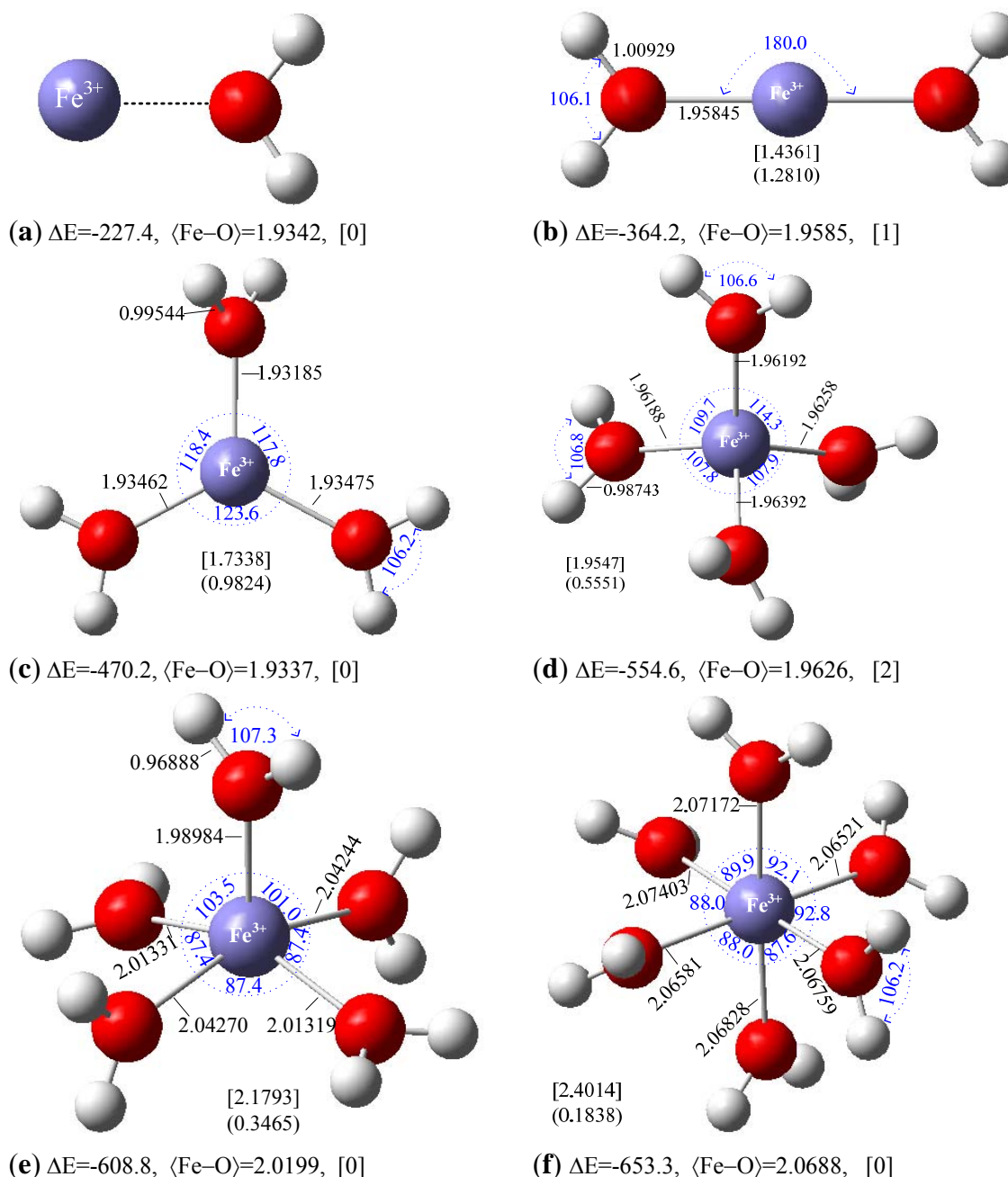


Figure 5.3: Optimized structures with geometrical parameters from DFT calculations using B3LYP/6-311g** (H,O) and B3LYP/SDD (Fe) for hydro-ferric, Fe(III), complexes, (a) $[\text{Fe}(\text{H}_2\text{O})_2]^{3+}$, (b) $[\text{Fe}(\text{H}_2\text{O})_3]^{3+}$, (c) $[\text{Fe}(\text{H}_2\text{O})_4]^{3+}$ (d) $[\text{Fe}(\text{H}_2\text{O})_5]^{3+}$ (e) $[\text{Fe}(\text{H}_2\text{O})_6]^{3+}$. Shown in these diagrams are bond length (Å), bond angles (°), binding energy (kcal mol^{-1}) and Fe-charge (electron unit). Values in square brackets are APT charges and in parentheses for Mulliken charges both with hydrogen summed into heavy atoms. Color code for atoms is: red for O, slate blue for Fe, and light gray for H.

For $n=5$, the optimized pentahydrated ferric complex has C_2 symmetry with total binning energy of -608.8 kcal/mol. This structure is trigonal bipyramid with all water molecules are in direct contact with ferric ion, and we are reposting this geometry to be the most stable until we carry further calculations on $[\text{Fe}(\text{H}_2\text{O})_4.\text{H}_2\text{O}]^{3+}$ and $[\text{Fe}(\text{H}_2\text{O})_3.2\text{H}_2\text{O}]^{3+}$. It has been suggested that at higher temperature the stable structure of pentaquo complex is a tetrahedral with one water molecule in the second shell as for Mg^{2+} (Markham et al., 2002). The average calculated bond distance of Fe–O is 2.02 Å and the energy needed for water molecules to rearrange and form this complex -575.5 kcal/mol. It is generally been inferred that six water molecules are required to complete the first coordination shall surrounding Fe^{3+} ions. The hexaquo complex has octahedral geometry with T_h symmetry as shown in Figure 5.3(f). The B3LYP approximation gives an Fe–O is 2.0688 Å which is in a good agreement with what has been reported in theoretical literature (Martin et al., 1997). The total binding energy for the hexahydro complex is -653.3 kcal/mol which is 44.5 kcal/mol higher than that for pentaquo cluster. In Figure 5.3, we have shown the atomic practical charge computed for all hydro structures using Mulliken population analysis and natural population analysis (NPA). The charge assigned for the ferric ion is substantially less than 3e.

5.4.3 $\text{Fe}[(\text{H}_2\text{O})_n.12\text{H}_2\text{O}]^{x+}$

Experimental information on the structural details of the second hydration shell of iron ions is scarce and uncertain compared with that for the first shell. X-ray diffraction measurements of some di- and trivalent manganese and iron salts suggest that the hydration number is about 12 (Ohtaki and Radnai, 1993). This has been supported by several molecular simulation analyses (King and Warshel, 1989). However, other Monte Carlo simulation data (Dégrève and Jr., 1996) suggests that the second hydration shell has about 13 water molecules for Fe^{2+} and 15 for Fe^{3+} ions. The arrangement of these 12 water molecules was not clear in the past as a full geometry optimization of the whole cluster $[\text{Fe}(\text{H}_2\text{O})_{18}]^{m+}$ by the density functional method was not feasible. Since direct bonding between the metal center and the second-shell water molecules is relatively

weak, the location is determined mainly by hydrogen-bonding and steric interactions. We positioned the 12 second-shell water molecules in such a way that each binds to only one hydrogen atom from a water molecule in the first shell with the second shell oxygen atoms oriented toward the corresponding hydrogen atom. The initial geometrical structures were taken from a great work carried out by Wales et al. (González et al., 2005) for $\text{Li}(\text{H}_2\text{O})_n^+$ and $\text{Ca}(\text{H}_2\text{O})_n^{2+}$ with $n \leq 20$. The Cambridge Structural Database (CSD) was also searched for other iron crystal geometries (Allen, 2002).

Figure 5.4 shows the optimized structure for $[\text{Fe}(\text{H}_2\text{O})_6.12\text{H}_2\text{O}]^{3+}$, which is similar to that of ferrous with 18-water cluster. The six water molecules in the inner shell are oriented with their oxygen atoms pointing toward the iron ion, whereas the hydrogen atoms are directed away from the central positively charge ion. These hydrogen atoms can form hydrogen bonds to oxygen from water molecules in the second hydration shell. The optimized structure shown in Figure 5.3(a) has approximately S_6 symmetry with 24 hydrogen bonds (HB). This structure is the lowest-energy local minimum that has been found (Bock et al., 2006). The six water molecules in the first hydration shell form 12 hydrogen bonds with water molecules in the second shell. The integrated hydrogen bond network found in this cluster consist of pentameric units each composed of four water molecules from the second shell and one from the first shell. The structure is not spherical as might look like, but flattened at two ends. The average $\text{Fe}^{3+}\text{--O}$ distance is 2.02 and 2.04 Å using B3LYP with LanL2DZ and SDD(Fe)/6-311++g** (H,O), respectively. The second (6,12) tested structure has 20 hydrogen bonds as shown in Figure 5.4(b). the six inner shell water molecules in this complex remain an essentially octahedral arrangement. Each water molecule from the first shell interacts with two water molecules in the second shell via hydrogen bonding. The average $\text{Fe}^{3+}\text{--O}$ distance is longer than what we have calculated for the 24-HB at the same level of theory and basis set as shown in Table 5.2. The total binding energy calculated for $[\text{Fe}(\text{H}_2\text{O})_6.12\text{H}_2\text{O}]^{3+}$ is -1140.7 and 950.2 kcal/mol at LanL2DZ and SDD, respectively.

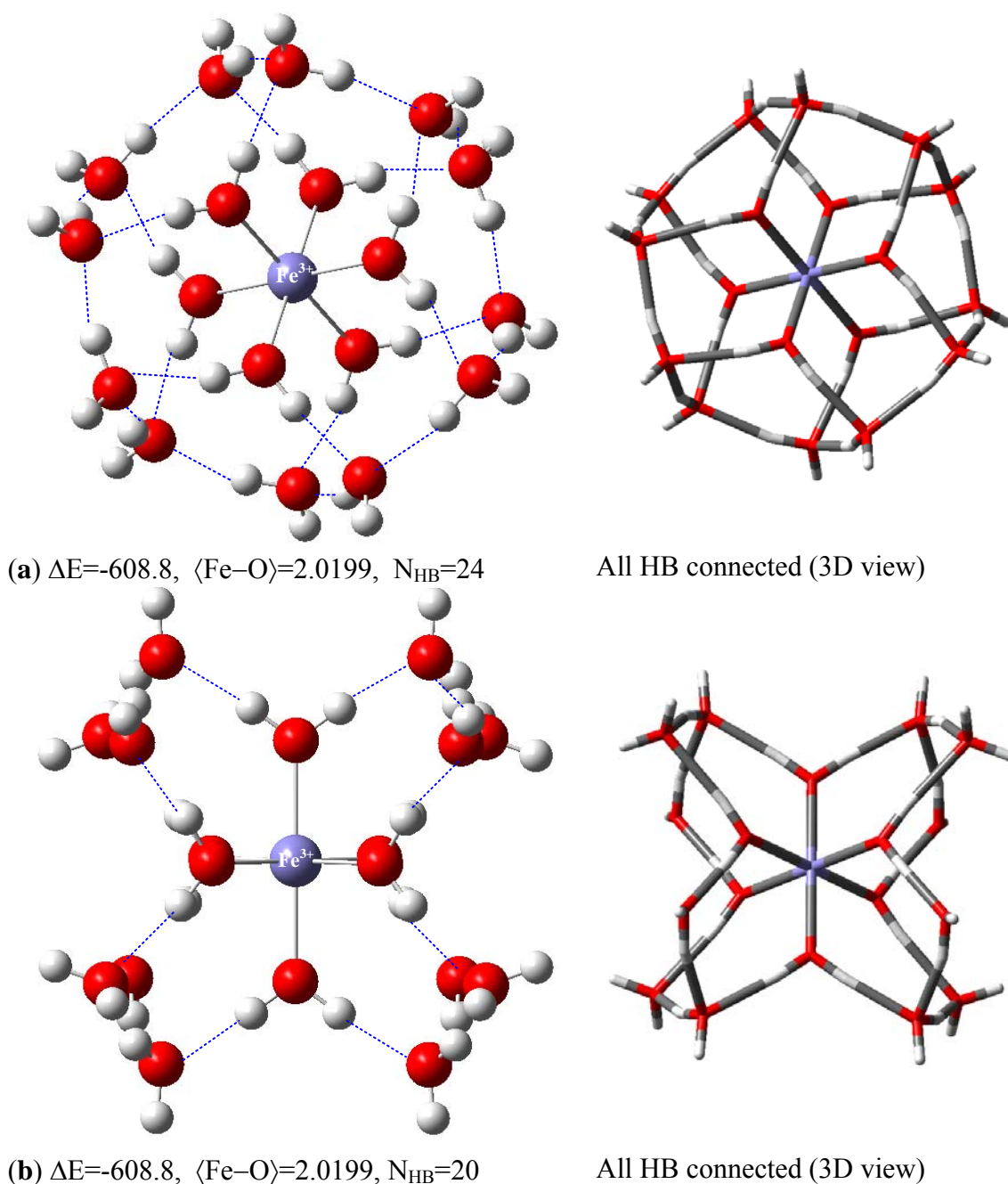


Figure 5.4: Optimized structures with geometrical parameters from DFT calculations using B3LYP/6-311g** (H,O) and B3LYP/SDD (Fe) for hydro-ferric, Fe(III), complexes, (a) 24-HB $[\text{Fe}(\text{H}_2\text{O})_2.12\text{H}_2\text{O}]^{3+}$, (b) 20-HB $[\text{Fe}(\text{H}_2\text{O})_2.12\text{H}_2\text{O}]^{3+}$. Shown in these diagrams are bond length (Å), bond angles (°), binding energy (kcal mol^{-1}) and Fe-charge (electron unit). Color code for atoms is: red for O, slate blue for Fe, and light gray for H.

Table 5.2: Calculated average bond length, average bond angle, and equilibrium binding energy for $[\text{Fe}(\text{H}_2\text{O})_6.12\text{H}_2\text{O}]^{x+}$, $\Delta E_i = E_{\text{cluster}} - (E_{\text{Fe}} + nE_{\text{H}_2\text{O}})$ at $T=298.15$ K and $p=1$ atm using B3LYP

(Charge, Multi)	Basis set	n HB ^a	ΔE_i (kcal mol ⁻¹)	$\langle \text{Fe}-\text{O} \rangle$ (Å) ^{†,d}	$\langle \text{Fe}-\text{O} \rangle$ (Å) ^{†,e}	$\angle \text{OFeO}$ (°) [†]	$\langle \text{HB} \rangle$ (Å) [†]
Fe (2,5)	LanL2DZ ^b	24	-672.9	2.13	3.99	90	1.81
		20	-639.1	2.14	4.34	92	1.82
	SDD/ 6-311++G(d,p) ^c	24	-511.9	2.15	4.15	90	1.88
		20	-500.1	2.16	4.44	90	1.87
Fe (3,6)	LanL2DZ ^b	24	-1140.7	2.02	3.91	87	1.66
		20	-1127.1	2.03	4.17	90	1.67
	SDD/ 6-311++G(d,p) ^c	24	-950.2	2.04	4.05	88	1.72
		20	-948.5	2.04	4.23	90	1.72

^a number of hydrogen bonds in the structure, ^b LanL2DZ used as a basis set for all atoms (H, O, Fe). ^c SDD for Fe atom and 6-311++G(d,p) for O and H atoms. ^d distance with water in the first shell. ^e distance with water in the second shell. [†] average value.

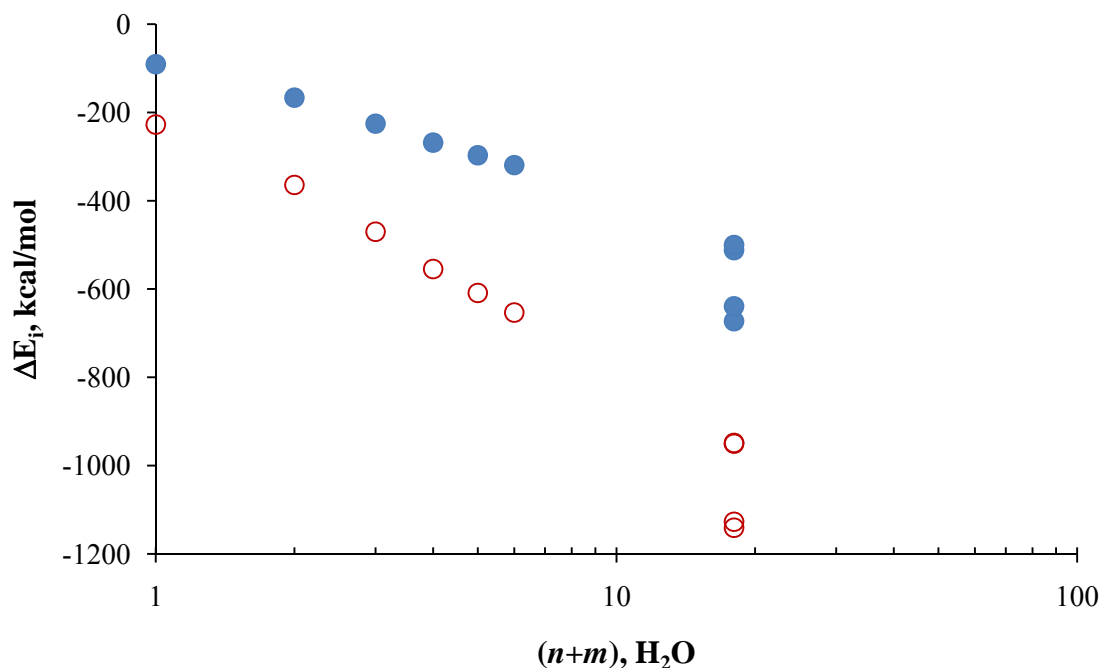


Figure 5.5: Binding energy as a function of water molecules in first shell (n) and second shell (m). (●) for $[\text{Fe}(\text{H}_2\text{O})_{n+m}]^{2+}$, and (○) $[\text{Fe}(\text{H}_2\text{O})_{n+m}]^{3+}$. The first 7-points are calculated using B3LYP/6-311++g**/SDD and the last 2-points are at B3LYP/LanL2DZ.

The same calculations on (6,12) have been carried out for the ferrous ion with six water molecules in the first shell and twelve in the second. Table 5.2 shows summary of the geometrical and thermodynamic properties of $[\text{Fe}(\text{H}_2\text{O})_6.12\text{H}_2\text{O}]^{2+}$. The binding energy for the stable structure with 24 hydrogen bonds is highly dependent on basis set. Using LanL2DZ for all atoms (O, H, Fe) results in binding energy of -672.9 kcal/mol, which is 161.0 kcal/mol higher compared to the mixed basis set (6-311++g**, SDD). The difference in binding energy between the 24-HB and 20-HB structures are 33.8 and 11.9 kcal/mol for B3LYP/LanL2DZ and B3LYP/(6-311++g**, SDD), respectively. The calculated binding energy is sensitive to the inclusion of multiple polarization functions into the basis set. Figure 5.5 shows change in total binding energy with number of water molecules surrounding ferrous (open circle) and ferric (closed circle). This relation is logarithmic in nature and has the following equation: $\Delta E_i = 145.9 \ln(n+m) - 70.9$ with correlation factor of 0.990 for $[\text{Fe}(\text{H}_2\text{O})_n.m\text{H}_2\text{O}]^{2+}$. Similar observation for hydroferric $[\text{Fe}(\text{H}_2\text{O})_n.m\text{H}_2\text{O}]^{3+}$ with $\Delta E_i = 243.4 \ln(n+m) - 204.2$ and $R^2 = 0.996$. To the best of our knowledge, neither DFT calculations nor direct experimental determination of the binding energy of iron with 18-water molecules are currently available, and therefore, we need to recalculate these values at higher level of theory.

The average bond distance $\text{Fe}^{\text{II}}-\text{O}$ in the first shell of (6,12) 24-HB structure is calculated to be 2.13 and 2.15 Å at LanL2DZ and (6-311++g**, SDD), respectively. These values fall in the range 2.10–2.28 Å reported experimentally (Ohtaki and Radnai, 1993). Molecular mechanic calculations result in Fe–O values ranging between 2.16 and 2.17 Å (Li et al., 1996). As the binding energy is overestimated using LanL2DZ, the values of Fe–O bond length is underestimated compared to the mixed basis set. The Fe–O bond distance with water molecules in the second hydration shell is found to be 4.15 and 3.99 Å at LanL2DZ and (6-311++g**, SDD), respectively. The variation between the minimum and maximum value is less than 0.07 Å, which means the 24-HB is stable structure with high symmetry. The average hydrogen bond is 1.88 Å between water molecules in the first and second hydration shell at B3LYP/(mixed).

5.4.4 $Fe[Cl_n(H_2O)_{6-n}]^{3-n}$

Iron (III) halides are obtained by direct halogenations of ferric ion. The main dominated complexes of Fe(III) in HCl solutions are: $[Fe(H_2O)_6]^{3+}$, $[FeCl(H_2O)_5]^{2+}$, $[FeCl_2(H_2O)_4]^+$, $[FeCl_3(H_2O)_3]$, $[FeCl_4]^-$. There are also trigonal bipyramidal, $[FeCl_5]^{2-}$, octahedral, $[FeCl_6]^{3-}$, and face-sharing bioctahedral, $[Fe_2Cl_9]^{3-}$, which can be obtained with large cations. Fe(III) has high affinity for fluoride, F^- , which are $\sim 10^4$ greater than those for Cl^- (Atkins et al., 2006). Therefore, special attention is need when designing stimulation treatment using HF acid as in sandstone reservoir. The distribution of Fe chloroaquo species as function of $[HCl]$ are shown in Figure B.1 by solving simultaneously the mass balance, and charge balance equations (Liu et al., 2006). Accurate knowledge of the HCl dissociation is necessary for the thermodynamic description of the process. The ferric-chloride reactions as well as the acid interaction with the rock are dependent on acidity which is mainly controlled by HCl dissociation. Despite the numerous experiential studies of HCl dissociation over a wide range of pressure and temperature that have been carried out, the thermodynamic properties of HCl are subject to uncertainty (Tagirov et al., 1997). Equation of state such as Redlikh-Kwong demonstrated high accuracy describing the dissociation of HCl at least in the temperature range of 25–300°C and pressure up to 2500 bar (Tagirov et al., 1997).

The simple and important reactions in water involve acids. In the case of strong acid such as HCl, almost all the molecules dissociation aqueous solution to form hydrated Cl^- and H^+ ions. acid dissociation is one of the simplest and most important solvation reaction. Strong acid such as HCl ($pK_a=-7$) readily dissociates in dilute aqueous solution tp form hydrated chloride and hydronium ion, whereas, under the same conditions, a weak acid such as HF ($pK_a=3$) barely ionizes. To our knowledge, there are very few experiments on the structure of HCl in water solution; however, good number of theoretical studies has been reported in the literature. Classical molecular dynamic simulations have been widely used for studying ion in aqueous solution but to describe ionization of HCl acid in water and the pH of the solution is very difficult using

empirical potential (Laasonen and Klein, 1994). *Ab initio* simulation has been used more frequently to study the clusters of HCl and water (Laassonen and Klein, 1997). The behavior of ions in concentrated aqueous solution is somewhat less clear. Water has only very limited solubility in concentrated HCl, but the solubility of HCl in water saturates at around 40 wt %. The objective in this part of the chapter is to gain some insight into the interaction parameters between single Cl^- and cluster of water molecules.

Figure 5.6 shows optimized molecule structures of $[\text{Cl}(\text{H}_2\text{O})_n]^-$, where $n=1,2,3, 9$ at B3LYP with 6-311++g** basis set for H, O atoms and SDD for Cl atom. Earlier study reported the difference between various anion (I^- , Cl^- , F^- , and OH^-) in water cluster of $n=1-6$ (Singh et al., 2006). Car-Parrinello density functional theory based on molecular dynamic (CPMD) study showed that the chloride ion has a coordination number that fluctuate between 4 and 5 (Laassonen and Klein, 1997). For $n=1$, the chloride ion form a complex with total binding energy of -25.6 kcal/mol and has a C_s symmetry. The Cl–H bond distance is 2.22 Å and $\angle\text{OHCl}$ angles is calculated to be 150° as shown in Figure 5.6(a). It worth noticing that the chloride ion alter $\angle\text{HOH}$ angle to 98° . Once a second water molecule is added to the cluster, chloride ion forms shorter bonding with hydrogen atom (2.17 Å) of two water molecules compared to that with single water. The binding energy is -44.7 kcal/mol which is 19.1 kcal/mol higher than $[\text{Cl}(\text{H}_2\text{O})]^-$. As we have seen in Chapter IV, the binding energy for water cluster of two molecules is -4.08 kcal/mol, and clearly the rearrangement of pure water molecules around Cl^- ion is thermodynamically favorable. The optimized structure of $[\text{Cl}(\text{H}_2\text{O})_2]^-$ is shown in Figure 5.6(b) with cyclic geometry similar to triaquo cluster with one water molecule has been replaced with Cl^- ion. For $n=3$, we have tested two structures which interestingly are very close in total binding energy. It has been reported recently that the C_3 symmetrical geometry with three water molecules forming cyclic base linked together via hydrogen bonding (Figure 5.6(d)) is the most stable for $[\text{Cl}(\text{H}_2\text{O})_3]^-$ (Singh et al., 2006). However, we found that structure of Cl^- ion surrounded by three water molecules each has Cl–H bond distance of 2.69 Å and $\angle\text{OHCl}$ of 111° is in the same binding energy level.

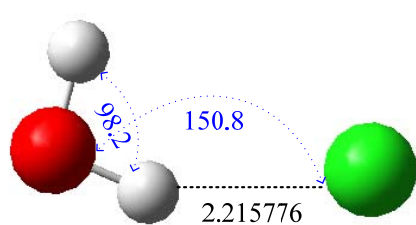
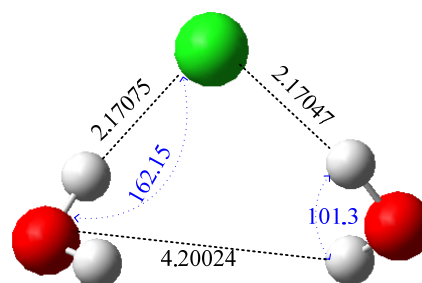
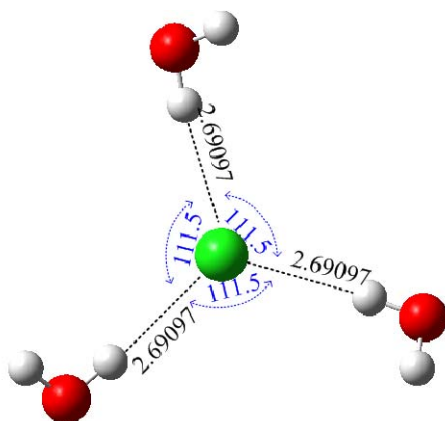
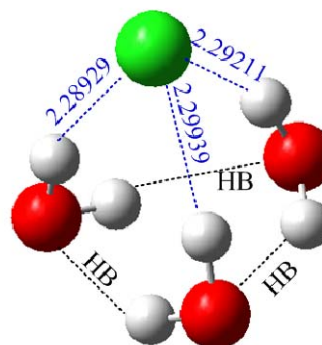
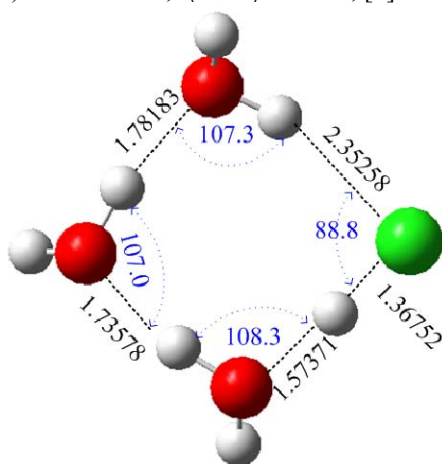
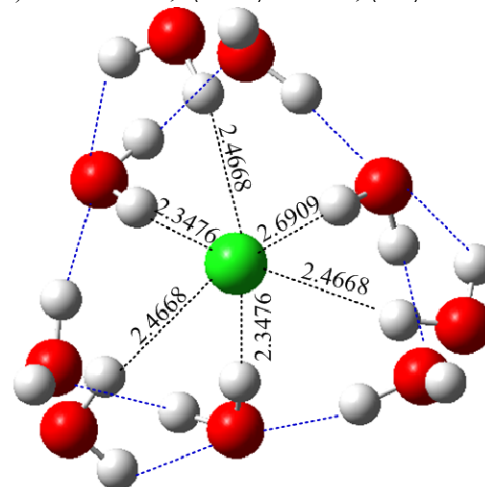
(a) $\Delta E = -25.6$, $\langle \text{Cl-H} \rangle = 2.1578$, [0](b) $\Delta E = -44.7$, $\langle \text{Cl-H} \rangle = 2.1706$, [0](c) $\Delta E = -60.952$, $\langle \text{Cl-H} \rangle = 2.6910$, [0](d) $\Delta E = -60.950$, $\langle \text{Cl-H} \rangle = 2.2936$, $\langle \text{HB} \rangle = 2.2276$, [0](e) $\Delta E = -206.4$, $\langle \text{Cl-H} \rangle = 1.8601$, $\langle \text{HB} \rangle = 1.6971$, [0](f) $\Delta E = -124.36$, $\langle \text{Cl-H} \rangle = 2.4073$, $\langle \text{HB} \rangle = 1.9104$, [0]

Figure 5.6: Optimized structures with geometrical parameters from *ab initio* calculations using B3LYP/6-311g** (H,O) and B3LYP/SDD (Cl) for hydro-chloride clusters: (a) $[\text{Cl} \cdots \text{H}_2\text{O}]^+$, (b) $[\text{Cl} \cdots 2\text{H}_2\text{O}]^+$, (c) $[\text{Cl} \cdots 3\text{H}_2\text{O}]^+$ with no HB, (d) $[\text{Cl} \cdots 3\text{H}_2\text{O}]^+$ with HB between trimer H_2O , (e) $\text{Cl}(\text{H}_3\text{O}) \cdot 2\text{H}_2\text{O}$, (f) $[\text{Cl} \cdots 9\text{H}_2\text{O}]^+$. Shown in these diagrams are bond length (Å), bond angles (°), binding energy (kcal/mol) and Fe-charge (electron unit). Color code for atoms is: red for O, slate blue for Fe, and light gray for H.

In Figure 5.6(e), we have added hydronium ion to the system of two water molecules and chloride ion to study the change in binding energy. This complex can be seen as three water molecule with HCl in solution. The initial structure was a tetramer water cluster with one water molecule has been replaced by HCl. The optimized geometry is cyclic with average hydrogen bond between three water molecules of 1.70 Å and $\langle \text{Cl-H} \rangle = 1.86$ Å. The total binding energy is 206.4 kcal/mol which is 8-times higher than that for pure tetramer water cluster (-25.0 kcal/mol), and triple the value calculated for $[\text{Cl}(\text{H}_2\text{O})_3]^-$. This reflects the strong interaction of HCl in water solution. We have not examine the molecular geometry of $[\text{Cl}(\text{H}_2\text{O})_n]^-$ with $n=4,5,6$, or 7 as it is ready been reported somewhere else (Singh et al., 2006). The $[\text{Cl}(\text{H}_2\text{O})_9]^-$ shows very interesting geometrical properties and we have cared it calculations at B3LYP with 6-311++g** (H,O) and SDD(Cl) basis sets. The optimized structure is shown in Figure 5.6(e) and it has a total binding energy of -124.4 kcal/mol. The arrangement of water molecules around chloride ion is shown in Appendix B (Figure B.2) with three cyclic trimers. Chloride ion forms six bonds with hydrogen from six different water molecules, two from each trimer. The third free hydrogen in every trimer is form a hydrogen bond between the trimers. The calculated average Cl-H bond distance is 2.41 Å with 2.47 Å ($\times 3$) and 2.35 ($\times 3$) Å. hydrogen bond forming cyclic water trimer is 1.91 Å while the average hydrogen bond between the trimers is 1.91 Å ($\times 3$).

As we have discussed the behavior of chloride ion in water solution, the chemistry of iron chloride is further inserting. There are number of complexations occur and might alter the functionality and solution properties of viscoelastic surfactant as we will see in Chapters VII and VIII. Iron chlorides are known for their high thermal stability, for example, FeCl_3 begins to decompose into FeCl_2 and Cl_2 at its melting point of 577 K, while FeCl_2 , on the other hand, has a high thermal stability and can have unnoticeable change up to 1297 K (Bach et al., 1996). In well acidizing treatment of hydrocarbon reservoir, the sources of iron are many. The reported iron concentration from a flow back of well after acidizing treatment is in the range of 9,000 to 100,000 mg/L (Taylor et

al., 1999). Complexation of ferric and ferrous ions with chloride has been the subject for many experimental and theoretical studies. The kinetics and rate of exchange between Fe(II) and Fe(III) in perchloric acid solution showed that ferrous iron diffuses three times faster than ferric (Silverman and Dodson, 1952). Thermodynamic and kinetics of ferric chloride complexes in acidic solution are shown in Table B.6.

We are not studying ferrous chloride complexes in this chapter rather the focus will be on ferric complexes in acidic solution. DFT is used to investigate the structure and energies of the form $[\text{FeCl}_n(\text{H}_2\text{O})_{6-n}]^{3-n}$, where $n=1-6$, both in gas-phase and water solution. For $n=1$, the optimized structure of monochloroferrate $[\text{FeCl}(\text{H}_2\text{O})_5]^{2+}$ is shown in Figure 5.7(a). It has a total binding energy of -987.9 kcal/mol which is 334.6 kcal/mol higher than the hexaaquo ferric cluster. The octahedral and tetrahedral forms of this complex exist equally in equilibrium in HCl solution (Brady et al., 1964). However, for the purpose of this study, we have not investigate the effect of hydration, $[\text{FeCl}(\text{H}_2\text{O})_x]^{2+}$, with $x=0-5$, on energy and structure of the complex. Similar analysis has been conducted for zinc chloro complexes (Pye et al., 2006) and it showed that the octahedral structure is the most stable for all chloroaquozinc complexes. To the best of our knowledge no theoretical calculations have been studied for the hydration effect on both ferric and ferrous chloride systems. These calculations will be carried out as the next phase of the study. The average Fe–Cl bond distance is 2.20 Å which is in a good agreement with experimental value of 2.13 Å (Apted et al., 1985). The value is higher when using solvation model (Fe–Cl=2.28 Å). For $n=2$, there are two configurations: [*trans*–FeCl(H₂O)₅]²⁺ and [*cis*–FeCl(H₂O)₅]²⁺ as shown in Figure 5.5 (b,c), respectively. The difference in total binding energy between the two structures is 4.04 kcal/mol with *trans* higher. Therefore, we have just run the solvation model for the *trans* configuration only. The calculated average bond for Fe–Cl and Fe–O of the *trans* structure in the gas-phase are 2.28 and 2.12 Å, respectively and 2.33 and 2.09 Å, respectively using PCM solvation model.

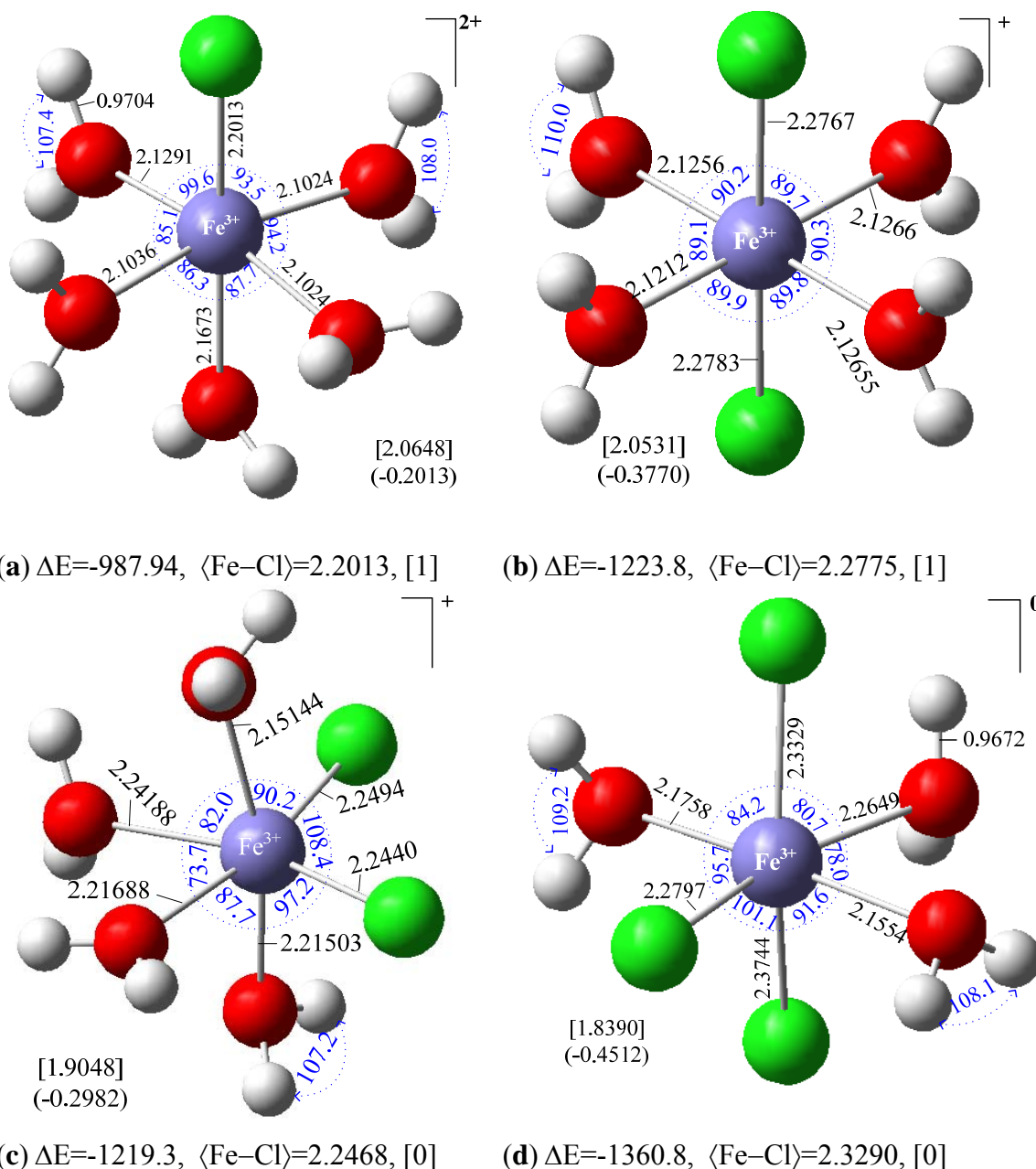


Figure 5.7: Optimized structures with geometrical parameters from *ab initio* calculations using B3LYP/6-311g** (H,O) and B3LYP/SDD (Fe) for ferricchloride complexes: (a) $[\text{FeCl.5H}_2\text{O}]^{2+}$, (b) $[\text{Fe-transCl}_2.4\text{H}_2\text{O}]^+$, (c) $[\text{Fe-cisCl}_2.4\text{H}_2\text{O}]^+$, (d) $[\text{FeCl}_3.3\text{H}_2\text{O}]$. Shown in these diagrams are bond length (Å), bond angles ($^\circ$), binding energy (kcal mol^{-1}) and Fe-charge (electron unit). Values in square brackets are APT charges and in parentheses for Mulliken charges both with hydrogen summed into heavy atoms. Color code for atoms is: red for O, slate blue for Fe, and light gray for H.

These values are closed to what is reported experimentally by Lind (Fe–Cl=2.30 Å and Fe–O=2.07 Å) (Lind, 1967). The solvation model gives lower value of Fe–O as expected (Hill and Schauble, 2008).

For $n=3$, the complex $\text{FeCl}_3 \cdot 3\text{H}_2\text{O}$ is solid and has a melting point of 37°C (Murata and Irish, 1988). The experimental analysis of Fe(III) solution with hydrochloric acid showed that every one mole of HCl and several mole of water can give one mole of FeCl_3 (Bjerrum and Lukes, 1980) and extracted product in the form HFeCl_4 . The optimized structure for trichlorotriaquoferric complex is shown in Figure 5.7(d). It has been shown that the octahedral structure with trihydrate of $\text{ZnCl}_3(\text{H}_2\text{O})_3^-$ is more stable than tetrahedral tetrahedral trichloroaqua with two water molecules in the second shell (Pye et al., 2006). The three chloride atoms are in *cis* with each other and with water molecule sharing the same plan. The average angle between the three Cl atoms in this plan, $\angle\text{ClFeCl}$, is 102° , while the angle between two Cl atoms and OH_2 sharing the same plan, $\angle\text{OFeCl}$, is 80° . The angle $\angle\text{ClFeCl}$ has been estimated recently to be around 106° using B3LYP with 6-31G(d), 6-311G(d) and VTZ basis sets (Hill and Schauble, 2008). The complex is deviated for octahedral geometry. The hydrogen atoms of two water molecules in *trans* are separated chloride atoms with Cl–H of 2.75 Å and the third water molecule has Cl–H of 2.82 Å with the other chloride atom. It has been reported that the $\text{Pt}(\text{cisCl}_3 \cdot 3\text{H}_2\text{O})^-$ has a lower energy compared to *trans* (Trazona-Vasquez and Balbuena, 2007). This complex has total binding energy of -1360.8 kcal/mol and the average calculated bond distance for Fe–Cl is 2.33 Å and 2.20 Å for Fe–O. These values are comparable to experimental results reported by Troyanov et al. (in German) with Fe–Cl is 2.33 Å and Fe–O 2.05 Å (Troyanov et al., 1999). In solvation model, the bond distance in this complex is calculated to be 2.37 and 2.12 Å for Fe–Cl and Fe–O, respectively. It seems the PCM solvation model is over estimated the value of Fe–Cl bond distance and underestimate Fe–O as compared to gas-phase calculations. However, the solvation model values are closer to experimental result which reported Fe–Cl to be

2.45 Å and Fe–O is 2.05 Å (Apted et al., 1985). The choice of basis set is critical in determining the value of bond length, and as the basis set increases the estimated value increases. Recently, Hill and Schuble estimated the value Fe–Cl at three basis sets 31G(d), 6-311G(d) and VTZ to be 2.25, 2.25, 2.29 Å, respectively (Hill and Schauble, 2008). Water molecules in the first shell tend to alter the geometry and increase the Fe–Cl bond distance. FeCl₃ without water molecules has a D_{3h} symmetrical structure with Fe–Cl of 2.10 Å and ∠ClFeCl of 120° at MP2(full)/WHsf (Bach et al., 1996).

The distribution curve of ferric chloride calculated from formation constants based on UV-Vis spectrophotometric data showed that at low chloride concentration, the FeCl²⁺ is more dominant, however, as the concentration of Cl increases FeCl₂⁺, FeCl₃ and FeCl₄[−] become more important. In a solution of hydrochloric acid and iron (III), FeCl₄[−] represents less than 50% of ferricchloride based on X-ray diffraction experiment (Luter and Wertz, 1981). In hydrocarbon well acidizing treatment, the formation of [FeCl₄][−] has a detrimental effect on performance of cationic viscoelastic surfactant, which can lead to a loss of viscosity (Teot, 1998). The optimized geometry of gas-phase [FeCl₄.2H₂O][−] and [FeCl₄][−] are shown in Figure 5.8(a,b), respectively. The tetrachloroferrate (tetrahedral) is 13.1 kcal/mol higher in binding energy compared to tetrachlorodiaquoferate. In gas-phase, the average calculated bond distance of Fe–Cl is 2.42 and 2.27 Å for [FeCl₄.2H₂O][−] and [FeCl₄][−], respectively. It seems the gas-phase calculations overestimate the former Fe–Cl value while underestimate the later. The reported experimental value for Fe–Cl distance in [FeCl₄.2H₂O][−] is 2.36 Å (2.42, 2.31, 2.35 × 2 Å) and 2.19 Å in the complex [FeCl₄][−] (Troyanov et al., 1999). The Fe–O bond distance calculated at B3LYP/6-311++g**(O,H)/SDD(Cl) is 2.15 Å which is larger than the experimental value (2.06 Å) (Troyanov et al., 1999). The ∠ClFeCl angle is 109° for the complex [FeCl₄][−], and 92° for [FeCl₄.2H₂O][−]. The first value is similar to previous results reported at lower basis set (Hill and Schauble, 2008). The solvation model gives 2.42 Å for Fe–Cl and 2.10 Å for Fe–O. Each water molecule in the complex of [FeCl₄.2H₂O][−] has in average Cl–H distance of 2.88 Å with two Cl atoms.

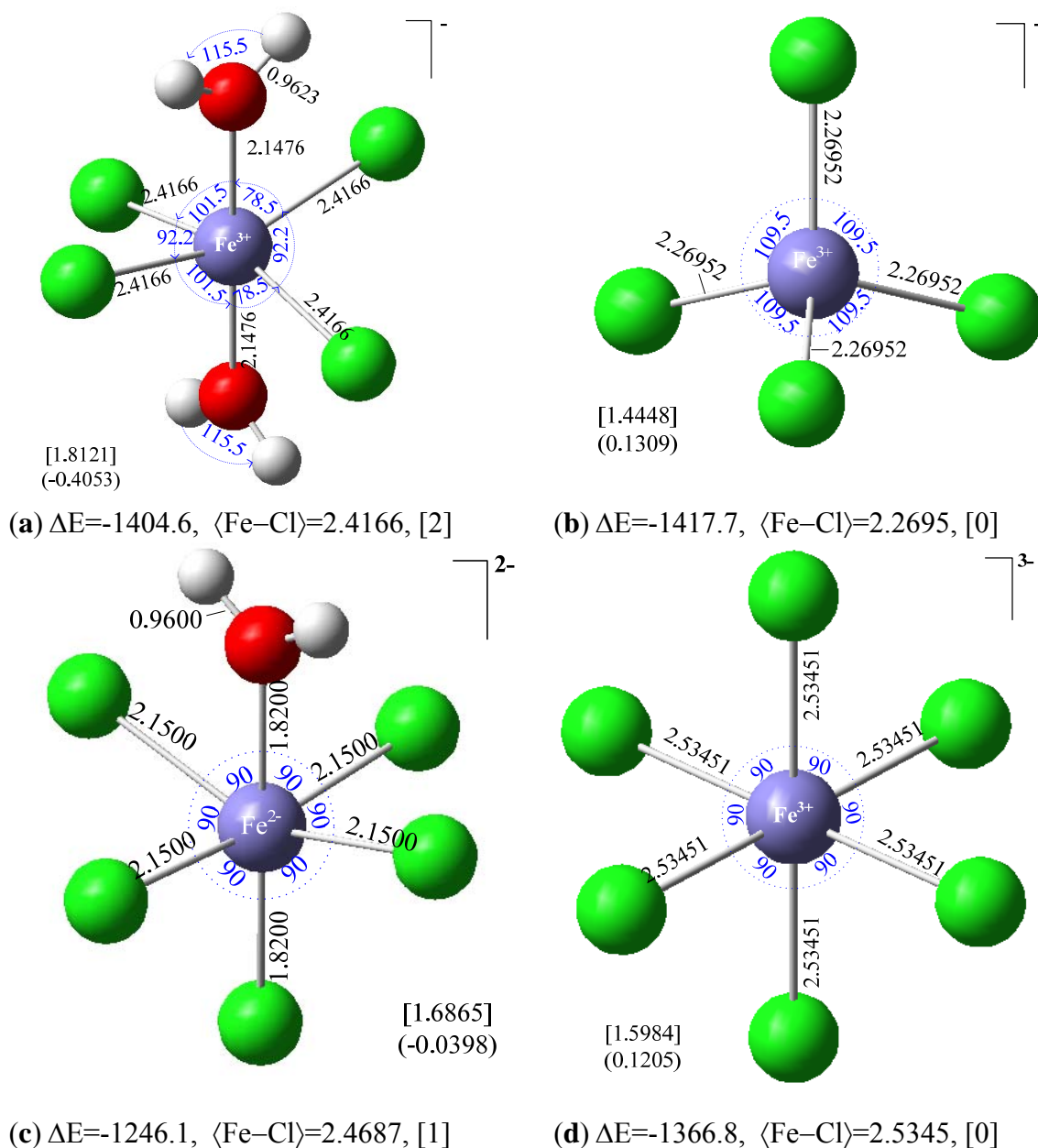


Figure 5.8: Optimized structures with geometrical parameters from *ab initio* calculations using B3LYP/6-311g** (H,O) and B3LYP/SDD (Fe) for ferricchloride complexes: (a) $[\text{FeCl}_4 \cdot 2\text{H}_2\text{O}]^-$, (b) $[\text{FeCl}_4]^-$, (c) $[\text{FeCl}_5 \cdot \text{H}_2\text{O}]^{2-}$, (d) $[\text{FeCl}_6]^{3-}$. Shown in these diagrams are bond length (Å), bond angles ($^\circ$), binding energy (kcal mol^{-1}) and Fe-charge (electron unit). Values in square brackets are APT charges and in parentheses for Mulliken charges both with hydrogen summed into heavy atoms. Color code for atoms is: red for O, slate blue for Fe, and light gray for H.

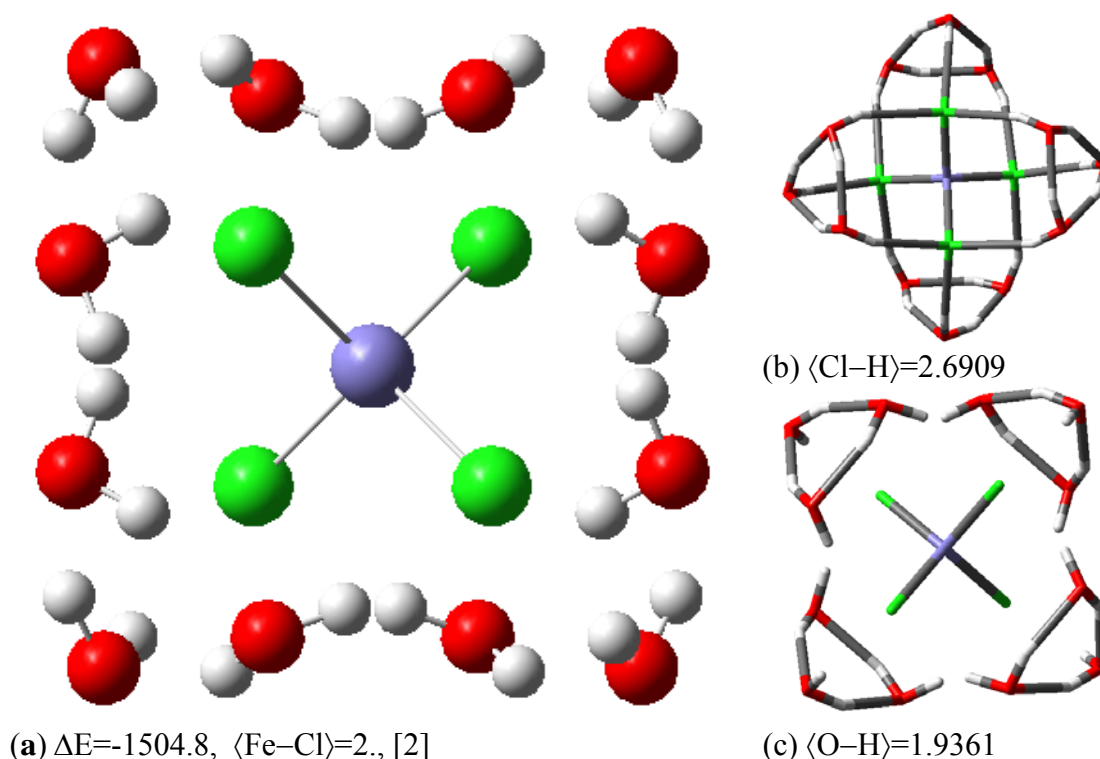


Figure 5.9: Optimized structures with geometrical parameters from *ab initio* calculations using B3LYP/6-311g** (H,O) and B3LYP/SDD (Fe, Cl) for ferricchloride complexes: (a) tetrachloroferrate $[\text{FeCl}_4 \cdot 12\text{H}_2\text{O}]^-$, (b) shows hydrogen and Cl-H bonds, (c) shows hydrogen bonds only. Shown in these diagrams are bond length (\AA), bond angles ($^\circ$), binding energy (kcal mol^{-1}) and Fe-charge (electron unit). Values in square brackets are APT charges and in parentheses for Mulliken charges both with hydrogen summed into heavy atoms. Color code for atoms is: red for O, slate blue for Fe, and light gray for H.

Figure 5.9 shows the FeCl_4^- with 12 water molecules surrounding the complex. This optimized structure has a total binding energy of -1504.8 kcal/mol , which is 87.1 kcal/mol larger than FeCl_4^- . The structure has a very interesting arrangement of water molecules around the complex, where each chloride atom is attached to three hydrogen atoms from three different water molecules with equal Cl-H bond distance of 2.69 \AA . water molecules form four tetramers, Figure 5.9(c), around each chloride atom with hydrogen bond equal to 1.94 \AA . The bond distance Fe-Cl is 2.28 \AA which is close to value experimental value in solution (2.25 \AA) (Magini and Radnai, 1979).

Table 5.3: Calculated average bond length, equilibrium binding energy (gas-phase and water solvent) for $[\text{FeCl}_x(\text{H}_2\text{O})_n]^{3-x}$, $\Delta E_i = E_{\text{complex}} - (E_{\text{Fe}} + nE_{\text{H}_2\text{O}} + xE_{\text{Cl}})$ at $T=298.15$ K and $p=1$ atm using B3LYP/6-311g**/SDD.

Complex	$n\text{H}_2\text{O}$	$\Delta E_{i,\text{gas}}$ (kcal mol ⁻¹)	$\Delta E_{i,\text{solvent}}$ (kcal mol ⁻¹)	$\langle \text{Fe-O} \rangle$ (Å) [†]	$\langle \text{Fe-Cl} \rangle$ (Å) [†]
$[\text{Fe}(\text{H}_2\text{O})_6]^{3+}$	6	-653.3	-43.0	2.07	—
$[\text{FeCl}(\text{H}_2\text{O})_5]^{2+}$	5	-987.9	-73.0	2.12	2.20
$[\text{Fe } \textit{cis}\text{Cl}_2(\text{H}_2\text{O})_4]^{2+}$	4	-1219.3	—	2.18	2.25
$[\text{Fe } \textit{trans}\text{Cl}_2(\text{H}_2\text{O})_4]^{2+}$	4	-1223.8	-95.8	2.12	2.28
$[\text{FeCl}_3(\text{H}_2\text{O})_3]^0$	3	-1360.8	-114.3	2.20	2.33
$[\text{FeCl}_4(\text{H}_2\text{O})_2]^-$	2	-1404.6	-125.9	2.15	2.42
$[\text{FeCl}_5(\text{H}_2\text{O})]^{2-}$	1	-1366.8	-133.9	2.21	2.47
$[\text{FeCl}_6]^{3-}$	0	-1246.1	-138.7	—	2.53

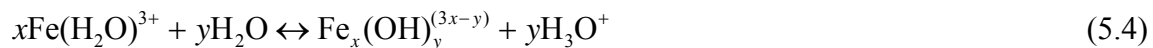
[†] average values calculated in gas-phase

As the concentration of acid increases, the speciation curve suggests that higher anionic complexes of ferric chloride to be formed. For $n=5$, the optimized octahedral structure of five Cl atoms and one water molecule has 90° between atoms and central iron ion. The total binding energy is calculated to be -1366.8 kcal/mol in gas-phase and -133.9 kcal/mol in implicit (PCM) water solution. The absolute value of this energy is lower than FeCl_4^- when comparing the gas-phase results, however, higher for solution case. In the polarizable continuum solvation model (PCM), the calculations assumed a cavity of small interlocking water spheres around the atoms of ferricchloride which represent an implicit effect of water molecules. In general, gas-phase complexes cannot give reliable energies of the real aqueous system. Much of the solvation effect in the aqueous phase can be accounted by simply including the inner shell explicit water molecules as we have seen in Figure 5.9. The Fe–Cl bond distance is 2.47 Å and 2.44 Å in gas-phase and water solution, respectively. Due to covalent bonding with hydrogen from water molecules, the calculated Fe–Cl in solution is larger. The single water molecule in this complex has Cl–H bonding distance of 2.66 Å in gas-phase, however, the value increase to 2.91 Å in solution. The central iron atom in the complex has shorter bond distance with oxygen compared to chloride. The calculated Fe–O length is found to be 2.21 Å

and 2.17 Å in gas-phase and solution, respectively. As we have seen, the agreement between gas-phase calculated results and values from aqueous model is quite poor. A large part of this discrepancy reflects the inner-sphere solvation of the complex by water molecules. For $n=6$, ferric ion is connected to six chloride atoms forming trianionic complex with O_h symmetry. The calculated Fe–Cl bond distance is 2.53 and 2.48 Å in gas-phase and solution, respectively. These values are the range reported by Hill and Schauble at the same theory level and different basis sets (2.51, 2.52, and 2.55 Å, at 6-31G(d), 6-311G(d) and VTZ, respectively) (Hill and Schauble, 2008). The binding energy is found to be larger than FeCl_4^- in solution, but lower in gas-phase as shown in Table 5.3.

5.4.5 $\text{Fe}^{x+}(\text{OH})_x(6-x)\text{H}_2\text{O}$

Hydrolysis is an important process in oilfield industry because most of the Earth rock-forming minerals are salt of weak acid and strong base (Faure, 1998). The anion of these minerals (for example CO_3^{2-} in CaCO_3) split water molecules in order to form the weak parental acid and thereby cause hydroxyl ion (OH^-) concentration of the solution to increase. The dissociation of salts into ions and subsequently hydrolysis of the ions takes place very rapidly, which means these reactions are usually at equilibrium. In stimulation process with high concentration of HCl injected in the reservoir to clean near wellbore area and open new channels for flow, the precipitation of iron hydroxide are critical. It has been shown that ferric chloride start to precipitate at pH~1 and nearly complete at pH~2 at room temperature (Taylor et al., 1999). As the temperature increased, Fe(III) become significantly less soluble in spent acid, and hence the precipitation of $\text{Fe}(\text{OH})_3$ is potentially more damaging to near wellbore area and can reduce reservoir permeability. The hydrolysis of iron (III) ions in aqueous solution has received considerable attention through the years. Ferric ion undergoes appreciable hydrolysis in aqueous solutions according to the reaction:



As the solution pH is increased, the ferric state is stabilized in a thermodynamic sense relative to the ferrous state because of the higher affinity of Fe^{3+} for the hydroxide ion relative to Fe^{2+} . Hydrolysis of ferric ion begins at about pH~1 with the formation of octahedral complex $[\text{Fe}(\text{H}_2\text{O})_5\text{OH}]^{2+}$, which is yellow due to charge transfer absorption band between ultraviolet and visible. Thermodynamic data on Fe (III) hydrolysis have been reviewed and compiled by many authors (Baes and Mesmer, 1976; Smith and Martell, 1976). Equilibrium data for hydrolysis reaction of Fe (III) are given in Table B.5. The species Fe^{3+} , $\text{Fe}(\text{OH})^{2+}$, $[\text{Fe}(\text{OH})_2]^+$, $[\text{Fe}_2(\text{OH})_2]^{4+}$ are well characterized. Whereas the species $[\text{Fe}_3(\text{OH})_4]^{5+}$ was reported in one study (Baes and Mesmer, 1976). The claim for $[\text{Fe}_{12}(\text{OH})_{34}]^{2+}$ by Ciavatta and Grimaldi (Ciavatta and Grimaldi, 1975) has been refuted (Dousma and Bruyn, 1976). The hydrolysis of inorganic Fe(III) solution consists of several steps as proposed by Flynn (Flynn, 1984): (1) formation of low-molecular-weight species such as $\text{Fe}(\text{OH})^{2+}$; (2) formation of a red cationic cluster once reacts with base; (3) aging with eventual conversion to oxide phases especially at high temperature; and (4) precipitation of oxide phases directly from low-molecular-weight precursors. Figure 5.10(b) shows the optimized structure of triaquoferric hydroxide at B3LYP/ SDD(Fe)/ 6-311++g**(H,O). The three hydroxyle groups are in *cis* with each other and two water molecules are in *trans*. One water molecules has moved to the second shell to form hydrogen bonding with two hydroxyl groups compared to the initial structure with all oxygen atoms are connected to Fe(III) ion. The angle $\angle\text{OFeO}$ for hydroxyl groups is 120° . The average hydrogen bond O–H is 1.97 Å which has influence on the Fe–O bond distance. The Fe–OH₂ is 2.26 Å in average, while Fe–OH ranges between 1.82–1.91 Å which makes the average Fe–O to be 2.03 Å. The total binding energy is calculated to be -1436.5 kcal/mol which is 18.8 kcal/mol larger than FeCl_4^- . So, which anion (OH^- , Cl^-) will form a complex with Fe(III) first, and is it exchangeable. Thermodynamic properties is fairly enough to predict how the complexation of ferric and ferrous ion with chloride and hydroxide in solution, however, kinetics calculations is needed to understand the path of reaction, rate and which

complex is faster than the other. This part of calculation will be carried out in the next phase of this research project.

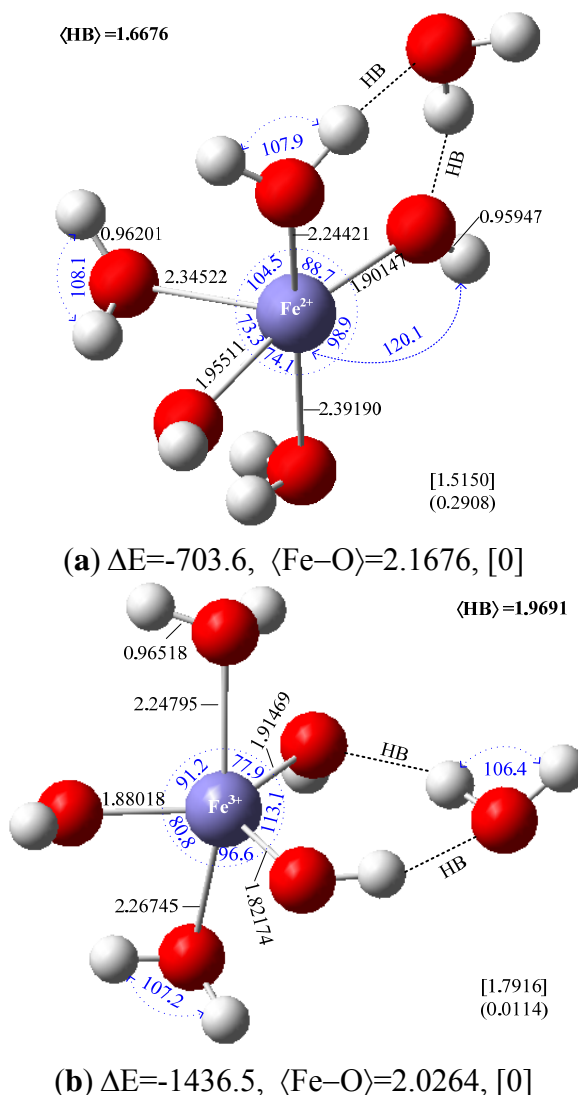


Figure 5.10: Optimized structures with geometrical parameters from DFT calculations using B3LYP/6-311g** (H,O) and B3LYP/SDD (Fe) for iron-hydroxide: (a) $[\text{Fe}(\text{OH})_2.4\text{H}_2\text{O}]$, (b) $[\text{Fe}(\text{OH})_3.3\text{H}_2\text{O}]$. Shown in these diagrams are bond length (\AA), bond angles ($^\circ$), binding energy (kcal mol^{-1}) and Fe-charge (electron unit). Values in square brackets are APT charges and in parentheses for Mulliken charges both with hydrogen summed into heavy atoms. Color code for atoms is: red for O, slate blue for Fe, and light gray for H.

Fe(II) forms white hydroxide precipitation $\text{Fe}(\text{OH})_2$ at high pH (≥ 6) value and then is rapidly oxidized in air turning red brown and eventually giving $\text{Fe}_2\text{O}_3 \cdot n\text{H}_2\text{O}$. However, if hydrogen sulfide is present, then Fe(II) can precipitate as iron (II) sulfide (Taylor et al., 1999). The mass balance of Fe(II) and OH^- ions in water solution including all possible hydroxides is giving by: $\text{Fe(II)}_{\text{total}} = [\text{Fe}^{2+}] + [\text{FeOH}]^+ + [\text{Fe}(\text{OH})_2]^0 + [\text{Fe}(\text{OH})_3]^-$, which can be rearranged to get the speciation equation as:

$$\text{Fe(II)}_{aq} = [\text{Fe}^{2+}] \left(\frac{10^{-10.10}}{[\text{H}^+]} + \frac{10^{-20.51}}{[\text{H}^+]^2} + \frac{10^{-29.41}}{[\text{H}^+]^3} \right) \quad (5.5)$$

The ratio of Fe(II) to Fe(III) in spent acid (i.e. after reaction) of matrix acidizing treatment is about 5 to 1 (Crowe, 1985). In pickling treatment of seawater injection well, the ratio is 0.7–2 to 1, while higher ratio of 2–8 to 1 has been observed in acid treatment after pickling (Taylor et al., 1999). Ferrous hydroxide does not start precipitation until pH~6 (Taylor et al., 1999) which is the same pH value $\text{Fe}(\text{CO}_3)$, $[\text{Fe}(\text{CO}_3)_2]^{2-}$ complexes starts to form (Santana-Casiano et al., 2005). In HCl solution, ferrous speciation is dominated by the $[\text{Fe}(\text{H}_2\text{O})_6]^{2+}$ complex as shown experimentally and the mono-chloro ferrous complex, $[\text{FeCl}(\text{H}_2\text{O})_5]^+$, comprises around 6% of the total ferrous iron at high Cl^- concentration (>100 mM) (Welch et al., 2003). Figure 5.10(a) shows optimized structure of ferrous hydroxide, $[\text{Fe}(\text{OH})_2 \cdot 4\text{H}_2\text{O}]$, which has a total binding energy of -703.6 kcal/mol. The initial structure was constructed by replacing two water molecules in octahedral geometry of hexaaquoferrous by two hydroxide groups. One water molecule moves from the first shell to the second shell in the final optimized structure leaving two hydroxides and three water molecules in the first shell. The average calculated Fe–O bond distance in the first shell is 2.17 Å, with hydroxides have shorter value of 1.93 Å, which can be explained by the fact that OH^- is an excellent π donor to metal. The angle between the two hydroxide groups, $\angle\text{OFeO}$, is found to be 170° . The water molecule in the second shell has Fe–O distance of 3.64 Å and forms hydrogen bonding with hydroxide and 1-water molecule. The second hydroxide has $\angle\text{OFeO}$ angle of 74° with two water molecules and forms hydrogen bonding with both of them. The average HB in the complex is 1.67 Å.

5.4.6 $H_2S(H_2O)_n$

Ab initio and DFT calculations are implemented to have more insight into the structures and corresponding energies of H_2S clusters particularly in presence of strong acid such as HCl. The literature of H_2S chemistry and related dissolved sulfur compounds, and iron sulfide minerals is widely scattered in many disciplines. Sulfur present in hydrocarbon reservoir as sulfate (SO_3^{2-}), hydrogen sulfide (H_2S), or bisulfide (HS^-). H_2S is soluble in acid and increasing temperature or salinity of water were found to decrease the solubility of H_2S (Morse et al., 1987). Hydrogen sulfide dissociates in solution to bisulfate and proton ion ($H_2S \rightarrow H^+ + HS^-$). During acidizing treatment, control of iron and sulfur precipitation is an important requirement. Therefore, hydrogen sulfide scavenger such as aliphatic acid or hydroxyalkyl triazine is added to the stimulation fluid. The presence of hydrogen sulfide in sour-carbonate reservoir is a challenge facing stimulation treatment and it can cause severe safety and operational problems (Nasr-El-Din, 2007). Therefore, hydrogen sulfide scavenger is added to the acid system when stimulating sour wells to prevent reprecipitation of iron sulfide and elemental sulfur. The interactions between H_2S scavenger and other molecules in solution are not clearly identified or even well understood. Despite the vast variety of experimental studies, the microscopic details of viscoelastic surfactant and their interaction with hydrogen sulfide, bisulfate or H_2S scavenger are not understood in detail yet. From both a fundamental and practical prospective it is therefore important to understand the relation between structure and chemistry of the surfactants and the dynamic rheological behavior and flow of the macroscopic fluid in porous media. Our current molecular-scale understanding of ion interaction, such as H_3O^+ , with water solvent molecules is established. The most extensive set of *ab initio* calculations of hydration energies for the hydronium water cluster system was reported (Jiang et al., 2000) and yielded binding enthalpies for $H_3O^+(H_2O)_{4-7}$ in close agreement with experimental HPMS results (Meot-Ner and Speller, 1986). To the best of our knowledge, the *ab initio* work dedicated to the calculation of solvent binding of H_2S , HS^- and H_3S^+ are limited. HF/4-31G level theory to calculate hydration energies for the $H_3S^+(H_2S)_{1-5}$ cluster series (Yamabe et al., 1985).

Recently, the structures and energetic trends associated with water clusters containing water- and hydrogen sulfide-proton clusters with the general form: $A^+(H_2O)_m(H_2S)_n + (H_2S) + (H_2O) \leftrightarrow A^+(H_2O)_{m+1}(H_2S)_{n+1}$ where A^+ is H_3O^+ , H_3S^+ or and $m + n$ are reported (Lemke and Seward, 2008). Also, they considered the competitive exchange of H_2O and H_2S in the same system. In this part of study, we considered the water-hydrogen sulfide and hydronium-hydrogen sulfide clusters of the general form $H_2S(H_2O)_n$ and $H_3O^+(H_2S)_n$, respectively, with $n=1-8$. For the cluster $H_2S(H_2O)_n$ with $n=1$, the optimized molecular structure at B3YLP/6-311++g** has a total binding energy of -1.9 kcal/mol (Figure 5.11(a)). This energy is lower than $H_2O(H_2O)$ cluster which has a total binding energy of -4.1 kcal/mol. This suggests H_2S has lower solubility in water compared to water-water system. The SH-O bond is 2.15 Å which is longer than hydrogen bond (OH-O) in $H_2O(H_2O)$ cluster as shown in Table 5.4. For $n=2$, the cluster forms trimer with $\angle HOH$ of 99 ° and $\angle HSH$ of 75° and total binding energy of -8.5 kcal/mol. This increment in energy of the cluster is due to hydrogen bonding between water molecules, $\langle OH-O \rangle$, which has an average bond length of 1.91 Å. As the number of water molecules increases in the cluster, the binding energy increases linearly as shown in Figure 5.12. Clusters with $n>2$ are forming cyclic structures which is the most stable as we have seen in Chapter IV (for pure water). For $n=8$, the structure is cubic with total binding energy of -63.9 kcal/mol and average hydrogen bonding of 1.82 Å. Similarly, we have also carried out calculation for H_2S in acidic medium. In Appendix B, the optimized geometrical structures of the cluster $H_3O^+(H_2S)_n$, ($n=1-8$) are presented. Recently, Lemake and Seward have shown similar calculations with $n=1-5$ at MP2/6-31G(d) (Lemke and Seward, 2008). For $n=1$, the cluster of $H_3O^+(H_2S)$ has a total binding energy of -217.8 kcal/mol. This high energy explains the solubility of H_2S in acidic solutions. The average bond between water-hydrogen and sulfur atoms, $\langle OH-S \rangle$, is 1.70 Å, which is shorter than hydrogen bonding between water dimer (1.93 Å). As the number of H_2S molecules increases, the total binding energy increases too but not in a linear manner as we observed for $H_2O(H_2O)_n$ and $H_2S(H_2O)_n$ clusters.

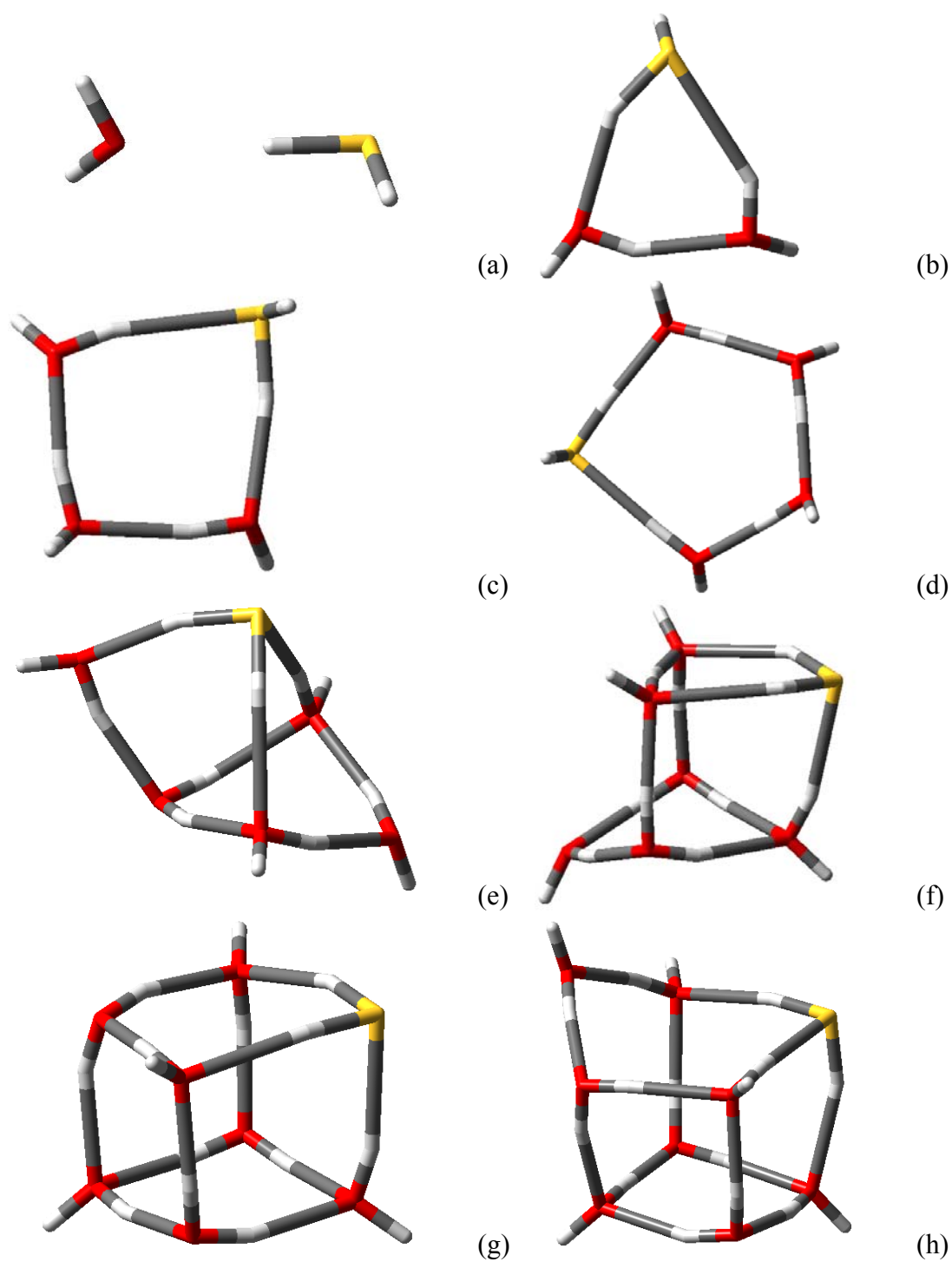


Figure 5.11: Optimized geometrical structure in gas-phase of hydrated hydrogen sulfide using B3LYP/6-311++g**. (a) $\text{H}_2\text{S}(\text{H}_2\text{O})$, (b) $\text{H}_2\text{S}(\text{H}_2\text{O})_2$, (c) $\text{H}_2\text{S}(\text{H}_2\text{O})_3$, (d) $\text{H}_2\text{S}(\text{H}_2\text{O})_4$, (e) $\text{H}_2\text{S}(\text{H}_2\text{O})_5$, (f) $\text{H}_2\text{S}(\text{H}_2\text{O})_6$, (g) $\text{H}_2\text{S}(\text{H}_2\text{O})_7$, and (h) $\text{H}_2\text{S}(\text{H}_2\text{O})_8$. Color code: red for O, light gray for H and yellow for S.

Table 5.4: Binding energy and geometrical properties of $\text{H}_2\text{O}(\text{H}_2\text{O})_n$, $\text{H}_2\text{S}(\text{H}_2\text{O})_n$ and $\text{H}_3\text{O}^+(\text{H}_2\text{S})_n$

n	$\text{H}_2\text{O}(\text{H}_2\text{O})_n$		$\text{H}_2\text{S}(\text{H}_2\text{O})_n$				$\text{H}_3\text{O}^+(\text{H}_2\text{S})_n$		
	ΔE_i (kcal/mol)	$\langle \text{HB} \rangle$ (Å)	ΔE_i (kcal/mol)	$\langle \text{HB} \rangle$ (Å)	$\langle \text{SH-O} \rangle$ (Å)	$\langle \text{OH-S} \rangle$ (Å)	ΔE_i (kcal/mol)	$\langle \text{OH-S} \rangle$ (Å)	$\langle \text{S-H} \rangle$ (Å)
1	-4.1	1.93	-1.9	—	2.15	—	-217.8	1.70	—
2	-13.5	1.90	-8.5	1.91	2.12	2.54	-231.8	1.98	—
3	-25.0	1.77	-17.9	1.80	1.96	2.39	-243.8	2.08	2.76
4	-33.3	1.74	-25.8	1.77	1.92	2.36	-248.5	2.08	2.73
5	-39.3	1.95	-31.6	1.90	2.20	2.31	-251.7	2.08	2.79
6	-49.9	1.89	-43.4	1.87	2.33	2.36	-255.0	2.07	2.63
7	-63.7	1.82	-55.3	1.86	2.17	2.32	-257.4	2.07	2.61
8	-72.7	1.85	-63.9	1.82	2.14	2.33	-261.6	2.07	2.79

The binding energy is logarithmic in behavior as a function of H_2S molecules: $\Delta E_{i,\text{H}_3\text{O}^+\text{H}_2\text{S}} = 21 \ln(n) - 218.5$ ($R^2=0.99$).

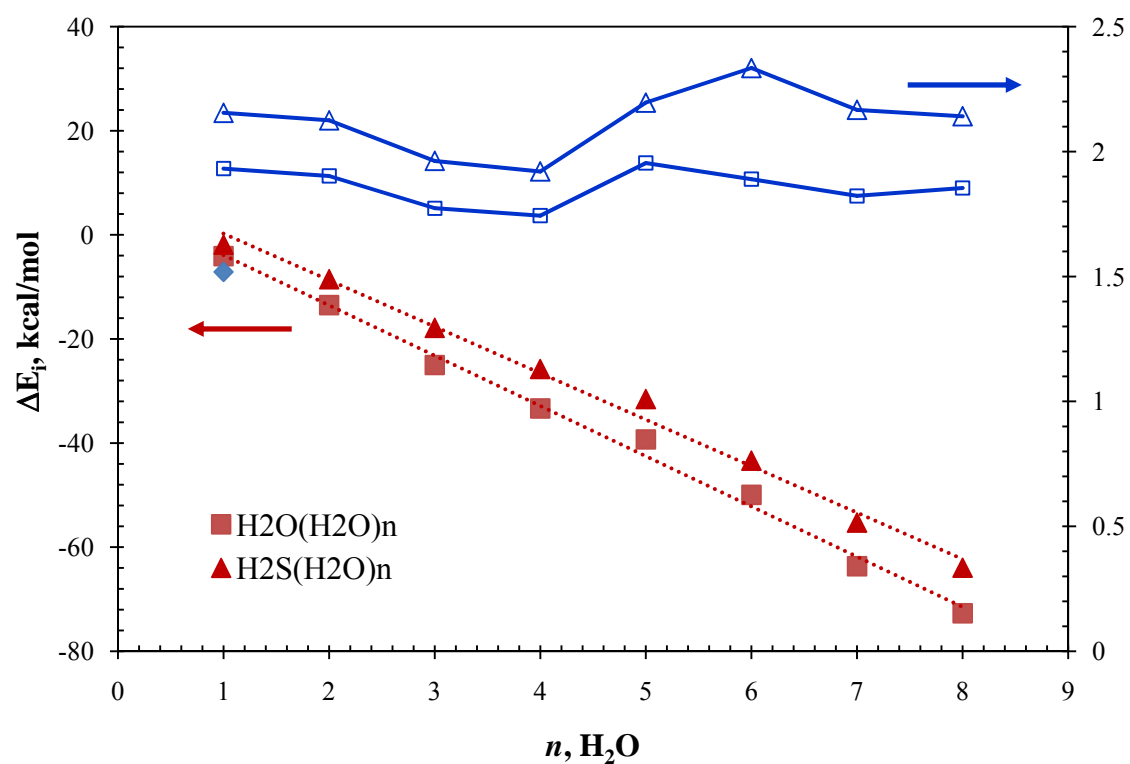


Figure 5.12: Binding energy and average bond length of $\text{H}_2\text{O}(\text{H}_2\text{O})_n$ and $\text{H}_2\text{S}(\text{H}_2\text{O})_n$ ($n=1-8$) clusters. (■) for $w\text{-H}_2\text{O}$ energy (left-y-axis) (□) for $\langle \text{HB} \rangle$ of $w\text{-H}_2\text{O}$ cluster (right-y-axis), (▲) for $w\text{-H}_2\text{S}$ energy (left-y-axis) and (△) for $\langle \text{SH-O} \rangle$ of $w\text{-H}_2\text{O}$ cluster (right-y-axis). $\Delta E_{w\text{-H}_2\text{O}} = -9.666(n) + 5.81$, ($R^2=0.994$) and $\Delta E_{w\text{-H}_2\text{S}} = -8.9352(n) + 9.17$, ($R^2=0.992$).

5.4.7 Fe-S Cluster

Iron–sulfur clusters are important chemical species in oilfield chemistry. At least seven different solids consisting only of iron and sulfur are known to occur naturally at reservoir temperatures (Table B2). There has been number of studies on the biological prospective of Fe–S systems which provide fundamental information about the structural, electronic, magnetic properties, and chemical bonding (Noodlemana et al., 1995; Ogino et al., 1998). A large number of iron–sulfur clusters and complexes have been synthesized and characterized, forming a large class of organometallic chemistry. There have also been extensive theoretical efforts devoted to iron–sulfur complexes. However, there have been relatively few studies on the Fe–S clusters; even the electronic structure of the simplest FeS diatomic molecule is still not well understood. We are interested in studying the electronic structure and chemical bonding of iron–sulfur systems in the gas phase using DFT. In this part, we focus on a series of relatively simple $\text{FeS}_2 \cdot 4\text{H}_2\text{O}$ clusters, and the monoiron sulfur clusters FeS_n^- ($n = 1-6$).

Metastable iron sulfides have been widely identified in oilfield industry with black sulfide-rich zone that tend to dissolve with HCl to produce H_2S gas. The addition of HCl to Fe–S will act to release H_2S . The $\text{p}K_{1,\text{H}_2\text{S}}$ is close to 7 which means that H_2S dominates the system at acid pH values and HS^- is the dominant species in alkaline solutions (Rickard and Luther, 2007). $\text{p}K_{2,\text{H}_2\text{S}}$ is estimated to be around (Schoonena and Barnes, 1988). This means that the aqueous sulfide ion, S^{2-} , has no significant activity in natural aqueous systems. The FeS cluster stoichiometry appears to range from Fe_2S_2 to $\text{Fe}_{150}\text{S}_{150}$ (Rickard and Luther, 2007). There are number of Fe–S forms that can be found in hydrocarbon reservoir including amorphous precipitates ($\text{Fe}_{\sim 1}\text{S}$), mackinawite ($\text{Fe}_{0.87-1.1}\text{S}$), and greigite ($\text{Fe}_{0.75}\text{S}$). They form a class distinct from HCl-insoluble iron sulfides such as pyrite (FeS_2). Pyrite, FeS_2 , is by far the most abundant sulfide mineral occurring in most types of geological formations. Pyrite and marcasite do not nucleate and precipitate directly from solution, but result from successive sulfidation of a series of metastable Fe(II) sulfides. The overall, FeS_2 -forming reaction involves polysulfides,

thiosulfate, and polythionate as shown in equations (B1-B3). Marcasite forms below about pH~5, whereas pyrite is favored at pH >6. Whenever sulfur is present and conditions are sufficiently anaerobic to cause sulfate reduction, Fe(II) precipitate almost quantitatively as sulfides. In contrast, Fe(III) forms strong complexes with most ligands that might be available in reservoir (Rickard and Luther, 2007). Thermodynamic data for iron aqueous species and solids at 25°C are given in Appendix B. There have been numerous experimental and theoretical reports on the monoiron–sulfur clusters in the literature. Schröder et al. have reported a detailed study on the structures of cationic, anionic, and neutral FeS₂ using both mass spectrometric methods and density functional theory (DFT) calculations (Schröder et al., 2003). Iron-sulfur complexes have been extensively studied because of their relationship to proteins systems. Optimized structures of Fe–S are shown in Figure 5.13. Two structures are possible for FeS₂, a bent structure without S–S bonding or a triangular structure with a S–S bond. The recent work by Schröder et al. reported an extensive experimental and theoretical investigation on the structures of FeS₂[−], FeS₂⁺, and FeS₂ (Schröder et al., 2003). Their DFT calculation showed that FeS₂[−] has a bent structure (A₁) with a ∠S–Fe–S angle of 167° and an Fe–S bond length of 2.12 Å. Their predicted neutral FeS₂ also has a bent structure, but it has a large bond angle change (∠S–Fe–S = 115°), as well as a bond length change (Fe–S = 2.03 Å).

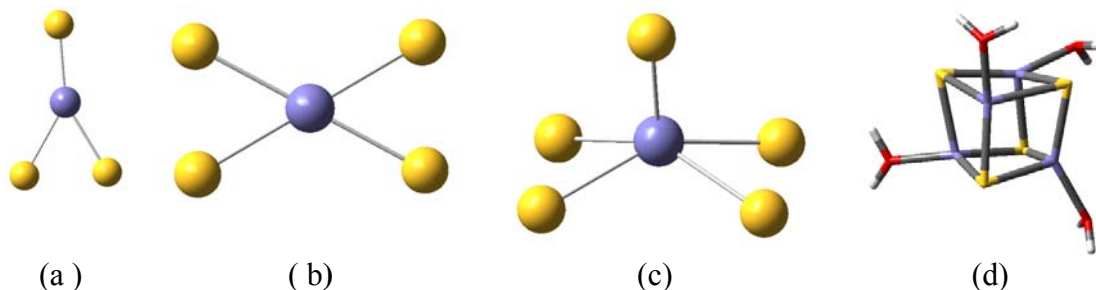


Figure 5.13: Optimized structure of Fe–S. (a) FeS₃, (b) FeS₄, (c) FeS₅, and (d) Fe₄S₄.4H₂O.

CHAPTER VI
***AB INITIO* AND MOLECULAR SIMULATION STUDIES OF INTERACTION**
BETWEEN INORGANIC COUNTERIONS AND ANIONIC VISCOELASTIC
SURFACTANTS

Everything should be made as simple as possible, but not simpler
—Albert Einstein

Viscoelastic surfactants have a wide range of applications in the oilfield industry, including acid fracturing and matrix acidizing. A problem associated with acidizing is the tendency of the live acid or spend acid to form sludge which can reduce the effectiveness of the treatment or plug the formation or production equipments. Formation of sludge results from precipitation of insoluble materials upon interaction with acid. Presence of cations such as ferric will enhance the aggregation process. Emulsion and corrosion are other problems associated with well acidizing and it can impact flow to the wellbore. It has been reported that anionic surfactants can address some of the problems associated with well stimulation and align themselves due to intermolecular attraction or non-covalent bonds to form wormlike micelles. The micelles can be absorbed on the formation or further interact to form a network exhibiting elastic behavior dependent on type of rocks. This increase in viscoelasticity helps in many cases to control fluid placement while acidizing multiple zones with variation in permeability and it also has sufficient properties to suspend and carry the proppant into the fractured zone. Several previous experimental studies highlighted the significant role of counterions in determining the apparent properties of aqueous solutions that contained viscoelastic surfactants. Wormlike micelles are formed by aggregation of amphiphiles. Presence of co-surfactant, additives, salts or appropriate counterions helps promote growth of such micelles. The effect of counterions can be detrimental on the properties of the whole system. Understanding how macroscopic properties depend on intermolecular interactions for complex fluids is the main focus of this study. Density functional theory and molecular dynamics simulations are employed to better understand

how organic and inorganic counterions can impact physical properties of viscoelastic surfactants and hence their functionality in carbonate reservoirs. Anionic surfactants with different head groups include acetic acid (AA), potassium butanoate (PB) and sodium butane-1-sulfonate (S1BS), together with their counterions are simulated over a wide range of parameters. Competition between mono-, di- and trivalent counterions was studied in the gas phase of three anionic surfactant head groups with organic counterions (sodium salicylate, NaSal, and sodium hydroxynaphthalene carboxylate, NaHNC) and inorganic counterions (Na^+ , Mg^{2+} , Ca^{2+} , Fe^{2+} and Fe^{3+}). Binding energy and thermodynamic properties show that trivalent counterions are more strongly bonded than di- and monovalent ones. The results give important insight into the links between molecular structure of surfactant and ions present in solution, which will help in developing more systematic procedures for treatment optimization, and better design of more efficient/effective viscoelastic diverting systems.

6.1 Introduction

The study of viscoelastic surfactant properties in the gas phase and water solution is very important from theoretical and practical points of view. At concentrations above the critical micelle concentration (CMC), surfactant molecules dissolved in aqueous solution assemble into colloidal aggregates which vary in shape and size depending on the system conditions. One of the micelle structures in solution that has wide applications in oilfield industry is wormlike micelles (WLM), also known as cylindrical, rodlike or threadlike micelles. The so called soap-type anionic surfactants such as potassium oleate are proved to be effective drag-reducing agents with good mechanical stability (Savins, 1968). Anionic surfactants can be added to hydratable polysaccharide in hydraulic fracturing treatment to adequately transport the proppant from the surface to the fracture (Carman, 2008). It has advantages over cationic surfactant in terms of cost and easiness of preparation. In most cases, it can be prepared at the wellsite by neutralizing the fatty acid with sodium hydroxide, and then pumping the solution into well. The maximum reported temperature this type of surfactant to be stable at is around 54°C , which is a main

drawback considering that the reservoir temperature can be as high as 100°C. Also, they have the tendency to precipitate in presence of di- and trivalent counterions (i.e. opposite charge metal). Anionic surfactants have a negative charge on the head group (HG) when they ionize in aqueous solution. The HG can be carboxylate ($-\text{COO}^-$), sulphate ($-\text{OSO}_3^-$), sulphonate ($-\text{SO}_3^-$), phosphate ($-\text{OPO}_3^{2-}$), or a phosphonate ($-\text{PO}_3^{2-}$). The tail on the other hand, can have a hydrocarbon chain with C18 to C22 with no double bond as in the case of Stearic acid; single double bond as in Oleic and Erucic acids or more double bonds as in Linolenic acids. In oilfield industry, surfactants used are mainly dissolved in brine water which has high concentration of metal ions most of the time. The anionic type of surfactant tends to interact with mono- and multivalent metal ions such as Zn^{2+} , Mn^{2+} , Mn^{3+} , Al^{3+} , Ca^{2+} , Mg^{2+} , or Na^+ that are usually present at low concentration ($\sim < 90$ ppm) in this water. The concentration of metal ions can reached 9,000 ppm in underground water, and more than 14,000 ppm if the acid was injected for stimulation treatment (Nasr-El-Din et al., 2006), which means higher probability for different aggregations with different metal ions.

In stimulation processes, hydrochloric acid is diluted in water and all other additives including viscoelastic surfactant are added to the solution. Before interaction with the reservoir rock (assuming carbonate formation), the pH is nearly zero (depends on concentration). Once the acid reacts with the rock, calcium or magnesium chloride (CaCl_2 , MgCl_2) with CO_2 are produced and hence the pH of solution will increase to nearly 4.0. At lower pH, hydrolysis of metal ions is negligible but complexation with chloride ion is crucially important, and at high pH, the surfactants will aggregate to form micelles and enhance viscosity. Micellization in absence of counterion could occur because of competition between the tails which provide a driving form for aggregation and the electrostatic or steric repulsion between the HGs. The interaction between anionic surfactant and counterion was studied experimentally by a number of authors (Vlachy et al., 2008; Jian-xiao et al., 2006). However, to our knowledge, we are the first group to use first principle calculations to study different molecular architectures to

better characterize the nature of interaction between anionic HG and selected counterions that are commonly present in hydrocarbon reservoirs.

There is much less known about the ability of anionic surfactants to form micelles and many studies have focused on precipitation, thermodynamics and ion interaction of sodium dodecyl sulfate (SDS) as their surfactant of choice. (Missel et al., 1980; Missel et al., 1989; Rathman and Scamehorn, 1987) Anionic surfactant offers advantage over their cationic counterpart especially in enhanced oil recovery (EOR) applications. (Maitland, 2000) The aim of this work is to gain a deeper insight through quantum computations into the structural and energetic properties of anionic surfactant head groups (HGs) in gas phase and in very diluted aqueous solutions, where only solute–solvent interactions are relevant. The information obtained may serve to understand the electronic origin of the factors that determine the properties of these simple molecules, and to get insights into the more complex ones in which the anionic surfactants form micelles in presence of counterion that are commonly presented in carbonate reservoir or tubing system, such as Ca^{2+} , Mg^{2+} , Fe^{2+} , Fe^{3+} and other organic salts, and how they are affected by the water environment. Also, it may be useful to study the water–surfactant interaction at a molecular level, which is extremely important to confirm the structuring effect that these molecules may have on the surrounding water medium. Three anionic surfactant HGs were selected in this work with the criterion of their functionality, and also because of their importance in forming micelles in many processes. The molecular structures for anionic HGs that are considered in this study include: acetic acid (AA), potassium butanoate (PB), sodium propyl sulfate (SPS) and sodium butane-1-sulfonate (SB1S). We report quantum calculations at density functional theory (DFT) levels of the molecular properties in the gas phase and water solutions. The energy differences, torsional energy profiles, and binding energy with counterions are also calculated, and the water effect on these properties is analyzed. Finally, the properties of surfactant HGs/water complexes are calculated to establish how the structure of the anionic HG affects the specific interactions through hydrogen bonding with water and how this effect can be related

with the proposed structuring effect of surfactant on the water-surrounding medium. The understanding of the properties of these self-assembled molecules requires an accurate knowledge of nonbonding interactions, such as the intramolecular HG–HG and the intermolecular HG–water hydrogen bondings, which are key contributors to the specificity of the interactions within and between macromolecules that can be modeled through the study of the simpler anionic surfactant molecules.

6.2 Simulation

The DFT computations were done with the Gaussian 03 package (Frisch et al., 2004). The DFT studies employed the Becke gradient corrected exchange functional (Becke, 1988) in conjunction with the Lee–Yang–Parr correlation functional (Lee et al., 1988) with the three parameters (B3LYP) method (Becke, 1993). B3LYP is a gradient corrected method that includes some of the effects of electron correlations. This DFT approach usually gives rise to greater accuracy than Hartree-Fock (HF) for structure, thermochemistry, and spectroscopic properties, with only a slightly greater computational effort; this combination of efficiency and accuracy has made it perhaps the most popular method for practical applications. Results obtained with DFT approach are compared with experimental ones when available.

The computations reported in this work may be divided into three groups: First: *gas-phase calculations* which are done with the 6-311++g** basis set at B3LYP levels to determine the geometric and energetic parameters of the different HGs and to establish the most stable ones. Second, *water solution calculations*, done within the self-consistent reaction field approach (SCRF) in which the solvent is treated as a continuum. We adopted the polarizable continuum model (PCM) because it provides a quantitative estimation of the different contributions to the total free energy of solvation. Although the SCRF methods do not account for specific solute–solvent interactions, such as hydrogen bonding, and results based on these methods are clearly dependent on the selected size and shape of the solute cavity, they proved to be successful on analysis of

the effect of solvents on solute properties and on isomer ratios. The coupling of PCM models with DFT to study the interactions of solutes and solvents is not frequent. In this work the properties of the anionic HG in solution were calculated at DFT theoretical levels with a 6-311++g** basis set. Comparison of gas and solution results allows clarifying the solute polarization effect. Third, the properties of AA HG/water complexes were computed and their structures optimized at B3LYP levels with the 6-311++g** basis set. In a consistent manner and for all calculations presented in this chapter, the 6-311++G(d,p) basis set was applied to Al, H, O, C, Ca, Mg, Na, N atoms and SDD for Fe, Mn, Zn atoms.

6.3 Results and Discussion

Results in this chapter will include the molecular orbital theory analysis of each HG, in gas-phase and aqueous solution, the interaction between HGs and counterions. Molecular dynamic simulation of divalent metal ion, Ca^{2+} , with $4 \times 4 \times 2$ anionic surfactants and more than 2000 water molecules are discussed at various counterion concentration.

6.3.1 AA HG in Solution

In molecular orbital (MO) theory (Carey and Sundberg, 2007), reactivity is related to the relative energies and shapes of the orbitals that are involved in the reaction and hence to the nature of substituents. Shape of the molecular orbitals and symmetry are particularly important for qualitative reactivity analysis. We are trying to understand how a change in molecular structure of an anionic surfactant HG will affect the (MOs). As molecules approach one another and reaction proceeds there is mutual perturbation of the orbitals. This process continues until the reaction is complete and the product is formed. The concept of frontier orbital control proposes that the most important interactions are between a particular pair of orbitals (Fukui, 1971). These orbitals are the highest occupied orbital of one reactant (HOMO) and the lowest unoccupied (LUMO) orbital of the other reactant. If they are close in energy they could be intimately involved in

chemical reactivity as postulated in perturbation molecular orbital theory. A further general feature of MOs theory is that only MOs of matching symmetry can interact and lead to bond formation. Figure 6.1 shows the optimized geometry structure of AA HG in gas-phase (a), and water solution (c). At high pH (> 2) when acid reacts as in stimulation treatment for example, the surfactant HG will deprotonate and become acetate anion as in Figure 6.1(b). The HOMO and LUMO of the three structures give clear indication about how the reaction might take place. The LUMO in (b) shows that the carboxylate group may accept electrons in a complexation reaction with cations. It worth noticing that both Oxygen atoms share the same probability of being involved in binding. This was clearly observed from running the first calculation for two acetate HGs with one Ca^{2+} ion which result in equal bond lengths between the metal cation and the four Oxygens from two carboxylate groups.

The total electron density, $\rho(\mathbf{r})$, is a function of the coordinates \mathbf{r} and defined such that the number of electrons inside a small volume of $d\mathbf{r}$. this is what is measured in an X-ray diffraction experiment (Hehre et al., 1998). It's a quantitative measure of trends in bonding of particular molecular structure and thereby helps developing good description of reactivity and complexation. The electrostatic potential is the energy of interaction of a point positive charge (an electrophile) with the nuclei and electrons of a molecule. Negative electrostatic potentials indicate areas that are prone to electrophilic attack. The electrostatic potential can then be mapped onto the electron density by using color to represent the value of the potential. The resulting model simultaneously displays molecular size and shape and electrostatic potential value. Figure 6.1(a₃) shows the electrostatic potential of AA-HG mapped onto the electron density. Colors toward “red” indicate negative values of the electrostatic potential; while colors toward “blue” indicate positive values of the potential. An electrostatic potential map conveys information about the distribution of charge in a molecule. The Oxygen atom in the carboxyl part of AA is negative and it's expected to form noncovalent bonds with other AA group or with water molecules in the solution through hydrogen bonding. On the

other hand, hydrogen in the carboxyl group is highly acidic with blue electrostatic potential. This suggests delocalization of charge with Oxygen has more negative charge and hydrogen has more positive. The methyl group attached to carboxyl is partially electron-poor region. The hydrogen delocalization suggests that in basic medium, the deprotonation will be favorable. Figure 6.1(b₃) shows the electrostatic potential for acetate HG with electron distributed equality between the Oxygen in the carboxyl group, which means both of them have equal affinity to form complexation with metal ion or noncovalent bond with AA or H₂O in solution.

The acetic acid can mimic the HG in *p*-oleate and other an anionic surfactant with carboxylate as main functional group which will align in presence of counterions and form micelles or even precipitate. We shall first study its interaction at atomistic level with water molecule, hydroxide ion (OH⁻), hydronium ion (H₃O⁺), and hydrogen sulfide (H₂S) as in most cases of oilfield treatments and particularly in acidizing, those ions and molecules are in solution. The vibrational spectra of monomeric and dimeric acetic acid have been attractive to number of experimentalists and theoreticians in the last few years (Burneau et al., 2000). There have been good amount of work in the literature related to the properties of AA particularly for its solvent characteristics (Davidson, 1931). Molecular association of acetic acid has been a subject of extensive investigation for many years and the thermodynamic properties of formic and acetic acid dimers have been the most studied of the carboxylic acids (Nakabayashi et al., 2001). Figure 6.2 (a,b) shows optimized structures of AA HG dimer in gas-phase. The calculations are also carried out in water-solution using PCM solvation model. In the gas phase, acetic acid forms a centrosymmetric cyclic dimer containing two hydrogen bonds. The possible hydrogen bonds that can be formed in AA dimer are either between O–H···O=C (Figure 6.2(a)), or C–H···O=C and O–H···O=C (Figure 6.2(b)). The second one is well known characteristic for crystalline state where acetic acid exists in polymer chains.

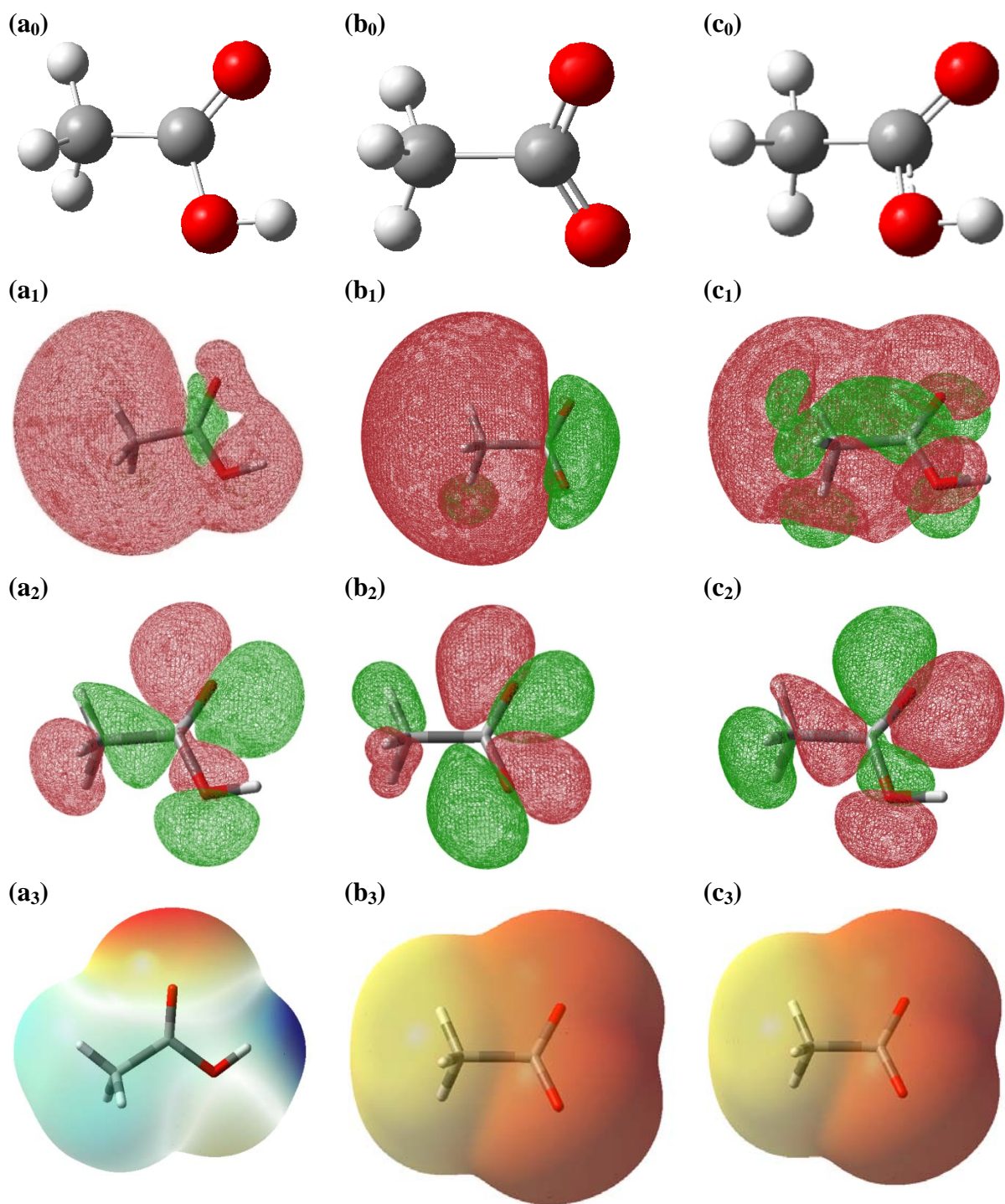


Figure 6.1: Optimized geometrical structure of acetic acid (AA) head group with localized HOMO, LUMO molecular orbitals, and electron density. (a) AA in gas-phase, (b) anionic $[AA]^-$ in gas-phase and (c) AA in water solution, with second row for LUMO, third for HOMO, and forth row for electron density potential, respectively. Isosurface value= $0.02 \text{ e}/\text{\AA}^3$, $0.0004 \text{ e}/\text{\AA}^3$ for MO and density, respectively.

The AA dimer in Figure 6.2(a) has a C_s plane containing the methyl hydrogen at the side of the C=O group. The calculated binding energy is -10.8 kcal/mol with an average hydrogen bond distance of 1.68 Å. The distances for the intermolecular hydrogen bonds of this cyclic dimer are calculated to be lengthened on going from the gas phase to aqueous solution. With no remarkable structural change in the cyclic dimer, the average hydrogen-bonding distance is found to be 0.28 Å longer in the solution (Appendix C) than in the gas phase. This result indicates that the intermolecular hydrogen-bonding interactions of both the dimers are weakened effectively by the local solute–solvent interactions. The C=O and O–H bond lengths of both the dimers also become longer in the solution than in the gas phase. Since the hydrogen bonds between the solute molecules become weaker in aqueous solution as mentioned above, this result can be attributable to the hydration around these sites. This means that the O–H···O=C interaction of the cyclic dimer becomes weaker on going from the gas phase to aqueous solution, which contributes the stabilization of a more linear dimer or favorable interaction with water molecules in the solution. It is known that in the gas-phase, the cyclic dimer with O–H···O=C is the most stable among the dimer species of acetic acid (Burneau et al., 2000). This cyclic dimer has approximately a linear angle between $\angle\text{OHO}$ with 178° in one side and 180° in the other side. However, for AA dimer (b) where one of the O–H···O=C has been replaced with C–H···O=C, the total binding energy is 7.4 kcal/mol lower than that in (a) with an average hydrogen bond of 2.14 Å. This means the rotational of AA surfactant HG is not highly favorable. The interaction with water molecules is also investigated and the optimized structures for AA and its acetate ion (^-OAc) are shown in Figure 6.2 (c) and (d), respectively. For acetate, both hydrogen atoms of water molecules are face-in toward the carboxylate group and the bonding energy is 9.1 kcal/mol higher than that calculated for AA–(H_2O). The average hydrogen bond for ^-OAc –(H_2O) cluster is 1.62 Å with $\angle\text{OHO}$ angle equal 136° . Results show that the cyclic AA dimer is lower in energy compared to interaction with water molecules, which might explain the aggregation of surfactant molecules to form spherical micelles at high concentration in water solution.

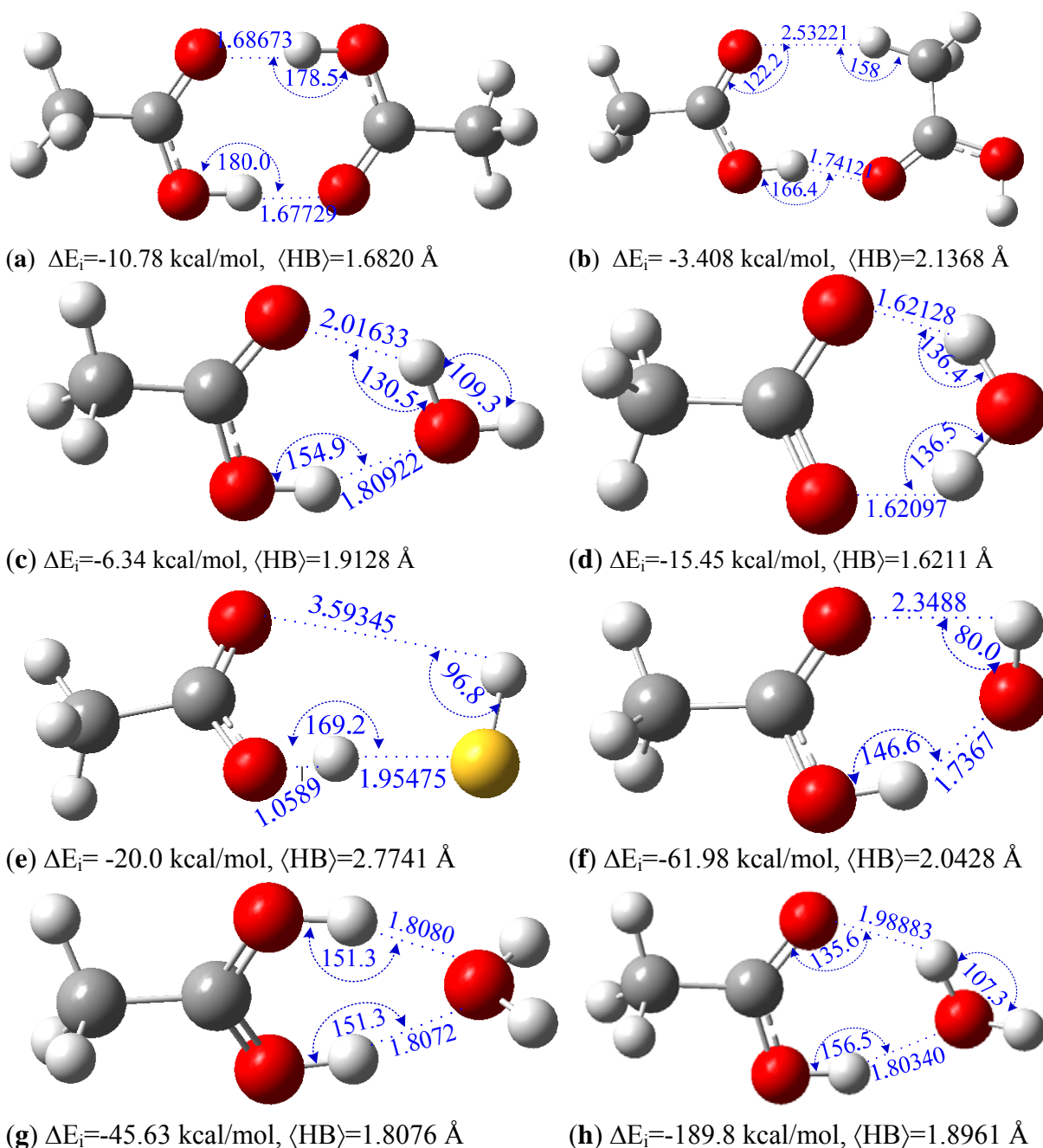


Figure 6.2: Optimized structures for acetic acid (AA) and acetate (^-OAc) in gas-phase calculated using B3LYP/6-311++G**: (a) dimers $(\text{AA})_2$, (b) dimers $(\text{AA})_2$, (c) $\text{AA} \cdot \text{H}_2\text{O}$, (d) $^-\text{OAc} \cdot \text{H}_2\text{O}$, (e) $\text{AA}(\text{HS})^-$, (f) $\text{AA}(\text{OH})^-$, (g) $\text{AA}(\text{H}_3\text{O})^+$, and (h) $^-\text{OAc}(\text{H}_3\text{O})$. Shown in this graphs binding energy, ΔE_i , and average hydrogen bond, $\langle \text{HB} \rangle$. Color code: red for O, light gray for H, dark gray for C and yellow for S.

Hydrogen sulfide (H_2S) is common in oilfield reservoir as we discussed previously in Chapter V and it might have its influence on surfactant properties. H_2S is soluble in acid solution and that makes it readily available for interactions with anionic surfactant. H_2S in aqueous solution dissociates to HS^- and H^+ at $\text{pK}_a=7.0$. Figure 6.4(e), shows the optimized molecular structure of HS^- ion with AA head group. The total binding energy is calculated to be -20.0 kcal/mol with the average hydrogen bond of 2.77 Å. This energy is lower than that for OH^- interaction with AA as shown in Figure 6.4(f). This can explain the affinity of AA toward anions (HS^- and OH^-) assuming high pH value with carboxylate group still protonated. Most carboxylic acids have a pK_a value around 4.8 (Kanicky et al., 2000). This value represents the ionic environment of the solution where 50% of the carboxylate HGs are protonated and other 50% are deprotonated. The value of pK_a can be raised by increasing the carbon chain length of the HG. However, because the electronic effects become negligible beyond four carbons in the alkyl chain, the pK_a value tends to level off. For this reason we have selected carboxylate HG with two methyl, and butyl for AA and PB, respectively.

In HCl acidic solution, the hydrogen tend to dissociate at very high rate and their interaction with AA and ^-OAc are shown in Figure 6.4(g,h), respectively. The AA- H_3O^+ complex has a binding energy of -45.6 kcal/mol and the average hydrogen bond is calculated to be 1.81 Å. the initial structure has three hydrogen atoms bonded directly to oxygen (H_3O^+), while the final optimized structure shows one hydrogen transfers to the carboxylic group. The ^-OAc interaction with H_3O^+ is highest in binding energy among all present ions in solution. This explains the tendency of anionic surfactant to be protonated at low pH. Most long-chain fatty acid undergo an ionization process between pH 4.0 and 10.0 where the ratio ($\text{RCOOH} : \text{RCOO}^-$) is in proportion 1:1 (Kanicky et al., 2000). At this pH an interaction between (RCOOH) and (RCCO^-) as well between ($\text{RCOOH}-\text{OH}$) and ($\text{RCOO}^--\text{H}_3\text{O}^+$) are expected. We have not shown the interaction between the protonated and deprotonated AA dimer or the effect of chain length because it beyond the scope of this study and will be included in the future study.

6.3.2 AA HG with Counterions

Although surfactant science is now a reasonably mature discipline, there is still room for new molecular design especially in a field like oil industry. Ion properties and their interaction with other molecules are still not understood in detail, and we are far away from being able to predict their behavior. Molecular self-assembly in surfactant systems is largely dependent on the number of water molecules surrounding the headgroups. When ions are added to a solution, they dehydrate the surfactant headgroups. This causes a decrease in the value of effective area, a , and consequently an increase of the structural packing parameter, P , which may result in the formation of micelles. The packing parameter is dependent on the length and volume of the hydrophobic tail and the size of the hydrophobic head of the surfactant molecule. These factors are often expressed in a packing parameter $P=v/(l_{\max}a)$, where v and l_{\max} are the volume and length of the hydrophobic part, respectively, and a the area per molecule at the interface. The effect of salts on a charged system can differ much depending on their hydrophobic or hydrophilic character. Each salt is therefore expected to have an individual influence on micelle formation, whether it tends to adsorb at the interface between micelle and water or remains strongly hydrated in the bulk. The maximum number of HGs that could bind to a metal (M^{q+}) of charge q , denoted by (HG_n-M^{q+}) , is therefore of interest, but the (HG_n-M^{q+}) , and the key factors determining this upper limit are generally not known (to the best of our knowledge).

In this part of the chapter, we study the effects of organic and inorganic counterions on AA HG behavior. Naturally existing metallic ions in carbonate reservoir such Magnesium (Mg^{2+}), Calcium (Ca^{2+}), are the main focus, however, non-natural mono-di- and triinorganic counterions such as Sodium (Na^+), Ferrous (Fe^{2+}), Ferric (Fe^{3+}), Aluminum (Al^{3+}), Zinc (Zn^{2+}), as well as Manganese (Mn^{2+} , Mn^{3+}) are also investigated. For consistency, six-coordinated system is assumed for all metals and the ligands $M^{q+}L_n$ with $n=1-6$ and $L=CH_3COO^-$ are studied. The binding energies of mostly common cationic and anionic organic salts are evaluated too.

The mechanism of micelles growth is a combination of dehydration effect and electrostatic interaction (Vlachy et al., 2008). Metals, in general, are strong water structure formers and their charge density, polarizability and availability of electron for covalent contributions are responsible for the short-rang interaction. Water molecules were included in the calculations to determine the role of hydration/dehydration effect on the formation of micelles and total binding energy. Viscoelastic surfactant systems aggregate in water solution and we are trying to quantify the hydrogen bonding effect between ^-OAc and H_2O to form stable complex ($M^{q+}L.mH_2O$). Also, another factor that we are trying to address in this chapter is the coordination number effect.

We first consider the interaction where acetate bounds to one calcium ion with two water been replaced ($Ca(H_2O)_2 \rightarrow Ca(OAc)_2 + 2H_2O$). Figure 6.4(a) shows the optimized structure of $Ca(OAc)_2$ which has a binding energy of -494.6 kcal/mol. The total binding energy is calculated as the difference in enthalpies between the complex and its constituents. The value calculated in this study is less than what have been estimated (522.1 kcal/mol) using HF/3-21G (Careja et al., 2007). Calcium ion favorably forms good bonding with all four oxygen atoms in the carboxylate group, which means carboxylate group in AA HG is bidentate. This concept of monodentate and bidentate where one of the carboxylate oxygens or both are being able to bind to the metal cation, respectively, is of great interest to evaluate. We have evaluated the binding energy of $[Ca(H_2O)_2]^{2+}$ to be -108.8 kcal/mol (as shown in Chapter IV). The difference in total binding energy between the two complexes $Ca(OAc)_2$ and $[Ca(H_2O)_2]^{2+}$ is 387.8 kcal/mol. This suggests that the driving mechanism for micelle formation is electrostatic interaction as a first order effect more than hydration/dehydration which we will evaluate shortly. The average calculated Ca–O bond distance is found to be 2.30 Å. The complex has a good symmetry with angle between calcium and oxygen atoms of the same acetate group is $\angle O_1CaO_1=58^\circ$ and that between two acetate groups $\angle O_1CaO_2=140^\circ$. For coordination number (CN=4) of calcium ion, we have examined the replacement of two water molecules from a tetrahedral structure ($Ca(H_2O)_4 \rightarrow$

$\text{Ca}(\text{OAc})_2 \cdot \text{H}_2\text{O} + 2\text{H}_2\text{O}$) by two acetate groups. Figure 6.4(b) shows the optimized structure with two *trans*-acetate groups. The average calculated $\text{Ca}-\text{OH}_2$ is 2.42 Å and $\text{Ca}-\text{OC}$ is 2.3859 Å. The $\text{Ca}-\text{OH}_2$ in the calcium acetate complex is lower than what we have calculated (2.34 Å) for the $[\text{Ca}(\text{H}_2\text{O})_4]^{2+}$ at B3LYP with the same basis set. The total binding energy for this complex is 26.0 and 332.7 kcal/mol higher than what we have found for $\text{Ca}(\text{OAc})_2$ and $[\text{Ca}(\text{H}_2\text{O})_4]^{2+}$. This can help addressing the three factors that we are trying to evaluate: coordination number, hydration/dehydration and electrostatic. Higher energy for $\text{Ca}(\text{OAc})_2 \cdot 2\text{H}_2\text{O}$ (520.6 kcal/mol) shows that the coordination number for stable Ca^{2+} is not 2. Also, hydration/dehydration process is a second mechanism for anionic surfactant interaction with metal ion to form micelles. Still we can see (Figure 6.3(b)) that both carboxylate oxygen atoms are binding to the central metal ion (bidentate). Figure 6.3(c) shows the optimized structure of tetraaquo calcium acetate, $\text{Ca}(\text{OAc})_2 \cdot 4\text{H}_2\text{O}$, with a total binding energy of -542.5 kcal/mol. The 3D view on the right-hand side of Figure 6.3 shows that the carboxylate group is monodentate in octahedral structure. Water molecules in the structure have an average hydrogen bond of 2.88 Å in between and 1.78 Å with carboxylate oxygen which is not bound to Ca^{2+} ion. Table 6.1 summarizes geometrical properties of $\text{Ca}(\text{OAc})_n \cdot m\text{H}_2\text{O}$.

Table 6.1: Thermodynamic property of the complex $\text{Ca}(\text{OAc})_n \cdot m\text{H}_2\text{O}$, with binding energy, $\Delta E_i = E_{\text{complex}} - (E_{\text{Ca}^{2+}} + nE_{\text{H}_2\text{O}} + mE_{\text{OAc}})$

(n,m)	CN	ΔE_i (kcal/mol)	$\langle \text{Ca}-\text{OH}_2 \rangle$ (Å)	$\langle \text{Ca}-\text{OC} \rangle$ (Å)	$\langle \text{HB} \rangle$ (Å)	$\angle \text{OCaO}$ (°)	APT
2,0	4	-494.6	—	2.30	—	99	1.72
2,2	4	-520.6	2.42	2.38	2.00	74	1.68
3,0	6	-554.2	—	2.42	—	80	1.66
2,4	6	-542.5	2.41	2.33	1.78	86	1.79
<i>cis</i> -2,4	6	-542.1	2.39	2.31	1.65	80	1.78
3,3	6	-583.2	2.44	2.36	1.67	78	1.79
4,2	6	-542.5	2.50	2.36	1.77	80	1.94
3,4	7	-589.6	2.51	2.41	1.91	75	1.75
4,3	7	-544.3	2.50	2.41	1.73	83	1.86
5,2	7	-429.9	2.45	2.45	1.58	80	1.84
4,0	8	-507.1	—	2.57	—	89	1.75

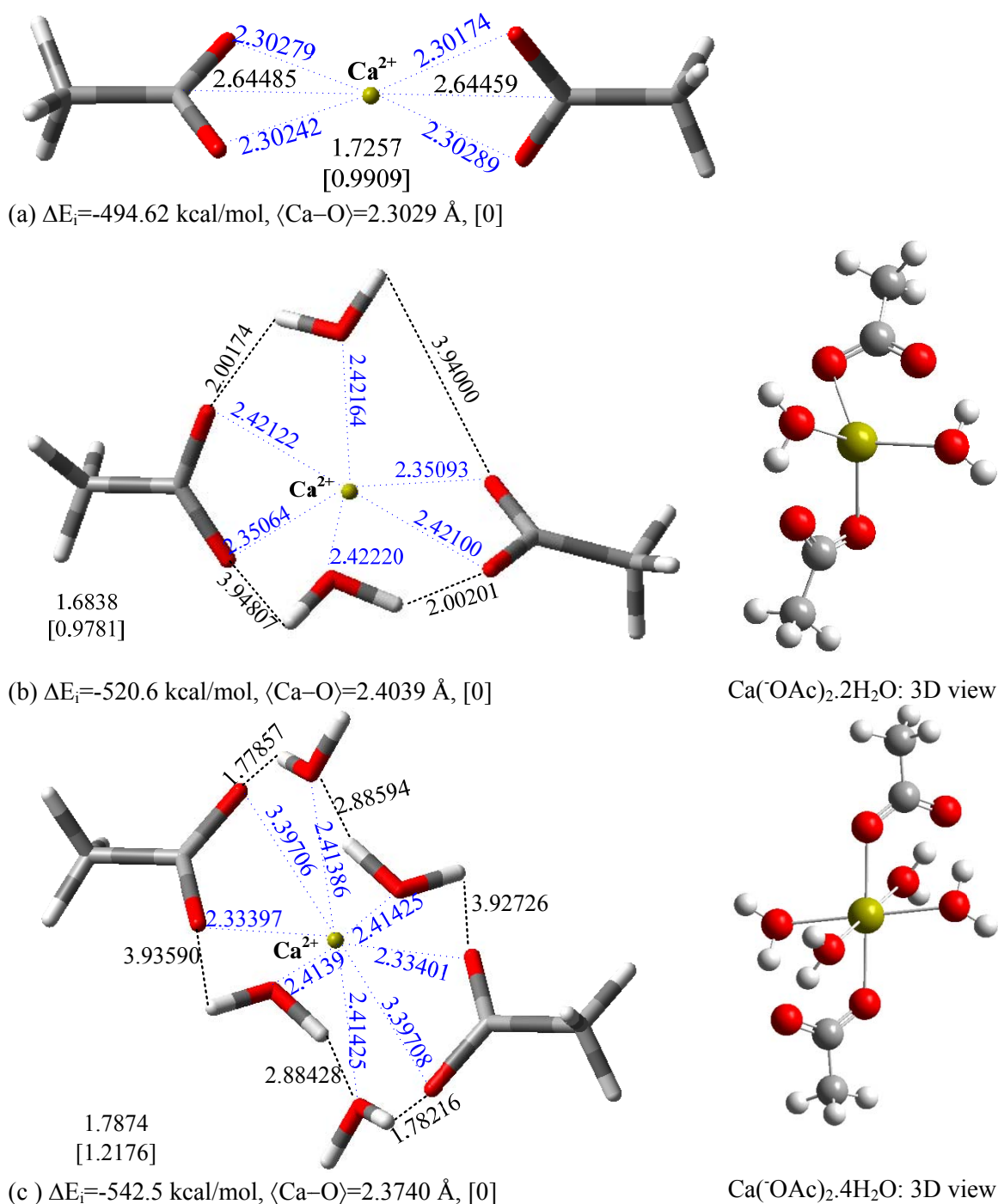


Figure 6.3: Optimized structures for acetate (⁻OAc) HG complexation in gas-phase with Ca²⁺ ion calculated using B3LYP/6-311++G^{**}: (a) Ca(⁻OAc)₂, (b) Ca(⁻OAc)₂.2H₂O, and (c) Ca(⁻OAc)₂.4H₂O. Shown in this graphs bond distance (Å), binding energy, ΔE_i , and average hydrogen bond, $\langle \text{HB} \rangle$. Color code: red for O, light gray for H, dark gray for C, and for Ca.

This structure is highly favorable with a good network of hydrogen bonding and result in a shorter Ca–O distance of 2.33 Å compared to 3.38 Å for Ca(OAc)₂·2H₂O. The question now, what is the maximum number of acetate groups that can bind to a divalent counterion such as calcium? or in other word, what is the surfactant to calcium ratio needed for sphere-to-wormlike transfer to take place. This is important because viscosity build up is a result of surfactant aggregation and micelle transformation from sphere-like to wormlike at given ratio of surfactant to counterions. It has been reported that multivalent counterions are much more effective than monovalent counterions as promoters of the formation of wormlike micelles (Alraggova et al., 1998). Let us define the ratio of surfactant HG that has influence on the sphere-to-wormlike transition as: $\xi = C_s / (Z \cdot C_l)$, where C_s is the molar concentration of surfactant, C_l is the total molar concentration of counterion, and Z is the valence of counterion. In other word, ξ equal the ration of net change of surfactant HG to the net charge of the dissolved counterion. In the excess of counterions, ($\xi < 1$), cylindrical micelles will be formed, whereas in the excess of surfactant, ($\xi > 1$), the micelles will stay spherical. It has been believed that the transition happens close to value of $\xi = 1$, which means for divalent ion such as Ca²⁺, the concentration needed is double the counterions (Alargova et al., 1995).

To determine the maximum number of acetate HGs that can bind to Ca²⁺, we carried out calculations for three, four and five acetates interacted with central calcium ion of six and seven coordination number, [Ca(OAc)_{*n*}·*m*H₂O]^{2-*n*}. For CN=6 with *n*=3, *m*=3, which we will refer to as (*n*,*m*), the optimized structure is shown in Figure 6.3 (c,d) with a total binding energy of -583.2 kcal/mol. This structure is more stable and thermodynamically favorable with 40.7 kcal/mol higher binding energy compared to (2,4) system. It has an octahedral geometry with all acetate groups bound to Ca²⁺ ion monodentately. The other oxygen atom in each carboxylate group is forming hydrogen bond with one water molecule with average length of ⟨HB⟩=1.67 Å. The average angle between acetate groups, ∠OCaO, is 119°, which is about the same to that between water molecules (120°).

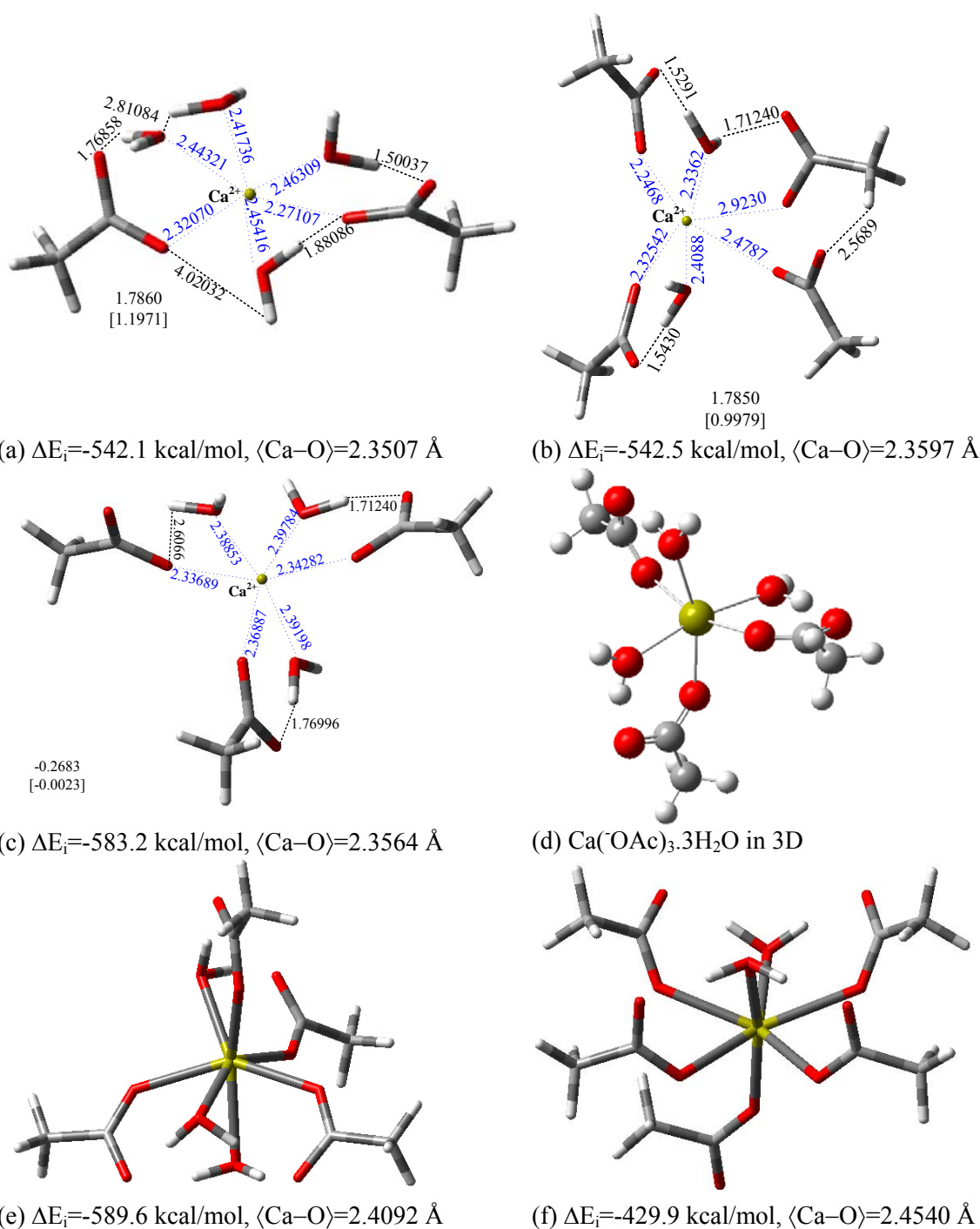


Figure 6.4: Optimized structures for *di*-, *tri*- and *tetra*acetate (OAc) HG complexation in gas-phase with Ca^{2+} ion calculated using B3LYP/6-311++G**.(a) $\text{Ca-cis}(\text{OAc})_2 \cdot \text{H}_2\text{O}$ (b) $\text{Ca}(\text{OAc})_4 \cdot 2\text{H}_2\text{O}$, (c) $\text{Ca}(\text{OAc})_3 \cdot 3\text{H}_2\text{O}$, (d) 3D view of $\text{Ca}(\text{OAc})_4 \cdot 2\text{H}_2\text{O}$, (e) $\text{Ca}(\text{OAc})_3 \cdot 4\text{H}_2\text{O}$ and (e) $\text{Ca}(\text{OAc})_4 \cdot 3\text{H}_2\text{O}$. Shown in this graphs bond distance (Å), binding energy, ΔE_i , and average hydrogen bond, $\langle \text{HB} \rangle$.

The calcium ion has a shorter bond distance with oxygen in the carboxylate group (2.36 Å) compared to that of water (2.44 Å), which means dehydration is favorable for calcium to bind with three OAc^- groups. For the system (4,2), with four acetates bind directly to the calcium the binding energy is in the range of (2,4) with 0.01 kcal/mol difference. This suggests that calcium ion has the affinity not just to counterbalance the charge of the HG, but also to bind with more than two acetate groups. In such a case, surfactant can aggregate with ξ -ratio larger than 1 (i.e. counterion is two-folds less than surfactant concentration). Though the binding energy of the two systems (2,4) and (4,2) is nearly the same, we believe that (4,2) is more stable. This can be explained by looking at Ca–O bond distance which is shorter for acetate oxygen compared to water oxygen suggesting that the dehydration of one water molecule from (3,3) is high likely to happen. The optimized (4,2) structure is shown in Figure 6.4(b) with average Ca–O bond distance of 2.36 and 2.50 Å for acetate oxygen and water oxygen, respectively. The two water molecules form four hydrogen bonds with oxygens in the carboxylate that are not in bonding with calcium. In an attempt to study the effect of coordination number on binding energy and stability of calcium–acetate system, three more complexes with CN=7 are examined. The first one is for calcium with three acetates and four water molecules (3,4). All seven molecules are in the first shell and connected directly to Ca^{2+} ion. The optimized structure has a total binding energy of -589.6 kcal/mol which is 6.4 kcal/mol larger than (3,3). Adding one more water molecule to the first shell of (3,3) results in more stable calcium acetate complex due to hydrogen bonding. The average bond distance Ca–OC is 2.41 Å while Ca–OH₂ increases to 2.51 Å compared to 2.44 Å for (3,3). When one water molecule in (3,4) is replaced with acetate group, the new structure (4,3), become less stable with total binding energy of -544.3 kcal/mol (45.4 kcal/mol less than (4,3) complex). This complex is also less stable compared to (3,3), however, the Ca–OC bond distance (2.41 Å) is lower than Ca–OH₂ (2.50 Å), which means the dehydration is favorable. For (5,2), the binding energy (-429.9 kcal/mol) is even lower compared to (4,3) or any other calcium acetate complex. This structure

represents the maximum number of acetate HG around calcium with Ca–OC bond length (2.45 Å) about the same of Ca–OH₂ (2.45 Å).

Calcium is not the only cation available in reservoir water or at the acid front during acid treatment. Other metal ions such Na⁺, Mg²⁺, Fe²⁺, Zn²⁺, Mn²⁺, Fe³⁺, Mn³⁺ and Al³⁺ can have high concentration too. The competition between mono-, di- and trivalent counterions will be evaluated based on their affinity to interact with acetate HG. For monovalent ion, we are considering sodium which can have concentration of more than 2000 ppm in aquifer water (Nasr-El-Din, 2004). The optimized structure of sodium acetate with 6-coordination number is shown in Figure 6.5(a). It has a total binding energy of -195.6 kcal/mol, which is three-folds lower than calcium acetate. For hexaaquo sodium cluster, [Na(H₂O)₆]⁺, the energy needed for dehydrating one-water molecule and replacing them by acetate HGs is -98.2 kcal/mol. The acetate group in the final optimized structure is not directly connected to Na⁺ compared to the starting structure. This suggests that acetate HG dose not penetrate the water shield around Na⁺ ion which can be attributed to high CN. Four water molecules around the central ion form Na–OH₂ bond distance of 2.31 Å while the five one is longer with value of 3.58 Å, which give an indication that Na⁺ might favor the CN=4 in such complex. Both the singly, and doubly bonded oxygen in the carboxylate group are forming hydrogen bond with water molecules. For divalent counterions, we have considered four common metallic ions each with 6-coordination number geometry. It is highly expensive (time, and CPU power) to study the effect of coordination number, and hydration/dehydration process on the acetate interaction with common counterions. It worth mentioning, this is not the immediate objective of this dissertation, however, we will carry out these calculations in the next phase of this project. For magnesium, the complex Mg(OC(=O)CH₃)₂·4H₂O is optimized at B3LYP/6-311++g** and has a total binding energy of -622.3 kcal/mol as shown in Figure 6.5(b). The average Mg–O bond distance is shorter than what we have calculated for Ca–O, with values 2.05 and 2.14 Å, for Mg–OC and Mg–OH₂, respectively.

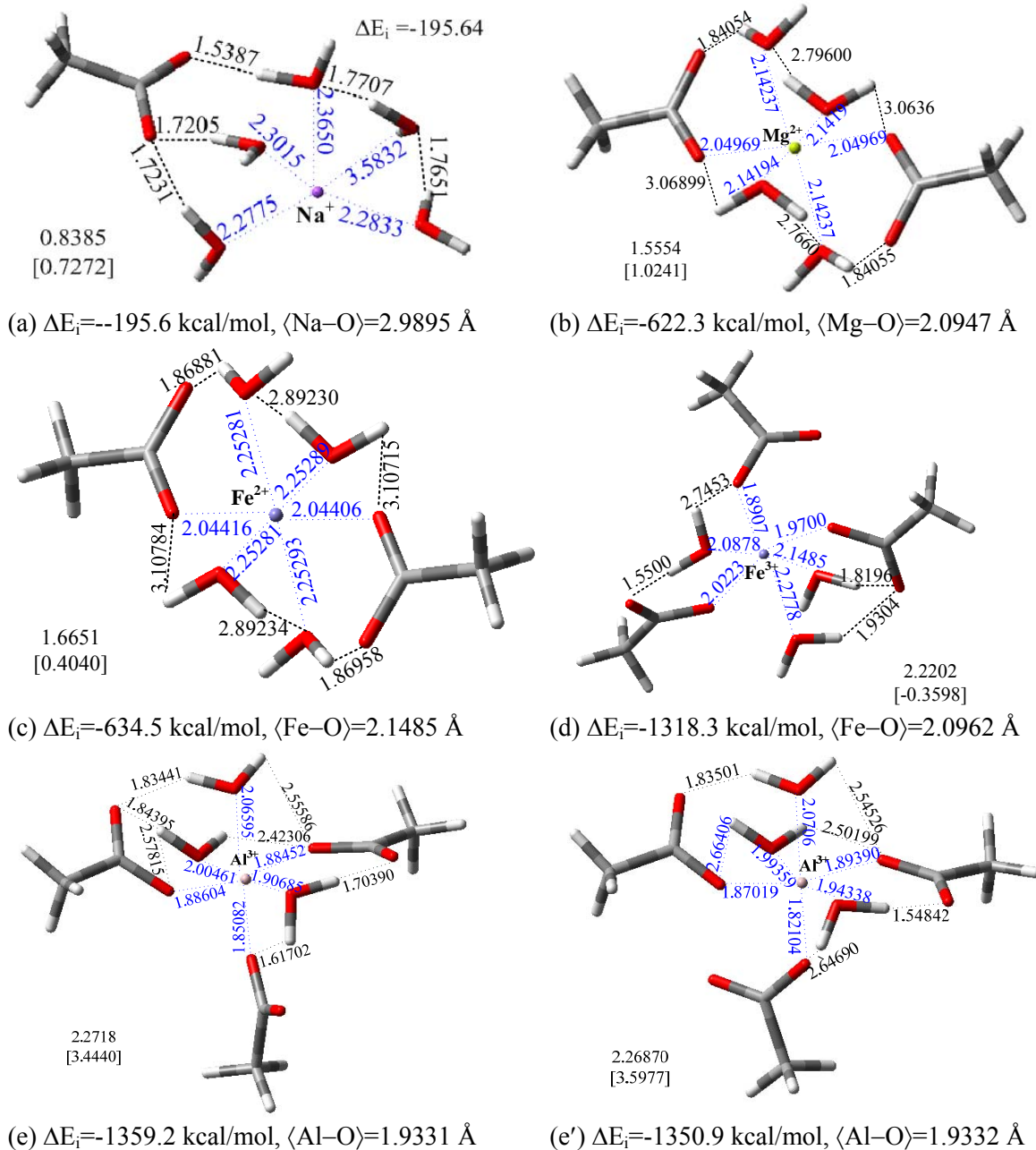


Figure 6.5: Optimized structures for acetate (OAc) HG complexation in gas-phase with metal ions calculated using B3LYP/6-311++G**:. (a) $\text{Na}(\text{OAc})_2 \cdot 4\text{H}_2\text{O}$, (b) $\text{Mg}(\text{OAc})_2 \cdot 4\text{H}_2\text{O}$, and (c) $\text{Fe}(\text{OAc})_2 \cdot 4\text{H}_2\text{O}$, (d) $\text{Fe}(\text{OAc})_3 \cdot 3\text{H}_2\text{O}$, (e,e') $\text{Al}(\text{OAc})_3 \cdot 3\text{H}_2\text{O}$. Shown in this graphs binding energy, ΔE_i , and average hydrogen bond, $\langle \text{HB} \rangle$. Color code: red for O, light gray for H, and dark gray for C.

Carboxylate groups bind with Mg atom monodentately, where the doubly bond oxygens form a hydrogen bond with water molecules. The average hydrogen bond in the magnesium acetate complex is calculated to be 1.88 Å. it is obvious that the size of metal ions plays a role in the geometrical properties and energy of the system. Ferrous, Fe^{2+} , acetate has higher binding energy compared to Mg^{2+} but similar geometrical structure. Table 6.2 shows structural properties and binding energy of ferrous acetate as well as other complexes included in this study. The Fe–OC bond distance (2.04 Å) is in the same range of Mg–OC (2.05 Å), however Fe–OH₂ is longer. In going from Ca, Mg, Fe acetate complexes to Zn complex, the gas-phase binding energy increases and the complex become more favorable. This means if we have multiple divalent ions in the acid stimulation fluid, the order of binding power with surfactant-acetate HG is: $\text{Zn} > \text{Fe(II)} > \text{Mg} > \text{Mn(II)} > \text{Ca}$. the optimized geometrical structures of Mn(II), Mn(III) and Zn hydrate as well as acetate are shown in Appendix C. For trivalent ions, results show that Mn(III) and Al^{3+} have the same binding energy power, which is larger than Fe(III). Acetate in all three trivalent systems binds monodentately to the central ion. The properties of bond length and hydrogen bonding are shown in Table 6.2. The rearrangement in the structure between Figure 6.5(e) and (e') are due to maximizing hydrogen bonding. This results in 8.3 kcal/mol more stable structure when the free carboxylate oxygen is forming short-hydrogen bond with water.

The difference in energy between hydrated metal clusters and metal acetate complexes indicates how favorable the process is thermodynamically as shown in Figure 6.6. The upper curve is for metal hydration with the general structure $[\text{M}(\text{H}_2\text{O})_n]^{x+}$, where M=Na, Ca, Mg, Zn, Mn(II), Fe(II), Al, Mn(III) and Fe(III), $n=0-6$ and $x=1-3$. As the size of the metal increases, the binding energy increases too, and hence Manganese, Aluminum and ferric ions form the highest binding energy complex with acetate compared to mono- and divalent atoms. All binding energies for metal acetate are less than the corresponding molecular conformation of hydrated metal, which means that the dehydration of water molecules from metal ion and replacement by acetate ion is an exothermic process. As the hydration energy differs from one metal ion to another, it is expected to have

individual influence on micelle formation, where the cation tends to adsorb at the interface between micelle and water or remain strongly hydrated in the bulk water solution. Mg^{2+} has 80 kcal/mol higher binding energy than Ca^{2+} , and consequently also higher than the monovalent ion (Na^+). Results shown in Figure 6.5 are for structures with $\text{CN}=6$, however the higher the number of water molecules in the metal cluster the higher the binding energy, and this reflects how favorable this complexation is in water solution. The Mn (III), Fe(III) and Al ions, have by far the highest binding energy among all metal ions, and though the difference between $\text{Mg}(\text{OAc})_2 \cdot 4\text{H}_2\text{O}$ and $\text{Fe}(\text{OAc})_2 \cdot 4\text{H}_2\text{O}$ energies are less than 12 kcal/mol, the $\text{Fe}(\text{OAc})_3 \cdot 3\text{H}_2\text{O}$ is double that of divalent and sextuple the monovalent. It is very interesting to observe that the difference in binding energy between the two clusters ($\Delta\Delta E_i = \Delta E_{\text{M-acetate}} - \Delta E_{\text{M-hydrated}}$) is highly correlated to ionic charge (q). The average value of this difference is 98.2, 309.8 and 669.0 kcal/mol for mono- di- and trivalent ions, respectively. This high complexation energy could explain the fast precipitation of anionic surfactants with addition of Fe^{3+} to the system (Jian-xiao et al., 2006).

To better characterize the stability and strength of the complex formed, we calculated the bond distance between the metal cation and the carboxylate Oxygens, $\text{M}-\text{OC}$, and water Oxygen, $\text{M}-\text{OH}_2$, in $\text{M}(\text{OAc})_n \cdot (6-n)\text{H}_2\text{O}$ complexes as shown in Figure 6.7. As the binding energy increases the $\text{M}-\text{O}$ bond distance becomes shortened, however, it does not decrease monotonically, but rather approaching a plateau in the case of di- and trivalent metals. Similarly, the distance with the doubly bonded Oxygen atom in the carboxylate group $\text{M}-\text{OC}$, is decreasing gradually from monovalent Na^+ ion to a minimum at Mg^{2+} and then increasing slightly for iron ions. The average distance between Oxygen in water molecules surrounding the metal ion, $\text{M}-\text{OH}_2$, is approximately constant Fe(II), Fe(III), Zn, and Mn(III), however, it has a maximum value of 2.56 Å for Na^+ and minimum of 1.99 Å for Al^{3+} .

Table 6.2: Thermodynamic property of the complex $M^{x+}(\text{OAc})_n(6-n)\text{H}_2\text{O}$

M^{x+}	CN	ΔE_i (kcal/mol)	$\langle \text{Ca-OH}_2 \rangle$ (Å) ^a	$\langle \text{Ca-OC} \rangle$ (Å) ^a	$\langle \text{HB} \rangle$ (Å) ^a	$\angle \text{OCaO}$ (°) ^a	APT
Na	6	-195.6	2.56	3.42	1.66	76	0.83
Mg	6	-622.3	2.14	2.05	1.84	89	1.55
Fe (II)	6	-634.5	2.25	2.04	1.87	89	1.66
Fe (III)	6	-1318.3	2.17	2.02	1.77	89	2.22
Al ^b	6	-1359.2	1.99	1.87	1.75	90	2.27
Al ^c	6	-1350.8	2.00	1.86	1.71	90	2.27
Al ^d	6	-1333.3	0.00	1.94	0.00	83	2.05
Zn	6	-658.6	2.21	2.03	1.85	89	1.68
Mn (II)	6	-608.9	2.28	2.13	1.83	89	1.71
Mn (III)	6	-1354.1	2.21	1.92	1.86	90	2.15

^a average values calculated at B3LYP/6-311++G**. ^b Octahedral structure with 4-HB. ^c octahedral structure with 2-HB. ^d octahedral structure with “zero” water and 3-acetates bind bidentately to Al.

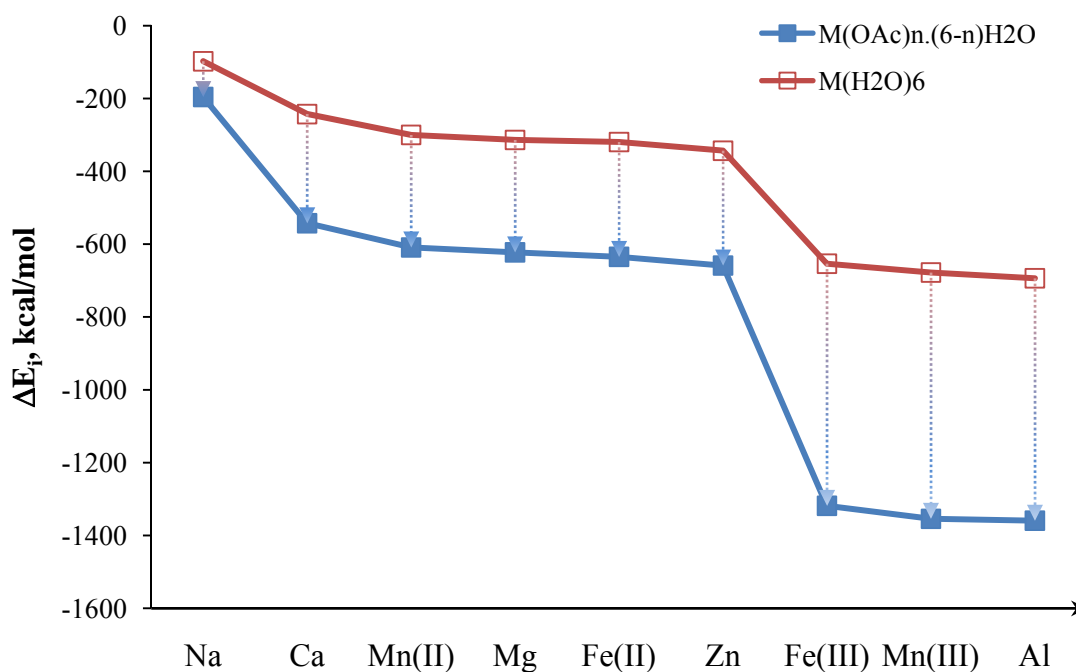


Figure 6.6: Binding energy of metal cations with water molecules, $[\text{M}(\text{H}_2\text{O})_6]^{x+}$ (\square) and with acetate, $\text{M}(\text{OAc})_x.(n-x)\text{H}_2\text{O}$ (\blacksquare). Replacement of x -water molecules with corresponding number of acetate anions is favorable (exothermic process).

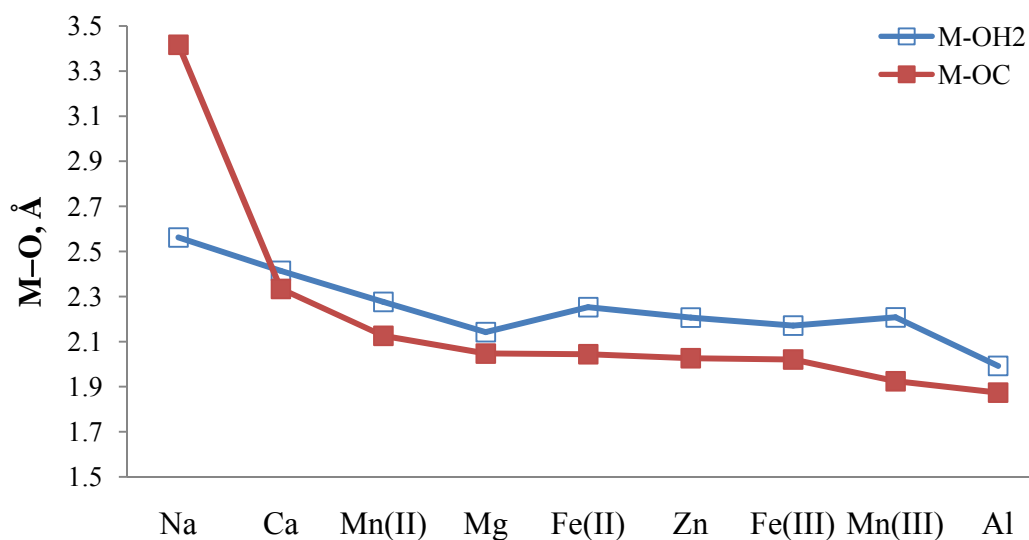


Figure 6.7: Bond length in octahedral metal acetate complex $M(OAc)_x(n-x)H_2O$. (\square) for metal ion with water oxygen, and (\blacksquare) for metal with carboxylate oxygen of HG.

6.3.3 AA and Organic Counterions

Organic salts such as sodium salicylate, NaSal, and sodium hydroxynaphthalene carboxylate, NaHNC have shown high influence on rheological properties of viscoelastic surfactant solution (Kumar et al., 2007). Though these two organic salts are anionic, they can enhance flow of an anionic surfactant solution in the pipes due to drag reduction (Zana and Kaler, 2007). The salt counterions (Sal^- and HNC^-) induce the growth of wormlike micelles of cationic surfactants by bind to their HG and thereby reduce the effective charge. However, when considering anionic surfactant or zwitterionic with carboxylate HG the sequence of binding is different as we believe. Since the counterion of those two organic salts is anionic and the OAc HG is anionic too, the adsorption of organic salt on rock surface will increase the charge on the HG. This will result in large effective area of HG and surfactant will transform from cylindrical to spherical micelles (Kalur, 2005). The addition of organic salt to anionic surfactant solution can help breaking viscosity, increase flow in pipe and decrease precipitation rate with inorganic salts.

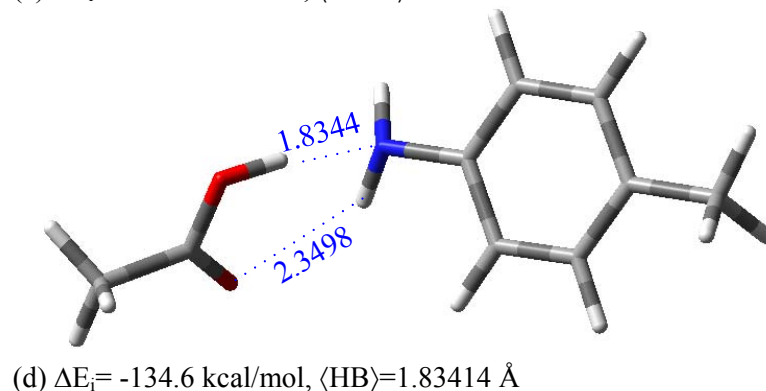
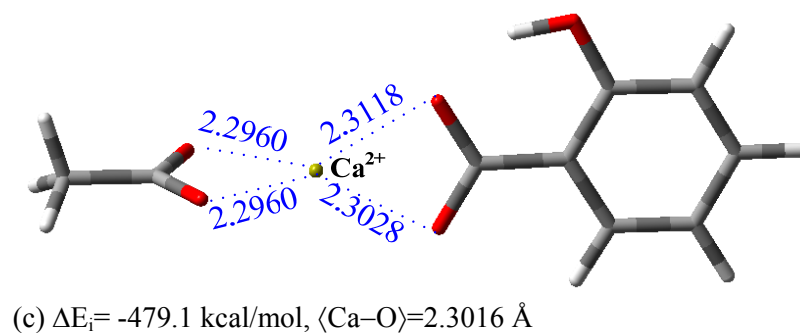
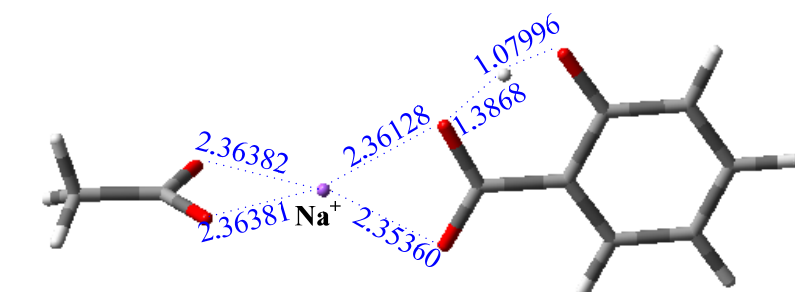
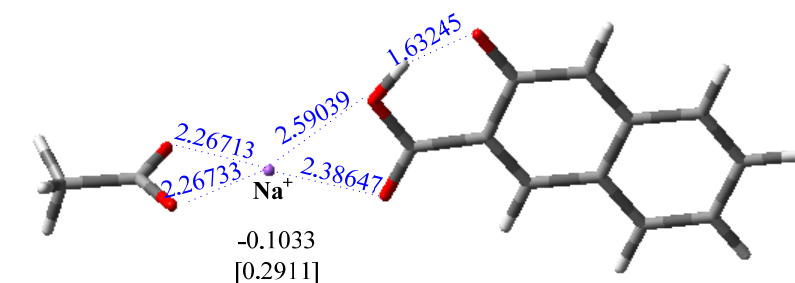


Figure 6.8: Optimized structures for acetate (^-OAc) HG interaction with organic salts in gas-phase calculated using B3LYP/6-311++G ** : (a) NaHNC-OAc, (b) NaSal-OAc, (c) CaSal-OAc and (d) PTH-OAc. Shown in this graphs binding energy, ΔE_i , and average hydrogen bond, $\langle \text{HB} \rangle$. Color code: red for O, light gray for H, dark gray for C, and

Both salts have the same molecular structure except that NaHNC has two rings, which means NaSal is less hydrophobic than NaHNC. Figure 6.8(a,b) shows the optimized structure of NaHNC and NaSal, respectively, with OAc HG in high pH acidic medium where the carboxylate HG is dehydrated. The binding energy of gas-phase calculations is about the same for both salts and sodium become a 4-coordination number ion with average Na–O bond distance of 2.38 and 2.36 Å for NaHNC and NaSal, respectively. The binding energy of NaSal with OAc HG has 6-flods increases once Na^+ is replaced with Ca^{2+} which freely available in solution upon reaction of HCl with carbonate rocks. Both oxygen atoms in the OAc Hg and Sal salt are bidentately binding to Ca^{2+} . The average Ca–O bond distance is found to be 2.30 Å and total binding energy is -479.1 kcal/mol. The complexation energy has increased to -537.5 kcal/mol once four water molecules are added explicitly to the system. The optimized structure is shown in Appendix C with Ca–OC average bond distance of 2.33 Å and Ca–OH₂ of 2.41 Å. the high binding energy of CaSal with calcium ion has 6-coordination number compared to 4-coordination indicates that the interaction is highly favorable in water solution. The other organic salts which we consider in this study are trimethylammonium chloride (Et_3NHCl) and p-toluidine hydrochloride (PTHCl). Both salts are cationic and optimized geometrical structures of all organic salts are shown in Appendix C. Rheological studies showed that organic counterions bind strongly to anionic surfactant micellar surface and highly effective in promoting micellar growth (Hassan, 2002; Kalur et al., 2005). It was observed there are maxima in the relaxation time and zero-shear viscosity as function of PTHC/SDS molar ratio due to formation of branches similar to micelle behavior in an inorganic salt (Hassan, 2002). The binding energy of organic salt with acetate HG is less than that of inorganic salts. Optimized structure of PTH^+ salt with acetate HG is shown in Figure 6.8(d) with -134.6 kcal/mol binding energy. This energy is 61.1 kcal/mol less than that of monovalent inorganic salt such as Na^+ . $\text{Et}_3\text{NH}(\text{OAc})$ do not favor the formation of cylindrical micelle and it has binding energy of -113.4 kcal/mol. The aromatic ring in PTH^+ help intercalated between the hydrocarbon chain and form high binding compared to Et_3NH^+ .

6.3.4 MD Simulation

We have run number of molecular dynamic simulation to study the behavior of anionic surfactant in large system of water and counterions. The acetate HG with tail consists of erucyl chain, chemically described as $(\text{CH}_2)_{12}-\text{CH}=\text{CH}-(\text{CH}_2)_7-\text{CH}_3$ are considered. Depending on the length of hydrocarbon chain, R-HG, surfactants with more than tetradecyle (C_{14}) are able to form wormlike micelles, while surfactant with shorter are not. Longer-linear chain such as octadecyle (C_{18}) has low solubility at room temperature. Oleyl group which include double bond in the middle of its alkyl chain has much lower crystallinity than the octadecyl and can form wormlike micelles at room temperature. The optimized structure of single surfactant monomer is shown in Appendix C along with charge distribution calculated at B3LYP/6-311++G** using ChelpG analysis based on single-point calculation. The simulation box was constructed with double layer by putting the surfactants tail-to-tail on square lattice in the x-z plane. The cluster builder utility in VegaZZ (Pedretti et al., 2004) was used to copy the first layer along x-y and y-z planes with 1000 minimization steps, 0% overlap, and RMS=0.01. Then the counterions and water molecules were added randomly in a predetermined box size of $80 \times 60 \times 50$ in x,y,z, respectively. Charge was calculated using Charmm force field (Brooks et al., 1983) included in Vega ZZ. Once the system is fully defined, MD simulation was carried out using NAnoscale Molecular Dynamics (NAMD) (Phillips et al., 2005). The system was allowed to equilibrate in 1000 steps with 1fs timestep size at a temperature $T=300$ K, following the equilibration, molecular dynamic run with 100,000 time steps of 1 fs step size, 12 Å cutoff, and periodic boundary is set to run. Figure 6.8(a) shows initial configuration of 32 erucate anionic surfactant with acetate HG, 2839 water molecules and 8 counterions (Ca^{2+}). The final system after 100,000 time steps (1 ns), is shown in Figure 6.8(b). It can be seen that as time progress, surfactant tail-molecules start to relax in solution while the HG maximize the contact with the cationic salt. Generally, the shape of micelles is still maintained after 1 ns simulation time. More results for various counterion concentrations at the same simulation conditions are shown in Appendix C.

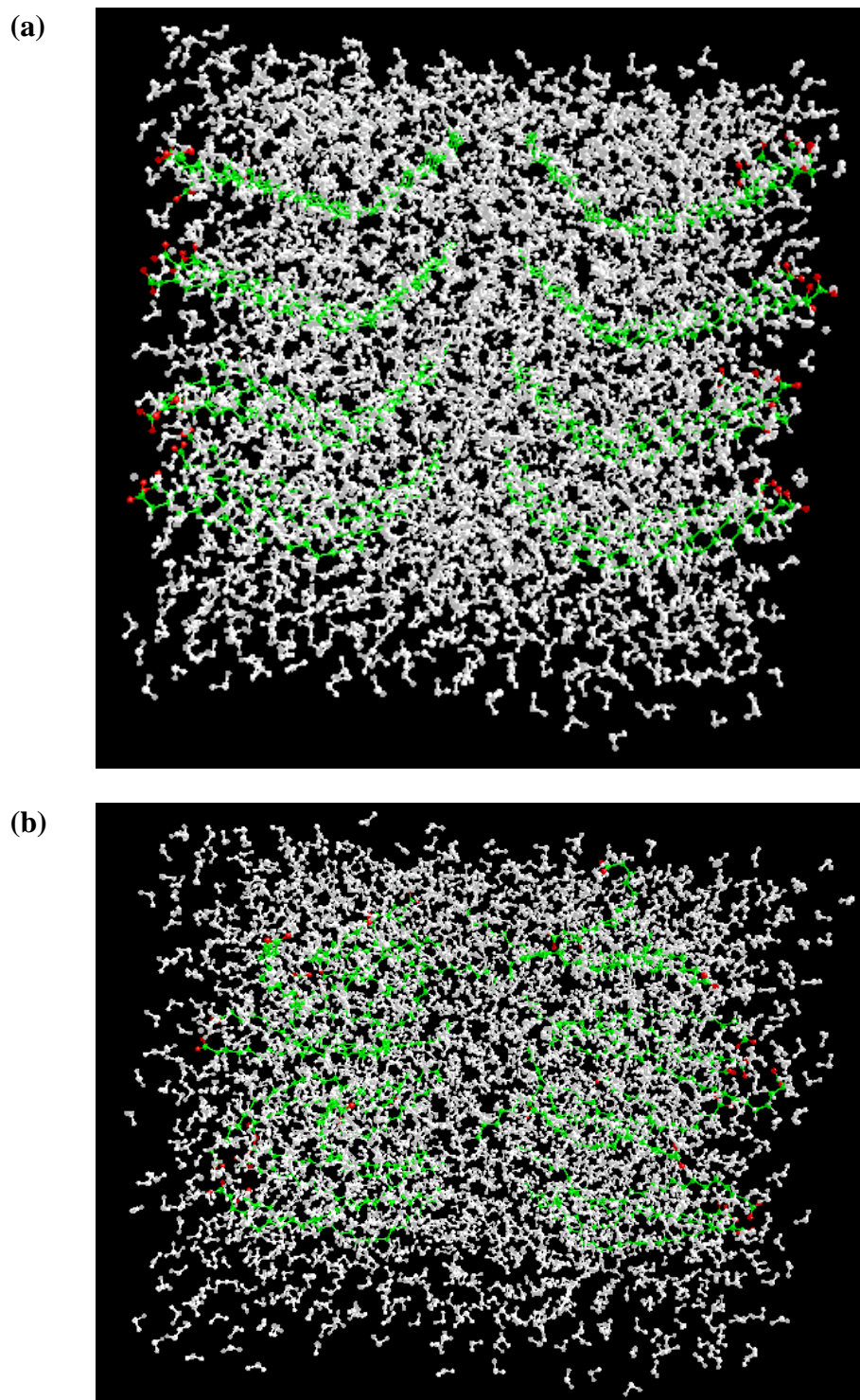


Figure 6.9: Molecular simulation snapshot for a system of 32 erucate anionic surfactants ($4 \times 4 \times 2$) with 2839 water molecules and 8 counterions (Ca^{2+}). (a) Initial geometry of 0.5 wt% and (b) final structure after 100,000 time steps (1 ns).

6.3.5 Potassium Butanoate (PB)

The second HG we have tested in this study is potassium butanoate. The difference between this HG and acetic acid HG is that AA has one methyl bonded to carboxylate functional group, whereas PB has an ethyl chain and potassium replacing hydrogen in the carboxylate group. If the hydrocarbon part of the surfactant is kept constant and only the headgroup is varied, then the difference in the aggregation behavior can be attributed solely to the properties of the polar headgroup. Potassium oleate is a common example of this HG. The objective here is to evaluate the effect of chain length (i.e. number of carbon atoms) of the HG and carboxylate external atom on HG interaction, its thermodynamic properties, binding energy and behavior in solution. Figure 6.8 shows the HOMO and LUMO calculated using DFT with 6-311++G** for PB in acidic and alkaline medium. Comparing PB MO with that for AA, we observe the effect of having one more methyl in the HG and how potassium redistributes electrons between the carboxylate oxygen atoms. In the case of [AA], the HOMO shows two regions of bonding and antibonding on carboxylate and methyl group, respectively, however, [PB]⁻ does not show that, but rather one oxygen is more involved in bonding than the other. Unlike conventional structure models, electron densities assume no prior knowledge about bonding and, therefore, can be used to elucidate bonding. Electrostatic potential of PB-HG mapped onto the electron density is shown in Figure 6.10 (a₃,b₃). Colors toward “red” indicate negative values of the electrostatic potential; while colors toward “blue” indicate positive values of the potential. Potassium atom (Figure 6.10a₃) minimizes the reactivity of carboxylate oxygen and eliminates the possibility of hydrogen bonding between two PB HGs as in the case of AA. Both oxygen atom in the carboxylate group have the same tendency to interact if K-atom is detached. Geometrical and thermodynamic properties of butanoate (Bu) interaction with Ca²⁺ and forming the complexes Ca(Bu)_n.mH₂O are summarized in Table 6.3. The binding energy for Ca(Bu)₂ is -492.3 kcal/mol, which is 2 kcal/mol less than that for acetate (Figure 6.11). This difference is attributed to addition of ethyl in the HG. Scanning relaxed potential energy for the dihedral angle, ϕ , of Bu is shown in Figure 6.12.

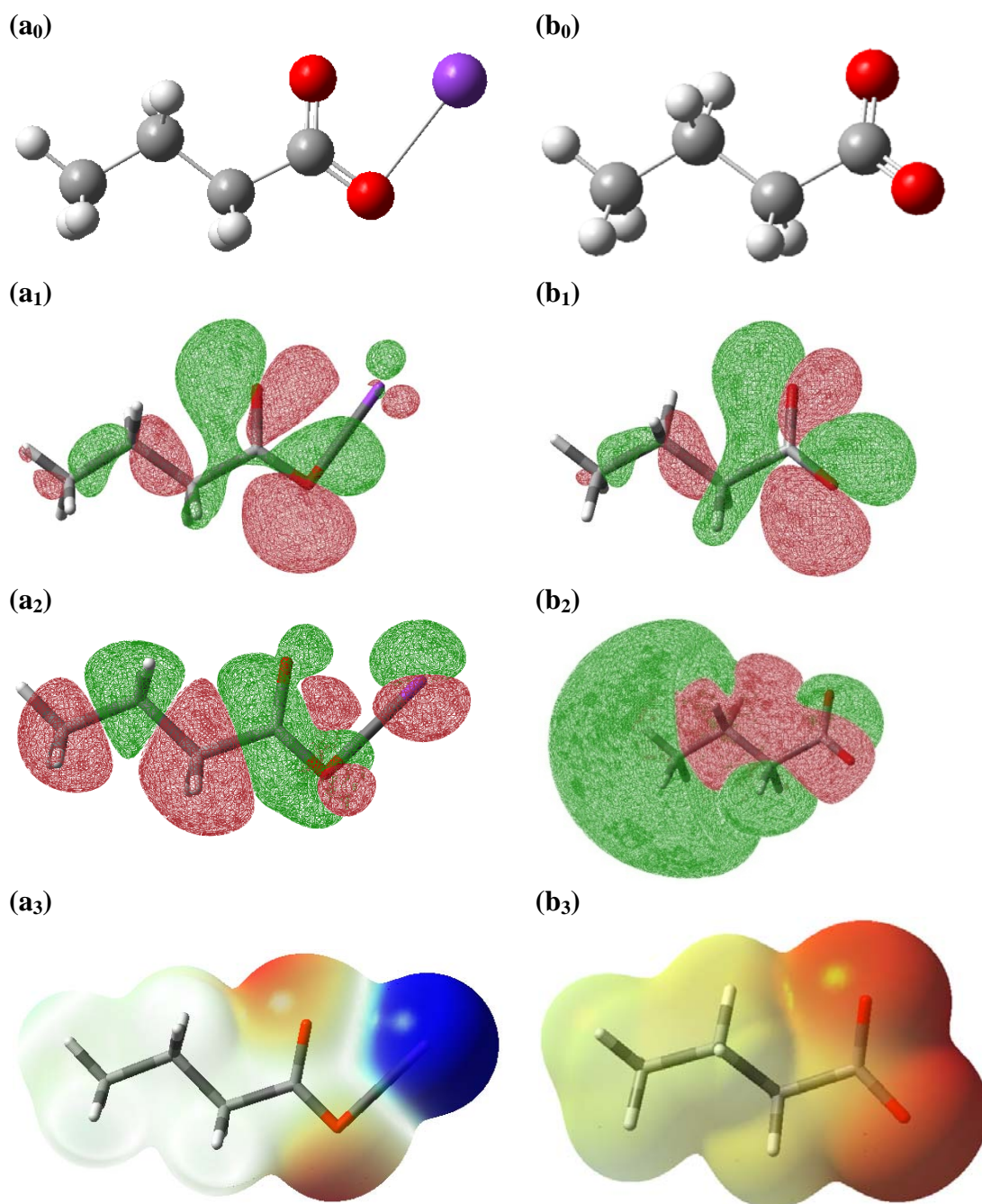


Figure 6.10: Optimized geometrical structure of potassium butanoate (PB) head group with localized HOMO and LUMO molecular orbitals. (a) PB in gas-phase, and (b) anionic [PB]⁻ in gas-phase with second row for HOMO, and third for LUMO and forth row for electron density potential, respectively. Isosurface value= $0.02 \text{ e}/\text{\AA}^3$, $0.004 \text{ e}/\text{\AA}^3$ for MO and density, respectively.

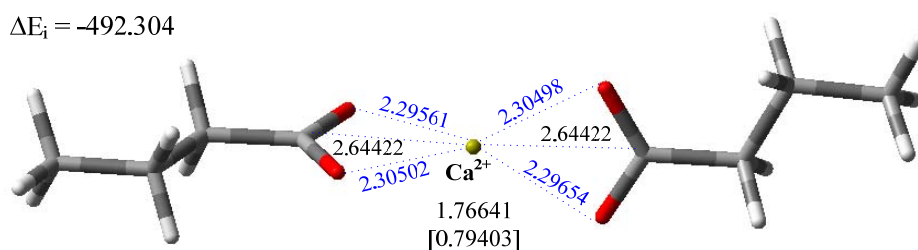


Figure 6.11: Complexation of potassium butanoate (PB) head group with Calcium (Ca²⁺) in gas-phase. Optimized structure at B3LYP/6-311++G**.

Table 6.3: Geometrical and binding properties of Ca(Bu)_n.mH₂O

(n,m)	CN	ΔE_i (kcal/mol)	M–OH ₂ (Å)	M–OC (Å)	$\langle \text{HB} \rangle$ (Å)	APT
2,0	4	-492.3	0.00	2.30	0.00	1.77
2,2	4	-520.4	2.30	2.23	1.52	1.83
2,3	5	-531.7	2.36	2.28	1.66	1.81
2,4	6	-652.7	2.42	2.33	1.79	1.82
2,5	7	-546.6	2.46	2.41	1.83	1.75
2,6	8	-559.0	2.89	2.37	1.80	1.78

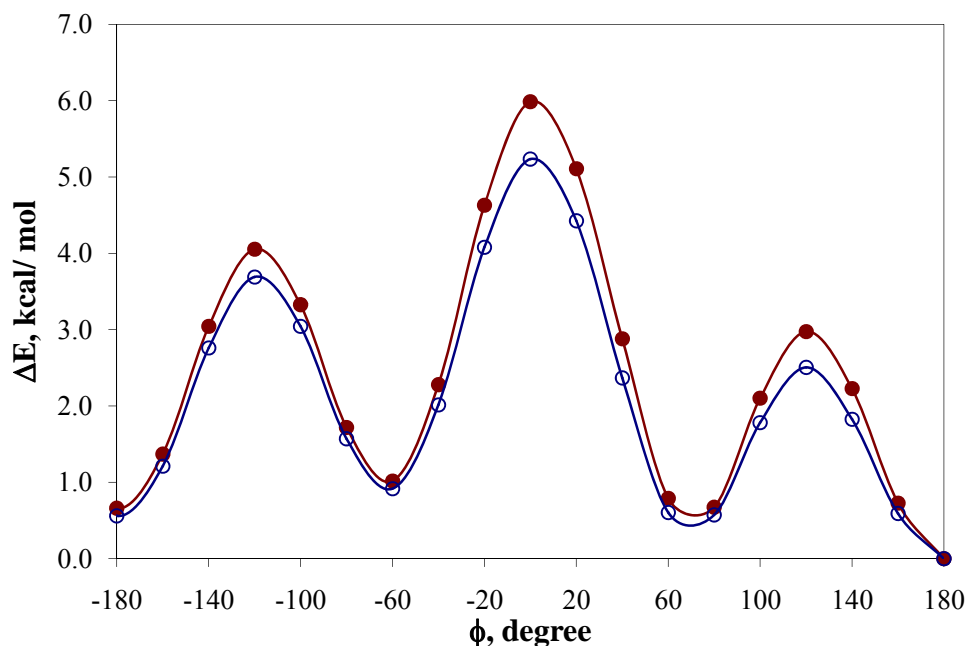


Figure 6.12: Calculated relaxed potential energy scanning for the dihedral angle, ϕ , C–C–C–C (1-2-6-11 in Figure C.1) using 6-31+g* at (●) HF and (○) B3LYP. ΔE is calculated as relative energy to the minimum value at $\phi=180^\circ$.

6.3.6 Sulfonate and Sulfate HGs

The smartness or switchability of viscoelastic surfactants in aqueous solution is not just a factor of the trigger (i.e. pH, T, etc.) but also depends on the molecular structure, the solution conditions such as temperature, concentration, and the presence of additives. Threadlike micelles are enormously long, sufficient to entangle each other and to cause pronounced viscoelasticity in solution. The addition of a sufficient amount of simple salts to spherical micellar systems effectively screens strong electrostatic repulsions between surfactant headgroups, so the effective size of the headgroup is reduced, inducing a micellar shape transition from a spherical to a threadlike shape. Sulfate (R-SO_4^-) and sulfonate (R-SO_3^-) are common example of anionic surfactant. We are considering two HGs with propyl and butyl chain and SO_4^{2-} , SO_3^{2-} groups, namely, sodium propyl sulfate (SPS) and sodium butane-1-sulfonate (SB1S), respectively. Figure 6.13 shows the molecular orbital of SB1S and its anion both in gas and water solution. The sulfonate group has three Oxygen atoms and all of them have good affinity to interact. The SB1S HG binding energy with Ca^{2+} and Mg^{2+} are -498.8 and -601.9 kcal/mol, respectively as shown in Figure 6.14. Those values are 40 kcal/mol and 20 kcal/mol lower than the corresponding $\text{Ca}(\text{OAc})_2 \cdot 4\text{H}_2\text{O}$ and $\text{Mg}(\text{OAc})_2 \cdot \text{H}_2\text{O}$, respectively. The affinity of sulfate HG toward interaction with cationic metal is higher as one more oxygen is added (Figure 6.14). Table 6.4 summarizes the binding energy and structural properties (Figure 6.15) of SB1S and SPS with Ca^{2+} and Mg^{2+} . In summary, counterions have great impact on the phase behavior and physical properties of anionic surfactants in solution. *Di-* and *trivalent* metal ions have the tendency to form micelles with more than two surfactants, which means that at the same surfactant concentration the sphere-to-rod transition will take place at much lower ionic strength compared to the case of monovalent such as Na^+ . This study suggests that in presence of more than one counterion, the interaction with carboxylate HG anionic surfactant, for example will be in the order: $\text{Al}^{3+} > \text{Fe}^{3+} > \text{Fe}^{2+} > \text{Mg}^{2+} > \text{Ca}^{2+} > \text{Na}^+$. The molecular architecture of the surfactant HG has great influence on the metal-HG interaction and hence on formation of micelles.

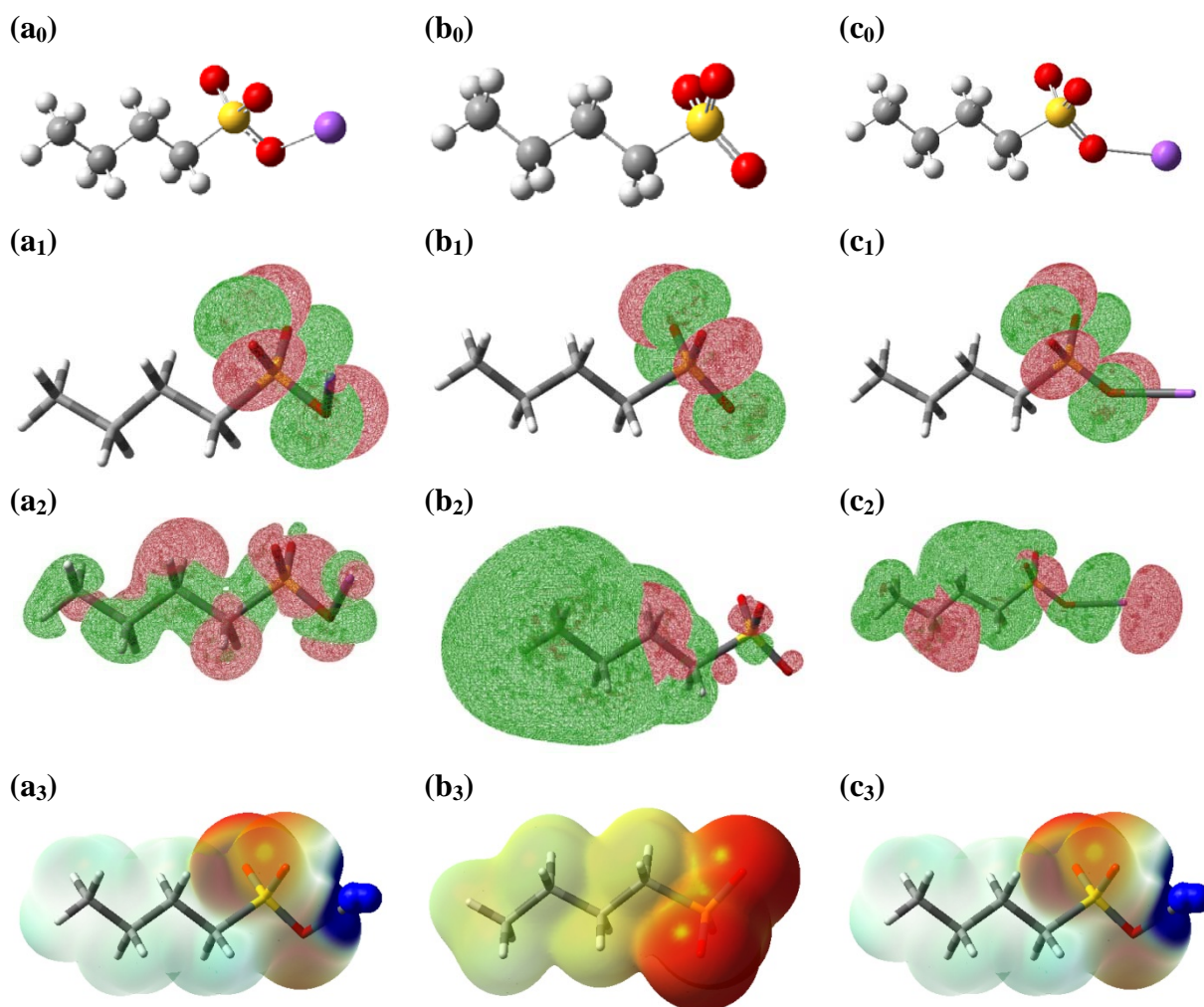


Figure 6.13: Optimized geometrical structure of sodium butane-1-sulfonate (S1BS) head group with localized HOMO and LUMO molecular orbitals. (a) S1BS in gas-phase, (b) anionic [S1BS][−] in gas-phase and (c) S1BS in water solution, with second row for HOMO, and third for LUMO, respectively.

Table 6.4: Binding energy, bond length and atomic charge calculated at B3LYP/6-311++G** for M(HG).4H₂O, (M= Ca²⁺, Mg²⁺; HG=H₂O, S1BS, SPS)

M	CN	HG	ΔE_i (kcal/mol)	$\langle M-O \rangle$ (Å)	$\angle OMO$ (°)	APT
Ca	6	H ₂ O	-242.4	0.00	90	1.86
	6	S1BS	-498.8	2.33	91	8.51
	6	SPS	-510.8	2.33	84	1.87
Mg	6	H ₂ O	-313.5	0.00	90	1.67
	6	S1BS	-601.9	2.06	88	1.65
	6	SPS	-587.6	2.05	89	1.63

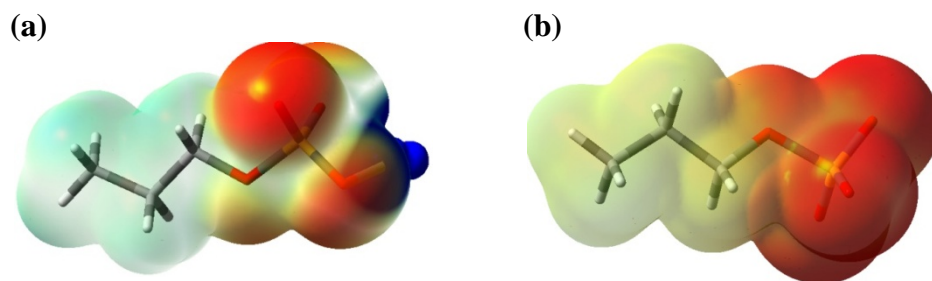


Figure 6.14: Potential density of sodium butane-1-sulfonate (S1BS) (a) S1BS in gas-phase, (b) anionic [S1BS]⁻ in gas-phase.

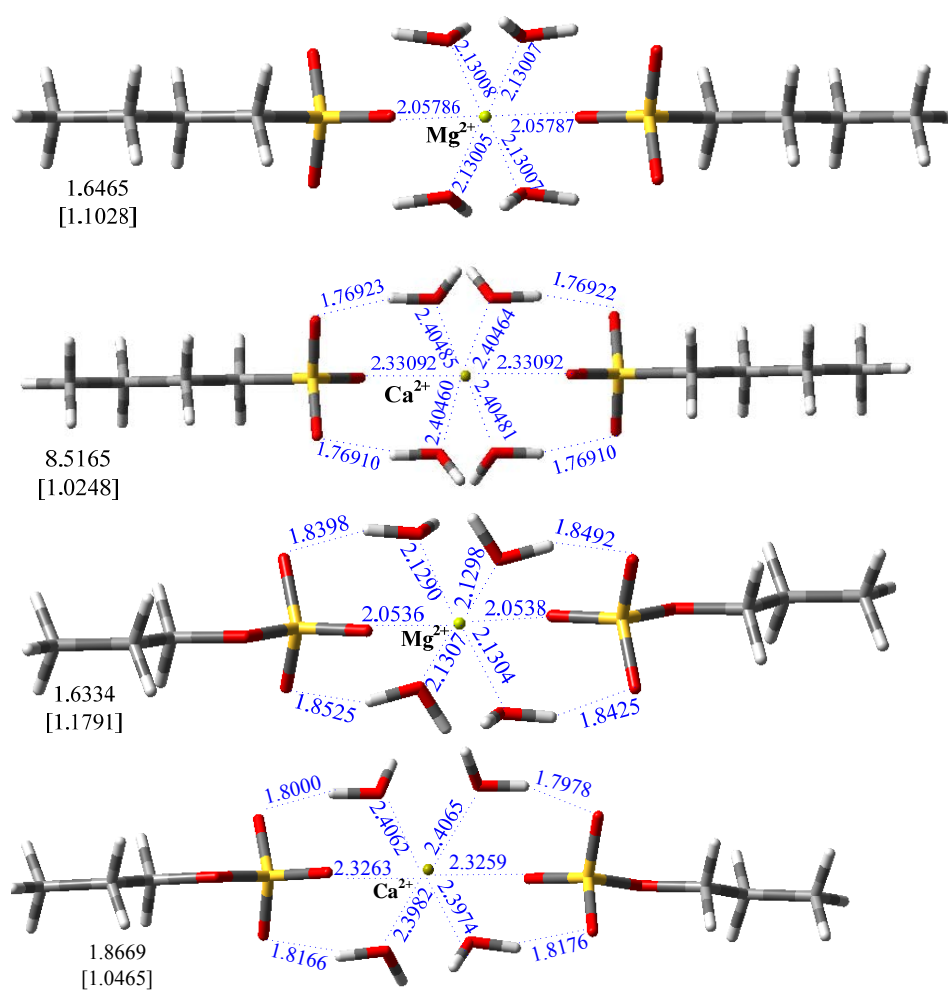


Figure 6.15:Complexation of sodium butane-1-sulfonate (S1BS) head group with (a) Ca²⁺, and (b) Mg²⁺ in gas-phase using B3LYP level of theory and 6-311++G** basis set. Binding energy for Mg(S1SB)₂ is 103.03 kcal/mol higher than that for Ca(S1SB)₂.

CHAPTER VII

THEORETICAL STUDY OF CATIONIC AND GEMINI SURFACTANTS IN ACID SOLUTION

And they ask you about the spirit. Say: the spirit is one of things, the knowledge of which is only with my Lord, and you are not given aught of knowledge but a little.
—Qur'an, Al-Israa, 17:85

Viscoelastic surfactants have been extensively used over the last few years in matrix acidizing and fracturing treatments. Injecting acid into carbonate reservoirs will result in reactions with the rocks and hence open up new channels around the wellbore, especially for low permeability reservoirs and in many cases remove any damage caused by spent drilling fluid, fine migration, paraffin, or mineral precipitation (scale). It is well known that cationic surfactants can self-assemble in aqueous solution into long flexible cylindrical shapes called wormlike micelles upon addition of salts. These wormlike micelles have a length in the order of microns and radii of ~ 2 nm, can entangle and enhance viscosity of the fluid. The salt serves to reduce the electrostatic interaction between the cationic headgroups which will result in effective area per headgroup and thereby enhancing the growth of micelles. Complete failure of cationic viscoelastic surfactants in presence of high ferric concentrations has been reported recently by one of the authors. Ferric ions work as viscosity enhancer at low concentration, cause phase separation at moderate concentrations and complete precipitation of surfactant at high concentration. The objective of this paper is to identify theoretically the mechanism by which ferric and tetrachloroferrate ions interact with cationic surfactants. Density functional theory (DFT) is used to study complexation of chloride, tetrachloroferrate, and $(\mu\text{-oxo})\text{bis-trichloroferrate(III)}$ ions with tetramethylammonium (TMA) and *N,N*-bis(hydroxymethyl)-*N*-methylethanaminium (HMMEA) head groups. Optimized geometrical structures and binding energies are reported in gas-phase and solution for all understudy headgroups. Classical molecular dynamic (MD) simulation is employed using erucyl chain with C22 as a tail for both head groups to resolve the full chemical details of chloride effect in solution. Results show strong dependence of micellar

structure on type and number of ions presented in solution. Four selected HG of cationic-gemini type of surfactant are also addressed in this chapter.

7.1 Introduction

The production of oil and gas from underground reservoir may often enhanced by stimulating the region of rocks (known as formation) surrounding the wellbore. Stimulation treatment fluid in many cases comprise acid. In carbonate reservoir, these acids will react with calcium carbonate to produce carbon dioxide, water and calcium chloride. After acidization is completed, the water and salts dissolved therein may be recovered by producing them to the surface by flowing back the well. To enhanced acidizing treatment various additives may be added to the treatment fluid. One such additive is a gelling agent which may increase viscosity and hence help to divert or properly place the acid fluids in a low permeability zone. Conventional chemical diversion methods include nitrogen foam, bridging agents like benzoic acid, and crosslinked polymer. These methods temporary plug high permeability carbonate zone to effectively divert the stimulation fluid to zones with lower permeability. Despite the advantage of using conventional chemical diverting fluid, some of them are problematic. For example, polymer gelling agents may leave an undesirable residue in the formation after use. As a result, potentially and costly remedial operation may be required to clean up the rock's pore. Surfactants with their viscoelastic behavior are found to be very useful in stimulation treatments. One of the very first choices was cationic surfactants. The most common cationic viscoelastic surfactants are based on quaternary ammonium salts of fatty acids. An early quaternary ammonium salt surfactant for oilfield applications was prepared from raw rapeseed oil (Zana and Kaler, 2007). The pure surfactant is a waxy solid at ambient temperature; therefore, a solvent is added to prepare solution form out of this surfactant that can be handled easily. The chemical and physical properties of cationic surfactant vary depend on length of the tail, functional group in the head and kind of the counterion (anion). The main feature of all quaternary compounds is the attractiveness to almost any surfaces that are negatively charged. Their salts are

considerably stable at ambient conditions and start decomposing above 100°C though a dealkylation reaction (Behler et al., 2001). Most cationic surfactants has quaternary ammonium head group and its maximum practical fluid temperature is about 54°C (Zana and Kaler, 2007). Once the HG molecular structure has ethoxylated quaternary ammonium salt based on erucic acid, the stability temperature increases to 79°C. This temperature can reach to 93°C by adding salicylate as a counterion to enhance the micelle growth (Kalur et al., 2005). Surfactant HGs were selected in this work based on their characteristics, availability and used as acid diverters. The five cationic HGs that will be presented in this chapter are: *N*-ethyl-2-hydroxy-*N*-(2-hydroxyethyl)-*N*-methylethanaminium (EhhMEA), *N,N,N*-trimethylethanaminium (TMEA), *N*-benzyl-*N,N*-dimethylethanaminium (BdMEA), *N,N*-bis(hydroxymethyl)-*N* methylethanaminium (HMMEA), *N,N,N*-trimethylmethanaminium or Tetramethyl-ammonium (TMA). We will refer to all of them hereafter by their abbreviation shown in the brackets. We report in this chapter quantum calculations at density functional theory (DFT) levels of the molecular properties in the gas phase and water solutions. The energy differences and the water effect on these HGs are analyzed. The objective of this chapter is to gain a deeper insight through quantum computations into the structural and energetic properties of selected cationic and gemini surfactant head groups (HGs) in gas phase and aqueous solutions. The information obtained will help us understand the electronic origin of the factors that determine the properties of these simple molecules, and to have better judgment when selecting VES for acid diversion in well stimulation treatment considering factors such as counterions, type of HG, and how they are affected by the water environment. The understanding of the properties of these self-assembly molecules requires an accurate knowledge of nonbonded interactions, such as the intramolecular HG–HG and the intermolecular HG–water hydrogen bondings, which are key contributors to the specificity of the interactions within and between macromolecules and that can be modeled through the study of the simpler anionic surfactant molecules. Molecular simulation of Cl[−] ions distribution around single surfactant monomer in water solution is presented.

7.2 Simulation

The DFT computations were performed using Gaussian 03 package (Frisch et al., 2004). The DFT studies employed the Becke gradient corrected exchange functional in conjunction with the Lee–Yang–Parr correlation functional with the three parameters (B3LYP) method (Becke, 1993). B3LYP is a gradient corrected method that includes some of the effects of electron correlations. This DFT approach usually gives rise to greater accuracy than Hartree-Fock (HF) for structure, thermochemistry, and spectroscopic properties, with only a slightly greater computational effort; this combination of efficiency and accuracy has made it perhaps the most popular method for practical applications. Results obtained with DFT approach are compared with experimental ones when available. Calculations are carried out in gas-phase with the 6-311++g** basis set at B3LYP levels to determine the geometric and energetic parameters of the different HGs and to establish the most stable ones. Also, water solution calculations, done with the self-consistent reaction field approach (SCRF) in which the solvent is treated as a continuum.

We adopted the polarizable continuum model (PCM) because it provides a quantitative estimation of the different contributions to the total free energy of solvation. Although the SCRF methods do not account for specific solute–solvent interactions, such as hydrogen bonding, and results based on these methods are clearly dependent on the selected size and shape of the solute cavity, they proved to be successful on analysis of the effect of solvents on solute properties and on isomer ratios. The coupling of PCM models with DFT to study the interactions of solutes and solvents is not frequent. In this work the properties of the anionic HG in solution were calculated at DFT theoretical levels with a 6-311++g** basis set. Comparison of gas and solution results allows clarifying the solute polarization effect. The properties of cationic HGs with water clusters were computed and their structures optimized at B3LYP levels with the 6-311++g** basis set. Finally, possible interaction between cationic HG and anionic species such as Cl^- , FeCl_4^- and $\text{Fe}_2\text{Cl}_6\text{O}^-$ are carried out using DFT.

7.3 Results and Discussion

Results in this chapter will include the molecular orbital theory analysis of each HG, in gas-phase and aqueous solution, the interaction between HGs and counterions. Molecular dynamic simulation of various Cl^- concentrations in water solutions with single BdMEA cationic surfactants is discussed.

7.3.1 Molecular Orbital Analysis

Orbitals fall into three groups, a very stable low energy group called the core, a higher occupied valence group and the group of unoccupied or virtual (Rauk, 2001). In molecular orbital (MO) theory (Carey and Sundberg, 2007), reactivity is related to the relative energies and shapes of the orbitals that are involved in the reaction and hence to the nature of substituents. Shape of the molecular orbitals and symmetry are particularly important for qualitative reactivity analysis. We are trying to understand how a change in molecular structure of an anionic surfactant HG will affect the (MOs). As molecules approach one another and reaction proceeds there is mutual perturbation of the orbitals. This process continues until the reaction is complete and the product is formed. The concept of frontier orbital control proposes that the most important interactions are between a particular pair of orbitals (Fukui, 1971). These orbitals are the highest occupied orbital of one reactant (HOMO) and the lowest unoccupied (LUMO) orbital of the other reactant. The HOMO represents the distribution and energy of the least tightly held electrons in the molecule while LUMO describes the easiest route to addition of more electrons to the system. If they are close in energy they could be intimately involved in chemical reactivity as postulated in perturbation molecular orbital theory. A further general feature of MOs theory is that only MOs of matching symmetry can interact and lead to bond formation. Error! Reference source not found.(a) shows the optimized geometry structure of BdMEA HG in gas-phase. The structure has ammonium group with benzene ring. The HOMO reflects reactivity of the ring and we are expecting that cations present in solution will probably interact with this side of the HG. At all pH values, cationic surfactant HGs do not undergo deprotonation as in the case of

carboxylic anionic HG. However, LUMO can qualitatively give an idea where the anions will interact with BdMEA HG. Figure 7.1(a'') shows that chloride ion, for example, can counterbalance the positive charge on the ammonium group by approaching N-atom from different possible directions. The shape of LUMO is mixed and spread over the ethyl, and three methyl groups attached to N. The tetramethylammonium (TMA), Figure 7.1(b) has been selected as the basic cationic surfactant HG with four methyl groups attached to N-atom in a tetrahedral geometrical structure. The Lewis structure shows that N^+ has one free electron which could explain the HOMO shape around nitrogen. All hydrogen atoms in TMA have mixed LUMO which makes them reactive toward chloride or other anions present in solution. The third cationic HG is *N*-ethyl-2-hydroxy-*N*-(2-hydroxyethyl)-*N*-methylethanaminium (EhhMEA) where nitrogen is connected to two *trans*-ethanol ($-CH_2CH_2OH$) groups, one ethyl and one methyl group. The oxygen atom in the ethanol groups provides reactive part with cations as we can see from HOMO representation, while LUMO shows that anions can counterbalance the positive charge on N by approaching the structure from two symmetrical angles. Figure 7.1(d) shows a similar structure to EhhMEA with the two ethanol groups replaced by methanol ($-CH_2OH$), *N,N,N*-trimethylethanaminium (TMEA). The reactivity of HOMO will increase as the oxygen atoms become closer to nitrogen with one free electron. The LUMO shows very interesting spherical shape with all hydrogen atoms from two-methyl, and two-ethanol groups are readily available for interaction with anions in acid solution. That last cationic HG that we are considering in this chapter is *N,N*-bis(hydroxymethyl)-*N*-methylethanaminium (HMMEA). This structure differs from TMA with one methyl group has been replaced with ethyl group. The HOMO shows the ethyl group shares similar orbitals around the carbon atoms, while LUMO has one mixed sphere around the central N. Mapping the electrostatic potential on electron density results in one positively charged cloud around the molecular structure of all cationic HGs. The color is in the range of blue with highest value on nitrogen atom, which indicates that the HG is readily acting as cation.

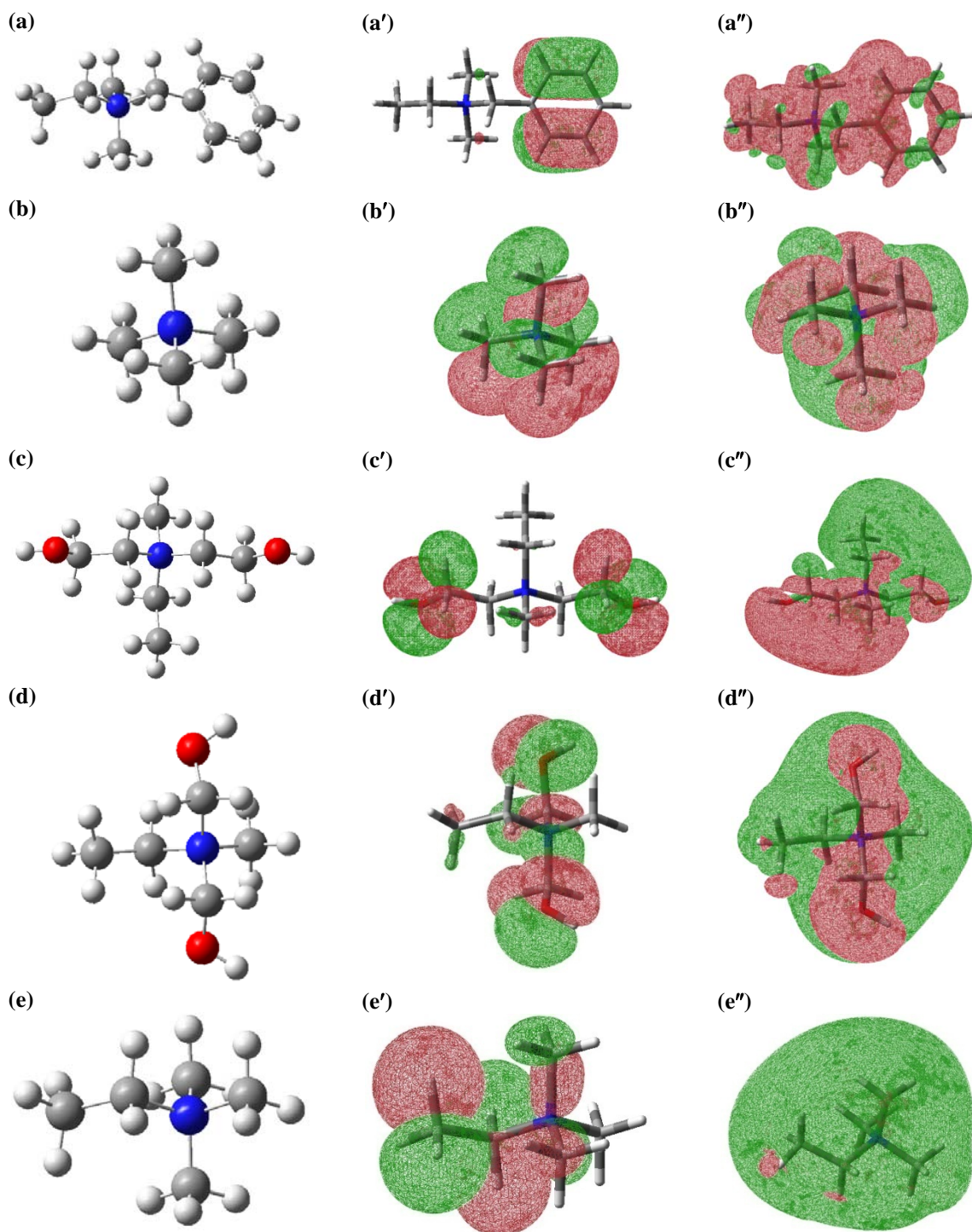


Figure 7.1: Optimized geometrical structure of selected *cationic* head groups (HGs) with localized HOMO and LUMO molecular orbitals in the second and third column, respectively. (a) BdMEA, (b) TMA, (c) EhhMEA, (d) HMMEA and (e) TMEA . Color code: red for O, blue for N, dark gray for C and light grey for H.

7.3.2 Interaction with *Cl*

The rate of HCl dissociation in acidic solution of stimulation treatment is high as we have seen in Chapter V. Cationic surfactants depend on organic and inorganic counterions to aggregate and form wormlike micelles. Studies on single chain surfactant have shown that the counterions exert a strong influence on critical micelle concentration (cmc), aggregation number, and shape of the aggregation (cate). Spherical micelles of cationic surfactant are formed in combination with halide counterions, whereas aromatic counterions often induce the formation of wormlike micelles at relatively low surfactant and counterion rates (Wattebled and Laschewsky, 2007). The most important property of cationic surfactant from an environmental perspective is that they are strongly sorbed by a wide variety of materials including natural sediments, clay minerals and soils by an ion exchange mechanism (Boethling, 1994). Displacement of small cations such as H^+ , Na^+ , and Ca^{2+} from the surface of clay minerals by large organic cations may significantly alter the properties of reservoir rocks. It has been shown that the process of adsorption of CTAB and DTAB cationic surfactant with Na- and Fe-montmorillonite is exothermic and the type of clay and the alkyl chain length of surfactant affect the adsorption rate and its enthalpy (Chen et al., 1998). In matrix acidizing treatment, cationic surfactants are used as corrosion inhibitor or drag reduction, while useful as viscosity builder in hydraulic fracturing and gravel packing applications. Viscosity of this type of surfactant is a high function of chloride ion concentration. The optimal chloride concentration in brine solution for maximum viscosity was found to be in the range of 0.6 – 0.8 mol/L, and viscosity drops below and above this range (Zana and Kaler, 2007). A major advantage of cationic viscoelastic surfactant in oilfield industry is their low sensitivity to variation in water quality, and presence of divalent cations, however, they are expensive. Another problem with cationic surfactant is their propensity to form emulsion with some crude oils, particularly those containing paraffins and Asphaltene, which will consequently hinder cleanup and lower the hydrocarbon production rate (Zana and Kaler, 2007). As a result, interaction of cationic surfactant with chloride is the main focus of this chapter.

The understanding of cationic surfactant chemistry in aqueous solution that contains chloride ions shall help designing more effective and efficient well stimulation treatment. Water molecules have strong networking structure of hydrogen bonding as we have seen in Chapter V. Competitive and cooperative interaction between water molecules and cationic HG will affect the hydrogen bonding network and hence the properties of the solution. Hydrogen bond can be formed and broken on extremely short time scale (pico-second) (Marcus, 2009). Figure 7.2 shows optimized structures for TMA^+ with chloride counterion and four water molecules. Recently, the structures of TMA^+ and phenyltrimethylammonium (PTMA^+) with 1–8 water molecules attached were investigated using infrared photodissociation spectroscopy (IRPD) (Prell and Williams, 2009). They reported that the binding energy of water to TMA^+ is 44.0 kJ/mol, which is significantly lower than water-metallic ions shown in chapter 4. The initial structure in Figure 7.2(a) was constructed with all water molecules are bound to Cl^- through one hydrogen and initial Cl-N bond distance of 2.11 Å. Two water molecules in the final optimized structure break symmetry around Cl^- and form hydrogen bonding with the other two water molecule and with the hydrogen from methyl group. The cluster $[\text{Cl}(\text{H}_2\text{O})_4]^-$ has a total binding energy of -73.8 kcal/mol and its optimized structure is shown in Appendix D. Water molecules are forming teracyclic ring with average hydrogen bond of 2.07 Å and the four free hydrogens are pointed out toward Cl ion and has an average $\langle\text{Cl-H}\rangle$ of 2.39 Å. The complex has a total binding energy of -169.8 kcal/mol and the Cl-N bond length of 4.66 Å. The average hydrogen bond between the two water molecules is 1.56 Å and each of the two side-water molecules which are not connected to Cl^- are forming hydrogen bonds with two methyl hydrogen of 2.24 Å in average. Chloride ion has an average bond length of 3.51 Å with three methyl hydrogens, and 1.98 Å with water hydrogen.

The structure in Figure 7.2(b) is the final optimized structure of $\text{TMA-Cl.4H}_2\text{O}$ where it has initial geometry similar to that in (a) but with Cl-N initial distance of 4.74 Å and some disorder in symmetry. The total binding energy of this complex is calculated to be

-170.2 kcal/mol. Unlike the first case, chloride is in good bonding with three hydrogen atoms from three water molecules with $\langle \text{Cl-H}_w \rangle$ of 2.11 Å. The fourth water molecule forms trimer with average hydrogen bonding of 1.760 Å. This structure is more stable than (a) because water molecules in the surrounding tend to form six hydrogen bonding with methyl hydrogen. The chloride ion is not in close contact with any methyl hydrogen atom and the calculated average distance $\langle \text{Cl-H} \rangle$ is 3.48 Å. The most stable (i.e. high binding energy) structure is shown in Figure 7.2(c). The starting structure in this case has Cl-N bond distance of 4.62 Å with two water molecules placed closed to 2-methyl groups. Total binding energy is calculated to be -170.7 kcal/mol which is 0.8 and 0.5 kcal/mol larger than case (a) and (b), respectively. This small increment in binding energy is due to the arrangement of water molecules around TMA^+ where they form a hemisphere with three water molecules are connected through average hydrogen bond of 1.62 Å. The chloride ion is acting as central connecting point between three water molecules with average $\langle \text{Cl-H}_w \rangle$ of 2.22 Å and. Also, Cl^- is in strong contact with two methyl hydrogen with bond length $\langle \text{Cl-H} \rangle$ of 2.81 Å. The networking of hydrogen bonding between water molecules and methyl hydrogen gives the structure high stability. The geometrical configuration in Figure 7.2(d) is the least stable compared to the three cases before. The initial structure was constructed by placing TAM^+ , two water molecules on its left, chloride ion and then two water molecules on the far left. Which means the Cl^- is caged between two water molecules on each side. Initial structures are shown in Appendix D in similar order. The two water molecules off the plane are migrating to form hydrogen bonding with the other 2-water molecules and with methyl hydrogen. This explains the tendency of water molecules to form shield around TAM^+ with less access or penetration of chloride ion. This complex has a total binding energy of -157.8 kcal/mol with zero hydrogen bonding between water molecules which could explain the low stability. The Cl-H bond distance with methyl hydrogen (3.39 Å) is weak compared to normal Cl-H length of 2.38 Å (Davies et al., 2003). The complex has 8-hydrogen bonding of average length $\langle \text{HB} \rangle = 2.52$ Å between water molecules and methyl hydrogen that contributes to its stability.

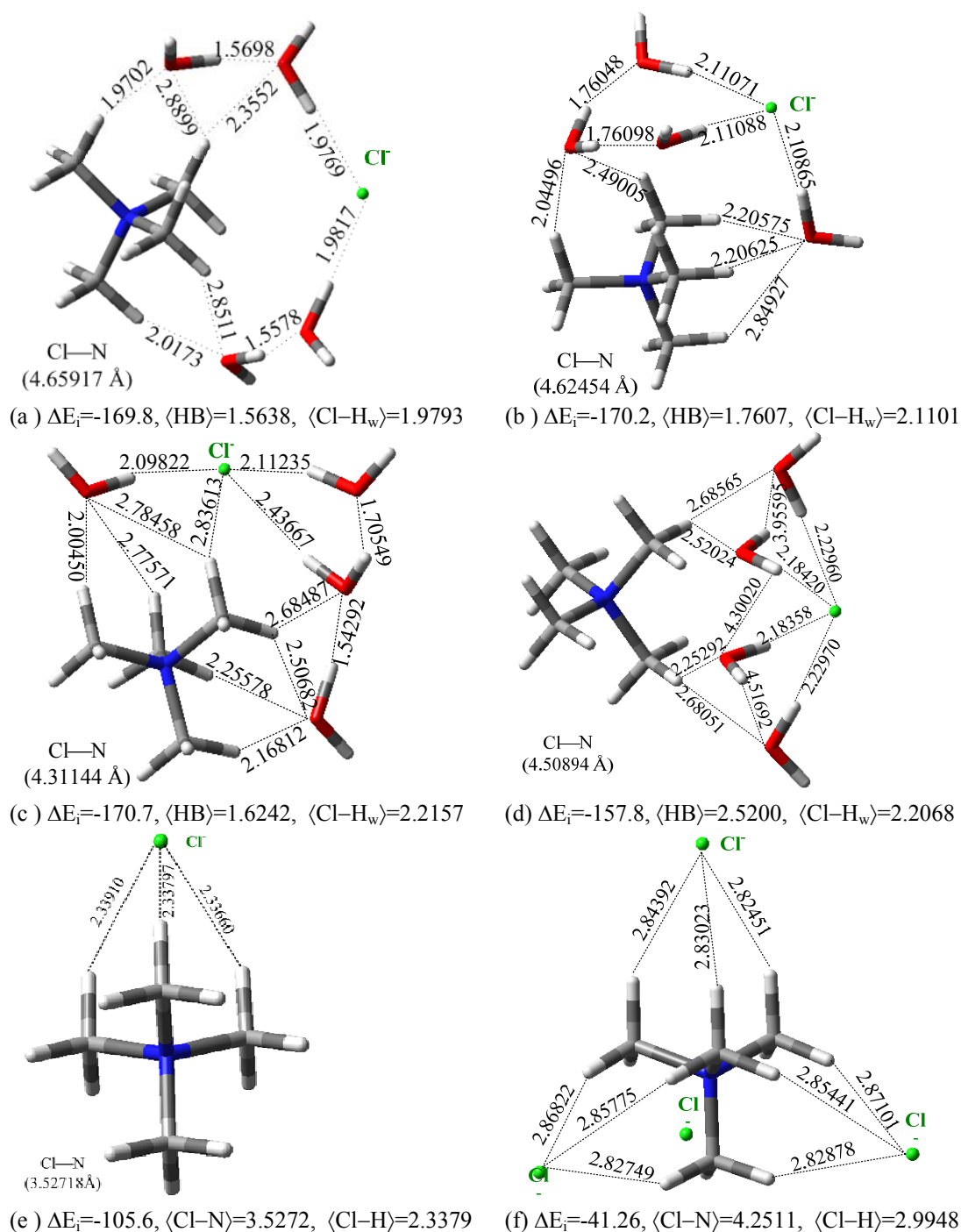


Figure 7.2: Optimized molecular structure for TMA interaction with Cl and 4-water molecules calculated at B3LYP/LAnL2DZ. (a) TMA[Cl.4H₂O], (b) TMA[Cl.4H₂O], (c) TMA[Cl.4H₂O], (d) TMA[Cl.4H₂O], (e) TMA-Cl and (f) [TMA-Cl₄]³⁻. Shown in the picture the total binding energy, kcal/mol, average hydrogen bond, Å and Cl-H bond distance Å. color code: red for O, green for Cl, dark gray for C and light gray for H.

For interaction between single chloride ion and TMA^+ , the optimized structure is shown in figure 7.2(e). It has been reported that the chloride forms more stable complex with TMA^+ compared to fluoride or hydroxide ions (Davies et al., 2003). The calculated total binding energy of TMA–Cl complex is -105.6 kcal/mol with average Cl–H bond distance of 2.34 Å. This result suggests the possibility of chloride ion to interact partially with three hydrogen atoms from three different methyl groups to more stable complex. In Figure 2.3(f), four chloride ions form average Cl–H bond of 2.99 Å, which is 0.66 Å larger than the average single Cl–H bond. The complex is stable and its total binding energy is highly dependent on the total charge assigned to the molecule at the same multiplicity (-41.3 and -91.3 kcal/mol for (-3) and (-1) charge, respectively). Values of binding energies indicate that free chloride ions in the solution will preferably counterbalance the positive charge on ammonium HG, however, it is less favorable for more than one Cl^- ion to complexate with the cationic part of the surfactant, though it is possible thermodynamically. High concentration of counterion does not necessarily increase the transition between spherical and wormlike micelles. Cationic surfactants have the tendency to aggregate in presence of strong counterion such as chloride or by increasing temperature (Zana and Kaler, 2007). The apparent surface area at the interface, a , of single surfactant HG decreases as the concentration of counterion increases. The packing parameter, $p = \nu / (l_{\text{max}} a)$, where ν and l_{max} are the volume and length of hydrophobic part of surfactant monomer, respectively, reaches value close to one when wormlike micelles formed. It has been reported that the hydrated headgroup apparent area increases as more salt added to solution (Vlachy et al., 2009). This increase in HG area is in agreement with the decrease in binding energy that we observe in this study. The additional ions will complete with the HG for water.

We have also examined the angle from which Cl^- ion could approach cationic HG and counterbalance the positive charge and the minim distance to nitrogen atom. Figure 7.3 shows initial structure of cationic HG in first column and the final optimized structure in the second column with bond distance shown in all cases.

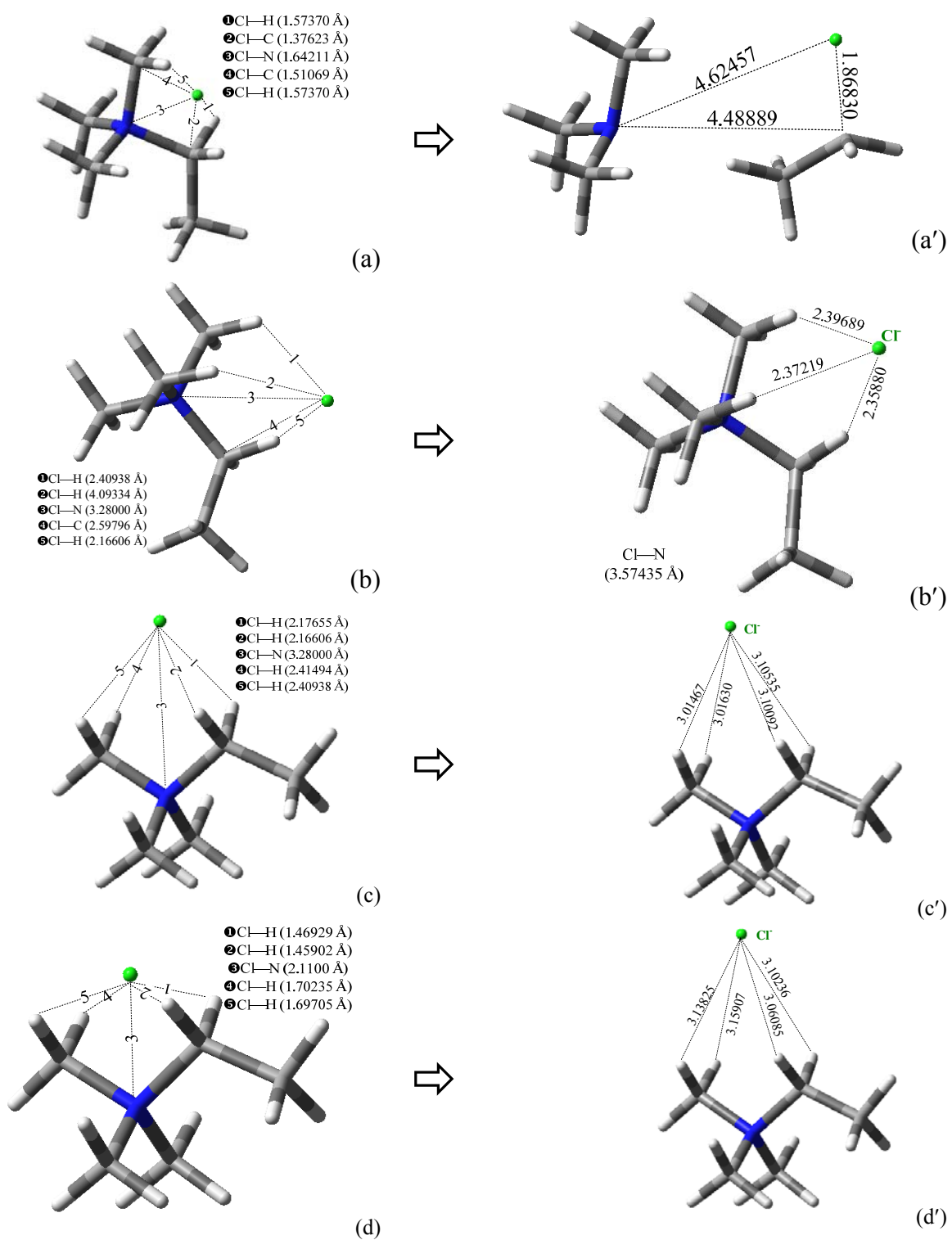


Figure 7.3: Initial (first column) and final optimized structure (second column) of TMEA cationic HG with Cl⁻ as a counterion.

The initial structure in Figure 7.3(a) has Cl–N distance of 1.64 Å and Cl–C_{ethyl} of 1.38 Å, which result in two complexes: ethyl-chloride and trimethyl ammonium. The ethyl chloride part of the final structure has Cl–C bond of 1.87 Å and the N–C bond increases to 4.49 Å. The final optimized complex has a binding energy of -118.8 kcal/mol. This result is not realistic, considering the fact that breaking N–C bond and forming the new bond Cl–C requires high energy. Therefore, we repeated the same calculations with different initial bond length between Cl–N and Cl–C_{ethyl} (2.38, 2.60 Å, respectively) as in Figure 7.3(b). The final optimized structure shows one complex with total binding energy of -114.8 kcal/mol which is 4.0 kcal/mol less than the first case. Results of gas-phase calculations suggests that there is a critical bond distance between the counterion and carbon atoms of the ammonium HG below which the cationic HG favor breaking one of the alkyl (R-groups) to form more stable complex composed of alkyl-chloride and tertiary amine. To further verify this concept, we have carried out the calculations in using implicit solvent (PCM) model with objective of mimicking behavior in solution as the case for real stimulation treatment. PCM model has been the choice for many researchers where solvent (water) is defined as a cavity of union of a series of multiple interlocking atomic spheres. The real representation of solvent effect is to add explicit water molecules around the counterion and HG, which is expensive computationally. Figure 7.3(c,c') shows initial and final optimized structure, respectively, of TMEA with Cl⁻ as counterion in water solution. This case is similar to Figure 7.3(b), however, the final structure shows that Cl⁻ ion bind with four hydrogen atoms from two alkyl group in the ammonium HG with average Cl–H bond distance of 3.08 Å. This value is larger than that in (b) because of the extra Cl–H bonding. The optimized complex has a binding energy of -10.4 kcal/mol and Cl–N bond length of 4.23 Å. The critical bond distance of counterion and its influence on the final structure that we observed in gas-phase need to be tested in water solution. Figure 7.3(d) has similar initial structure to (a), with calculation has been carried out using PCM model. The optimized complex has a total binding energy of -13.1 kcal/mol and with no breaking in the N–C_{ethyl} bond. Chloride ion tends to form four Cl–H bonding with average bonding length of 3.11 Å. the Cl–N bond

distance in solution is larger than that in gas-phase which suggest a competition between counterion and the hydrophilic-HG for water molecules.

We also have carried out calculations of chloride counterion interaction with other cationic HGs to understand the effect of molecular structure on binding energy. Figure 7.4(a) shows the initial and final structure of HMMEA with Cl^- ion has been placed very close to the quaternary ammonium group. The $\text{Cl}-\text{C}_{\text{methyl}}$ bond distance in the initial structure is 1.31 Å which is less than the normal $\text{N}-\text{C}_{\text{methyl}}$ bond (1.47 Å). The gas-phase final optimized complex results in methyl chloride and (ethylimino)dimethanol (also called bishydroxymethyl) with total binding energy of -111.6 kcal/mol. This breaking in the methyl group is not observed in water solution calculation (Figure 7.4(d)), which clearly indicates that the initial bond distance between chloride ion and other atoms in the HG is critical in determining the final complex. When Cl^- ion is placed between atoms C(1), C(4), C(15) and N (Figure D2(a)) is the gives lower energy compared to chloride approaching the HG from the side of alcohol group (between atoms C(12), C(8), O(19) and N). The later result in larger total binding energy of -124.5 kcal/mol and average shorter $\text{Cl}-\text{N}$ bond of 3.69 Å (Figure D.2(b)). The average $\text{Cl}-\text{H}$ is shorter than the case of Figure 7.4(b) because $\text{Cl}-\text{OH}$ is 1.92 Å. Our calculations suggest that replacing the two CH_3 in the ethyl part of TMEA with OH results in higher binding energy with Cl^- counterion. Also, Cl^- ions in gas-phase calculations form shorted distance with hydrogen from OH (alcohol group) compared to methyl hydrogen. Once one more CH_2 is added to the alcoholic group in HMMEA to form bishydroxyethyl (EhhMEA) HG, the binding energy decreases to the range of -(113–115) kcal/mol depending on how Cl^- approaches the HG (Figure D.5). Similarly, benzene ring in BdMEA decreases the total binding energy with Cl^- to around -113 kcal/mol compared to -124 kcal/mol in HMMEA. As we have seen in Chapter VI, an organic salt has lower binding energy compared to inorganic as Figure D. Organic salts induce formation of wormlike micelles with increasing temperature of the solution (Davies et al., 2006).

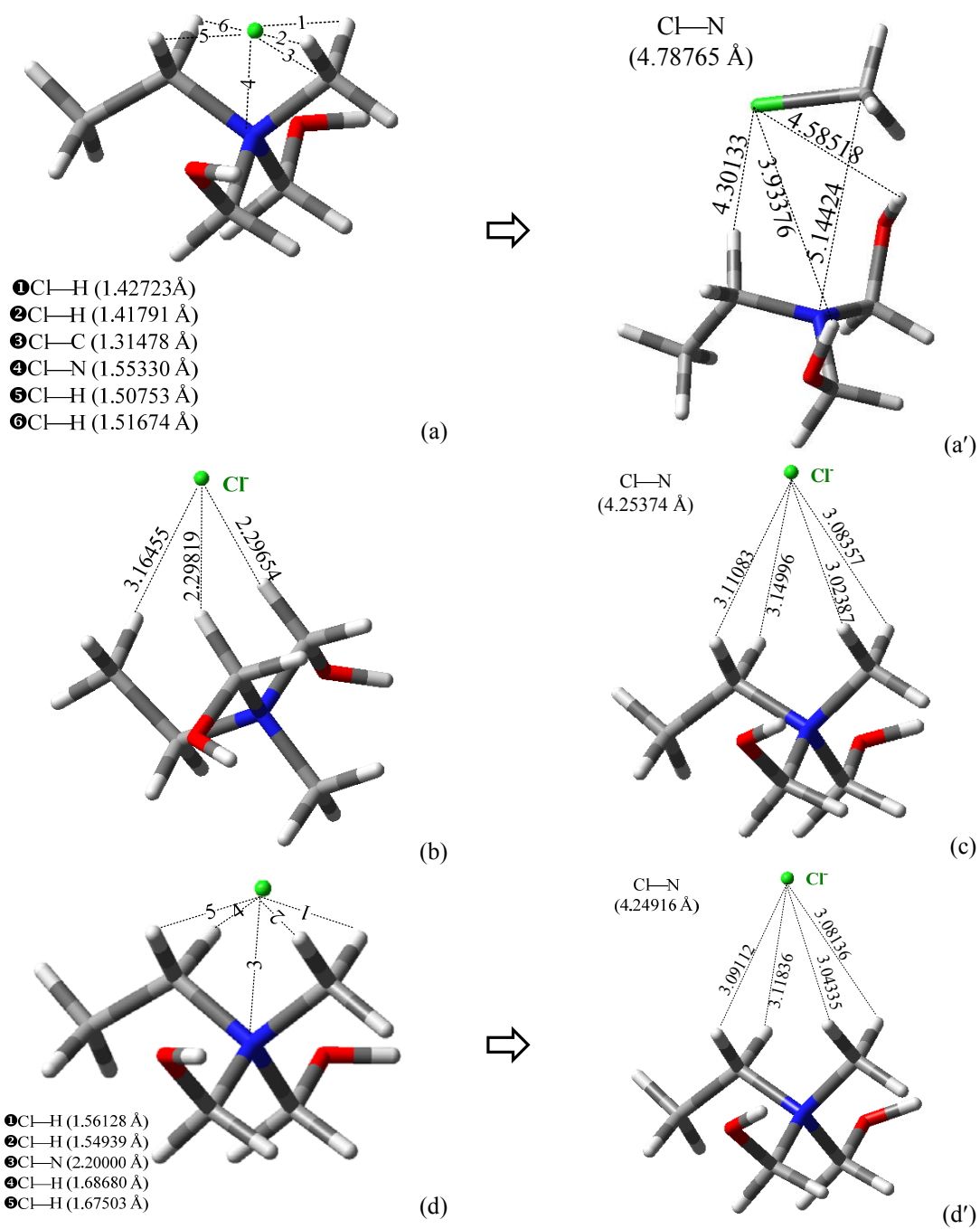


Figure 7.4: Initial (first column) and final optimized structure (second column) of HMMEA cationic HG with Cl⁻ as a counterion.

7.3.3 Complexation with $[\text{FeCl}_4]^-$

Viscoelastic surfactant in particular has enjoyed successful applications in well stimulation treatments over the last 10-years. Recently, Nasr-El-Din and his group reported that cationic surfactant shows increases in viscosity with ferric ions in an acidic solution until $[\text{Fe}^{3+}] = 1,000 \text{ mg/l}$, then decreases to a value close to zero at $10,000 \text{ mg/l}$ (Al-Nakhli et al., 2008). Separation of two immiscible liquids was observed at $[\text{Fe}^{3+}] = 5,000 \text{ mg/l}$. The addition of alcohol (propargyl alcohol and methanol) as a corrosion inhibitor increases initial viscosity at $[\text{Fe}^{3+}] = 1,000 \text{ mg/l}$, but then drops in a similar manner compared to the case with no alcohol. The effect of adding alcohol or amine to viscoelastic systems has shown an increase in viscosity of EHAC cationic surfactant in previous studies (Hartshorne et al., 2007). Both quaternary ammonium surfactants and ferric ions have a positive charge, however, the precipitation of surfactant at high concentration of iron means there is an anionic moiety present in solution responsible for phase-separation and drop in viscosity.

This part of the chapter will show theoretical evidence of possible complexation between tetrachloroferrate $[\text{FeCl}_4]^-$ and cationic surfactant. We have presented in Chapter 5 the complexation of ferric ion with chloride presented in acidic solution. Also, we have noticed that $[\text{FeCl}_4]^-$ is the most stable in energy (gas-phase) compared to other higher anionic complexes such as $[\text{FeCl}_5]^{2-}$, and $[\text{FeCl}_6]^{3-}$ which might be found in solution at higher HCl concentration. Complex anions of chloroferrate containing four, five and six chloride have been reported with less attention on $[\text{FeCl}_5]^{2-}$. A Gummy and insoluble polymer precipitation has been observed before with ferric ion present in acid solution of viscoelastic surfactant (Teot, 1998). It has been attributed to formation of tetrachloroferrate, which was suggested to work as a diverting agent. As the acid is spent, the hydrogen ion concentration decreases and tetrachloroferrate dissociates and redissolves in water solution, and thereby facilitating the removal of spent acid composition from formation (Teot, 1998). To the best of our knowledge, there is no systematic study that showed the dissociation of $[\text{FeCl}_4]^-$ upon decreasing acid concentration.

$[\text{FeCl}_4]^-$ decomposes in DMSO and methanol (MeOH) and it is not stable in amphiprotic solvent due to the propensity of the solvent form hydrogen bonding (Wyrzkowski et al., 2006). The complexation of tetrahalogenoferrate with tetramethylammonium has been studied experimentally by number of authors. Magnetic and crystal properties of synthesized $[\text{CH}_3)_4\text{N}][\text{FeBr}_{4-n}\text{Cl}_n]$ ($n=1-4$) showed isostructural complex in solid state (Wyrzkowski et al., 2008). Tetrahalogenoferrate (III) anions form stable compounds with quaternary aliphatic amine cations (Wyrzkowski et al., 2006). The resulting complex does not decompose when dried until upto 120 °C and has high stability at ambient temperature over a year or longer (Wyrzkowski et al., 2006). The tetrabutylammonium tetrachloroferrates (III), $[\text{C}_2\text{H}_9)_4\text{N}][\text{FeCl}_4]$, has high molar conductivity in alcoholic medium ($\sim 268 \text{ S.cm}^2/\text{mol}$ in methanol) which suggest good conducting complex. Crystal molecular structure of $[\text{FeCl}_4]^-$ complex with aromatic cationic ring of 4-methylpyridinium has shown that the position of methyl substituent affect the properties of the complex (Wyrzkowski et al., 2007).

The tetramethylammonium–tetrachloroferrate, $[(\text{CH}_3)_4\text{N}][\text{FeCl}_4]$, complex has a yellow color as reported by other study (Neuse and Meirim, 1984) which is similar to the color observed by Nasr-El-Din et al. (Al-Nakhli et al., 2008). Figure 7.5 shows $[\text{FeCl}_4]^-$ complexes with TAM^+ and HMMEA^+ . The TAM– FeCl_4 complex in gas-phase with no water molecules has a total binding energy of -69.3 kcal/mol. The binding energy is defined by: $\Delta E_i = E_{\text{complex}} - (E_{\text{HG}} + E_{\text{FeCl}_4} + n\text{H}_2\text{O})$ for all complexes. Both TAM^+ and FeCl_4^- has a tetrahedral structure with $\langle \text{Fe}-\text{Cl} \rangle$ average value of 2.27 Å which is larger than what found experimentally using X-ray diffraction (~ 2.19 Å) (Wyrzkowski et al., 2008). Three chloride atom from FeCl_4 are facing the TAM^+ and forming average $\langle \text{Cl}-\text{H} \rangle$ of 2.82 Å. Adding one water molecule to the other side of $[\text{FeCl}_4]^-$ complex increases the binding energy to 75.2 kcal/mol, which means this interaction is highly favorable in water solution. The same complex is optimized using PCM and has total binding energy of -40.2 kcal/mol. Changing the molecular structure does not result in critical change in binding energy with $[\text{FeCl}_4]^-$ as shown in Figure 7.5(d) for HMMEA^+ .

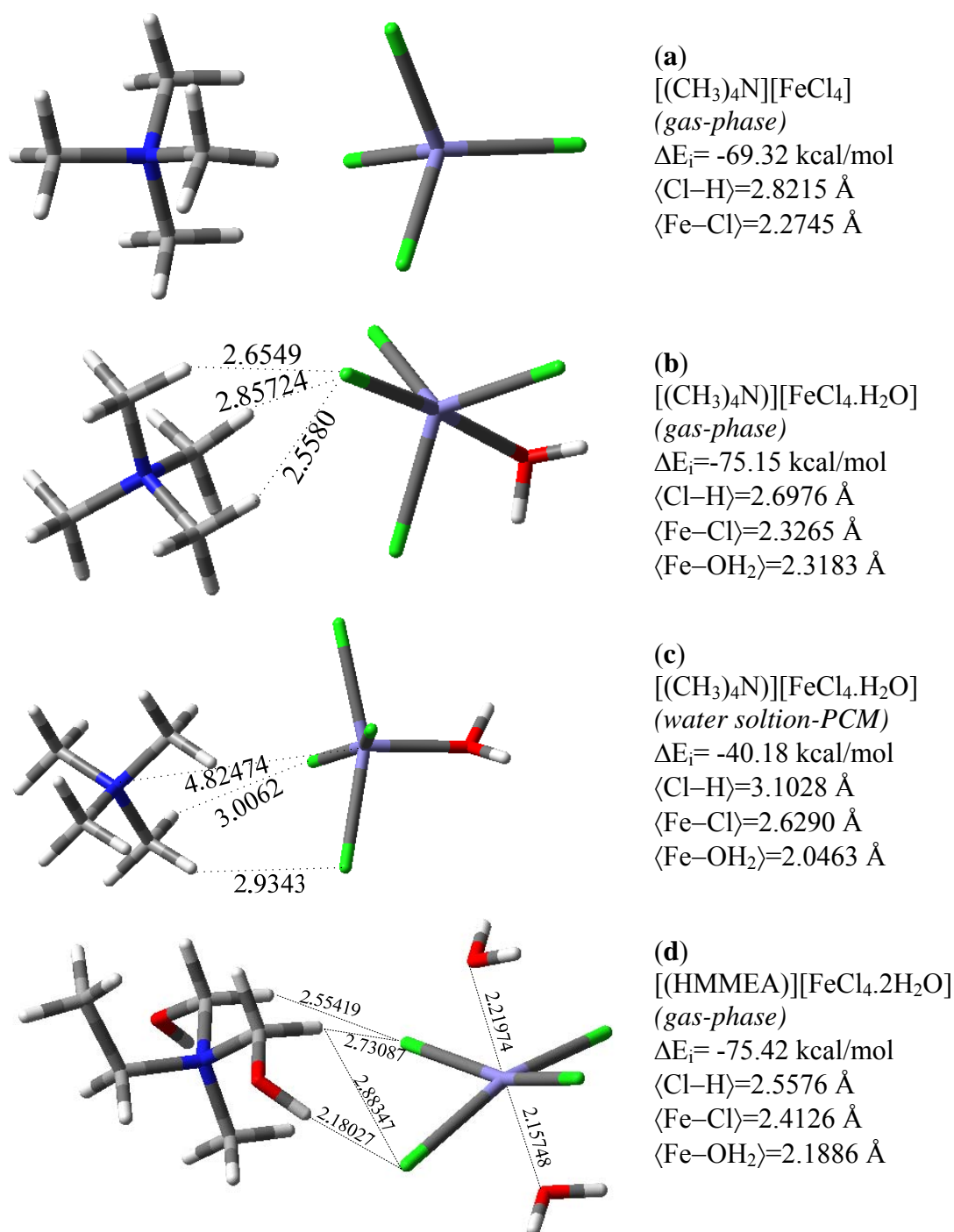
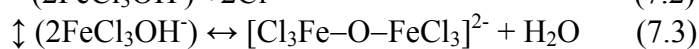
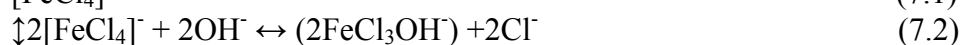


Figure 7.5: Optimized structures of cationic HG complexes with tetrachloroferrate. (a) TMA-FeCl₄, (b) TMA-FeCl₄·H₂O, (c) TMA-FeCl₄·H₂O, and (d) HMMA-FeCl₄·2H₂O. shown on the right-hand side binding energy, kcal/mol, and bond length, Å. color code: green for Cl, red for O, dark blue for Fe, dark gray for C and light gray for H.

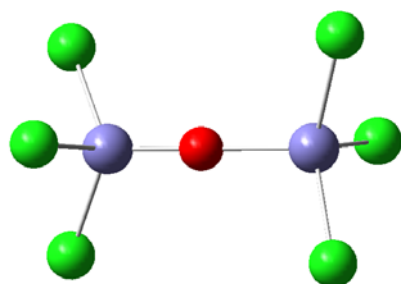
7.3.4 Complexation with $[Fe_2Cl_6O]$ and $[Fe_2Cl_9]^{3-}$

It is until late stages of this research, we have not considered other possible anions way form $[FeCl_4]^-$ that may result from the interaction of ferric ion with chloride in acidic solutions. Tetrachloroferrate is a possible mechanism of cationic surfactant precipitation at high concentration of ferric ions, however, the Cl:Fe ratio was found experimentally to be between 5–6, which suggest there might be another mechanism. It has been shown that in HCl solution the following complexation takes place (Neuse and Meirim, 1984):

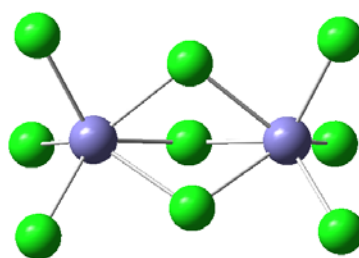


Where chloride ions start forming the complexes: $[FeCl]^{2+}$, $[FeCl_2]^+$, $[FeCl_3]$ and the most stable $[FeCl_4]^-$ according to speciation curve (Liu et al., 2006). Then, tetrachloroferrate undergoes the reaction of replacing one Cl^- with OH^- ion that present in solution (especially at high pH) to form hydroxytrichloroferrate intermediate complex, $[FeCl_3OH]^-$, which dehydrated to form the anionic complex $[Cl_3Fe-O-FeCl_3]^{2-}$. This complex is known as μ -oxo-bis(trichloroferrate) salt. The $H_2O/[FeCl_4]^-$ molar ratio needs to be in the range 5–10 to have high yield (Neuse and Meirim, 1984). The optimized structure of $[Cl_3Fe-O-FeCl_3]^{2-}$ is shown in Figure 7.6(a) with total binding energy of -2980.9 and -3088.7 kcal/mol at B3LYP/LanL2DZ and B3LYP/6-311++g**(O)/SDD(Fe, Cl), respectively. The value of binding energy is double what have calculated for $[FeCl_4]^-$, -1417.7 kcal/mol, at the same level of theory and basis set. The structure has an average bond length, $\langle Fe-Cl \rangle$ of 2.3099 Å (2.26–2.36 Å) which is in a good agreements with experimental data which in the range 2.320–2.099 Å (Haselhorst et al., 1993). The average value of $\langle Fe-Cl \rangle$ calculated using B3LYP/genecp is 2.30 Å with shorter range of variation. Oxygen is a good bridging agent and the average $\langle Fe-O \rangle$ distance is calculated to be 1.82 and 1.77 Å using B3LYP/LanL2DZ and B3LYP/genecp, respectively. The reported experimental value is 1.74 Å (Haselhorst et al., 1993). An interesting feature of this complex is the $\angle Fe-O-Fe$ angle which has values ranging between 140–180° depends on the counterion and state of the crystal.

This angle has the value of 180 and 174°, using B3LYP/genecp and B3LYP/LanL2DZ, respectively. the other feature angle in this complex are $\angle\text{Cl-Fe-Cl}$ and $\angle\text{Cl-Fe-O}$ which found to be 109 and 109°, respectively using LanL2DZ basis set which are in a good agreement with experimental values (Lledos et al., 2003). The second complex shown in Figure 7.6(b) is a trianionic, $[\text{Fe}_2\text{Cl}_9]^{3-}$ with total binding energy of -2642.4 kcal/mol. The bioctahedral complex, $[\text{Fe}_2\text{Cl}_9]^{3-}$, as well as $[\text{Fe}_2\text{Cl}_{10}]^{4-}$ has been reported in the literature (Warnke et al., 2003). The optimized structure at B3LYP/LanL2DZ has an average bond length, $\langle\text{Fe-Cl}\rangle$, of 2.28 Å, and angle, $\angle\text{ClFeCl}$ of 103°. at the same level of theory and basis set, we have examined the interaction between the dianionic, and trianionic ferric complexes with TMA^+ , then, compared results with monoimoinc tetrachloroferrate. Figure 7.7(a,b) shows two optimized structures of $(\text{TAM})_2-(\text{Fe}_2\text{Cl}_6\text{O})$. In part (a), the two TAM^+ HG was placed in way to form hydrogen bonding with oxygen and maximum Cl-H bonding. The initial structure was first optimized using molecular mechanis simultion, then with DTF. The total binding energy is caluated to be -159.9 kcal/mol. Hoever, when the two TAM^+ HGs are placed on both sides of $\text{Cl}_3\text{FeOFeCl}_3$, the energy drops to -155.3 kcal/mol. The trianionic chloroferrate forms highest binding energy with TAM compaed to both $[\text{FeCl}_4]^-$ and $[\text{Fe}_2\text{Cl}_6\text{O}]^{2-}$, Figure 7.7(d).



(a) $\Delta E_i = -3088.7$ kcal/mol, $\langle\text{Fe-Cl}\rangle = 2.3099$ Å, $\langle\text{Fe-O}\rangle = 1.8191$ Å, $\angle\text{ClFeCl} = 109.7^\circ$, $\angle\text{ClFeO} = 109.0^\circ$



(b) $\Delta E_i = -2642.4$ kcal/mol, $\langle\text{Fe-Cl}\rangle = 2.2780$ Å, $\angle\text{ClFeCl} = 102.80^\circ$

Figure 7.6: Optimized geometrical structure in gas-phase calculated using B3LYP/LanL2DZ for (a) $[\text{Cl}_3\text{Fe-O-FeCl}_3]^{2-}$, (b) $[\text{Fe}_2\text{Cl}_9]^{3-}$, (c) $(\text{TMA})_2-\text{Fe}_2\text{OCl}_6$, (d) $(\text{TAM})-\text{Fe}_2\text{Cl}_9$.

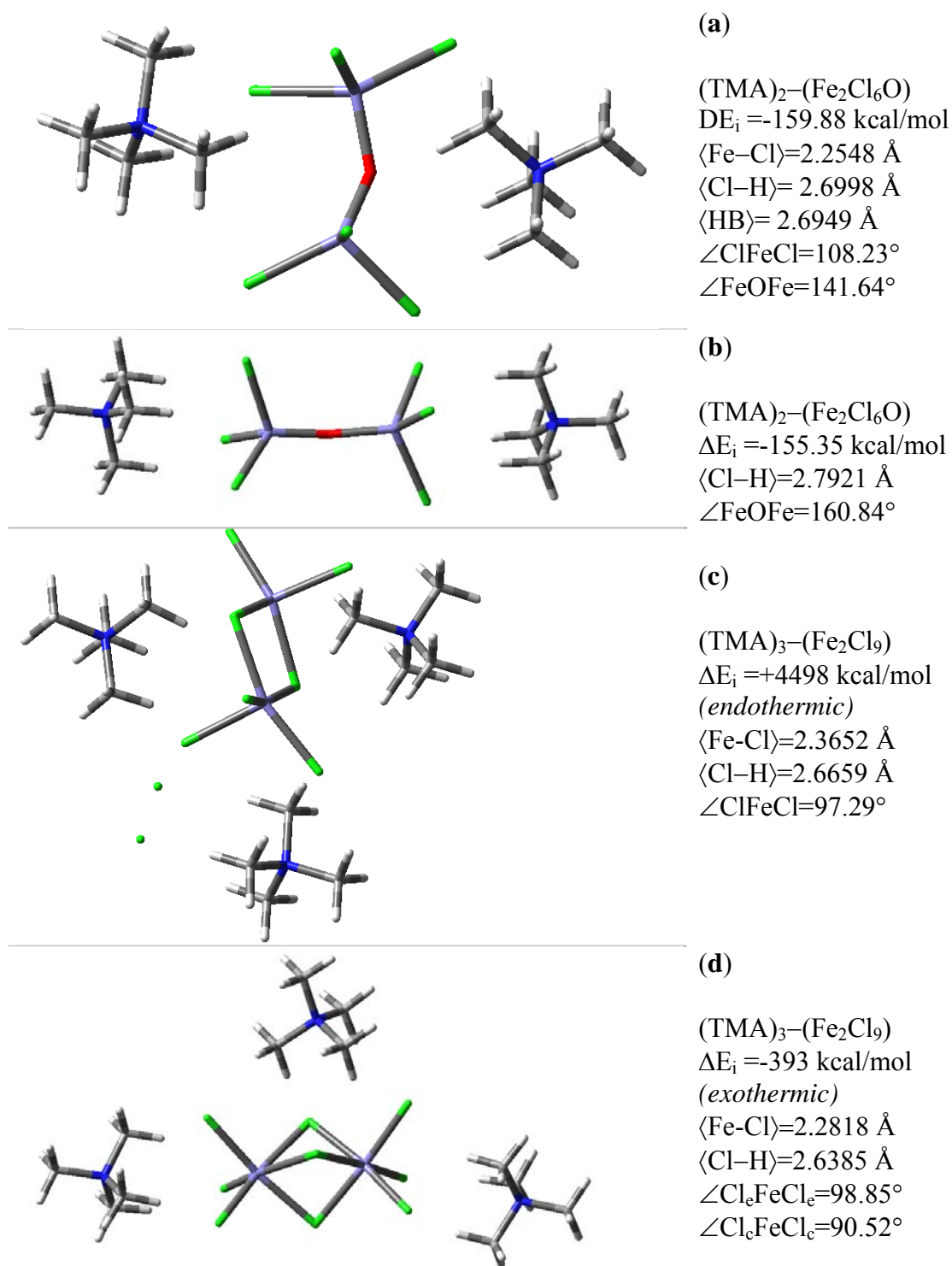


Figure 7.7: Optimized structures of TMA⁺ complexes with di- and trianionic compounds in gas-phase using B3LYP/LanL2DZ. (a,b) $(\text{TMA})_2-\text{Fe}_2\text{OCl}_6$, (c,d) $(\text{TAM})-\text{Fe}_2\text{Cl}_9$.

7.3.5 Gemini Surfactant

Gemini surfactants are characterized by critical micelle concentration, cmc , that is 10 to 100 times lower than that of corresponding conventional surfactant (monomer) (In, 2001). The general relation: $\text{cmc}_x = x(\text{cmc}_1)^x$, has been applied successfully to determine cmc value of oilgomers, cmc_x , based on the corresponding monomer value, cmc_1 . In this study, we are considering the general gemini structure (*bis*-quaternary ammonium) $R-N-s-N-R$ where R is the end fragment group connected to each nitrogen atom, and s is spacer between N (Figure 7.8). The optimized molecular structures of selected gemini surfactants are shown in Figure 7.9. Presence of counterion such as Cl^- , results in higher binding energy compared to single charged cationic surfactant. Due to the high affinity of Cl^- ion to form short bonding with hydrogen atom, the optimized molecular structures of gemini surfactant have been affected.

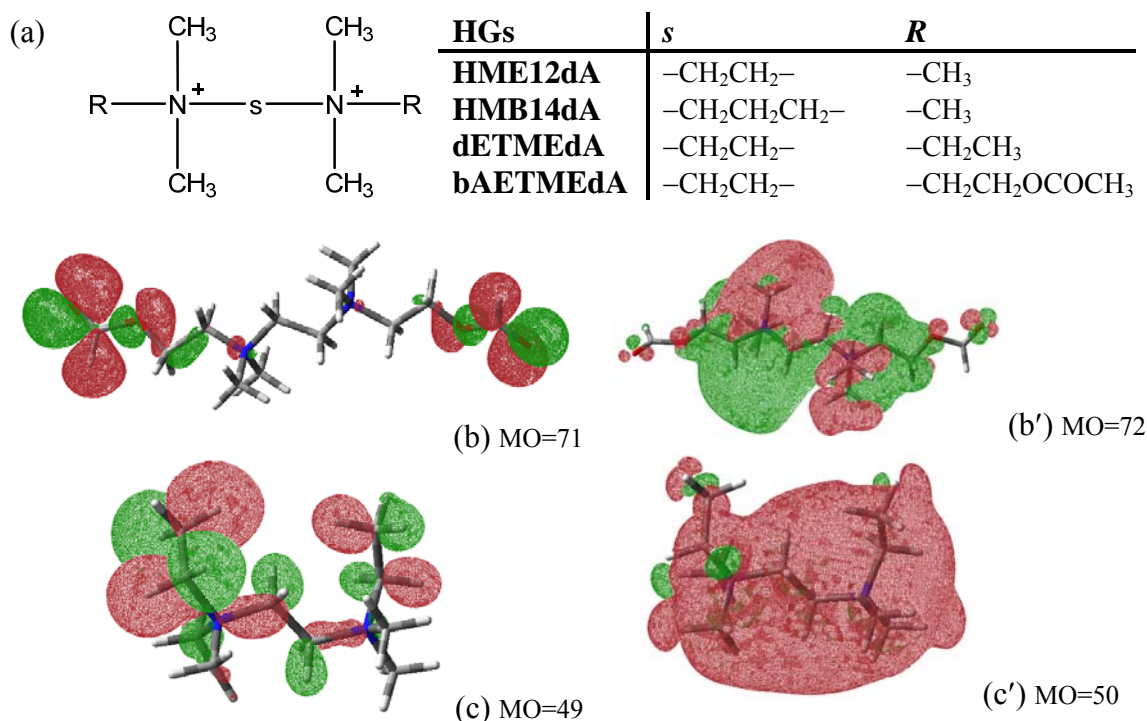


Figure 7.8: General structure of (a) symmetrical *bis*-quaternary ammonium salt with s and R groups are specified for each gemini HG considered in this study, and molecular orbital (HOMO, LUMO) of (b) bAETMEdA, and (c) dETMEdA.

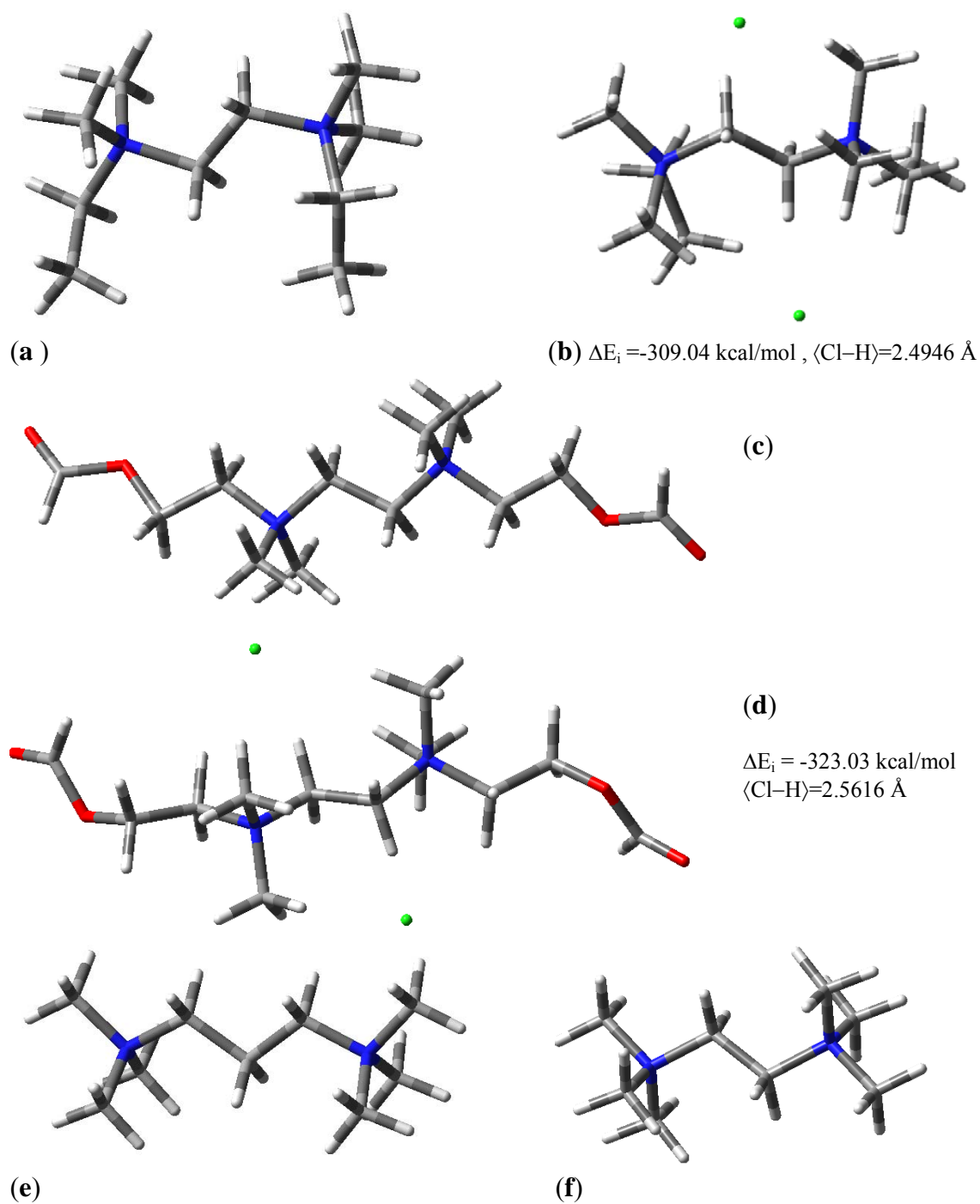


Figure 7.9: Optimized structures of gemini surfactant HGs. (a) dETMedA²⁺, (b) dETMedA-Cl₂, (c) bAETMedA²⁺, (d) bAETMedA-Cl₂, (e) HMB14dA, and (f) HME12dA.

7.4 Molecular Simulation

We have run number of molecular dynamic simulation to study the behavior chloride ions surrounding single cationic surfactant in large system of water. The acetate HG with tail consists of erucyl chain, are considered. The simulation box was constructed by putting the surfactants in the x-z plane. The cluster builder utility in VegaZZ (Pedretti et al., 2004) was used to add randomly chloride ions in a predetermined box size of $30 \times 30 \times 50$ in x,y,z, respectively. Charge was calculated using Charmm force field (Brooks et al., 1983) included in Vega ZZ. Once the system is fully defined, MD simulation was carried out using NANOScale Molecular Dynamics (NAMD) (Phillips et al., 2005). The system was allowed to equilibrate in 1000 steps with 1fs timestep size at a temperature $T=300$ K, following the equilibration, molecular dynamic run with 100,000 time steps of 1 fs step size, 12 Å cutoff, and periodic boundary is set to run. The final systems (1 ns), are shown in Figure 7.10. It can be seen that as the number of chloride ions increases in the box, surfactant tail-molecules start to relax in solution while the HG maximize the contact with the Cl. Generally, the shape of optimized BdMEA monomer is still maintained after 1 ns simulation time, however, distribution of water molecules surrounding the surfactant changes. More results for higher concentrations at the same simulation conditions are shown in Appendix D. With chloride ion concentration increases the average bond distance between Cl ion and closest hydrogen becomes stronger which can explain the behavior of viscosity as HCl concentration changes.

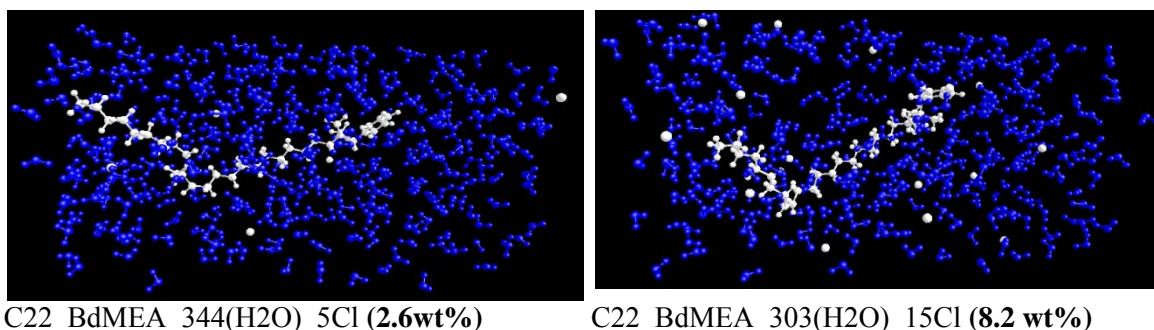


Figure 7.10: MD simulation snapshot after 1 ns.

CHAPTER VIII

GEOMETRY OPTIMIZATION AND MOLECULAR SIMULATION OF BETAINE AND AMIDOAMINE OXIDE SURFACTANTS

It is by logic that we prove, but by intuition that we discover
—J. H. Poincare, ca 1900

pH-sensitive surfactants are becoming increasingly important in many novel applications in various fields including medicine, fabrication, sensing, optical and oilfield. In particular, alkylamine oxide surfactants represent a promising and well-characterized class of responsive fluid. A common reason for a decline in oil production is damage to the formation particularly the near wellbore area. This damage generally arises from deliberately injecting another fluid into the wellbore which may dehydrate and form a coating on the wellbore. The natural effect of this coating is to decrease the permeability to oil moving from the reservoir in the direction of the wellbore. Matrix acidizing, hydraulic and acid fracturing are commonly use to clean the near wellbore area and remove restore permeability. Viscoelastic surfactants (VES) that are responsive to pH change are used in such treatments for acid delivery (diversion) or to carry proppants. Another application of VES is placement of scale inhibitor in hydrocarbon production formation to prevent deposits of mineral scales that reduce flow of oil (Morris, 2008). Viscoelastic surfactant can be used for water shut off, drag reduction, and viscosity enhancer.

Betaine and amidoamine oxide surfactants have shown good thermal and rheological properties. We have considered ten HG groups namely: AAMCDEEA, CtMMA, CtMEA, CMdMEA, CpMBdA, TmoEA, dMNPA, APhMA, AAPhdMA, and AAPhP. We have used DFT to optimize their molecular structures both in gas-phase and water-solvent, and evaluate their binding energy with Ca^{2+} , Cl^- counterions. Molecular simulation for single surfactant in water solution has been carried out to study the effect of chloride ion distribution around surfactant molecules.

8.1 Introduction

Polymers such as guar or hydroxyethyl cellulose have been used traditionally as fluid thickeners in oilfield applications. They are inexpensive, readily available and relatively environmentally friendly. The polymer must hydrate in water and requires several chemical additives to adjust its performance and develop the in-situ gelled acid. The polymer-based acid system initially has a low viscosity to allow pumping through the tubing and once the HCl reacts with carbonate rock, the polymer crosslinks when the pH rises to 2. The viscosity increase restricts further flow of “live” acid the wormholes, thereby diverting fresh acid to zones with low permeabilities. As the acid continues to dissolve the rock, the pH increases further. Once the pH reaches about 3.5 the gelled acid breaks, reducing the viscosity and enabling the fluid cleanup process. However, there were several concerns raised about polymer system such as precipitation in presence of Fe(III) ions in sour environment, losing its functionality once interacts with hydrogen sulfide scavenger and forming damage to the near wellbore area. Polymer-based acid system has a narrow pH window which makes the crosslinking and the breaking phenomenon difficult to be controlled. Moreover, the stability of polymer at high reservoir temperature is questionable. In average, surfactants acid-based system are more expensive than polymer one but easier to prepare with much less additives required (Zana and Kaler, 2007).

It has been a practice since the early 1990s to add viscoelastic surfactant to acid system for diversion purpose in reservoir stimulation. They were successfully used in acid treatments of vertical, horizontal, long horizontal, and multilateral wells, with harsh sour environment where the hydrogen sulfide, (H_2S), levels reached to nearly 10 mol%. It has been reported that VES was also utilized in gas wells to reduce acid leakoff, and to stimulate water injectors and disposal wells (Nasr-El-Din and Samuel, 2007). Viscoelastic surfactants (VES) based on wormlike micelles have generated considerable scientific interest in oilfield industry and have wide range of applications including acid diversion, proppant placement in fracturing, slurry transport, drag reduction and drilling

fluid. VES has the ability to increase solution apparent viscosity and elastic properties by self-assembly which is unlike conventional polymer fluid that they rely on crosslinkers to form entanglement and build viscosity. The wormlike micellar structure is dynamic in nature and can be controlled by the local fluid environment. The principle conditions affecting the behavior of wormlike micelles are surfactant concentration, solvent characteristics, and temperature.

Amidoamine oxide is becoming a more popular diverting material as it has been claimed that this class of surfactants do not undergo phase separation over extended period of time and exhibit high thermal stability (Doboson et al., 2003). Surfactant HGs were selected in this work based on their characteristics, availability and used as acid diverters. The six betaine surfactant HGs included in this study are: *N*-[(acetylamino)methyl]-2-carboxy-*N,N*-dimethylethanaminium (AAMCDEEA), carboxy-*N,N,N*-trimethylmethanaminium (CtMMA), 2-carboxy-*N,N,N*-trimethylethan aminium (CtMEA), *N*-(carboxymethyl)-*N,N*-dimethylethanaminium (CMdMEA), *N*-carboxy-*N,N,N',N',N'*-pentamethylbutane-1,4-diaminium (CpMBdA), 2-methoxy-*N,N,N*-trimethyl-2-oxoethanaminium (TMoEA). The four amidoamine oxide HGs presented in this chapter are: [3-(acetylamino)propyl] (hydroxy)bis(hydroxymethyl) ammonium (APhMA), *N*-[3-(dimethylnitro)propyl]acetamide (dMNPA), [3-(acetylamino)propyl] (hydroxy) dimethylammonium (AAPHdMA), 1-[3-(acetylamino)propyl]-1-hydroxypyrrolidinium (AAPHp). We will refer to all of them hereafter by their abbreviation shown in the brackets.

Surfactant solutions are studied by different experimental and theoretical methods. Recently, computer simulation is increasingly employed to predict the rheological behavior of VES and understand the relation between molecular structure and end properties. The objective of this chapter is to gain predictive understanding, at molecular level, of betaine and amidoamine oxide aggregation in water solution and their interaction with counterions present in acidic medium. We report in this chapter

quantum calculations at density functional theory (DFT) levels of the molecular properties in the gas phase and water solutions. The energy differences and the water effect on these HGs are analyzed. The information obtained will help us understand the electronic origin of the factors that determine the properties of these simple molecules, and to have better judgment when selecting VES for acid diversion in well stimulation treatment considering factors such as counterions, type of HG, and how they are affected by the water environment. The understanding of the properties of these self-assembly molecules requires an accurate knowledge of nonbonded interactions, such as the intramolecular HG–HG and the intermolecular HG–water hydrogen bondings, which are key contributors to the specificity of the interactions within and between macromolecules and that can be modeled through the study of the simpler anionic surfactant molecules. Molecular simulation of Cl^- ions distribution around single surfactant monomer in water solution is presented.

8.2 Simulation

The DFT computations were done with the Gaussian 03 package (Frisch et al., 2004). The DFT studies employed the Becke gradient corrected exchange functional in conjunction with the Lee–Yang–Parr correlation functional with the three parameters (B3LYP) method (Becke, 1993). B3LYP is a gradient corrected method that includes some of the effects of electron correlations. This DFT approach usually gives rise to greater accuracy than Hartree-Fock (HF) for structure, thermochemistry, and spectroscopic properties, with only a slightly greater computational effort; this combination of efficiency and accuracy has made it perhaps the most popular method for practical applications. Results obtained with DFT approach are compared with experimental ones when available.

The computations reported in this work may be divided into three groups: First: *gas-phase calculations* which are done with the 6-311++g** basis set at B3LYP levels to determine the geometric and energetic parameters of the different HGs and to establish

the most stable ones. Second, *water solution calculations*, done within the self-consistent reaction field approach (SCRF) in which the solvent is treated as a continuum. We adopted the polarizable continuum model (PCM) because it provides a quantitative estimation of the different contributions to the total free energy of solvation. Although the SCRF methods do not account for specific solute–solvent interactions, such as hydrogen bonding, and results based on these methods are clearly dependent on the selected size and shape of the solute cavity, they proved to be successful on analysis of the effect of solvents on solute properties and on isomer ratios. The coupling of PCM models with DFT to study the interactions of solutes and solvents is not frequent. In this work the properties of the anionic HG in solution were calculated at DFT theoretical levels with a 6-311++g** basis set. Comparison of gas and solution results allows clarifying the solute polarization effect. Third, the properties of AA HG/water complexes were computed and their structures optimized at B3LYP levels with the 6-311++g** basis set. In a consistent manner and for all calculations presented in this chapter, the 6-311++G(d,p) basis set was applied to H, O, C, Ca, Mg, Na, N atoms and SDD for Fe, Mn, Zn atoms.

8.3 Results and Discussion

Results in this chapter will include the molecular orbital theory analysis of each HG, in gas-phase and aqueous solution, the interaction between HGs and counterions. Molecular dynamic simulations of various Cl⁻ concentrations in water solutions with single AAMCEDEEA Betaine surfactant are discussed.

8.3.1 Betaine MO

Reactivity is related to the relative energies and shapes of the orbitals that are involved in the reaction and hence to the nature of substituents. Shape of the molecular orbitals and symmetry are particularly important for qualitative reactivity analysis. We are trying to understand how a change in molecular structure of an anionic surfactant HG will affect the (MOs). As molecules approach one another and reaction proceeds there is

mutual perturbation of the orbitals. This process continues until the reaction is complete and the product is formed. The concept of frontier orbital control proposes that the most important interactions are between a particular pair of orbitals (Fukui, 1971). These orbitals are the highest occupied orbital of one reactant (HOMO) and the lowest unoccupied (LUMO) orbital of the other reactant. The HOMO represents the distribution and energy of the least tightly held electrons in the molecule while LUMO describes the easiest route to addition of more electrons to the system. If they are close in energy they could be intimately involved in chemical reactivity as postulated in perturbation molecular orbital theory. A further general feature of MOs theory is that only MOs of matching symmetry can interact and lead to bond formation. Figure 8.1(a) shows the optimized geometrical structure of AAMCDEEA HG in gas-phase. This HG represents the general form of alkylamidobetaine surfactant. The HG has permanently positively charged moiety regardless of pH and negatively charged moiety at alkaline pH due to deprotonation of carboxylate hydrogen. For CMDMEA represents the general structure of alkyl betaine with one carboxylate group and quaternary ammonium group. HOMO and LUMO of CMDMEA are shown in Figure 8.1(b',b''), respectively. The spacing between carboxylate group and N is ethyl group in for AAMCDEEA and methyl in the case of CMDMEA. This spacing has its influence on the optimized geometrical structure, free electrons on O, N, and hence the reactivity and binding energy of the HG.

8.3.2 Betaine Interaction

The addition of organic or inorganic compounds to the solution of viscoelastic surfactant causes complex phase behavior in the system (Zana and Kaler, 2007). At low concentration, the amphiphilic nature of betaine surfactants results in the formation of different nano- and mesoscopic spherical structures in the solution. Moreover, when the concentration of surfactant increases, or more electrolytes compounds are added to the solution, spherical micelles can form a wormlike aggregates responsible for development of viscoelastic properties of the solution.

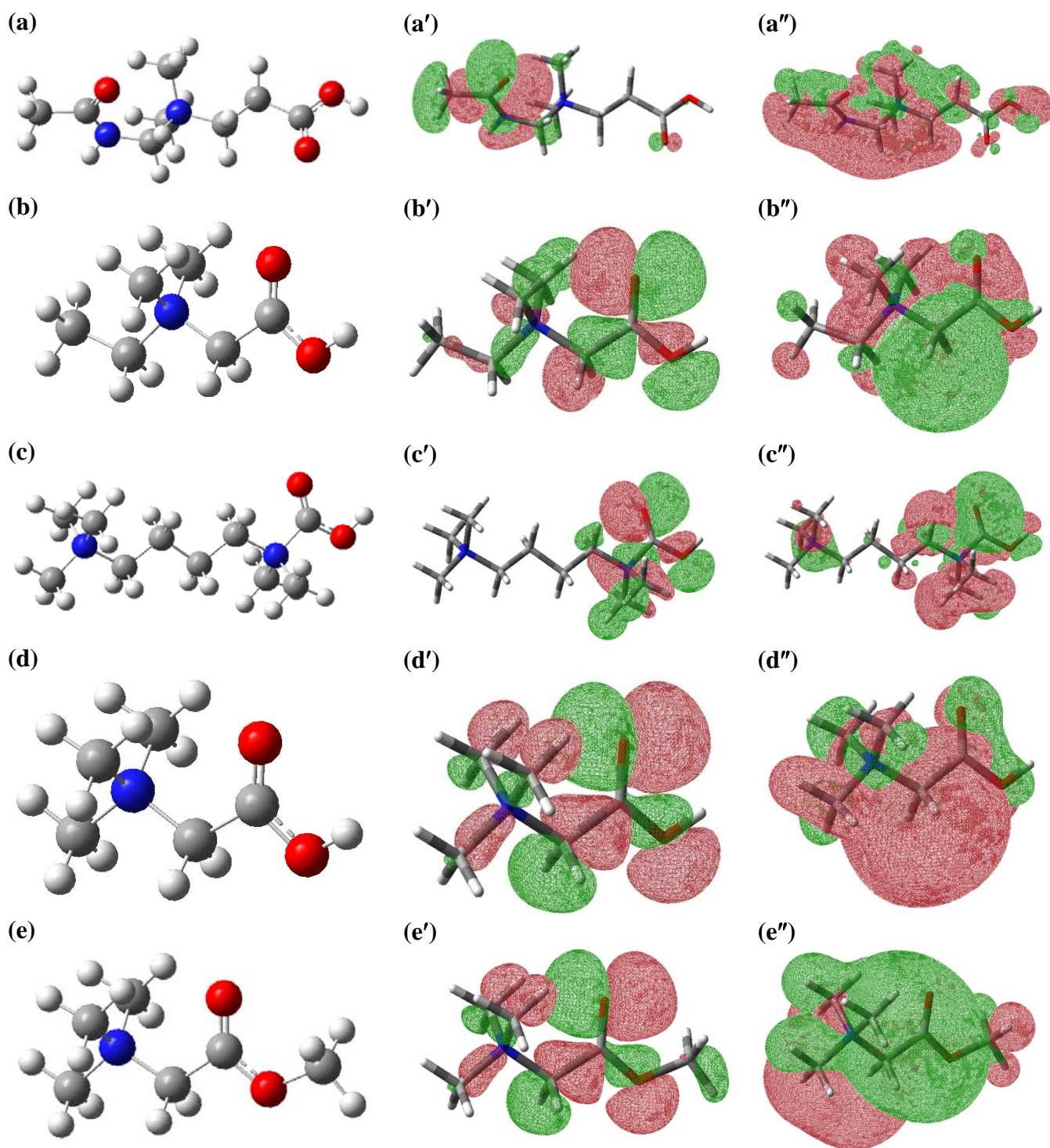


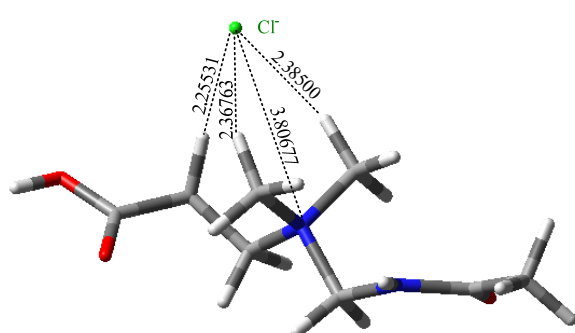
Figure 8.1: Optimized geometrical structure of selected *betaine* head groups (HGs) with localized HOMO and LUMO molecular orbitals in the second and third columns, respectively. (a) AAMCDEEA, (b) CMDMEA, (c) CMPMBdA (d) CtMMA, and (e) TMoEA. Color code: red for O, blue for N, dark gray for C and light grey for H.

The formation of these aggregates is substantially attributable to the duality of betaine surfactants as they have both hydrophilic and hydrophobic moieties. In stimulation treatment of hydrocarbon reservoir, acid solution contains ions such as (H_3O^+ , Fe^{2+} , Fe^{3+} , Cl^- , and OH^-) before reaction with rocks takes place, and more ions such as Ca^{2+} , Mg^{2+} , HCO_3^- will be released to the solutions once the acid enter the formation. All ion are of great interest as they can interact with both positive and negative moieties of betaine surfactant HG.

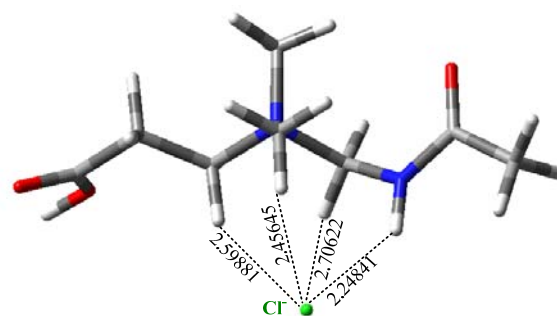
We have examined first the effect of water molecules on the geometry of HG. Figure E.1 shows AAMCDEEA HG with two water molecules. The calculated total binding energy is -20.84 kcal/mol, with hydrogen binding angle, $\angle\text{CHO}$, of 145.5° , and hydrogen bonding length of 2.2905, and 2.2255 Å for each water molecule, respectively. Interaction of betaine HG with chloride ion in an acidic medium (i.e. the carboxylate hydrogen is not deprotonated) are shown in Figure 8.2. For all cases with single quaternary ammonium group, the total binding energy is approximately the same. However, it is double in the for CMPMBdA with value of -300.7 kcal/mol. Complexation with tetrachloroferrate is shown in Figure 8.3.

8.3.3 Molecular Simulation

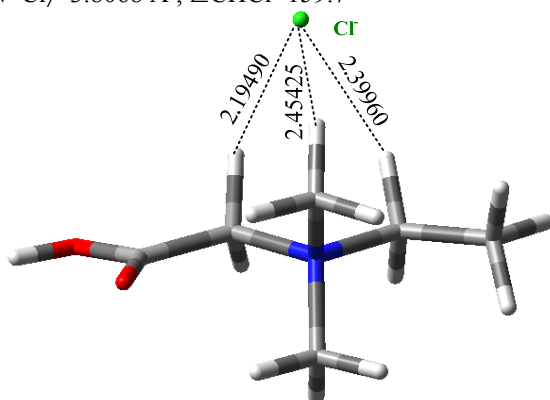
We have run number of molecular dynamic simulation to study the behavior chloride ions surrounding single cationic surfactant in large system of water. The acetate HG with tail consists of erucyl chain, are considered. The simulation box was constructed by putting the surfactants in the x-z plane. The cluster builder utility in VegaZZ (Pedretti et al., 2004) was used to add randomly chloride ions in a predetermined box size of $30 \times 30 \times 50$ in x,y,z, respectively. Charge was calculated using Charmm force field (Brooks et al., 1983) included in Vega ZZ. Once the system is fully defined, MD simulation was carried out using NANOScale Molecular Dynamics (NAMD) (Phillips et al., 2005). The system was allowed to equilibrate in 1000 steps with 1fs timestep size at a temperature $T=300$ K.



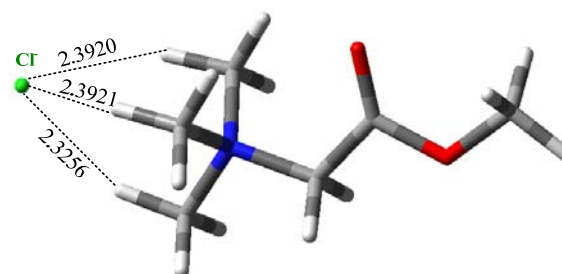
(a) $\Delta E_i = -114.46$ kcal/mol, $\langle \text{H-Cl} \rangle = 2.3360$ Å, $\langle \text{N-Cl} \rangle = 3.8068$ Å, $\angle \text{CHCl} = 159.7^\circ$



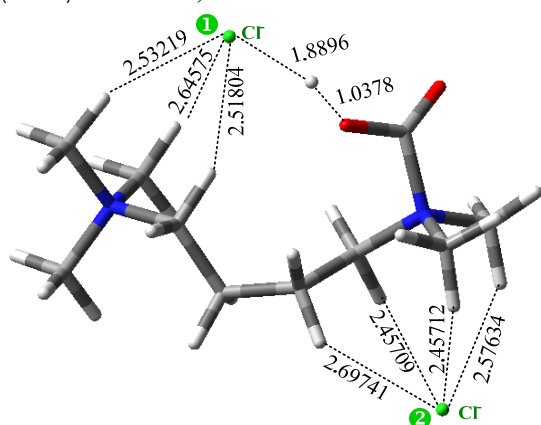
(b) $\Delta E_i = -120.8$ kcal/mol, $\langle \text{H-Cl} \rangle = 2.5025$ Å, $\langle \text{N-Cl} \rangle = 3.6036$ Å, $\angle \text{CHCl} = 133.9^\circ$



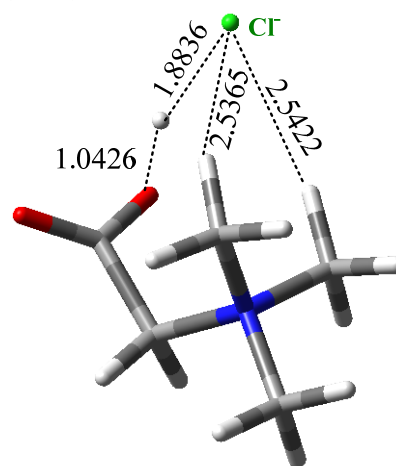
(c) $\Delta E_i = -118.6$ kcal/mol, $\langle \text{H-Cl} \rangle = 2.3496$ Å, $\langle \text{N-Cl} \rangle = 3.5661$ Å, $\angle \text{CHCl} = 149.8^\circ$



(d) $\Delta E_i = -113.2$ kcal/mol, $\langle \text{H-Cl} \rangle = 2.3699$ Å, $\langle \text{N-Cl} \rangle = 3.5780$ Å, $\angle \text{CHCl} = 149.6^\circ$



(e) $\Delta E_i = -300.7$ kcal/mol, $\langle \text{H-Cl} \rangle_1 = 2.2.3964$ Å, $\langle \text{H-Cl} \rangle_2 = 2.5470$ Å, $\langle \text{N-Cl} \rangle_1 = 3.7962$ Å, $\langle \text{N-Cl} \rangle_2 = 3.5635$ Å, $\angle \text{CHCl}^1 = 151.4^\circ$, $\angle \text{CHCl}^2 = 143.8^\circ$



(f) $\Delta E_i = -115.2$ kcal/mol, $\langle \text{H-Cl} \rangle = 2.2.3208$ Å, $\langle \text{N-Cl} \rangle = 3.5661$ Å, $\angle \text{CHCl} = 157.2^\circ$

Figure 8.2: Optimized structure of Betaine HG with chloride ion. (a) AAMCEDEEA, (b) AAMCEDEEA, (c) CMDMEA, (d) TMOA, (e) CMPMBdA, and (f) CTMMA.

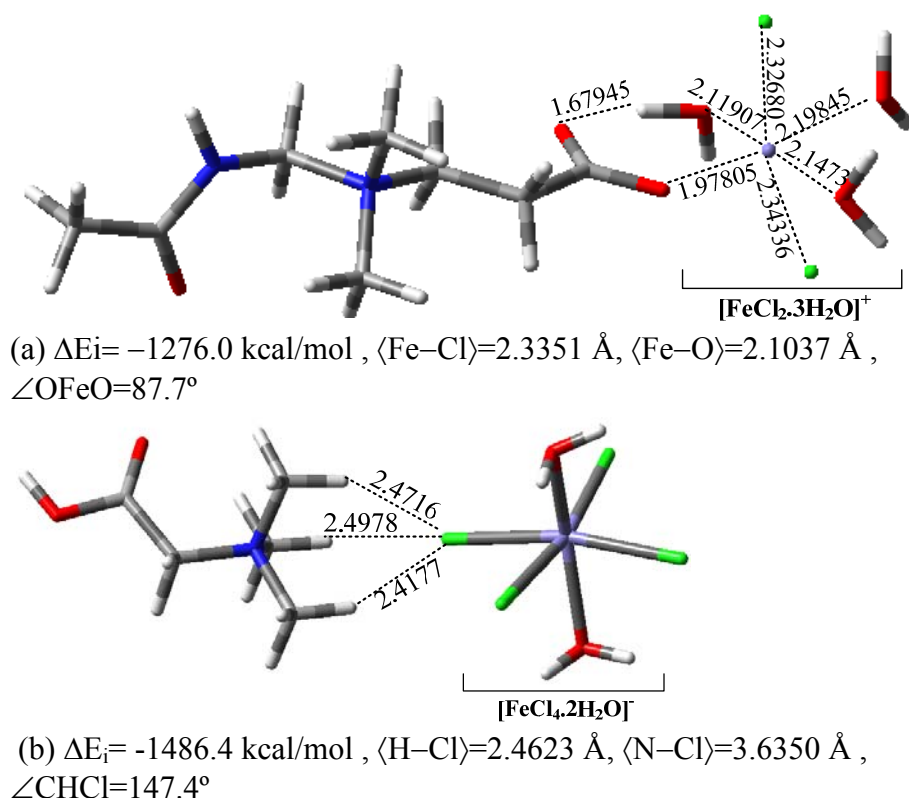
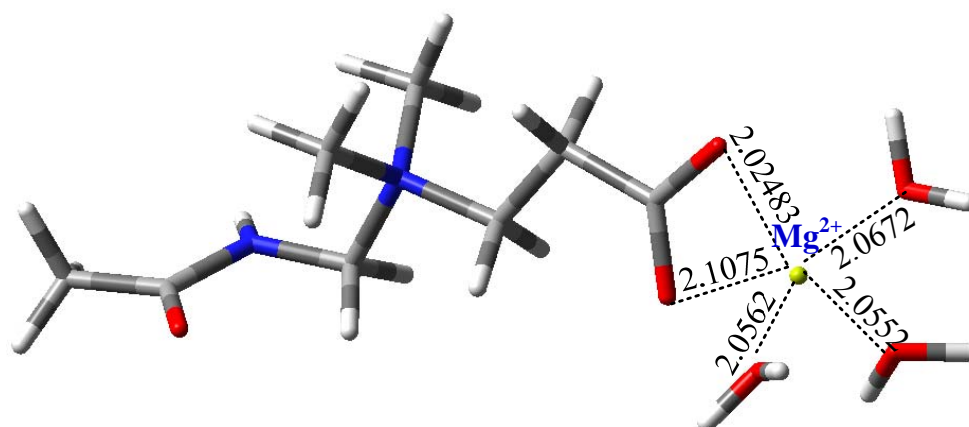
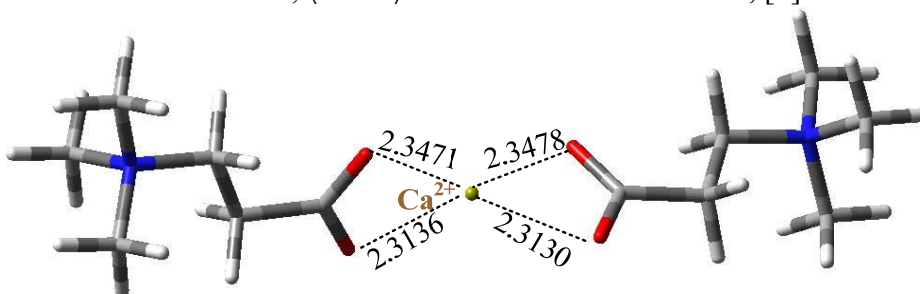


Figure 8.3: Optimized structures of betaine HG complexes with tetrachloroferrate. (a) AAMCDEEA, and (b) CTEEA.

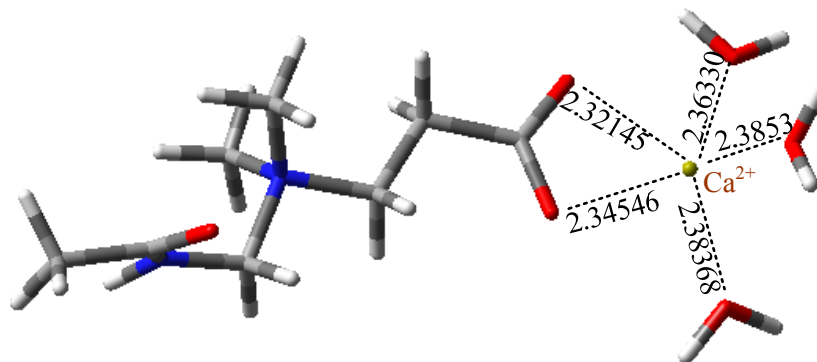
Following the equilibration, molecular dynamic run with 100,000 time steps of 1 fs step size, 12 Å cutoff, and periodic boundary is set to run. The final systems (1 ns), are shown in Figure 8.5. It can be seen that as the number of chloride ions increases in the box, surfactant tail-molecules start to relax in solution while the HG maximize the contact with the Cl. Generally, the shape of optimized AAMCDEEA monomer is still maintained after 1 ns simulation time, however, distribution of water molecules surrounding the surfactant changes. More results for higher concentrations at the same simulation conditions are shown in Appendix D. With chloride ion concentration increases the average bond distance between Cl ion and closest hydrogen becomes stronger which can explain the behavior of viscosity as HCl concentration changes.



$\Delta E_i = -356.9$ kcal/mol , $\langle \text{Ca-O} \rangle = 2.0669$ Å $\angle \text{OCaO} = 87.7^\circ$, [1]



$\Delta E_i = -$ kcal/mol , $\langle \text{Ca-O} \rangle = 2.3304$ Å, $\angle \text{CHCl} = 98.8^\circ$



$\Delta E_i = -279.8$ kcal/mol , $\langle \text{Ca-O} \rangle = 2.3598$ Å $\angle \text{OCaO} = 89.1^\circ$, [0]

Figure 8.4: Optimized geometrical structure of AAMCDEEA with cationic metals.

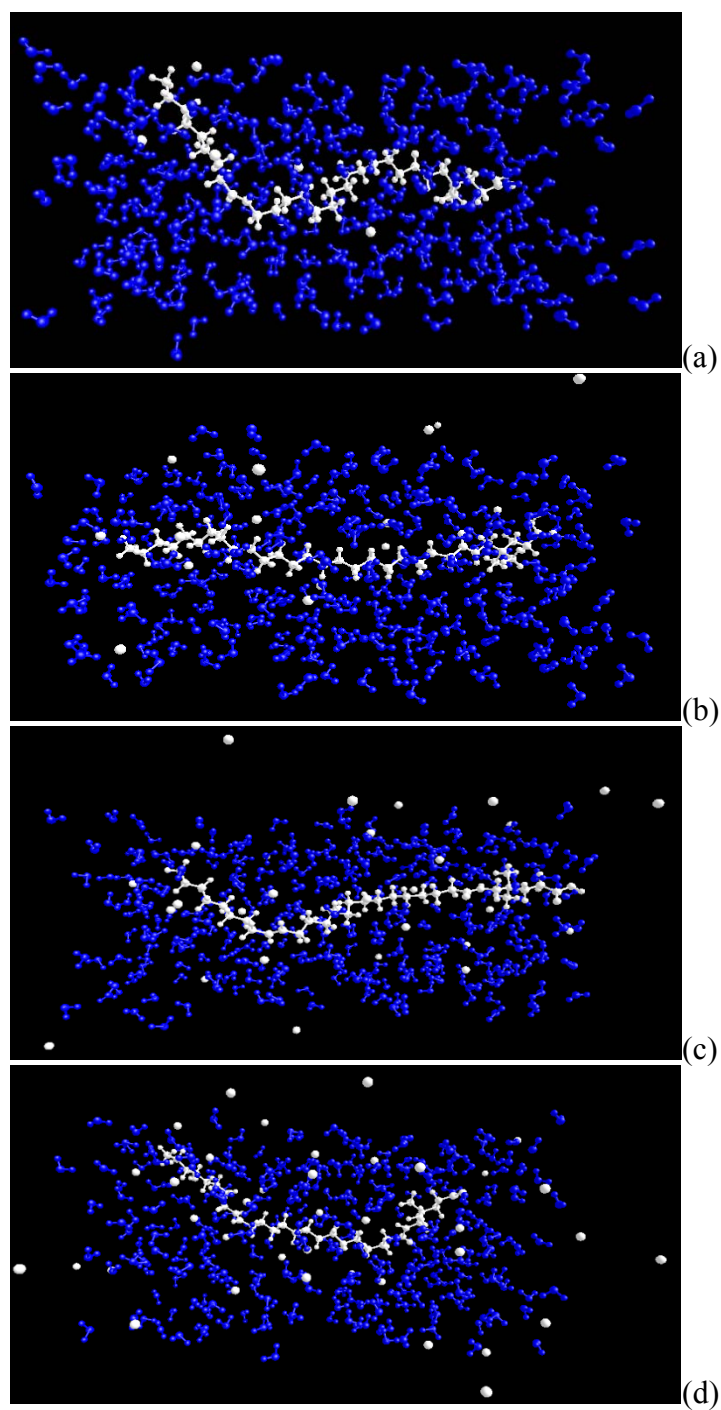


Figure 8.5: MD simulation snapshot after 1 ns of C22 AAMCDEEA with (a) 284(H₂O)_5Cl (3.1wt%), (b) 289(H₂O)_15Cl (8.5 wt%), (c) 285(H₂O)_30Cl (15.9wt%) and (d) 287(H₂O)_40Cl (20.0 wt%).

CHAPTER IX

CONCLUSIONS AND RECOMMENDATIONS

The yeoman work in any science...is done by experimentalist, who must keep the
theoretician honest
— M. Kaku, professor of theoretical physics

The use of computer simulation and detailed colloid-surface analytical techniques is bringing new insight to the mechanisms underlying the behaviour of complex oilfield fluids and their interaction with mineral surfaces. Indeed, these tools now play a significant role in the more systematic design of new fluids and processes. However, much remains to be understood about the mechanisms underlying reservoir treatments and the way molecules can modify porous rock environment to control fluid flow. Future trends will be to smarter, responsive fluids with property changes activated by downhole triggers, and colloidal materials capable of operating under more extreme conditions of temperature, pressure and solvent environment. There is also a need for more systematic work on the flow of complex structured fluids in porous media. This chapter is organized in two parts: conclusions based on our calculations and recommendations for future work. In the conclusion part, every paragraph is relevant to one chapter in the dissertation, while the recommendations are listed in order of importance according to “my personal” judgment.

9.1 Summary and Conclusions

Chapter II is a general review of nanotechnology and its possible applications in oilfield industry. This chapter serves as the theoretical background to all *ab initio*, DFT and molecular dynamic simulation results that are presented in later chapters of the dissertation.

Chapter III explains the necessary chemical background, thermodynamic behavior and presents general understanding of chemical structure influence on dynamic properties of

VES systems which may be useful for many scientists and engineers working in this field. This chapter also presents general review of what is called “responsive” or smart fluids and their possible applications in oilfield industry.

In Chapter IV, we study metal ion hydration for most common elements (Ca^{2+} , Mg^{2+} , Na^+) in carbonate reservoir. Although, cluster of 2–8 water molecules have been the subject of a number of earlier studies, we have repeated some of them to have a consistent level of theory and basis set which is needed for analysis and comparison in later chapters of the dissertation. To the best of our knowledge, we have not seen a complete study on the behavior of aqueous solutions of fracturing or acidizing fluid in oilfield industry literature, and the objective of this chapter was to identify theoretically the structural properties of water–electrolyte systems. Calculations in this chapter are the first to be reported in oilfield chemistry literature. Starting with pure water system, we have reported the energetic properties of water clusters, $(\text{H}_2\text{O})_n$, $n=1-9, 18$, using DFT with B3LYP/6-311++g(d,p) basis set. It has been observed that clusters with $n=3-5$ are cyclic quasi-planar structures, while three dimensional structures start at $n=6$. We have observed that for clusters with $n>6$, the most stable structure contains tri-, tetra- or penta cyclic rings or a combination of them. The outstanding cause of structuredness of the water is its extended hydrogen bond network. With the increases in the size of water clusters, there is an increase in the number of hydrogen bonds and hence an increase in the total binding energy. For $n=2-5$, there are only one single-donor hydrogen bonds, whereas for $n \geq 6$, there are single-donor as well as double-donor hydrogen bonds.

The structure and dynamics of hydrogen bonds network (HBs) in water solutions are perturbed by ions. The terms “structure-maker” and “structure-breaker” have almost universally been adopted to describe the effect of different ions on the surrounding water network (Marcus, 2009). We have reported results for first shell, $[\text{M}(\text{H}_2\text{O})_n]^{x+}$, and second shell, $[\text{M}(\text{H}_2\text{O})_n.m\text{H}_2\text{O}]^{x+}$ hydration structures of $\text{M} = \text{Na}^+$, Ca^{2+} , and Mg^{2+} . The structures of the hydrated complex formed by these ions in aqueous solutions have long

remained an object of investigations in geochemistry, chemistry and biology. For sodium, the coordination number (CN) values were markedly scattered (Vinogradov et al., 2003), however, six is the most reported coordination number which decreases to four at high concentrated solution. Due to the high biochemical importance of the hydrated Mg^{2+} and Ca^{2+} ions, numerous structural studies of its salts in aqueous solutions have been performed. The coordination numbers used in this study are 6 for calcium and magnesium. In the general structure $[\text{M}(\text{H}_2\text{O})_n.\text{mH}_2\text{O}]^{x+}$, the C_{2v} symmetry is calculated to be the stable structure for all (2,0) metal ions. For $n=2$, the angle $\angle\text{OMO}$ is 180° for Na^+ and Mg^{2+} , however, $\angle\text{OCa}^{2+}\text{O}$ is found to be bent for the structure to be stable with value of 127.1° . This bent in angle has not been observed in $\text{Mg}(\text{H}_2\text{O})_2$ due to water-water repulsion which is less important in the case of Ca^{2+} due to larger ionic radius of Ca^{2+} . For trihydrated complex, all metal ions have three water molecules directly connected to the central ion with binding energy factor ~ 2.5 greater than monohydrated complex. For the case with $n=4$, we have examined the (4,0) geometry with all four water molecules are in the first shell, and the total binding energy is found to be ~ 3.1 times higher than the monohydrated. For pentahydrated metal complex, the (4, 1) with four water molecules in the first shell and one in the second shell is lower in energy than (5, 0) for Na^+ due to crowding effect. However, the (5, 0) complex with C_{2v} symmetry is the stable structure for Ca^{2+} and Mg^{2+} . For $n=6$, (4, 2) was more stable and has lower energy than (6, 0) for Na^+ , whereas, both divalent metal ions, the (6, 0) was optimized as the most stable first shell hydrated complex. For all metal ions, the (6, 1) and (6, 2) were the most stable structures for hepta- and octahydrated complexes. The second hydration shell is recognized to be the first solvation sphere. For complete second shell hydration, we have used 12 water molecules with six in the first shell for all metal ions. The lowest energy for all cation metal has been found for a cluster with 18 water molecules that has nearly S_6 symmetry. It is not yet known if this is the global minimum on PES. The optimized structures have binding energies of -224.9, -423.2 and -502.5 kcal/mol for Na^+ , Ca^{2+} , and Mg^{2+} , respectively. In summary, we have demonstrated in this chapter water-water interaction and stability of hydration of three

metal ions in 18-water structure. Our results are in accord with previous findings at the same or different theory level and basis sets. The extension of this study to third shell will substantially enhance the understanding of ion behavior in solution and rearrangement of water molecules. These calculations as well as the first and second shell hydration will help in determining the degree of involvement and nature of interaction between water molecules surrounding metal counterions and VES HGs.

In Chapter V, we focused on iron which is perhaps the most underestimated problem of all acidizing treatments because we rely on pickling process to clean out all tubing systems. However, when looking carefully to surface tanks, lines, mixing and pumping equipments and well tubular are all routinely made of steel, which dissolves to a greater or lesser extent in acid, even when considering only the iron that would enter solution as a result of allowable corrosion rate on clean steel that would add up to thousands of ppm. We first reported hydration of ferric and ferrous ions of the form $[\text{Fe}(\text{H}_2\text{O})_n.m\text{H}_2\text{O}]^{2,3+}$ ($n=1-6, m=12$) at B3LYP with 6-311++g**(H, O) and SDD (Fe) basis sets. Although the hydration of $\text{Fe}(\text{H}_2\text{O})_6$ has been reported in early study (Li et al., 1996), this work, to the best of our knowledge is the first to present complete analysis of first and second shell iron hydration with various coordination numbers at this level of theory and basis set. Our calculations provide optimized geometries of two iron hydrated structures up to 18 water molecules at high level of theory, B3LYP/(genecp) and B3LYP/LanL2DZ. Results of Fe–OH₂ bond length in the first shell hydration are in good agreement with experimental values. We have demonstrated that hydrogen bonding networks helps stabilizing the complex of $[\text{Fe}(\text{H}_2\text{O})_6.12\text{H}_2\text{O}]^{2,3+}$. Interaction between water molecules and chloride ions from HCl, $[\text{Cl}(\text{H}_2\text{O})_n]^-$ ($n=1,2,3,, 9$), are reported. Our results provide a complete set of optimized geometrical structures with Cl⁻ treated by effective core potential basis set (SDD). The $[\text{Cl}(\text{H}_2\text{O})_9]^-$ shows very interesting geometrical properties with total binding energy of -124.4 kcal/mol. The arrangement of water molecules around chloride ion form three cyclic trimers (cages) connected to each other through hydrogen bonding. Iron ions promote formation of micelles in water solution, however,

form anionic complexes in HCl solution that might influence the phase behavior and viscoelastic properties of VES system.

The second part of the chapter discussed complexation of ferric and ferrous ion with chloride, hydroxide and bisulfate as a common anions in well stimulation treatment. Ferric chloride complex might alter the solution properties of viscoelastic surfactant. Our results showed for the first time a systematic DFT calculation of binding energy and geometrical structures of the complex $[\text{FeCl}_n(\text{H}_2\text{O})_{6-n}]^{3-n}$, where $n=1-6$, in gas-phase and water solution. The PCM solvation model is over estimating the value of Fe–Cl bond length; however, underestimating the Fe–OH₂ compared to gas-phase calculation. The total binding energy in gas-phase increases as number of chloride ions increases and reached a maximum of -1404.8 kcal/mol for $[\text{FeCl}_4]^-$ and then decreases for higher Cl/Fe ratio of 5 and 6. This suggests that tetrachloroferrate is the most stable structure at low-moderate chloride concentration. However, binding energy in water solution using PCM solvation model increases monotonically as the number of chloride ion increases in the complex. The results of the PCM model may be less precise because it does not incorporate the actual water molecules, which are only represented implicitly by a dielectric constant. Speciation model is consistent with gas-phase calculation where the complex $[\text{FeCl}_4]^-$ is the most dominant in solution, however, the solvation model clearly indicates the complexation reaction is thermodynamically favorable in solution. Reaction kinetic calculations are highly recommended at the same level of theory and basis set to predict the rate of reaction for formation of all ferric chloride complexes in both gas-phase and water solution. The third objective of this chapter, was to examine the structural and thermodynamic properties of iron ion with hydroxide and bisulfate. There were significant differences between hydrated and hydrolysis complexes in charge distribution, bond lengths, binding energies due to the fact that OH⁻ had a stronger repulsion to OH⁻ and H₂O molecules in octahedral geometry but very attractive to iron ions. Iron hydroxide complex resulted in collapse of the octahedral structure and both ferric and ferrous hydroxide complexes have coordination numbers less than 6 as one-

water molecule leaves the first hydration shell to the second. Binding energy of $\text{Fe}(\text{OH})_3 \cdot 3\text{H}_2\text{O}$ is larger than any ferric chloride complex which means that ferric ions are readily available to precipitate as hydroxide, however, as the pH of solution increases, the ferric chloride complex becomes dominant in solution.

In Chapter VI, we reported *ab initio* and classical molecular simulations on possible interaction between various anionic surfactant HGs with counterions present in stimulation fluid. This work addresses for the first time the effect of organic and inorganic counterions on binding energy, geometrical structural and thermodynamic properties of carboxylate, sulfate and sulfonate anionic surfactant HGs. We have found that the binding power of inorganic salts depends on atomic radius and total charge which is in agreement with previous work. Monovalent cation such as Na^+ is the lowest binding salt to acetate HG. The di- and trivalent ions has higher binding energy and shorted $\text{M}^{q+}-\text{O}$ bond length. In stimulation fluid, the order of binding power between inorganic salts and surfactant-acetate HG is: $\text{Al} > \text{Mn}(\text{III}) > \text{Fe}(\text{III}) > \text{Zn} > \text{Fe}(\text{II}) > \text{Mg} > \text{Mn}(\text{II}) > \text{Ca} > \text{Na}$. All binding energies for metal acetate are less than the corresponding molecular conformation of hydrated metal, which means that the dehydration of water molecules from metal ion and replacement by acetate ion is an exothermic process. As the hydration energy differs from one metal ion to another, it is expected to have individual influence on micelle formation, where the cation tends to adsorb at the interface between micelle and water or remain strongly hydrated in the bulk water solution. It is very interesting to observe that the difference in binding energy between the two clusters ($\Delta\Delta E_i = \Delta E_{\text{M-acetate}} - \Delta E_{\text{M-hydrated}}$) is highly correlated to ionic charge (q). The average value of this difference is 98.2, 309.8 and 669.0 kcal/mol for mono- di- and trivalent ions, respectively. This means that trivalent ions can form stable micelles and enhance viscosity faster with one-third concentration compared to monovalent. Results presented in this chapter show that the maximum number of surfactant HGs bind to cationic metal is not necessarily equivalent to the valence number. For the case of acetate with Ca^{2+} , the most stable structure is: $\text{Ca}(\text{OAc})_3 \cdot 4\text{H}_2\text{O}$. DFT calculations show

that there are number of factors determining the nature of metal ion interaction with free oxygen in carboxylate HG. In absence of water molecules, the bidentate interaction is more stable than the monodentate. Once water molecules are added to the system, hydrogen bonding starts to form with one free oxygen in the carboxylate HG, and hence monodentate binding is preferable. Switching the carboxylate-binding mode from monodentate to bidentate favors the $\text{H}_2\text{O} \rightarrow \text{CH}_3\text{COO}^-$ exchange. We have also shown the effect of increasing number of carbons in the HG on its binding energy is negligible. This chapter, to the best of our knowledge, presents the first DFT calculations of organic salt interaction with carboxylate surfactant HG, which is highly dependant on the nature of organic structure and associated inorganic salt. Sulfate and sulfonate have larger binding energy with metal cationic salts compared to carboxylate due to more freely oxygen atoms in the HG that are available for electron sharing interaction.

In Chapter VII, we have carried out DFT calculations in gas-phase with the 6-311++g** basis set at B3LYP levels to determine the geometric and energetic parameters of the different cationic HGs and to establish the most stable ones. In a consistent manner and for all calculations presented in this chapter, the 6-311++G(d,p) basis set was applied to H, O, C, Ca, Mg, Na, N atoms and SDD for Fe, Cl, atoms. The binding energy and hence the optimized geometrical structure are highly dependent on the location from which chloride ion counterbalance the positive charge on the HG. From the calculations of $\text{TMA}-\text{Cl}(\text{H}_2\text{O})_4$, we have found that water molecules form shield around TMA^+ HG with less access or penetration of chloride ion. Gas-phase calculations of $\text{Cl}-\text{HG}$ interactions shows that there is a minimum bond distance after which chloride ion does not exceed to counterbalance the HG positive charge. Values of binding energies indicate that free chloride ions in the solution will preferably counterbalance the positive charge on ammonium HG, however, it is less favorable for more than one Cl^- ion to complexate with the cationic part of the surfactant, though it is possible thermodynamically. The second part of the chapter presents for the first time a theoretical evidence of possible complexation mechanism between tetrachloroferrate $[\text{FeCl}_4]^-$ and cationic surfactant.

Our calculations indicate that the precipitation of cationic surfactant at high concentration of ferric ions in HCl solution is due to more than one possible mechanism. At $\text{pH} < 2.0$, the formation of the complex $[\text{FeCl}_n]^{3-n}$ is thermodynamically favorable which leads to FeCl_4^- as the most stable anion. Due to the molecular structure of tetrachloroferrate, the complex TMA- FeCl_4 is not favoring the formation of micelles, and hence phase separation and precipitation was observed experimentally. With high concentration of Fe(III), diatomic complex of the form $[\text{Fe}_2\text{Cl}_n]^{6-n}$ are expected. We have discussed the structure of $[\text{Fe}_2\text{Cl}_9]^{-3}$ which can result from excess amount of ferric chloride (FeCl_3) in solution. The third possible cause of surfactant precipitation is μ -oxo-bis(trichloroferrate) salt. tetrachloro-ferrate undergoes the reaction of replacing one Cl^- with OH^- ion that present in solution (especially at high pH) to form hydroxytrichloroferrate intermediate complex, $[\text{FeCl}_3\text{OH}]^-$, which dehydrate to form the anionic complex $[\text{Cl}_3\text{Fe}-\text{O}-\text{FeCl}_3]^{2-}$. Our calculation shows that $[\text{Fe}_2\text{Cl}_9]^{-3}$ has the highest binding power followed by $[\text{Fe}_2\text{Cl}_6\text{O}]^{2-}$, and then $[\text{FeCl}_4]^-$. Classical molecular dynamic (MD) simulation is employed to resolve the full chemical details of chloride effect in solution. Preliminary results show strong dependence of micellar structure on the number of Cl ions presented in solution.

In Chapter VIII, we have presented DFT calculation of various betaine and amidoamine oxide HGs. The most stable configurations in gas-phase and implicit water solution have been discussed. For betaine surfactants with HG that has both positive and negative charges, we have evaluated the binding energy dependence on the nature of counterion and discussed its influence on micelle formation and solution properties. Similarly to Chapter VII, the complex of AAMCDEEA- FeCl_4 has higher binding energy compared to other surfactant, which can explain the fast drop in viscosity and formation of precipitate when high Fe(III) concentration is present in HCl solution. The MD simulation showed clearly that distribution of chloride ions around single betaine surfactant has a dramatic influence on molecular configuration in water solution, which can explain the fuzzy behavior of viscosity as HCl concentration changes. Our *ab initio*

calculations showed that Cl^- ions can form up to three bonding with hydrogen atoms in surfactant HG, and as the concentration of Cl^- increases, more ions tend to get closer to surfactant backbone, and hence change the configuration of micelles, which ultimately affect solution viscosity. We believe that we are the first group to report the precipitation mechanism and to show computationally that chloride ions might play a crucial role in optimizing surfactant viscosity.

Generally speaking, and based on first-principle theoretical calculations result presented in this dissertation we can conclude that the molecular structure of surfactant, type and nature of counterions present in matrix acidizing treatment determine the properties of the stimulation solution and hence the successfulness of the operation. It is very important for oilfield industry engineers and R&D scientists to determine carefully all ions that might be present in solution before designing stimulation treatment.

9.2 Recommendations

One of the themes in the science of nanotechnology is the study of similarities and differences between the properties of clusters (small systems) and those of the corresponding bulk material. We anticipated that achievements of this study will help to better understand the behavior of larger acid system. Toward the objective of mapping the relation between various surfactant head groups and their functionality in acid diversion treatment or other applications in oilfield industry, we recommend the following studies to be carried out as an extension of this work:

1. Metal hydration of other key ions available in sea and field water such as Barium (Ba), Strontium (Sr), Manganese (Mn), silicon (Si) and Zinc (Zn) at their first shell coordination number (CN) and with water molecules in the second hydration shell ranging from ($m=5-14$) are critical to design more effective and efficient well treatments. Also, this will improve our understanding of the reaction kinetics in sandstone acidizing which is still unclearly comprehensively defined.

2. All calculations we carried out in this study were performed at $T=298.15$ K, and $P=1$ bar. Therefore, it is highly recommended to run single-point calculation on optimized structures of all metal ions in the study (Na^+ , Ca^{2+} , Mg^{2+} , Fe^{2+} , and Fe^{3+}) at higher temperature, and correlate changes in binding energy, bond length, and other structural properties with temperature. This will greatly benefit the oilfield industry as reservoir conditions fall in the range of high pressure and temperature. Previous leading studies on metal hydration solution behavior are concern in many cases with their applications in biological systems and medical where temperature is not a factor.
3. We have observed clear effect of water molecules on the structural properties and thermochemistry of ferric chloride complex. Therefore, it is recommended to examine the explicit effect of water in the first coordination shell with both tetrahedral and octahedral geometries. In this study we investigate the ferric and ferrous complexes based on six coordination numbers of iron atom. However, it has been shown experimentally that in the HCl and LiCl solution, for example, octahedral ferric chloride complexes comprise approximately 12 and 50% of the total ferric ion, respectively. Tetrahedrally coordinated ferric chloride complexes are more stable at high chloride concentration as in the case of FeCl_4^- shown in Chapter V.
4. We have not considered fractionation between Fe(II) and Fe(III) in this work, though other studies reported the rate constant for ferric-ferrous ($^{56}\text{Fe}^{2+} + ^{54}\text{Fe}^{3+} \leftrightarrow ^{56}\text{Fe}^{3+} + ^{54}\text{Fe}^{2+}$) exchange can be as high as $1000 \text{ M}^{-1}\text{sec}^{-1}$ (Welch et al., 2003). The direct exchange between two Fe atoms is unlikely to occur in aqueous solutions, because the cations are hydrated or complexed by other ligands. However, more than 99% of ferric-ferrous exchange occurs between $[\text{Fe}^{\text{II}}(\text{H}_2\text{O})_6]^{2+}$ and $[\text{Fe}^{\text{III}}(\text{H}_2\text{O})_5(\text{OH})]^{2+}$ in acidic solutions (Welch et al., 2003). DFT was used to study fractionation between ferric chloride complex with hexaaquoferrate (Hill and Schauble, 2008), but no systematic theoretical work has been done, to the best of our knowledge, to support numerous experimental observations of ferric chloride,

ferric-hydroxyl exchange with ferrous ions. Therefore, it is highly recommended to study fractionation between iron chloride and iron hydroxide complexes at the same level of theory. This study will enhance our understanding of iron complexations in acidic solutions, and will

5. Molecular species such as Sr^{2+} , SO_4^{2-} , CO_2 , CO_3^{2-} , HCO_3^- are in equilibrium in spent acid. Their interaction with VES and various metal ions present in solution is of great interest. Elemental chemistry and *ab initio* calculations are highly recommended to combine together to draw ions interactions map for live/spent acid solution.
6. Oligomeric and cleavable-sugar surfactants are becoming more efficient, requires less concentration (less expensive), and overcome many environmental problems (Hughes et al., 2002).
7. Construction of transparent-micromodel is very essential to determine the exact mechanism by which acid is diverted in porous media. The idea is based on similar approach taken by Browning and Fogler (Browning and Fogler, 1996) to study precipitating conditions of Calcium–HEDP system. The setup will have two glassy or any other transparent plates with symmetrical-grooves in one-side of both plates. Random generation model can be used to draw a picture of the pores and their connectivity. Also, a real image from CT-scan of rock sample can be used a model to be grooved on the plates. Then, the grooves are filled with CaCO_3 powder, and sealed. The acid with VES is to be injected from one side and observation of viscosity build up, creation of wormhole are recorded using high resolution camera. This is a powerful tool and it has been used recently to investigate biofilm accumulation and bacterial transport in porous matrices (Dunsmore et al., 2003). To mimic the wellbore area, it is highly recommend in this model to be cylindrical (different from existing reservoir micromodels) with fluid-in opening similar to perforation scalable size. The injection rate and experimental conditions are monitored using computer machine.
8. It is highly recommended to use MD simulation to calculate viscosity of solutions.

REFERENCES

- Aakesson, R., Pettersson, L.G.M., Sandstroem, M. and Wahlgren, U., 1992. Theoretical calculations of the Jahn-Teller effect in the hexahydrated copper(II), chromium(II), and manganese(III) ions, hexaaquacopper(2+), hexaaquachromium(2+) and hexaaquamanganese(3+), and comparisons with the hexahydrated copper(I), chromium(III), and manganese(II) clusters. *J. Phys. Chem.*, 96(1): 150-156.
- Abel, S., Waks, M., Marchi, M. and Urbach, W., 2006. Effect of surfactant conformation on the structures of small size nonionic reverse micelles: A molecular dynamics simulation study. *Langmuir*, 22: 9112-9120.
- Abou-Sayed, I.S., C.E. Shuchart and Gong, M., 2005. Well stimulation technology for thick carbonate reservoirs. Society of Petroleum Engineering. Paper IPTC 10647 presented at International Petroleum Technology Conference. November 21-23 Doha, Qatar.
- Al-Ghamdi, A.H., Nasr-El-Din, H.A., Al-Qahtani, A. and Samuel, M.M., 2004. Impact of acid additives on the rheological properties of viscoelastic surfactants and their influence on field application. Society of Petroleum Engineering. Paper SPE 89418 presented at SPE/DOE Symposium on Improved Oil Recovery. April 17-21 Tulsa, OK.
- Al-Mutairi, S.A. and Nasr-El-Din, H.A., 2005. Tube pickling procedures: Case studies. SPE paper presented at SPE European Formation Damage Conference. 25-27 May, Scheveningen, The Netherlands.
- Al-Nakhli, A.R., Nasr-El-Din, H.A. and Al-Baiyat, A.A., 2008. Interactions of iron(III) and viscoelastic surfactants: A new formation damage mechanism. Society of Petroleum Engineering. Paper SPE 112465 presented at SPE International Symposium and Exhibition on Formation Damage Control. February 13-15, Lafayette, LA.
- Alargova, R., Petkov, J., Petsev, D., Ivanov, I.B., Broze, G. and Mehreteab, A., 1995. Light scattering study of sodium dodecyl polyoxyethylene-2-sulfonate micelles in the presence of multivalent counterions. *Langmuir*, 11(5): 1530-1536.
- Allen, F.H., 2002. The Cambridge Structural Database: A quarter of a million crystal structures and rising. *Acta Cryst.*, B58: 380-388.
- Allen, M.P., 1987. *Computer Simulation of Liquids*. Clarendon Press, Oxford.

- Allen, R., Bandyopadhyay, S., and Klein, M., 2000. C12E2 Reverse micelle: A molecular dynamics study. *Langmuir*, 16: 10547-10552.
- Alruggova, R.G., Danov, K.D., Kralchevsky, P.A., Broze, C. and Mehreteab, A., 1998. Growth of giant rodlike micelles of ionic surfactant in the presence of Al^{3+} counterions. *Langmuir*, 14: 4036-4049.
- Appelo, C.A.J. and Postma, D., 2005. *Geochemistry, Groundwater and Pollution*. Taylor & Francis, Amsterdam, the Netherlands.
- Apted, M.J., Waychunas, G.A. and Brown, G.E., 1985. Structure and specification of iron complexes in aqueous solution determined by X-ray absorption spectroscopy. *Geochim. Cosmochim. Acta* 49: 2081-2089.
- Atkins, P., Overton, T., Rourke, J., Weller, M. and Armstrong, F., 2006. *Inorganic Chemistry*. Oxford University Press, Oxford.
- Bach, R.D., Shobe, D.S., Schlegel, B.B. and Nagel, C.J., 1996. Thermochemistry of iron chlorides and their positive and negative ions. *J. Phys. Chem.*, 100: 8770-8776.
- Baes, C.F. and Mesmer, R.E., 1976. *The Hydrolysis of Cations*. John Wiley & Sons, New York.
- Balbuena, P.B. and Seminario, J.M., 1999. *Molecular Dynamics: From Classical to Quantum Methods*. Theoretical and Computational Chemistry, 7. Elsevier, New York.
- Becke, A.D., 1988. Density-functional exchange-energy approximation with correct asymptotic behavior. *Phys. Rev. A*, 38(6): 3098-3100.
- Becke, A.D., 1993. Density-functional thermochemistry. III. The role of exact exchange. *J. Chem. Phys.*, 98(7): 5648-5652.
- Behler, A., Biermann, M., Hill, K., Raths, H., Victor, M.S. and Uphues, G., 2001. Industrial surfactant syntheses. In: J. Texter (Ed.), *Reactions and Synthesis in Surfactant Systems*. Surfactant Science Marcel Dekker, Inc., New York, pp. 1-44.
- Bene, J.D. and Pople, J.A., 1970. Theory of molecular interactions. I. Molecular orbital studies of water polymers using a minimal slater-type basis. *J. Chem. Phys.*, 52(9): 4858-4866.
- Bentwood, R.M., Barnes, A.J. and Orville-Thomas, W.J., 1980. Studies of intermolecular interactions by matrix isolation vibrational spectroscopy: Self-association of water. *J. Mol. Spectrosc.*, 84(2): 391-404.

- Bernal-Uruchurtu, M.I. and Ortega-Blake, I., 1995. A refined Monte Carlo study of Mg^{2+} and Ca^{2+} hydration. *J. Chem. Phys.*, 103(4): 1588-1598.
- Bjerrum, J. and Lukes, I., 1980. The iron(III)-chloride system, a study of the stability constants and of the distribution of the tetrachloro species between organic solvents and aqueous chloride solutions. *Acta Chemica Scandinavica A*, 40: 31-40.
- Bock, C.W., Markham, G.D., Katz, A.K. and Glusker, J.P., 2006. The arrangement of first- and second-shell water molecules around metal ions: Effects of charge and size. *Theor. Chem. Acc.* 115: 100-112.
- Boek, E.S., Jusufi, A., Lowen, H. and Maitland, G.C., 2002. Molecular design of responsive fluids: Molecular dynamics studies of viscoelastic surfactant solutions. *J. Phys.: Condens. Matter*, 14: 9413-9430.
- Boethling, R.S., 1994. Cationic Surfactants: Analytical and Biological Evaluation. *Surfactant Sciences* 53. Marcel Dekker, Inc., New York.
- Brady, G.W., Robin, M.B. and Varimbi, J., 1964. The structure of ferric chloride in natural and acid solutions. *Inorg. Chem.*, 3(8): 1168-1173.
- Brooks, B.R., Bruccoleri, R.E., Olafson, B.D., States, D.J., Swaminathan, S. and Karplus, M., 1983. CHARMM: A program for macromolecular energy, minimization, and dynamics calculations. *J. Comp. Chem.*, 4: 187-217.
- Browning, F.H. and Fogler, H.S., 1996. Effect of precipitating conditions on the formation of calcium-HEDP precipitates. *Langmuir*, 12(21): 5231-5238.
- Brudermann, J., Melzer, M., Buck, U., Kazimirski, J.K., Sadlej, J. and Bush, V., 1999. The asymmetric cage structure of $(\text{H}_2\text{O})_7$ from a combined spectroscopic and computational study. *J. Chem. Phys.*, 110(22): 10649-10652.
- Buck, U., Ettischer, I., Melzer, M., Buch, V. and Sadlej, J., 1998. Structure and spectra of three-dimensional $(\text{H}_2\text{O})_n$ clusters, $n = 8, 9, 10$. *Phys. Rev. Lett.*, 80: 2578 - 2581.
- Buhler, E., Mendes, E. Boltenhagen, P. Munch, J. P. Zana, R. and Candau, S.J., 1997. Phase behavior of aqueous solutions of a dimeric surfactant. *Langmuir*, 13: 3096-3102.
- Burke, L.A., Jensen, J.O., Jensen, J.L. and Krishnan, P.N., 1993. Theoretical study of water clusters. I. Pentamers. *Chem. Phys. Lett.*, 206(1-4): 293-296.

- Burneau, A., Genin, F. and Quiles, F., 2000. *Ab initio* study of the vibrational properties of acetic acid monomers and dimers. *Phys. Chem. Chem. Phys.*, 2: 5020-5029.
- Careja, V., Muntean, S., Marcec, M., Sayti, L. and Simon, Z., 2007. Molecular modeling of some calcium and magnesium ionic bridges. *Int. J. Quantum Chem.*, 107(1714-1718).
- Carey, F.A. and Sundberg, R.J., 2007. *Advanced Organic Chemistry: Part A: Structure and Mechanisms*. Springer, New York.
- Carl, D.R., Moision, R.M. and Armentrout, P.B., 2007. Binding energies for the inner hydration shells of Ca^{2+} : An experimental and theoretical investigation of $\text{Ca}^{2+}(\text{H}_2\text{O})_x$ complexes ($x=5-9$). *Int. J. Mass Spectrom.*, 265: 308-325.
- Carman, P.S., 2008. Use of anionic surfactants as hydration aid for fracturing fluid. US Patent No. 0108522 A1.
- Cates, M.E. and Candau, S.J., 1990. Static and dynamics of wormlike surfactant micelles. *J. Phys.: Condens. Matter* 2(33): 6869-6892.
- Chang, F.F., Love, T., Affeld, C.J., Blevins, J.B., Thomas, R.L. and Fu, D.K., 1999. Case study of a novel acid-diversion technique in carbonate reservoirs. Paper SPE 56529 presented at SPE Annual Technical Conference and Exhibition. 3-6 October, Houston, TX.
- Chang, F.F., Qu, Q. and Miller, M.J., 2002. Fluid system having controllable reversible viscosity US Patent No. 6,399,546 B1.
- Chase, B., Chmilowski, W. Marcinew, R., Mitchell, C., Dang, Y., Krauss, K. and Plummer, J., 1997. Clear fracturing fluid for increased well productivity. *Oilfield review*, 9(3): 20-23.
- Chen, C.-M. and Warr, G.G., 1997. Light scattering from wormlike micelles in an elongational field. *Langmuir*, 13: 1374-1376.
- Chen, G., Han, B. and Yan, H., 1998. Interaction of cationic surfactants with iron and sodium montmorillonite suspension. *J. Colloid Interface Sci.*, 201: 158-163.
- Christanti, Y., Fu, D. and Zhou, J., 2008. Fluid having recyclable viscosity. US Patent No. 0063681 A1.
- Ciavatta, L. and Grimaldi, M., 1975. On the hydrolysis of the iron(III) ion, Fe^{3+} , in perchlorate media. *J. Inorg. Nucl. Chem.*, 37(1): 163-169.

- Clementi, E. and Barsotti, R., 1978. Study of the structure of molecular complexes. Coordination numbers for Li^+ , Na^+ , K^+ , F^- and Cl^- in water. *Chem. Phys. Lett.*, 59(1): 21-25.
- Colaco, A., Marchand, J., Li, F. and Dahanayake, M.S., 2006. Viscoelastic surfactant fluids having enhanced shear recovery, rheology and stability performance US Patent No. 0105919 A1.
- Cotton, F.A., Daniels, L.M., Murillo, C.A. and Quesada, J.F., 1993. Hexaaqua dipositive ions of the first transition series: new and accurate structures; expected and unexpected trends. *Inorg. Chem.*, 32(22): 4861-4867.
- Crews, J.B. and Huang, T., 2008. Unsaturated fatty acids and mineral oils as internal breakers for VES-gelled fluids. US Patent No. 0227672 A1
- Crowe, C.W., 1985. Evaluation of agents for preventing precipitation of ferric hydroxide from spent treating acid. *J. Pet. Technol.*, 37(4): 691-695.
- Davidson, A.W., 1931. An introduction to the chemistry of acetic acid solutions. *Chem. Rev.*, 8(2): 175-190.
- Davidson, E.R., 2000. Computational transition metal chemistry. *Chem. Rev.*, 100(2): 351-352.
- Davies, A.S., George, W.O. and Howard, S.T., 2003. *Ab initio* and DFT computer studies of complexes of quaternary nitrogen cations: Trimethylammonium, tetramethylammonium, trimethylethylammonium, choline and acetylcholine with hydroxide, fluoride and chloride anions. *Phys. Chem. Chem. Phys.*, 5: 4533 - 4540.
- Davies, T.S., Ketner, A.M. and Raghavan, S.R., 2006. Self-assembly of surfactant vesicles that transform into viscoelastic wormlike micelles upon heating. *J. Am. Chem. Soc.*, 128(20): 6669–6675.
- Dégréve, L. and Jr., C.Q., 1996. The interfacial structure around ferric and ferrous ions in aqueous solution: The nature of the second hydration shell. *J. Electroanal Chem.*, 409(1-2): 25-31.
- deJong, J.J.D., Feringa, B.L. and Esch, J.V., 2006. Responsive molecular gels. In: R.G. Weiss and P. Terech (Ed.), *Molecular Gels: Materials with Self-Assembled Fibrillar Networks*. Springer, Dordrecht, The Netherlands, pp. 895-928.
- Doboson, R.E., Moss, D.K. and Premachandran, R.S., 2003. Thickened acid composition and uses thereof. World Intellectual Property Organization. Patent No.WO 03/093641 A1.

- Dousma, J. and Bruyn, P.L.D., 1976. Hydrolysis-precipitation studies of iron solutions. I. Model for hydrolysis and precipitation from Fe(III) nitrate solutions. *J. Colloid Interface Sci.*, 56(3): 527-539.
- Dreiss, C.A., 2007. Wormlike micelles: Where do we stand? Recent developments, linear rheology and scattering techniques. *Soft Matter*, 3: 956-970.
- Dunsmore, B.C., Bass, C.J. and Lappin-Scott, H.M., 2003. A novel approach to investigate biofilm accumulation and bacterial transport in porous matrices. *Enviro. Microbiol.*, 6(2): 183-187.
- Dzidic, I. and Kebarle, P., 1970. Hydration of the alkali ions in the gas phase. Enthalpies and entropies of reactions $M^+(H_2O)_{n-1} + H_2O = M^+(H_2O)_n$. *J. Phys. Chem.*, 74(7): 1466-1474.
- Economides, M.J., and Nolte, K.G. (Ed.), 2000. *Reservoir Stimulation*. John Wiley & Sons Ltd., New York.
- Faralli, C., Pagliai, M., Cardini, G. and Schettino, V., 2008. *Ab initio* molecular dynamics study of Mg^{2+} and Ca^{2+} ions in liquid methanol. *J. Chem. Theory Comput.*, 4 (1): 156-163.
- Faure, G., 1998. *Principles and Applications of Geochemistry* Prentice. Hall, Upper Saddle River, NJ.
- Floris, F.M., Persico, M., Tani, A. and Tomasi, J., 1994. Hydration shell structure of the calcium ion from simulations with *ab initio* effective pair potentials. *Chem. Phys. Lett.*, 227(1-2): 126-132.
- Flynn, C.M., 1984. Hydrolysis of inorganic iron(III) salts. *Chem. Rev.*, 84: 31-41.
- Foresman, J.B. and Frisch, A., 1993. *Exploring Chemistry with Electronic Structure Methods*. Gaussian, Inc. , Pittsburgh, PA.
- Frasch, H., 1896. Increasing the flow of oil wells. US Patent No. 556669
- Frindi, M., Michels, B., Levy, H. and Zana, R., 1994. Alkanediyl-.alpha.,.omega.-bis(dimethylalkylammonium bromide) Surfactants. 4. Ultrasonic absorption studies of amphiphile exchange between micelles and bulk phase in aqueous micellar solution. *Langmuir*, 10: 1140-1145.
- Frisch, M.J. Trucks, G. W., Schlegel, H. B., Scuseria, G. E., Robb, M. A. et al., 2004. *Gaussian 03*. Gaussian, Inc., Wallingford CT.

- Fukui, K., 1971. Recognition of stereochemical paths by orbital interaction. *Acc. Chem Res.*, 4(2): 57 - 64.
- George, M. and Weiss, R.G., 2002. Chemically reversible organogels via “latent” gelators. Aliphatic amines with carbon dioxide and their ammonium carbamates. *Langmuir*, 18(19): 7124-7135.
- Goddard, W.A., Brenner, D.W., Lyshevski, S.E. and Iafrate, G.J., 2002. *Handbook of Nanoscience, Engineering, and Technology*. CRC, Boca Raton, FL.
- Goldsipe, A. and Blankschtein, D., 2007. Molecular-thermodynamic theory of micellization of multicomponent surfactant mixtures: 2. pH-sensitive surfactants. *Langmuir*, 23(11): 5953 - 5962.
- González, B.S., Hernández-Rojas, J. and Wales, D.J., 2005. Global minima and energetics of $\text{Li}^+(\text{H}_2\text{O})_n$ and $\text{Ca}^{2+}(\text{H}_2\text{O})_n$ clusters for $n < 20$. *Chem. Phys. Lett.*, 412(1-3): 23-28.
- Gougier, P.D., Hendrick, J.E. and Coulter, A.W., 1985. Field investigation identifies sources and magnitude of iron problems. Paper SPE 13812 presented at SPE Production Operation Symposium. Tulsa, OK, March 10-12,
- Hansen, J.-P. and Löwen, H., 2000. Effective interaction between electronic double layers. *Annu. Rev. Phys. Chem.*, 51: 209-242.
- Hardy, M., Botermans, W., Hamouda, A., Valdal, J. and Warren, J., 1999. The first carbonate field application of a new organically crosslinked water shutoff polymer system,. Society of Petroleum Engineering. Paper SPE 50738 presented at International Symposium on Oilfield Chemistry. Houston, TX.
- Harris, D., Loew, G.H. and Komornicki, A., 1997. Structure and relative spin-state energetics of $[\text{Fe}(\text{H}_2\text{O})_6]^{3+}$: A comparison of UHF, Miller-Plesset, nonlocal DFT, and semiempirical INDO/S Calculations *J. Phys. Chem. A*, 101(21): 3959-3965.
- Harris, P.C. and Batenburg, D.v., 1999. A comparison of freshwater- and seawater-based borate-crosslinked fracturing fluids. Society of Petroleum Engineering. Paper SPE 50777 presented at International Symposium on Oilfield Chemistry. Houston, TX.
- Harry, D.N., Putzig, D.E., Moorhouse, R., DelPesco, T. and Jernakoff, P., 1999. Chemical structures of group 4 metal crosslinkers for polygalactomannans. Society of Petroleum Engineering. Paper SPE 50731 presented at International Symposium on Oilfield Chemistry. Houston, TX.

- Hartshorne, R.S., Hughes, T.L., Tustin, G.J., Zhou, J., Gareth, T. and Gones, T., 2007. Viscoelastic surfactant gels with reduced salt concentration. US Patent No. 0213232 A1
- Haselhorst, G., Wieghardt, K., Keller, S. and Schrader, B., 1993. The (μ -oxo)bis[trichloroferrate(III)] dianion revisited. *Inorg. Chem.*, 32(5): 520-525.
- Hassan, P.A., Candau, S.J., Kern, F. and Manohar, C., 1998. Rheology of wormlike micelles with varying hydrophobicity of the counterion. *Langmuir*, 14: 6025-6029.
- Hassan, P.A., Raghavan, S.R. and Kaler, E.W., 2002. Microstructural changes in SDS micelles induced by hydrotropic salt. *Langmuir*, 18: 2543-2548.
- Hehre, W.J., Yu, J., Klunzinger, P.E. and Lou, L., 1998. A Guide to Molecular Mechanics and Quantum Chemical Calculations. Wavefunction, Irvine, CA.
- Helgeson, H.C. and Kirkham, D.H., 1974. Theoretical prediction of the thermodynamic behavior of aqueous electrolytes at high pressures and temperatures; II, Debye-Huckel parameters for activity coefficients and relative partial molal properties. *Am. J. Sci.*, 274: 1199-1261
- Helgeson, H.C., Kirkham, D.H. and Flowers, G.C., 1981. Theoretical prediction of the thermodynamic behavior of aqueous electrolytes by high pressures and temperatures; IV, Calculation of activity coefficients, osmotic coefficients, and apparent molal and standard and relative partial molal properties to 600 °C and 5kb. *Am. J. Sci.*, 281: 1249-1516
- Hill, P.S. and Schauble, E.A., 2008. Modeling the effect of bond environment on equilibrium iron isotope fractionation in ferric aquo-chloro complexes. *Geochimica et Cosmochimica Acta*, 72: 1939-1958.
- Howell, I. and Neilson, G.W., 1996. Hydration in concentrated aqueous solution. *J. Phys.: Condens. Matter*, 8 (25): 4455-4463.
- Hu, Y.T., Boltenhagen, P. and Pine, D.J., 1998. Shear thickening in low-concentration solutions of wormlike micelles. I direct visualization of transient behaviour and phase transitions. *J. Rheol.*, 42: 1185-1208.
- Huang, T. and Crews, J.B., 2008. Do viscoelastic-surfactant diverting fluids for acid treatments need internal breaker. Society of Petroleum Engineering. Paper SPE 112484 presented at SPE International Symposium and Exhibition on Formation Damage Control. February 13-15, Lafayette, LA.

- Hughes, T., Jones, T., Gareth, J., Tustin, G.J. and Zhou, J., 2002. Viscoelastic wellbore treatment fluid. World Intellectual Property Organization. Patent No. WO 02/11874 A1
- In, M., 2001. Gemini surfactants and surfactant oligomers. In: J. Texter (Ed.), *Reactions and Synthesis in Surfactant Systems*. Surfactant Science. Marcel Dekker, Inc., New York, pp. 59-110.
- Israelachvili, J.N., 1991. *Intermolecular and Surface Forces, with Applications to Colloidal and Biological Systems*. Academic Press, London
- Janzen, C., Spangenberg, D., Roth, W. and Kleinermanns, K., 1999. Structure and vibrations of phenol(H₂O)_{7,8} studied by infrared-ultraviolet and ultraviolet-ultraviolet double-resonance spectroscopy and *ab initio* theory. *J. Chem. Phys.*, 110(20): 9898-9907.
- Jensen, J.O., Krishnan, P.N. and Burke, L.A., 1996. Theoretical study of water clusters: Nonamers. *Chem. Phys. Lett.*, 260,(3-4): 499-506
- Jian-xiao, L.V., Dong, W. and Ji-ti, Z., 2006. Interaction mechanisms between anionic surfactant micelles and different metal ions in aqueous solutions. *J. Dispersion Sci. Technol.*, 27(8): 1073-1077
- Jiang, J.-C., Wang, Y.-S., Chang, H.-C., Lin, S.H., Lee, Y.T., Niedner-Schatteburg, G. and Chang, H.-C., 2000. Infrared spectra of H⁺(H₂O)₅₋₈ clusters: Evidence for symmetric proton hydration. *J. Am. Chem. Soc.*, 122(7): 1398-1410.
- Jun, X., Wenqi, S., Ganzuo, L., and Gaoyong, Z., 2007. Simulation of micelle of zwitterionic DSB in NaCl aqueous solution. *Chem. Phys. Lett.*, 438: 326-329.
- Kalfayan, L., 2000. *Production Enhancement with Acid Stimulation*. PennWell Corporation, Tulsa, OK.
- Kalur, G., and Raghavan, S.R., 2005. Anionic wormlike micellar fluids that display cloud points: Rheology and phase behavior. *J. Phys. Chem. B*, 109: 8599-8604.
- Kalur, G.C., Frounfelker, B.D., Cipriano, B.H., Norman, A.I. and Raghavan, S.R., 2005. Viscosity increase with temperature in cationic surfactant solutions due to the growth of wormlike micelles. *Langmuir*, 21: 10998-11004.
- Kanicky, J.R., Poniatowski, A.F., Mehta, N.R. and Shah, D.O., 2000. Cooperativity among molecules at interfaces in relation to various technological processes: Effect of chain length on the pK_a of fatty acid salt solutions. *Langmuir*, 16(1): 172-177.

- Katz, A.K., Glusker, J.P., Beebe, S.A. and Bock, C.W., 1996. Calcium ion coordination: A comparison with that of beryllium, magnesium, and zinc. *J. Am. Chem. Soc.*, 118(24): 5752-5763.
- Kaupp, M., Schleyer, P.v.R., Stoll, H. and Preuss, H., 1991. Pseudopotential approaches to Ca, Sr, and Ba hydrides. Why are some alkaline earth MX_2 compounds bent? *J. Chem. Phys.*, 94: 1360-1366.
- Kefi, S., Lee, J., Pope, T., Sullivan, P., Nelson, E., Hernandez, A., Olsen, T., Parlar, M., Powers, B., Roy, A. and Twynam, A.. Expanding Applications for Viscoelastic Surfactants. *Oilfield Review*, Winter 2004/2005., 10-23.
- Kelly, R.M., Khan, S.A., Leduc, P., Tayal, A. and Prud'homme, R.K., 1995. Compositions for fracturing subterranean formations. US Patent No. 5214412.
- Khurana, E., Nielsen, S.O. and Klein, M.L., 2006. Gemini surfactants at the air/water interface: A fully atomistic molecular dynamics study. *J. Phys. Chem. B*, 110: 22136-22142.
- Kim, J., Mhin, B.J., Leeo, S.J. and Kim, K.S., 1994. Entropy-driven structures of the water octamer. *Chemical Physics Letters*, 219(3-4): 243-246.
- Kim, T.-S., Kida, T., Nakatsuji, Y., Hirao, T. and Ikeda, I., 1996a. Surface-active properties of novel cationic surfactants with two alkyl chains and two ammonio groups. *J. Am. Oil Chem. Soc.*, 73(7): 907-911.
- King, G. and Warshel, A., 1989. A surface constrained all-atom solvent model for effective simulations of polar solutions. *J. Chem. Phys.*, 91(6): 3647-3661.
- Knox, P., 2008. Polycationic viscoelastic compositions. US Patent No. 0255009 A1.
- Kruger, G., Boltersdorf, D. and Overkempe, K., 2003. Esterquats. In: K. Holmberg (Ed.), *Novel Surfactants: Properties, Applications and Biodegradability*. Surfactant Science. Marcel Dekker, Inc., New York, pp. 50-58.
- Kumar, R., Kalur, G.C., Ziserman, L., Danino, D. and Raghavan, S.R., 2007. Wormlike micelles of a C22-tailed zwitterionic betaine surfactant: From viscoelastic solutions to elastic gels. *Langmuir*, 23(26): 12849-12856.
- Kumar, R. and Raghavan, S.R., 2009. Photogelling fluids based on light-activated growth of zwitterionic wormlike micelles. *Soft Matter*, 5: 797-803.
- Laasonen, L. and Klein, M.L., 1994. *Ab initio* molecular dynamic study of hydrochloric acid in water. *J. Am. Chem. Soc.*, 116: 11620-11621.

- Laassonen, K.E. and Klein, M.L., 1997. *Ab initio* of aqueous hydrochloric acid. J. Phys. Chem. A, 101: 98-102.
- Lee, C., Chen, H. and Fitzgerald, G., 1995. Chemical bonding in water clusters. J. Chem. Phys. , 102(3): 1266-1269.
- Lee, C., Yang, W. and Parr, R.G., 1988. Development of the Colle-Salvetti correlation-energy formula into a functional of the electron density. Phys. Rev. B, 37(2): 785-789.
- Lemke, K.H. and Seward, T.M., 2008. Solvation processes in steam: *Ab initio* calculations of ion-solvent structures and clustering equilibria. Geochim. Cosmochim. Acta, 72(15): 3293-3310.
- Lequeux, F. and Candau, S.J., 1994. Dynamical properties of wormlike micelles: deviations from classical picture. In: C.A. Herb and R.K. Prud'homme (Ed.), Structure and Flow in Surfactant Solutions. ACS, pp. 51-62.
- Levin, Y., 2002. Electrostatic correlations: From plasma to biology. Rep. Prog. Phys, 65 1577-1632.
- Li, J., Fisher, C.L., Chen, J.L., Bashford, D. and Noodleman, L., 1996. Calculation of redox potentials and pKa values of hydrated transition metal cations by a combined density functional and continuum dielectric theory. Inorg. Chem., 35(16): 4694-4702.
- Li, L., Lin, L., Abad, C. and Bui, T., 2008. Acid internal breaker for viscoelastic surfactant fluid in brine. US Patent No. 0066916 A1.
- Lin, Z., Lu, B., Zakin, J.L., Talmon, Y., Zheng, Y., Davis, H.T. and Scriven, L.E., 2001. Influence of surfactant concentration and counterion to surfactant ratio on rheology of wormlike micelles. J. Colloid Interface Sci. , 239(2): 543-554.
- Lind, M.D., 1967. Structure of ferric chloride in aqueous solutions. J. Chem. Phys., 46: 2010-2011.
- Liu, W., Etschmann, B., Brugger, J., Spiccia, L., Foran, G. and McInnes, B., 2006. UV-vis spectrophotometric and XAFS studies of ferric chloride complexes in hypersaline LiCl solutions at 25–90 °C. Chem. Geol., 231(4): 326-349
- Lledos, A., Moreno-Manas, M., Sodupe, M., Vallribera, A., Mata, I., Martinez, B. and Molins, E., 2003. Bent and linear forms of the (m-oxo)bis[trichloroferrate(III)] dianion: An intermolecular effect - structural, electronic and magnetic properties. Eur. J. Inorg. Chem., 2003(23): 4187-4194.

- Luo, M., and Dai, L.L., 2007. Molecular dynamics simulations of surfactant and nanoparticle self-assembly at liquid–liquid interfaces. *J. Phys.: Condens. Matter* 19: 375109.
- Luter, M.D. and Wertz, D.L., 1981. Existence of tetrachloroironate(III) in hydrochloric acid solutions. *J. Phys. Chem.*, 85: 3542-3543.
- Magid, L.J., Han, Z., Li, Z. and Butler, P.D., 2000. Tuning the contour lengths and persistence lengths of cationic micelles: The role of electrostatics and specific ion binding. *J Phys Chem B*, 104: 6717-6727.
- Magini, M. and Radnai, T., 1979. X-ray diffraction study of ferric chloride solutions and hydrated melt. Analysis of the iron (III)–chloride complexes formation. *J. Chem. Phys.* , 71: 4255-4262.
- Maheshwary, S., Patel, N., Sathyamurthy, N., Kulkarni, A.D. and Gadre, S.R., 2001. Structure and stability of water clusters $(\text{H}_2\text{O})_n$, $n = 8-20$: An *ab initio* investigation. *J. Phys. Chem. A*, 105(46): 10525-10537.
- Maillet, J.-B., Lachet, V., and Coveney, P.V., 1999. Large scale molecular dynamics simulation of self-assembly processes in short and long chain cationic surfactants. *Phys. Chem. Chem. Phys.*, 1(5277-5290).
- Maitland, G.C., 2000. Oil and gas production. *Curr. Opin. Solid State Mater. Sci.*, 5(5-6): 301-311.
- Marcus, Y., 2009. Effect of ions on the structure of water: Structure making and breaking. *Chem. Rev.*, 109: 1346-1370.
- Markham, G.D., Glusker, J.P. and Bock, C.W., 2002. The arrangement of first- and second-sphere water molecules in divalent magnesium complexes: Results from molecular orbital and density functional theory and from structural crystallography. *J. Phys. Chem. B*, 106(19): 5118-5134.
- Martin, R.L., Hay, P.J. and Pratt, L.R., 1997. Hydrolysis of ferric ion in water and conformational equilibrium. *J. Phys. Chem. A*, 102(20): 3565 -3573.
- Menger, F.M., Keiper, J.S. and Azov, V., 2000. Gemini surfactants with acetylenic spacers. *Langmuir*, 16(5): 2062-2067.
- Meot-Ner, M. and Speller, C.V., 1986. Filling of solvent shells about ions. 1. Thermochemical criteria and the effects of isomeric clusters. *J. Phys. Chem.*, 90(25): 6616-6624.

- Michel, D.a.C., D.J., 2007. Coarse-grained simulation of amphiphilic self-assembly. *J. Chem. Phys.*, 126: 034506-1 - 034506-12.
- Missel, P.J., Mazer, M.A., Bendek, G.B. and Young, C.Y., 1980. Thermodynamic analysis of the growth of sodium dodecyl sulfate micelles. *J. Phys. Chem.*, 84: 1044-1057.
- Missel, P.J., Mazer, M.A., Carey, M.C. and Benedek, G.B., 1989. Influence of alkali-metal counterion identity on the sphere-to-rod transition in alkyl sulfate micelles. *J. Phys. Chem.*, 93: 8354-8366.
- Molchanov, V.S., Philippova, O.E., Khokhlov, A.R., Kovalev, Y.A. and Kuklin, A.I., 2007. Self-assembled networks highly responsive to hydrocarbons. *Langmuir*, 23(1): 105-111.
- Morris, L., 2008. Methods of chemical diversion of scale inhibitors. US Patent No. 20080257551 A1
- Morse, J.W., Millero, F.J., Cornwell, J.C. and Rickard, D., 1987. The chemistry of the hydrogen sulfide and iron sulfide systems in natural waters. *Earth Sci. Rev.*, 24(1): 1-42.
- Muller-Dethlefs, K. and Hobza, P., 2000. Noncovalent interactions: A challenge for experiment and theory. *Chem Rev*, 100: 143-167.
- Murata, K. and Irish, D.E., 1988. Raman studies of the hydrated melt of $\text{FeCl}_3 \cdot 6\text{H}_2\text{O}$. *Spectroch. Acta*, 44A(7): 739-743.
- Nakabayashi, T., Sato, H., Hirata, F. and Nishi, N., 2001. Theoretical study on the structures and energies of acetic acid dimers in aqueous solution. *J. Phys. Chem. A*, 105(1): 245-250.
- Nasr-El-Din, H.A., Al-Mohammad, A.M., Al-Shurei, A.A., Merwat, N.K., Erbil, M.M. and Samuel, M., 2006. Restoring the injectivity of water disposal wells using a viscoelastic surfactant-based acid. *J. Pet. Sci. Technol.*, 54(1-2): 10-24
- Nasr-El-Din, H.A., Al-Mohammad, A.M., Al-Shurei, A.A., Merwat, N.K., Erbil, M.M. and Samuel, M., 2004. Matrix stimulation of water disposal wells using viscoelastic surfactant-based acid. Paper SPE 88588 presented at SPE Asia Pacific Oil and Gas Conference and Exhibition. 18-20 October, Perth, Australia,
- Nasr-El-Din, H.A., Al-Zahrani, A.A., Garzon, F.O., Giraldo, C.A.F., Al-Hakami, I.M. and Al-Marri, H.M., 2009. Acid fracturing of gas wells by use of an acid precursor in the form of solid beads: Lessons learned from first field application. *SPEPO*, 24(2): 320-335.

- Nasr-El-Din, H.A. and Samuel, M., 2007. Lessons learned from using viscoelastic surfactants in well stimulation. SPEPO, 22(1): 112-120.
- Nasr-El-Din, H.A., Zabihi, M., Kelkar, S.K. and Samuel, M., 2007. Development and field application of a new hydrogen sulfide scavenger for acidizing sour-water injectors. Paper SPE 106442 presented at International Symposium on Oilfield Chemistry. 28 February-2 March, Houston, TX.
- Neuse, E.W. and Meirim, M.G., 1984. Synthesis and spectroscopic features of bis(tetramethylammonium) and bis(benzyltriethylammonium) salts possessing a μ -oxo-bis(trichloroferrate) anion structure. Transition Met. Chem. , 9(6): 205-208.
- Niu, S. and Hall, M.B., 2000. Theoretical studies on reactions of transition-metal complexes. Chem. Rev., 100: 353-405.
- Noodlemana, L., Penga, C.Y., Casea, D.A. and Mouescab, J.-M., 1995. Orbital interactions, electron delocalization and spin coupling in iron-sulfur clusters. Coordination Chemistry Reviews, 144: 199-244.
- Ogino, H., Inomata, S. and Tobita, H., 1998. Abiological iron-sulfur clusters. Chem. Rev., 98(6): 2093-2122.
- Ohtaki, H. and Radnai, T., 1993. Structure and dynamics of hydrated ions. Chem. Rev., 93(9): 1157-1204.
- Padding, J.T., Boek, E.S., and Briels, W.J., 2005. Rheology of wormlike micellar fluids from Brownian and molecular dynamics simulations. J. Phys.: Condens. Matter, 17: S3347-S3353.
- Page, A.J. and Nagy-Felsobuki, E.I.v., 2008. *Ab initio* study of ground state MH_2 , HMH^{e+} and MHe_2^{2+} , $M = Mg, Ca$. Phys. Chem. Chem. Phys., 10: 1285-1285.
- Pavlov, M., Siegban, P.E.M. and Sanstrom, M., 1998. Hydration of beryllium, magnesium, calcium and zinc ions using density functional theory. J. Phys. Chem. A, 102: 219-228.
- Pedretti, A., Villa, L. and Vistoli, G., 2004. VEGA - An open platform to develop chemo-bio-informatics applications, using plug-in architecture and script programming. J. Comput. Aided Mol. Des., 18: 167-173.
- Periole, X., Allouche, D., Daudey, J.-P. and Sanejouand, Y.-H., 1997. Simple two-body cation-water interaction potentials derived from *ab Initio* calculations. comparison to results obtained with an empirical approach. J. Phys. Chem. B, 101 (25): 5018 -5025.

- Phillips, J.C. et al., 2005. Scalable molecular dynamics with NAMD. *Journal of Computational Chemistry*, 26(16): 1781-1802.
- Porter, M.R., 1994. *Handbook of Surfactants*. Springer, New York, pp. 113-121.
- Prell, J.S. and Williams, E.R., 2009. Structures of thermal, mass-selected water clusters probed with hydrophobic ion tags infrared photodissociation spectroscopy. *J. Am. Chem. Soc.*, 131(11): 4110-4119.
- Pribble, R.N. and Zwier, T.S., 1994a. Size-specific infrared spectra of benzene-(H₂O)_n clusters (n = 1 through 7): Evidence for noncyclic (H₂O)_n. *Structures Science*, 265(5168): 75-79.
- Pugliano, N. and Saykally, R.J., 1992. Measurement of quantum tunneling between chiral isomers of the cyclic water trimer. *Science*, 257(5078): 1937 - 1940.
- Pye, C.C., Corbeil, C.R. and Rudolph, W.W., 2006. An *ab initio* investigation of zinc chloro complex. *Phys. Chem. Chem. Phys.*, 8: 5428-5436.
- Raghavan, S.R.a.K., E.W., 2001. Highly viscoelastic wormlike micellar solutions formed by cationic surfactants with long unsaturated tails. *Langmuir*, 17: 300-306.
- Rae, P. and di-Lillo, G., 2003. Matrix acid stimulation - A review of the state-of-the-art. Paper SPE 82260 presented at the European Formation Damage Conference. Society of Petroleum Engineering. 13-14 May, The Hague, The Netherlands.
- Rao, J.S., Dinadayalane, T.C., Leszczynski, J. and Sastry, G.N., 2008. Comprehensive study on the solvation of mono- and divalent metal cations: Li⁺, Na⁺, K⁺, Be²⁺, Mg²⁺ and Ca²⁺. *J. Phys. Chem. A*, 112(50): 12944-12953.
- Rathman, J.F. and Scamehorn, J.F., 1987. Counterions binding on micelles: Effect of surfactant structure. *Langmuir*, 3: 372-377.
- Rauk, A., 2001. *Orbital Interaction: Theorey of Organic Chemistry*. John Wiley & Sons, Inc. , New York.
- Remsungnen, T. and Rode, B.M., 2004. Molecular dynamic simulation of the hydration of transition meta ions: The role of non-additive effect in the hydration shells of Fe²⁺ and Fe³⁺ ions. *Chem. Phys. Lett.*, 385: 491-497.
- Renouf, P., Hebrault, D., Desmurs, J.-R., Mercier, J.-M., Mioskowski, C. and Lebeau, L., 1999. Synthesis and surface-active properties of a series of new anionic gemini compounds. *Chem. Phys. Lipids*, 99(1): 21-32

- Rickard, D. and Luther, G.W., 2007. Chemistry of iron sulfides. *Chem Rev.*, 107: 514-562.
- Roco, M.C. and Bainbridge, W.S., 2001. Societal Implications of Nanoscience and Nanotechnology. National Science Foundation, Arlington, VA.
- Santana-Casiano, J.M., González-Dávila, M. and Millero, F.J., 2005. Oxidation of nanomolar levels of Fe(II) with oxygen in natural waters. *Environ. Sci. Technol.*, 39(7): 2073-2079.
- Satyanarayana, L., Madhusudan, R.K. and Manorama, S.V., 2003. Synthesis of nanocrystalline $\text{Ni}_{1-x}\text{Co}_x\text{Mn}_x\text{Fe}_{2-x}\text{O}_4$: A material for liquefied petroleum gas sensing. *Sensors and Actuators B*, 89(1): 62-67.
- Sasol Olefins & Surfactants. 2005. Sasol Company Brochure, Marl, Germany.
- Savins, J.G., 1968. Shear thickening phenomena in poly(vinyl)alcohol-borate complexes. *Rheologica Acta*, 7(1): 87-93.
- Schechter, R.S., 1992. Oil Well Stimulation. Prentice Hall, Inc., Englewood Cliffs, NJ.
- Schoonena, M.A.A. and Barnes, H.L., 1988. An approximation of the second dissociation constant for H_2S . *Geochimica et Cosmochimica Acta*, 52(3): 649-654
- Schröder, D., Kretzschmar, I. and Schwarz, H., 2003. On the structural dichotomy of cationic, anionic, and neutral FeS_2 . *J. Phys. Chem. A*, 107(16): 2821-2828.
- Sein, A., Engberts, J.B.F.N., van der Linden, E. and van de Pus, T., 1993. Salt-induced transition from a micellar to a lamellar liquid crystalline phase in dilute mixtures of anionic and nonionic surfactants in aqueous solution. *Langmuir*, 9(7): 1714-1720.
- Seminario, J.M., 1999. *Ab initio* and DFT for the strength of classical molecular dynamics. In: P.B. Balbuena and J.M. Seminario (Ed.), *Molecular dynamics: From Classical to Quantum Methods Theoretical and Computational Chemistry* Elsevier, New York, pp. 101-127.
- Sengul, M. and Remisio, L.H., 2002. Applied carbonate stimulation - An engineering approach. Society of Petroleum Engineering. Paper SPE 78560 presented at Abu Dhabi International Petroleum Exhibition and Conference. October 13-16 Abu Dhabi, United Arab Emirates.

- Shang, C.X., Bououdina, M., Song, Y. and Guo, Z.X., 2004. Mechanical alloying and electronic simulations of (MgH^{2+}M) systems ($\text{M}=\text{Al}$, Ti , Fe , Ni , Cu and Nb) for hydrogen storage. *International Journal of Hydrogen Energy*, 29(1): 73-80.
- Sherman, D.M., 2001. Quantum chemistry and classical simulations of metal complexes in aqueous solutions. In: J.J. Rosso and P.H. Ribbe (Ed.), *Molecular Modeling Theory: Applications in the Geosciences*. The Mineralogical Society of America, Washington, DC, pp. 273-317.
- Silverman, J. and Dodson, R.W., 1952. The exchange reaction between the two oxidation states of iron in acid solution. *J. Phys. Chem.*, 56(7): 846-852.
- Singh, N.J., Olleta, A.C., Kumar, A., Park, M., Yi, H.-B., Bandyopadhyay, I., Lee, H.M., Tarakeshwar, P. and Kim, K.S., 2006. Study of interactions of various ionic species with solvents toward the design of receptors. *Theoretical Chemistry Accounts*, 115(2-3): 127-135.
- Smalley, R.E. and Yakobsonb, B.I., 1998. The future of the fullerenes. *Solid State Communications*, 107(11): 597-606.
- Smith, C.F., Crowe, C.W. and Nolan, T.J., 1969. Secondary deposition of iron compounds following acidizing treatments. *JPT*, 21(9): 1121-1129.
- Smith, R.M. and Martell, A.E., 1976. *Critical Stability Constants*. Plenum, New York, pp. 7-20.
- Stumm, W., 1990. *Aquatic Chemical Kinetics: Reaction Rates of Processes in Natural Waters*. Wiley-Interscience New York, pp. 91-110.
- Stumm, W. and Morgan, J.J., 1996. *Aquatic Chemistry*. Wiley-Interscience, New York.
- Tagirov, B.R., Zotov, A.V. and Akinfiev, N.N., 1997. Experimental study of dissociation of HCl from 350 to 500°C and from 500 to 2500 bar: Thermodynamic properties of $\text{HCl}^{\text{0(aq)}}$. *Geochimica et Cosmochimica Acta*, 61(20): 4267-4280.
- Taylor, K.C., Nasr-El-Din, H.A. and Al-Alawi, M.J., 1999. Systematic study of iron control chemicals used during well stimulation. *SPE J.*, 4(1): 19-24.
- Teot, A.S., 1998. Chemical methods of ferric Ion removal from acid solution. US Patent No. 4,790,958.
- Tissandier, M.D., Singer, S.J. and Coe, J.V., 2000. Enumeration and evaluation of the water hexamer cage structure. *J. Phys. Chem. A* 104(4): 752-757.

- Tongraar, A. and Rodeb, B.M., 2004. Dynamical properties of water molecules in the hydration shells of Na^+ and K^+ : *ab initio* QM/MM molecular dynamics simulations. *Chem. Phys. Lett.*, 385(5-6): 378-383
- Trachtman, M., Markham, G.D., Glusker, J.P., George, P. and Bock, C.W., 1998. Interactions of metal ions with water: Ab initio molecular orbital studies of structure, bonding enthalpies, vibrational frequencies and charge distributions. Monohydrates. *Inorg. Chem.*, 37(17): 4421-4431.
- Trazona-Vasquez, F. and Balbuena, P.B., 2007. Dendrimer-tetrachloroplatinate precursor interactions. 1. Hydration of Pt(II) species and PAMAM outer pockets. *J. Phys. Chem. A*, 111: 932-944.
- Troyanov, S.I., Feist, M. and Kemnitz, E., 1999. Halogeno metallates of transition elements with cations of nitrogen-containing heterocyclic bases. VIII Syntheses and crystal structures of novel bromoferrates(III), chloro-, and aquachloroferrates(III) with tetrahedral and octahedral Iron coordination, among them two neutral complexes of iron(II) and (III). *Zeitschrift Für Anorganische und Allgemeine Chemie*, 625(5): 806 - 812.
- Tsai, C.J. and Jordan, K.D., 1993. Theoretical study of the $(\text{H}_2\text{O})_6$ cluster. *Chem. Phys. Lett.*, 213(1-2): 181-188.
- Ugalde, J.M., Alkorta, I. and Elguero, J., 2000. Water clusters: Towards an understanding based on first principles of their static and dynamic properties. *Angew. Chem. Int. Ed.*, 39(4): 717-721.
- Ungerer, P., Tavitian, B. and Boutin, A., 2005. Applications of Molecular Simulation in the Oil and Gas Industry: Monte Carlo Methods. Editions Technip, Paris.
- Uphues, G., 1998. Chemistry of amphoteric surfactants. *Fett/Lipid* 100(11): 490-497.
- Vinogradov, E.V., Smirnov, P.R. and Trostin, V.N., 2003. Structure of hydrated complexes formed by metal ions of Groups I—III of the Periodic Table in aqueous electrolyte solutions under ambient conditions. *Russ. Chem. Bull., International Edition*, 52(6): 1253-1271.
- Vlachy, N., Drechsler, M., Verbavatz, J.-M., Touraud, D. and Kunz, W., 2008. Role of the surfactant headgroup on the counterion specificity in the micelle-to-vesicle transition through salt addition. *J. Colloid Interface Sci.*, 319(2): 542-548.
- Vlachy, N., Jagoda-Cwiklik, B., Vácha, R., Touraud, D., Jungwirth, P. and Kunz, W., 2009. Hofmeister series and specific interactions of charged headgroups with aqueous ions. *Adv. Colloid Interface Sci.*, 146(1-2): 42-47.

- Waizumi, K., Ohtaki, H., Masuda, H., Fukushima, N. and Watanabe, Y., 1992. Density functional calculations on the geometries and dissociation energies of $[M(H_2O)_6]^{2+}$ ions. $M^{2+} = Cr^{2+}, Mn^{2+}, Fe^{2+}, Co^{2+}, Ni^{2+}, Cu^{2+}$, and Zn^{2+} . *Chem. Lett.*, 21(8): 1489-1496.
- Warnke, Z., Wyrzkowski, D. and Warwzyniak, G., 2003. Synthesis, spectroscopic characteristics and conductometric investigation of new tetrachloro- and tetrabromoferrates(1-). *Polish J. Chem.*, 77: 1121-1129.
- Wattebled, L. and Laschewsky, A., 2007. Effect of organic additives on the behavior of dimeric "gemini" surfactants in aqueous solution. *Langmuir*, 23: 10044-10052.
- Welch, S.A., Beard, B.L., Johnson, C.M. and Brateman, P.S., 2003. Kinetic and equilibrium Fe isotope fractionation between aqueous Fe(II) and Fe(III). *Geochim. Cosmochim. Acta*, 67(22): 4231-4250.
- Welton, T.D., 2008. Ortho ester breakers for viscoelastic surfactant gels and associated methods. US Patent No. 0103070 A1
- Welton, T.D., Lewis, S.J. and Funkhouser, G.P., 2007. Viscoelastic surfactant fluids and associated acidizing methods. US Patent No. 7,159,659 B2
- Wyrzkowski, D., Kruszynski, R., Klak, J., Mrozinski, J. and Warnke, Z., 2006. Structural and physiochemical characteristics of tetrabutylammonium tetrahalogenoferrates(III), $[C_4H_9)_4N][FeBr_{4-n}Cl_n]$. *Z. Anorg. Allg. Chem.*, 632: 624-628.
- Wyrzkowski, D., Kruszynski, R., Klak, J., Mrozinski, J. and Warnke, Z., 2007. Synthesis and magnetic characteristics of new tetrachloroferrates(III) with 2-methylpyridinium, 3-methylpyridinium and 4-methylpyridinium cations: X-ray crystal structure of 4-methylpyridinium tetrachloroferrate(III). *Inorg. Chim. Acta*, 360(10): 3354-3360
- Wyrzkowski, D., Kruszynski, R., Klak, J., Mrozinski, J. and Warnke, Z., 2008. Structural and magnetic characteristics of tetraammonium tetrahalogenoferrates (III). *Inorg. Chim. Acta* 361: 262-268.
- Xu, Y., Feng, J., Shang, Y., and Liu, H., 2007. Molecular dynamics simulation for the effect of chain length of spacer and tail of cationic gemini surfactant on the complex with anionic polyelectrolyte. *Chin. J. Chem. Eng.*, 15(4): 560-565.
- Yamabe, S., Minato, T., Sakamoto, M. and Hirao, K., 1985. A theoretical study on the structures and stabilities of protonated hydrogen sulphide – hydrogen sulfide clusters. *Can. J. Chem.*, 63(9): 2571-2574.

- Young, D.C., 2001. Computational Chemistry: A Practical Guide for Applying Techniques to Real-World Problem. John Wiley & Sons, Inc. , New York.
- Zana, R., 2002. Alkanediyl- α,ω -bis(dimethylalkylammonium bromide) Surfactants: II. krafft temperature and melting temperature. *Journal of Colloid and Interface Science*, 252(1): 259-261.
- Zana, R., Benrraou, M. and Rueff, R., 1991. Alkanediyl-.alpha.,.omega.-bis(dimethylalkylammonium bromide) surfactants. 1. Effect of the spacer chain length on the critical micelle concentration and micelle ionization degree. *Langmuir*, 7(6): 1072-1075.
- Zana, R. and Kaler, E.W. (Ed.), 2007. Giant Micelles: Properties and Applications. *Surfactant Science*, 140. CRC Press, New York, pp.453-470.
- Zana, R.R. and Alami, E.O., 2003. Gemini surfactant. In: K. Holmberg (Ed.), *Novel Surfactants: Properties, Applications, and Biodegradability*. Surfactants science. Marcel Dekker, Inc., New York, pp. 385-424.
- Zana, R.R. and Xia, J. (Ed.), 2004. Gemini surfactants: Synthesis, Interfeacial and Solution-phase Behavior, and Applications. *Surfactant Science*, 117. Marcel Dekker, Inc., New York, pp. 10-31.
- Zhou, J. and Hughes, T., 2006. Aqueous viscoelastic fluid. US Patent No. 7,036,585 B2
- Zhou, J. and Trevor, H., 2002. Wiscoelastic compositions. World Intellectual Property Organization Patent No. WO 02/064945 A1
- Zhu, Y.-p., Masuyama, A. and Okahara, M., 1990. Preparation and surface active properties of amphipathic compounds with two sulfate groups and two lipophilic alkyl chains. *J. Am. Oil Chem. Soc.*, 67(7): 459-463.
- Zimmerman, J.A. and Schnaare, R.L., 1999. Predicting the critical micelle concentration in a pH-mediated ternary-surfactant mixture using the regular solution approximation. *J. Colloid Interface Sci.*, 220(1): 75-80.

APPENDIX A

SUPPORTING MATERIALS FOR CHAPTER IV

***Ab initio* Study of Hydration and Binding Energies for $M^x (H_2O)_n \cdot mH_2O$ Clusters ($M=Ca^{2+}, Mg^{2+}, Na^+$, $n=1-9$, $m=1-3$) in Carbonate Reservoirs**

This appendix presents supporting materials to the main text in CHAPTER IV including schematic diagram of the problem, tables of sequential binding energy and thermodynamic properties at optimized structure using B3LYP/6-311++G(d,p).

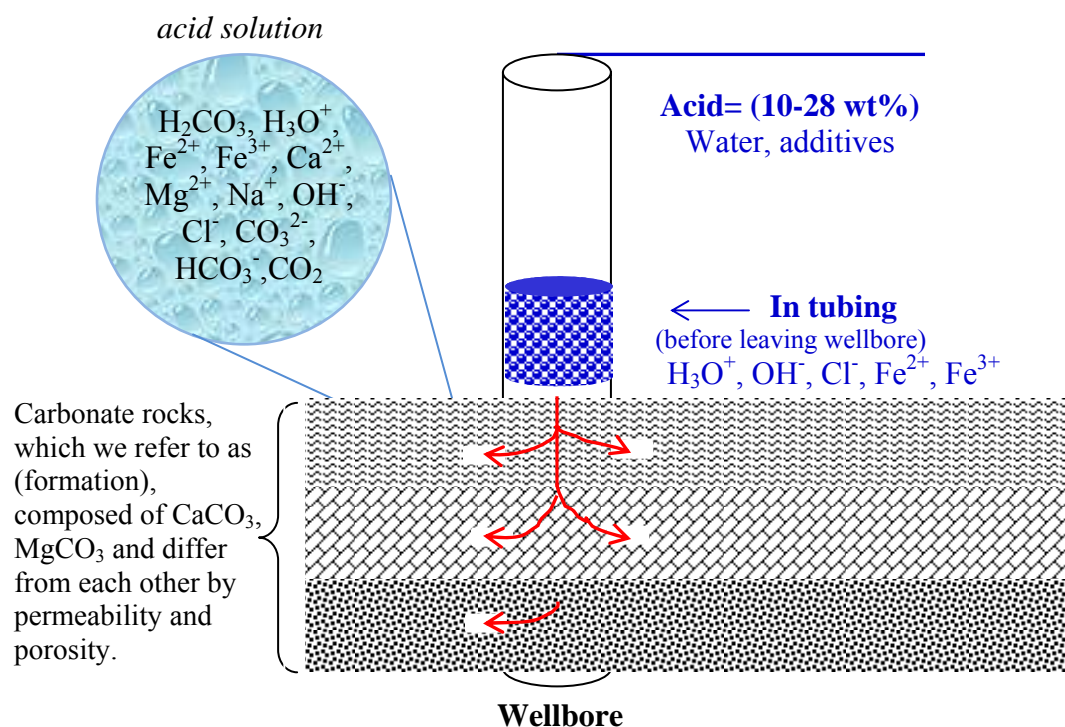


Figure A.1: Schematic diagram of the problem.

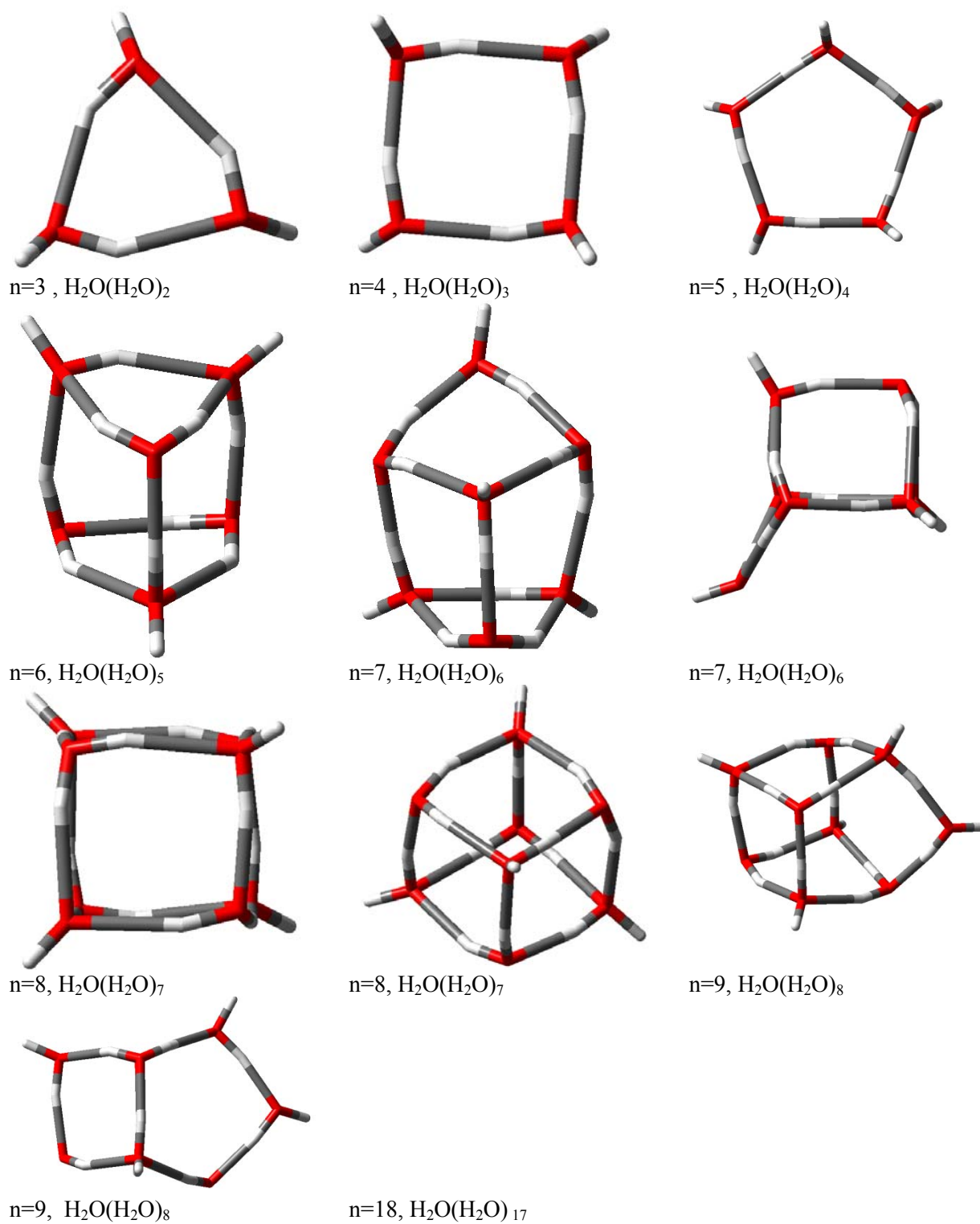


Figure A.2: Schematic representation of the most stable water-cluster, $\text{H}_2\text{O}(\text{H}_2\text{O})_n$, ($n=1-9,18$) calculated at B3LYP/6-311++G(d,p).

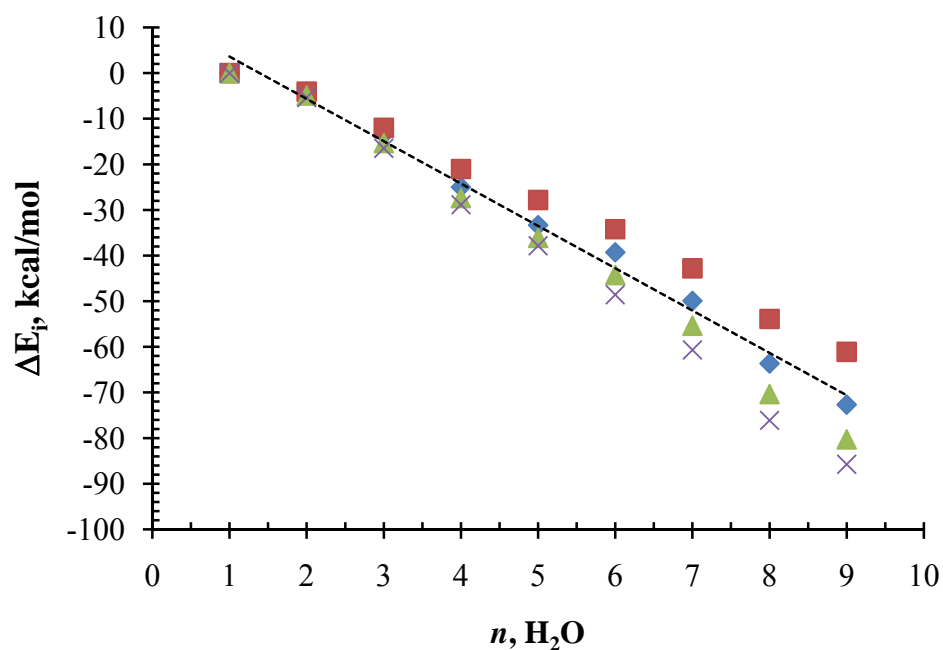


Figure A.3: Binding energy of water cluster as function of water monomers for $(\text{H}_2\text{O})_n$, ($n=1-9$) calculated at: (♦) B3LYP/6-311++G(d,p) from this study, (■) HF/6-311++G(2d,2p), (▲) B3LYP/6-311++G(2d,2p) and (×) MP2/6-311++G(2d,2p). The last three are taken from Ref.(Maheshwary et al., 2001). The dotted line shows a linear fitting of $\Delta E_{i,b} = A + B/n$, with $B = 12.89$ and $A = -9.278$.

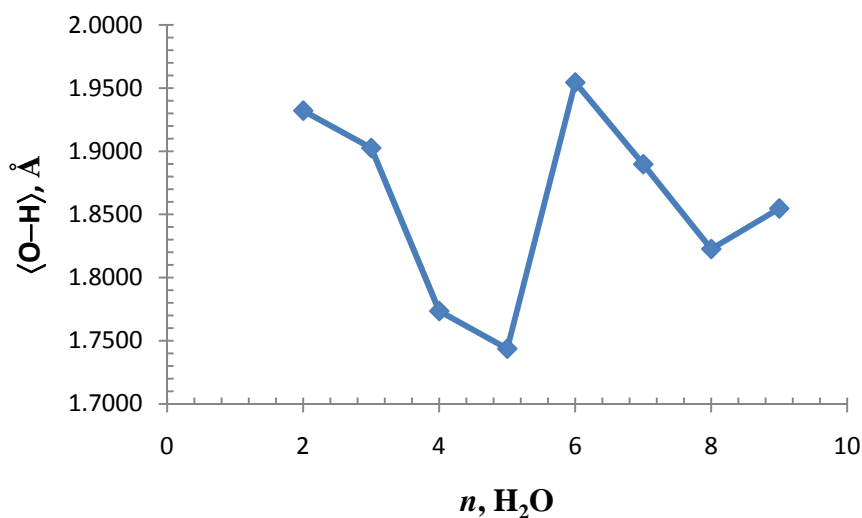


Figure A.4: Average hydrogen bond for water clusters, $(\text{H}_2\text{O})_n$, ($n=1-9$) calculated at: B3LYP/6-311++G(d,p).

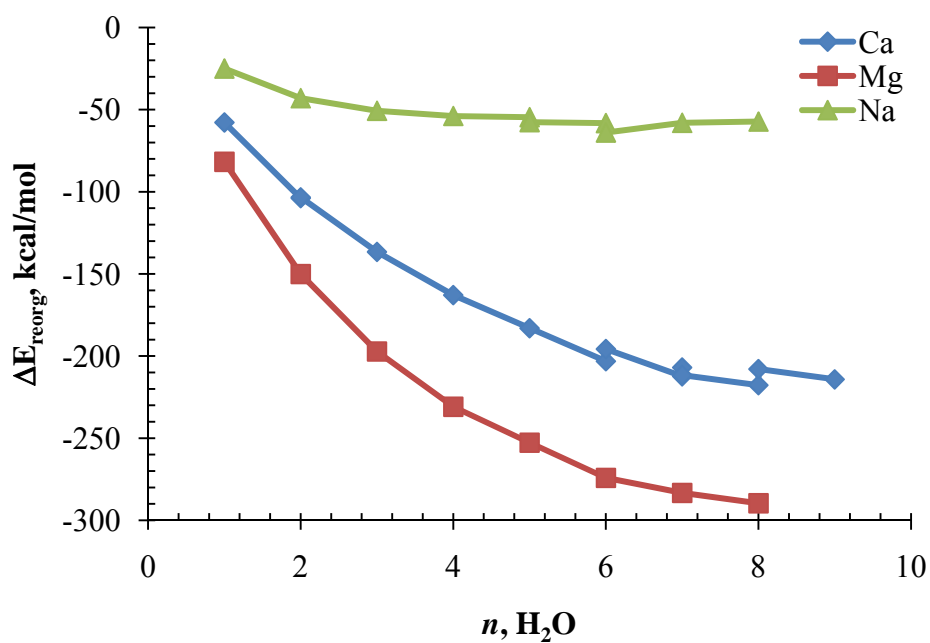


Figure A.5: Reorganization energy for the clusters, $[M(H_2O)_n]^{x+}$, ($n=1-9$) calculated at: B3LYP/6-311++G(d,p) . As the size of metal ion increases, the reorganization energy decreases.

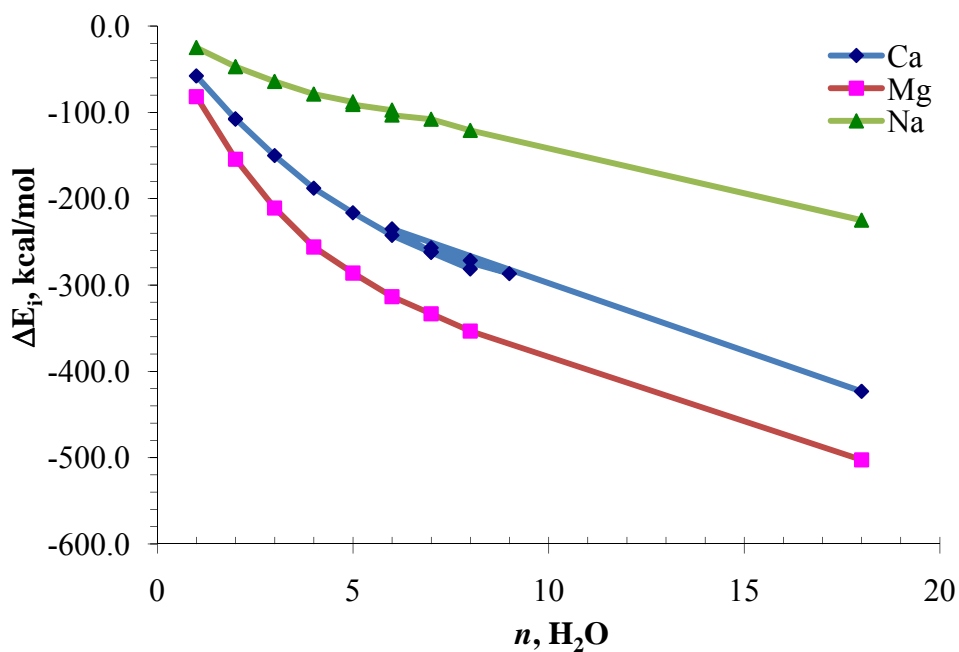


Figure A.6: Binding energy for the clusters, $[M(H_2O)_n]^{x+}$, ($n=1-18$) calculated at: B3LYP/6-311++G(d,p) .

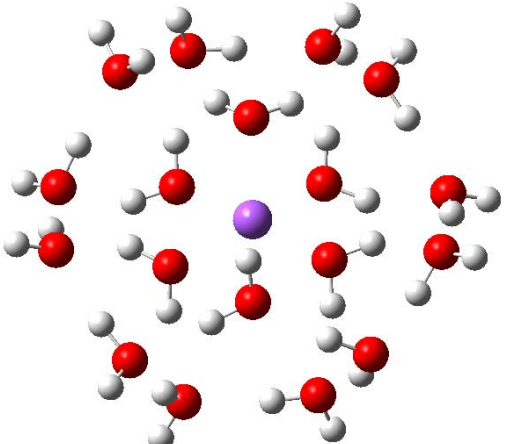
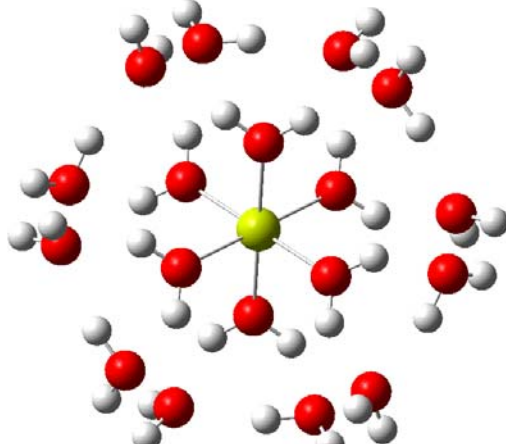
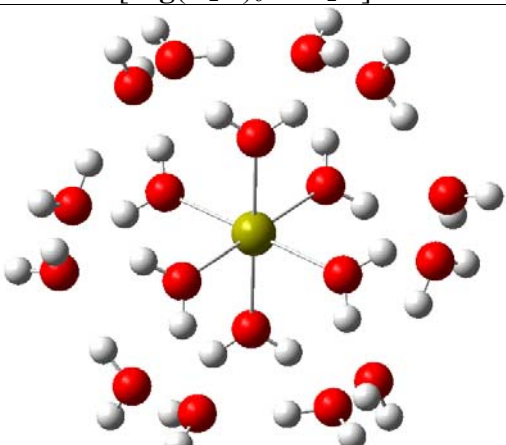
	Na	0.033192	-0.005818	-0.212056
	O	1.539975	-1.041822	-1.67459
	O	-1.468123	0.866787	1.548033
	O	-1.801371	-0.788385	-1.431822
	O	1.618144	0.569549	1.526502
	O	0.257901	2.134113	-1.185104
	O	-0.165862	-1.732766	1.70695
	H	1.488021	-2.008657	-1.740048
	H	2.478573	-0.803558	-1.674952
	H	-2.416606	0.667985	1.541514
	H	-1.375787	1.829705	1.625357
	H	-2.592583	-0.285084	-1.670523
	H	-1.942963	-1.714135	-1.675112
	H	1.791769	1.516787	1.634147
	H	2.473125	0.11311	1.601714
	H	1.120113	2.328177	-1.583424
	H	-0.426068	2.541509	-1.730007
	H	-0.155787	-0.868426	2.145235
	H	-1.079476	-2.058655	1.750271
	O	-0.897719	3.690733	1.233089
	O	-4.152801	-0.155851	1.047487
	O	-1.863926	-3.656502	-1.101817
	O	3.903748	-1.149927	1.270072
	O	3.074022	2.611002	-1.292257
	O	2.168725	-3.125632	1.188746
	O	4.188096	0.070183	-1.127125
	O	0.968339	-3.851531	-1.365796
	H	0.070424	3.624773	1.085875
	H	-1.020966	4.360599	1.914297
	H	-4.966133	0.06217	1.515211
	H	-4.20942	0.27823	0.167901
	H	-2.23943	-3.423715	-0.226734
	H	-2.426202	-4.350536	-1.462112
	H	3.309443	-1.957434	1.2134
	H	4.582143	-1.349693	1.923395
	H	3.610764	3.149842	-1.882884
	H	3.518111	1.73405	-1.236497
	H	1.339934	-2.71398	1.508146
	H	1.920792	-3.515008	0.333962
	H	4.215225	-0.370972	-0.242542
	H	5.004472	-0.166281	-1.579828
	H	1.192445	-4.602647	-1.924909
	H	-0.005456	-3.860418	-1.269572
	O	-3.948033	1.1533	-1.381814
	O	1.935174	3.444197	1.137258
	O	-2.367948	3.419714	-1.132761
	H	-4.643662	1.324369	-2.025405
	H	-3.42822	1.985732	-1.300333
	H	2.521186	4.033133	1.624455
	H	2.371634	3.263835	0.277789
	H	-1.889186	3.581752	-0.290656
	H	-2.666694	4.280412	-1.444367
	O	-2.881551	-2.653515	1.316953
	H	-3.390607	-1.823622	1.192509
	H	-3.352358	-3.168526	1.981326
<hr/> Z-Matrix for optimized $[\text{Na}(\text{H}_2\text{O})_6.12\text{H}_2\text{O}]^+$ at B3LY/6311++G(d,p) \Rightarrow				

Table A.1: Thermodynamic properties for water clusters, H_2O_n using B3LYP/6-311++G**

# H_2O	ΔE_i^a (kcal/mol)	ΔE_i^b (kcal/mol)	ΔE_i^c (kcal/mol)	$\langle \text{HB} \rangle^d$ (Å)
1	0.000	0.00	0.00	1.9321
2	-4.080	-5.50	-5.37	1.9026
3	-13.490	-17.10	-16.49	1.7735
4	-25.000	-29.10	-28.85	1.7437
5	-33.338	-37.70	-37.86	1.9545
6	-39.295	-49.60	-48.34	1.8897
7	-49.945	-60.53	60.69	1.8227
8	-63.665	-76.01		1.8547
9	-72.692	-85.05		1.9321
18				

^a this work. ^b binding energy using HF/6-31G(d,p) from ref.(Maheshwary et al., 2001). ^c MP2/6-311+++G(2d,2p) from ref. (Maheshwary et al., 2001). ^d average hydrogen bond from this work

Table A.2: Thermodynamic properties of $[\text{Na}(\text{H}_2\text{O})_n.\text{mH}_2\text{O}]^+$ using B3LYP/6-311++G**

# H_2O	(n,m)	$R_{\text{min,M-O}}$ (Å)	$R_{\text{max,M-O}}$ (Å)	$R_{\text{avg,M-O}}$ (Å)	APT
1	(1,0)	2.2254	2.2254	2.2254	0.9571
2	(2,0)	2.2486	2.2486	2.2486	0.9253
3	(3,0)	2.2748	2.2766	2.2755	0.9001
4	(4,0)	2.3111	2.3111	2.3111	0.8873
5	(5,0)	2.3075	2.4402	2.3642	0.8767
5	(4,1)	2.2944	2.3086	2.3015	0.8756
6	(6,0)	2.4191	2.4321	2.4263	0.8661
6	(4,2)	2.2979	2.2979	2.2979	0.8726
7	(6,1)	2.3289	2.5280	2.4362	0.8688
8	(6,2)	2.3093	3.7557	2.6249	0.8577
18	(6,12)	2.3379	3.3615	2.5874	0.8180

Table A. 3: Thermodynamic properties of $[M(H_2O)_n.mH_2O]^{2+}$ using B3LYP/6-311++G**

M	# H ₂ O	(n,m)	R _{min,MO} (Å)	R _{max,MO} (Å)	R _{avg,MO} (Å)	APT
Mg	1	(1,0)	1.9428	1.9428	1.9428	1.8285
	2	(2,0)	1.9597	1.9597	1.9597	1.7070
	3	(3,0)	1.9859	1.9922	1.9881	1.6538
	4	(4,0)	2.0230	2.0230	2.0230	1.6380
	5	(5,0)	2.0520	2.1048	2.0746	1.6497
	6	(6,0)	2.1063	2.1194	2.1123	1.6684
	7	(6,1)	2.0652	2.1197	2.1090	1.6586
	8	(6,2)	2.1141	2.1182	2.1156	1.6488
Ca	1	(1, 0)	2.2445	2.2445	2.2445	1.9396
	2	(2, 0)	2.2819	2.2819	2.2819	1.9092
	2	(2, 0)	2.2956	2.2956	2.2956	1.9395
	3	(3, 0)	2.3126	2.3135	2.3132	1.8794
	4	(4, 0)	2.3420	2.3421	2.3420	1.8470
	5	(5, 0)	2.3547	2.3862	2.3771	1.8437
	6	(4, 2)	2.3177	2.3183	2.3180	1.8296
	6	(6, 0)	2.3989	2.4067	2.4039	1.8596
	7	(7, 0)	2.4498	2.4757	2.4595	1.8509
	7	(5, 2)	2.3444	2.3750	2.3593	1.8214
	7	(6, 1)	2.3763	2.4222	2.4028	1.8479
	8	(8, 0)	2.4858	2.5085	2.4982	1.8652
	8	(6, 2)	2.3979	2.4046	2.4004	1.8410
	9	(8, 1)	2.4796	2.5311	2.5075	1.8462
	18	(6,12)	2.3653	2.3669	2.3660	1.7480

Table A.4: Total Sequential Binding Energy, $\Delta E_S = E_{M(H_2O)_{n+1}} - [E_{M(H_2O)_n} + E_{H_2O}]$, (kcal/mol) for $[M(H_2O)_n \cdot mH_2O]^{x+}$ Complexes at Various Level of Theory. Values in the table are for $-\Delta E_S$

M	(n,m)	MP2(full)				CCSD(T)		G3 ^c	Exptl.
		6-31+ G(d) ^c	6-311++ G(d,p) ^c	6-311++ G(2d,2p) ^c	6-311++ G(3d,3p) ^c	6-311++ G(3d,3p) ^c			
Na ⁺	(1,0)	24.496	23.327	22.878	23.148	22.588	24.386	23.977 ^d	
	(2,0)	21.630	20.980	20.461	20.750	20.160	21.121	19.780 ^d	
	(3,0)	18.222	17.744	17.483	17.533	16.836	17.863	15.784 ^d	
	(4,0)	14.546	14.367	14.235	14.465	13.217	15.545	13.786 ^d	
	(5,0)	13.518	12.507	13.028	13.248	12.177	11.838	12.287 ^d	
	(6,0)	13.057	12.278	12.749	12.899	12.058	12.008	10.691 ^d	
Mg ²⁺	(1,0)	78.246	77.407	77.115	78.255	76.537	80.294	—	
	(2,0)	69.823	70.502	68.956	69.493	69.732	71.042	—	
	(3,0)	57.486	57.364	56.396	56.946	57.067	56.704	—	
	(4,0)	46.824	47.467	45.805	46.226	47.304	46.876	—	
	(5,0)	31.671	33.817	31.451	31.649	33.647	32.149	—	
	(6,0)	26.663	14.625	24.546	24.857	14.596	26.625	—	
Ca ²⁺	(1,0)	52.029	53.599	53.019	53.958	52.849	53.568	—	
	(2,0)	47.586	47.404	46.537	47.096	46.826	47.244	—	
	(3,0)	42.560	42.909	42.488	43.028	42.450	42.082	—	
	(4,0)	37.933	37.395	36.955	37.285	37.084	37.063	—	
	(5,0)	30.691	30.261	30.151	30.559	30.122	30.700	—	
	(6,0)	25.356	24.766	24.967	25.315	24.725	26.326	—	

^a from frequency and geometry optimization are in this work. ^b Single point calculations based on B3LYP/6-311++G(d,p) optimized geometries. ^c taken from ref (Rao et al., 2008). ^d taken from ref (Dzidic and Kebarle, 1970).

APPENDIX B
SUPPORTING MATERIALS FOR CHAPTER V

**Theoretical Study of Ferric and Ferrous Hydro-Clusters and its Complexes
with Chloride, and Sulfur Ions**

Table B.1: Solubility of iron oxides and green rust at T=298.15 K, p=1 bar

Iron Compound	Name	Reaction	ΔG_f^0 (kJ/mol)
Fe_3O_4	magnetite	$\text{Fe}_3\text{O}_4 + 8\text{H}^+ = 2\text{Fe}^{3+} + \text{Fe}^{2+} + 4\text{H}_2$	-1015.5
$\alpha\text{-Fe}_2\text{O}_3$	hematite	$\alpha\text{-Fe}_2\text{O}_3 + 6\text{H}^+ = 2\text{Fe}^{3+} + 3\text{H}_2\text{O}$	-755.5
$\gamma\text{-Fe}_2\text{O}_3$	maghemite	$\gamma\text{-Fe}_2\text{O}_3 + 6\text{H}^+ = 2\text{Fe}^{3+} + 3\text{H}_2\text{O}$	727.9
$\alpha\text{-FeOOH}$	goethite	$\alpha\text{-FeOOH} + 3\text{H}^+ = \text{Fe}^{3+} + 2\text{H}_2\text{O}$	-488.8
$\gamma\text{-FeOOH}$	lepidocrocite	$\gamma\text{-FeOOH} + 3\text{H}^+ = \text{Fe}^{3+} + 2\text{H}_2\text{O}$	-469.7
$\text{Fe}(\text{OH})_2$	ferrohydrate	$\text{Fe}(\text{OH})_2 + 2\text{H}^+ = \text{Fe}^{2+} + 2\text{H}_2\text{O}$	-489.8
$\text{Fe}(\text{OH})_3$	ferrihydrite	$\text{Fe}(\text{OH})_3 + 3\text{H}^+ = \text{Fe}^{3+} + 3\text{H}_2\text{O}$	-711.0
$\text{Fe}^{\text{II}}_3\text{Fe}^{\text{III}}(\text{OH})_8\text{Cl}$	Green Rust (Cl ⁻)	$\text{Fe}_4(\text{OH})_8\text{Cl} + 8\text{H}^+ = 3\text{Fe}^{2+} + \text{Fe}^{3+} + \text{Cl}^- + 8\text{H}_2\text{O}$	-2145.0
$\text{Fe}^{\text{II}}_4\text{Fe}^{\text{III}}_2(\text{OH})_{12}\text{CO}_3$	Green Rust (CO ₃ ²⁻)	$\text{Fe}_6(\text{OH})_{12}\text{CO}_3 + 13\text{H}^+ = 4\text{Fe}^{2+} + 2\text{Fe}^{3+} + \text{HCO}_3^- + 12\text{H}_2\text{O}$	-3588.0
$\text{Fe}^{\text{II}}_4\text{Fe}^{\text{III}}_2(\text{OH})_{12}\text{SO}_4$	Green Rust (SO ₄ ²⁻)	$\text{Fe}_6(\text{OH})_{12}\text{SO}_4 + 12\text{H}^+ = 4\text{Fe}^{2+} + 2\text{Fe}^{3+} + \text{SO}_4^{2-} + 12\text{H}_2\text{O}$	-3785.0
$\text{Fe}^{\text{III}}_2\text{Fe}^{\text{II}}(\text{OH})_8$	ferrosoferric hydroxide	$\text{Fe}_3(\text{OH})_8 + 8\text{H}^+ = 2\text{Fe}^{3+} + \text{Fe}^{2+} + 8\text{H}_2\text{O}$	-1681.0
$\text{Fe}^{\text{II}}_2\text{Fe}^{\text{III}}(\text{OH})_7$	fougerite	$\text{Fe}_3(\text{OH})_7 + \text{e}^- + 7\text{H}^+ = 3\text{Fe}^{2+} + 7\text{H}_2\text{O}$	-1770.0
$\text{Fe}^{\text{II}}\text{Fe}^{\text{III}}(\text{OH})_5$	hydroxy Green Rust	$\text{Fe}_2(\text{OH})_5 + \text{e}^- + 5\text{H}^+ = 2\text{Fe}^{2+} + 5\text{H}_2\text{O}$	-1244.1
$\text{Fe}^{\text{III}}_2\text{Fe}^{\text{II}}(\text{OH})_8$	hydroxy Green Rust	$\text{Fe}_3(\text{OH})_8 + 2\text{e}^- + 8\text{H}^+ = 3\text{Fe}^{2+} + 8\text{H}_2\text{O}$	-1944.3
$\text{FeO}(\text{OH})_{0.74}(\text{SO}_4)_{0.13}$	schwertmannite	$\text{FeO}(\text{OH})_{0.74}(\text{SO}_4)_{0.13} + 2.74\text{H}^+ = \text{Fe}^{3+} + 0.13\text{SO}_4^{2-} + 1.74\text{H}_2\text{O}$	-518.0

Table B.2: Thermodynamic Properties

Molecule	$\Delta_f G^0$ (kcal/mol)	$\Delta_f H^0$ (kcal/mol)	S^0 (cal/mol K)	C_p^0 (Cal/mol K)
H ₂ O	-65.28			
Fe ²⁺	-21.63			
Fe ³⁺	-4.12	-12.65	-68.9	-24.95
Cl ⁻	-31.38	-39.93	13.6	-29.3
SO ₄ ²⁻	-177.82			

Table B.3: Effect of multiplicity on thermodynamic properties of Ions and complexes using DFT in gas-phase. All calculations performed using B3LYP level of theory and 6-311++G** (for H, O, S), SDD (for Fe, Cl) basis sets. Minimum spin state is in parenthesis.

Ion or complex	Multiplicity	$E_0=E^{\text{el}}+E_{\text{ZPE}}$	$E=E^{\text{el}}+E_{\text{therm}}$	$H=E^{\text{el}}+H_{\text{therm}}$	$G=E^{\text{el}}+H_{\text{free}}$
		Hartree/particle			
Cl^-	(1)	-460.231989	-460.230573	-460.229628	-460.247012
Cl^-	3	-459.480874	-459.479458	-459.478514	-459.496934
S^{2-}	(1)	-398.065098	-398.063682	-398.062738	-398.079994
S^{2-}	3	-397.969912	-397.964896	-397.967551	-397.985845
HS^-	(1)	-398.853015	-398.850655	-98.849711	-398.870875
HS^-	3	-398.743278	-398.740916	-398.739971	-398.762268
H_3S^+	(1)	-399.628700	-399.625815	-399.624871	-399.647886
H_3S^+	3	-399.482497	-399.479576	-399.478631	-399.503117
Fe^{2+}	1	-122.828489	-122.827072	-122.826128	-122.844177
Fe^{2+}	3	-122.878364	-122.876948	-122.876003	-122.895089
Fe^{2+}	(5)	-122.971960	-122.970544	-122.969600	-122.989168
Fe^{2+}	7	-122.822441	-122.821025	-122.820080	-122.839966
Fe^{3+}	2	-121.579056	-122.57764	-122.576696	-121.595399
Fe^{3+}	4	-121.669621	-121.668205	-121.667261	-121.686618
Fe^{3+}	(6)	-121.811925	-121.810509	-121.809565	-121.829305
Fe^{3+}	8	-119.484085	-119.482668	-119.481724	-119.501736
$[\text{Fe}(\text{H}_2\text{O})_6]^{2+}$	1				
$[\text{Fe}(\text{H}_2\text{O})_6]^{2+}$	5				

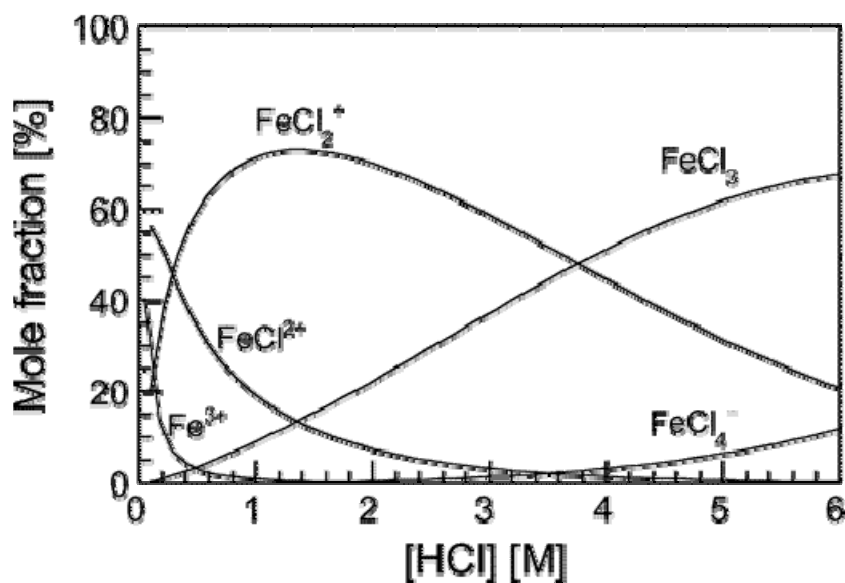


Figure B.1: Formations of the Fe(III) species in HCl solutions. The mole fractions were calculated from the reported stability constants.

Table B.4: Effect of theory level and basis on the thermodynamic properties of Fe^{x+} ($x=2,3$). Spin Sates are: 5 for Fe^{2+} and 6 for Fe^{3+} .

Ion	Method/ basis set	$E_0=E^{\text{el}}+E_{\text{ZPE}}$	$E=E^{\text{el}}+E_{\text{therm}}$	$H=E^{\text{el}}+H_{\text{therm}}$	$G=E^{\text{el}}+H_{\text{free}}$
		Hartree/particle			
Fe (2,5)	HF/LanL2DZ	-121.8143	-121.8129	-121.8119	-121.8315
	B3LYP/ 6-311++G**	-1262.7506	-1262.7491	-1262.7482	-1262.7678
	B3LYP/ LanL2DZ	-122.4810	-122.4796	-122.4786	-122.4982
	HF/SDD	-122.2946	-122.2932	-122.2922	-122.3118
	B3LYP/SDD	-122.9720	-122.9705	-122.9696	-122.9892
	B3PW91/SDD	-123.0076	-123.0062	-123.0052	-123.0248
	MP2/SDD	-122.6050	-122.6036	-122.6027	-122.6222
Fe (3,6)	HF/LanL2DZ	-120.7450	-120.7436	-120.7427	-120.7624
	B3LYP/ 6-311++G**	-1261.5902	-1261.5888	-1261.5879	-1261.6076
	B3LYP/ LanL2DZ	-121.2976	-121.2962	-121.2952	-121.3150
	HF/SDD	-121.2477	-121.2463	-121.2454	-121.2651
	B3LYP/SDD	-121.8119	-121.8105	-121.8097	-121.8293
	B3PW91/SDD	-121.8539	-121.8525	-121.8516	-121.8713
	MP2/SDD	-121.5101	-121.5087	-121.5078	-121.5275

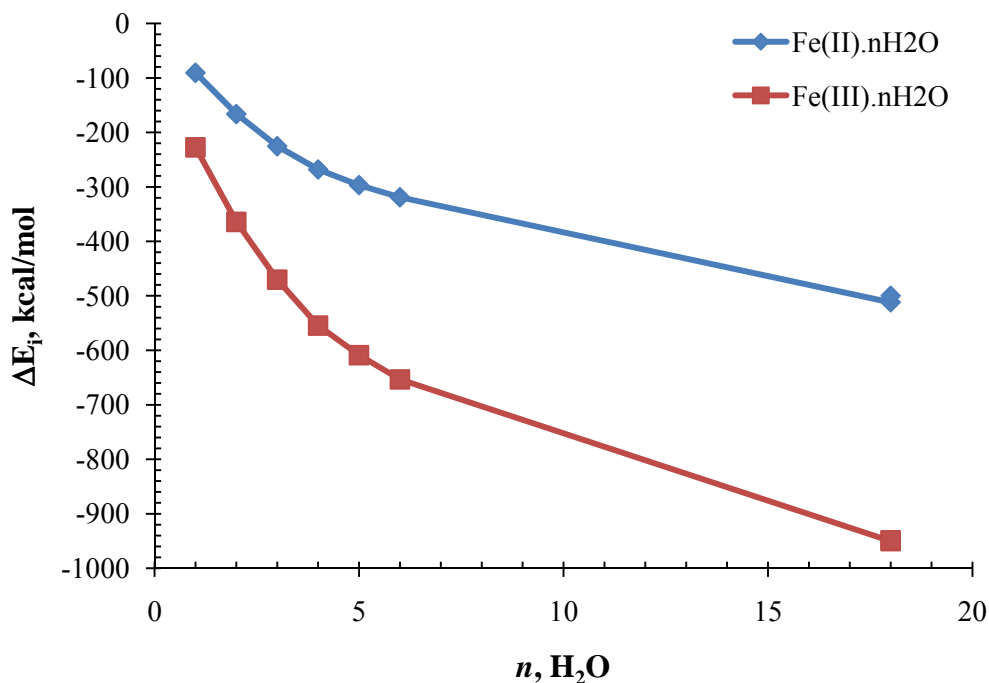


Figure B.2: Change of Binding energy as function of water molecules in hydro iron complex calculated at B3LYP/6-311++G(d,p)/SDD.

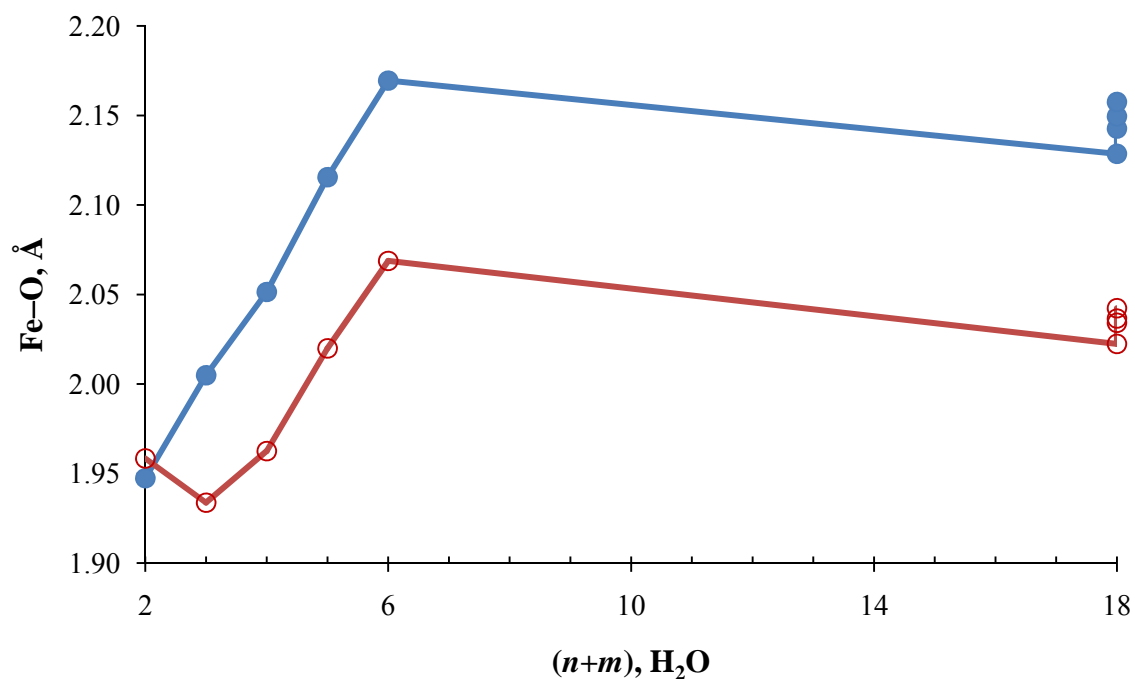


Figure B.3: Binding energy as a function of water molecules in first shell (n) and second shell (m). (●) for $[\text{Fe}(\text{H}_2\text{O})_n.m\text{H}_2\text{O}]^{2+}$, and (○) $[\text{Fe}(\text{H}_2\text{O})_n.m\text{H}_2\text{O}]^{3+}$. The first 7-points are calculated using B3LYP/6-311++g**/SDD and the last 2-points are at B3LYP/LanL2DZ.

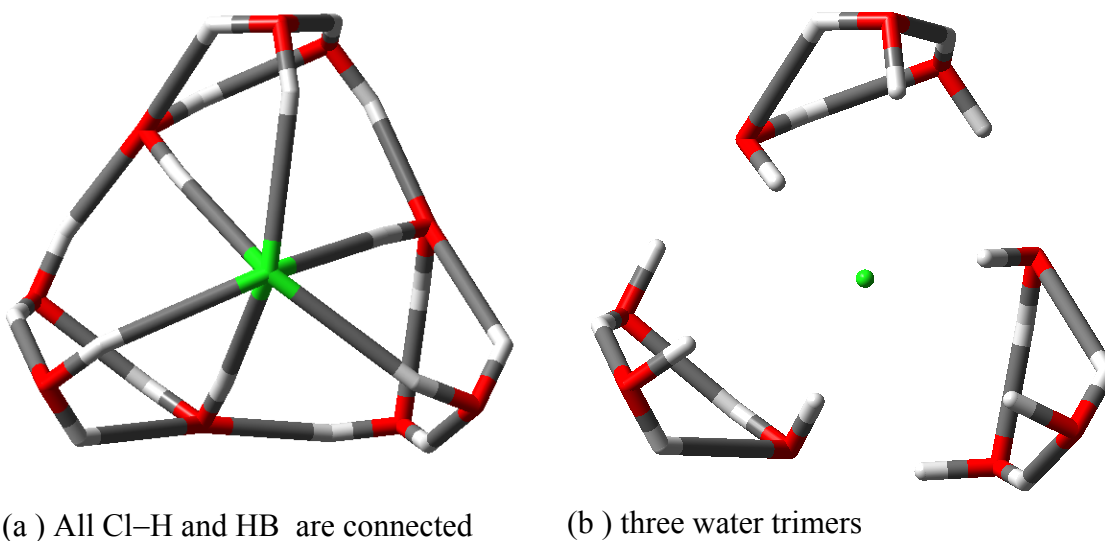


Figure B.4: 3D geometrical structure of $[\text{Cl}(\text{H}_2\text{O})_9]^-$ with (a) all hydrogen bonding (HB) and Cl-H are connected and (b) all three H_2O trimers around Cl^- ion calculated at B3LYP/6-311++G(d,p)/SDD.

Table B.5: Equilibrium reactions of Fe(III), Fe(II) with various anions in solution and their precipitation conditions

Ions	Chemical reaction	Complex	Stability constant	Note
Cl ⁻	$\text{Fe}(\text{H}_2\text{O})_6^{3+} + \text{Cl}^- \leftrightarrow \text{FeCl}(\text{H}_2\text{O})_5^{2+}$		$K_1=30$ $K_2=4.5$	
	$\text{FeCl}(\text{H}_2\text{O})_5^{2+} + \text{Cl}^- \leftrightarrow \text{FeCl}_2(\text{H}_2\text{O})_4^{1+}$		$K_3=0.15$	
	$\text{FeCl}_2(\text{H}_2\text{O})_4^{1+} + \text{Cl}^- \leftrightarrow \text{FeCl}_3(\text{H}_2\text{O})_3^0$		$K_4=0.0078$	
	$\text{FeCl}_3(\text{H}_2\text{O})_3^0 + \text{Cl}^- \leftrightarrow \text{FeCl}_4^-$			
S ²⁻	$\text{Fe}^{2+} + \text{H}_2\text{S} \leftrightarrow \text{FeS}$	FeS ^a	pK=2.96	↓ pH=1.9
		FeS ^b	pK=3.69	
		FeS ^c	pK=4.28	
		FeS ^d	pK=16.38	
		FeS ^e	pK=16.05	
OH ⁻	$\text{Fe}^{3+} + \text{H}_2\text{O} \leftrightarrow (\text{FeOH})^{2+} + \text{H}^+$	Fe(OH) ²⁺	K=2.2	
	$(\text{FeOH})^{2+} + \text{H}_2\text{O} \leftrightarrow \text{Fe}(\text{OH})_2^+ + \text{H}^+$		K=3.5	
	$\text{Fe}(\text{OH})_2^+ + \text{H}_2\text{O} \leftrightarrow \text{Fe}(\text{OH})_3 + \text{H}^+$		K= 6	
	$\text{Fe}(\text{OH})_3 + \text{H}_2\text{O} \leftrightarrow \text{Fe}(\text{OH})_4^- + \text{H}^+$		K= 10	
	$2\text{Fe}^{3+} + 2\text{H}_2\text{O} \leftrightarrow [\text{Fe}_2(\text{OH})_2]^{4+} + 2\text{H}^+$		K=2.9	
	$3\text{Fe}^{3+} + 4\text{H}_2\text{O} \leftrightarrow [\text{Fe}_3(\text{OH})_4]^{5+} + 4\text{H}^+$		K=6.3	

Table B.6: Thermodynamic properties of aquoiron complexes, $[\text{Fe}(\text{H}_2\text{O})_n.m\text{H}_2\text{O}]^{2,3+}$

Iron ion	(n,m)	# Img freq	$E_0=E^{\text{el}}+E_{\text{ZPE}}$	$E=E^{\text{el}}+E_{\text{therm}}$	$H=E^{\text{el}}+H_{\text{therm}}$	$G=E^{\text{el}}+H_{\text{free}}$
			Hartree/particle			
Fe (2,5)	(1,0)	0	-199.5516	-199.5483	-199.5473	-199.5767
	(2,0)	0	-276.1084	-276.1026	-276.1016	-276.1369
	(3,0)	0	-352.6389	-352.6300	-352.6291	-352.6740
	(4,0)	0	-429.1437	-429.1317	-429.1308	-429.1828
	(5,0)	1	-505.6251	-505.6110	-505.6100	-505.6657
	(6,0)	0	-582.0973	-582.0800	-582.0791	-582.1416
	(6,12)	0	-1498.6058	-1498.5678	-1498.5669	-1498.6713
	(6,12)	2	-1498.5578	-1498.5140	-1498.5130	-1498.6377
	(6,12)	1	-1499.6326	-1499.5887	-1499.5878	-1499.7059
	(6,12)	1	-1499.6190	-1499.5698	-1499.5688	-1499.7050
Fe (3,6)	(1,0)	-	-198.6109	-198.6064	-198.6054	-198.6376
	(2,0)	2	-275.2626	-275.2579	-275.2570	-275.2900
	(3,0)	0	-351.8689	-351.8604	-351.8594	-351.9048
	(4,0)	1	-428.4382	-428.4282	-428.4273	-428.4743
	(5,0)	0	-504.9608	-504.9481	-504.9472	-504.9996
	(6,0)	2	-581.4673	-581.4525	-581.4516	-581.5077
	(6,12)	0	-1498.1651	-1498.1299	-1498.1290	-1498.2270
	(6,12)	1	-1498.1484	-1498.1082	-1498.1072	-1498.2200
	(6,12)	0	-1499.1693	-1499.1271	-1499.1262	-1499.2411
	(6,12)	2	-1499.1699	-1499.1245	-1499.1235	-1499.2489

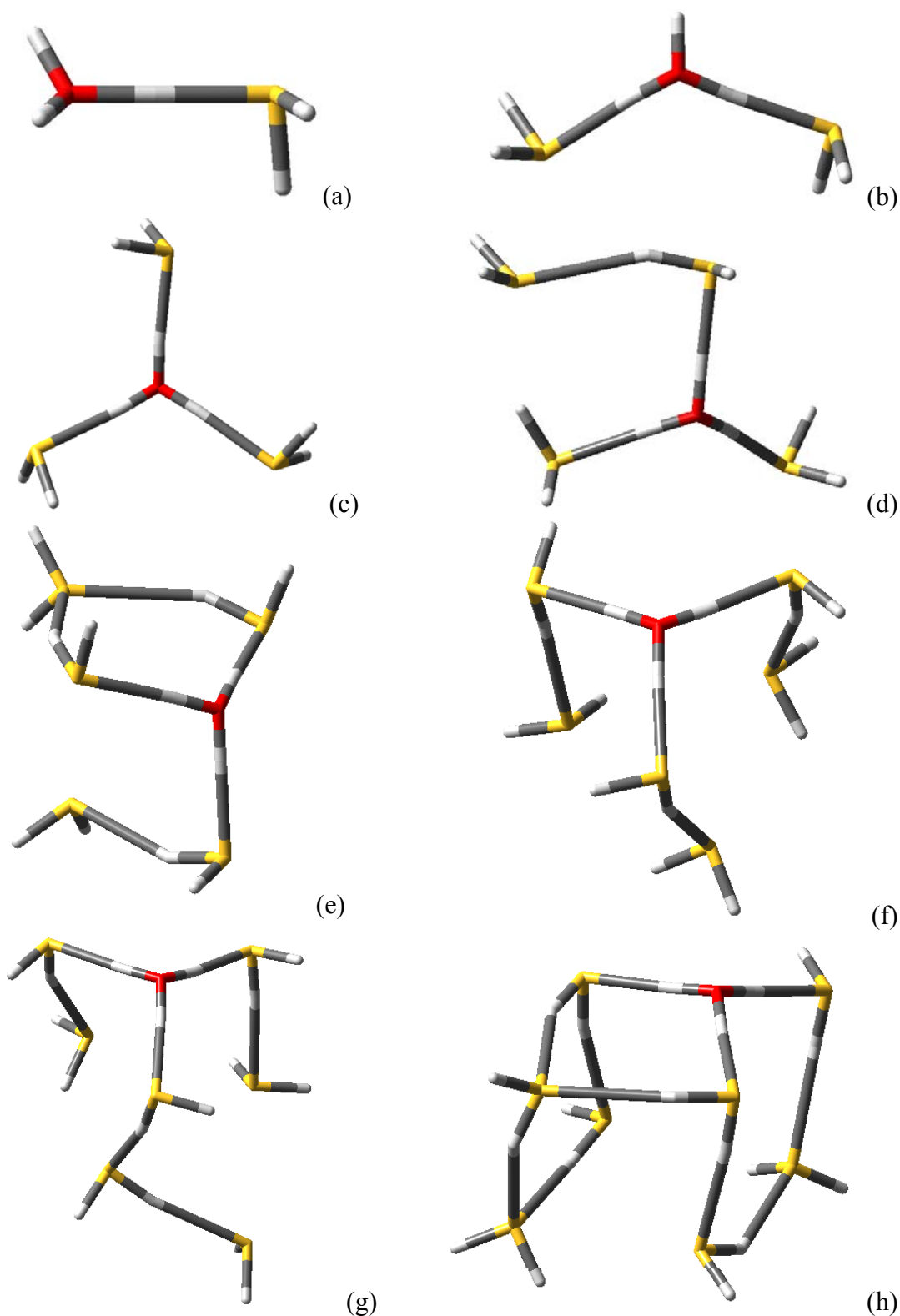


Figure B.5: Optimized geometrical structure in gas-phase of hydrated hydrogen sulfide using B3LYP/6-311++g**. (a) $[\text{H}_3\text{O}(\text{H}_2\text{S})]^+$, (b) $[\text{H}_3\text{O}(\text{H}_2\text{S})_2]^+$, (c) $[\text{H}_3\text{O}(\text{H}_2\text{S})_3]^+$, (d) $[\text{H}_3\text{O}(\text{H}_2\text{S})_4]^+$, (e) $[\text{H}_3\text{O}(\text{H}_2\text{S})_5]^+$, (f) $[\text{H}_3\text{O}(\text{H}_2\text{S})_6]^+$, (g) $[\text{H}_3\text{O}(\text{H}_2\text{S})_7]^+$, and (h) $[\text{H}_3\text{O}(\text{H}_2\text{S})_8]^+$. Color code: red for O, light gray for H and yellow for S.

Table B.6: List of most common Fe–S systems with their properties and natural abundance

Name	Molecular structure	Properties	Availability
Mackinawite	FeS_m	metastable material that is the major constituent of the FeS precipitated from aqueous solutions	widespread mineral in low-temperature aqueous environments
Cubic FeS	FeS_c	highly unstable phase formed before FeS_m	not found naturally
Troilite	FeS_t	stoichiometric end member of the Fe_{1-x}S group	mainly found in meteorites
Pyrrhotite	Fe_{1-x}S	nonstoichiometric stable group where $x > 0.2$; monoclinic form is approximately Fe_7S_8 ; hexagonal form is approximately $\text{Fe}_{10}\text{S}_{11}$	most abundant iron sulfides in the Earth and solar system; rare in marine systems
Smythite	$\text{Fe}_9\text{S}_{11s}$	metastable phase related to the Fe_{1-x}S group	rare mineral mainly found in hydrothermal systems usually associated with carbonates
Greigite	Fe_3S_{4g}	metastable $\text{Fe}^{\text{II}}\text{Fe}^{\text{III}}$ sulfide; the thiospinel of iron	fairly widespread mineral particularly associated with fresh water systems
Pyrite	FeS_{2p}	stable iron(II) disulfide known as “fool's gold”	the most abundant mineral on the Earth's surface
Marcasite	FeS_{2m}	metastable iron(II) disulfide	locally common mineral in hydrothermal systems and in sedimentary rocks

Table B.7: Geometrical properties of first shell, $\text{Fe}(\text{H}_2\text{O})_n$, hydration

Ion	# H_2O	APT charge	$R_{\text{avg,Fe-O}}$ (Å) ^a	$R_{\text{avg,O-H}}$ (Å) ^a	$\angle\text{OFeO}$ (°) ^a	ΔE_{seq} (kcal mol ⁻¹)	$\Delta E_{\text{arrng.}}$ (kcal mol ⁻¹)
Fe^{2+} (2,5)	1	1.7913	1.9342	0.98316	180.0	-90.534	-90.534
	2	1.6769	1.9474	0.97813	180.0	-75.828	-162.282
	3	1.6734	2.0049	0.97418	120.0	-58.982	-211.855
	4	1.6871	2.0514	0.97102	110.4	-42.804	-243.148
	5	1.7089	2.1156	0.96877	93.5	-28.730	-263.541
	6	1.7523	2.1695	0.96725	89.1	-22.356	-279.939
Fe^{3+} (3,6)	1*	4.2963				-227.350	-227.350
	2	1.4361	1.95845	1.00929	180.00	-136.866	-360.136
	3	1.7338	1.93374	0.99608	120.00	-106.020	-456.747
	4	1.9548	1.96258	0.98732	109.97	-84.354	-529.591
	5	2.1793	2.01990	0.98071	93.35	-54.210	-575.463
	6	2.4014	2.06877	0.97625	89.72	-44.543	-614.048

^a this work. ^b Tutton salt, mean $\text{Fe(II)}-\text{O}$ value from ref. * based on single-point energy calculation.

Table B.8: Thermodynamic properties and hydrogen bond in the structure $[\text{Fe}(\text{H}_2\text{O})_6.12\text{H}_2\text{O}]^{2,3+}$

(Charge, Multi)	Basis set	n HB ^a	APT charge	$\text{Fe}-\text{O}$ (Å) _{1sh}	$\text{Fe}-\text{O}$ (Å) _{2sh}	$R_{\text{avg,HB1}}$ (Å) ^a	$R_{\text{avg,HB2}}$ (Å) ^b
Fe (2,5)	LanL2DZ ^b	24	1.5762	2.1286	3.9955	1.8110	1.5901
		20	1.6339	2.1427	4.3424	1.8196	1.6581
	SDD/ 6-311++G(d,p) ^c	24	1.6451	2.1495	4.1464	1.8804	1.8683
		20	1.7190	2.1575	4.4430	1.8721	1.8892
Fe (3,6)	LanL2DZ ^b	24	2.3037	2.0224	3.9091	1.6628	1.6905
		20	2.4216	2.0342	4.1718	1.6692	1.7068
	SDD/ 6-311++G(d,p) ^c	24	2.4072	2.0366	4.0476	1.7202	2.0002
		20	2.5147	2.0423	4.2327	1.7215	1.9629

^a HB (H–O...H) between H_2O in the first shell and H_2O in the second shell. ^b HB (H–O...H) between H_2O molecules in the second shell

APPENDIX C

SUPPORTING MATERIALS FOR CHAPTER VI

***Ab Initio* and Molecular Simulation Studies of Interaction Between Organic/Inorganic Counterions and Anionic Viscoelastic Surfactants**

Note on Interaction forces:

We will describe briefly these interactions. For further reading, we refer to ref. (Israelachvili, 1991).

Van der Waals

These forces result from the correlations in the fluctuating polarizations of nearby molecules and include three major contributions: (i) interaction between permanent dipoles, (ii) permanent dipole-induced dipole, often referred as induction forces, and (iii) instantaneous dipole-induced dipole, usually called dispersion forces. Nevertheless, some texts use the term Van der Waals to refer simply to dispersion forces. Induction and dispersion forces are always attractive while the interaction among permanent dipoles depends upon the relative orientation of the molecules and can, therefore, be attractive or repulsive. Van der Waals interactions are always present and its range spans from typical interatomic distances to nanometers, playing an important role in the structure of macromolecules such as polymer or proteins. Since they are based on interactions between dipoles, they are expected to be more relevant in non-polar solvents.

Hydrophobic

This interaction describes the unusual strong attraction occurring between hydrophobic molecules immersed in water. It has an entropic origin that physically arises from the rearrangement of water molecules in the overlapping hydration zone when the molecules approach. As a result, the water molecules become more ordered than in pure water forming ice-like structures with the consequent loss of local entropy. In order to maximize the entropy the chains are forced to aggregate. The hydrophobic effect can be also enhanced upon the addition of organic solvents such as alcohols because the hydrocarbon molecules can encapsulate the neighbouring water molecules in a more ordered structure

Hydrogen bonding

The hydrogen bonding is an attractive interaction that appears when a hydrogen atom is located between two closely separated atoms with high electronegativity, e.g., O, N and F. It is required an adequate orientation of the involved groups to form the bounds. In the case of gels the flexibility of the polymer chains allows the formation of intra-chain and inter-chain bounding, both cases contributing to the network collapse since the force is

always attractive. Hydrogen bonding is particularly important for the properties of biological assemblies such as membranes, proteins, nucleic acids, etc.

Electrostatic

The electrostatic interaction is a long-range force that appears between charged molecules or ions. It is the strongest of the intermolecular interaction exposed here and play an important role in the volume transition of ionic gels through two distinct mechanisms, (i) direct Coulombian interactions, which can be repulsive or attractive depending of the charge sign, and (ii) the effect of the counterions that establish an osmotic pressure, as consequence of the ion redistribution, attempting to swell the gel. When the network carries a net charge, positive or negative, the Coulomb repulsion is usually screened by water and the dominant mechanism is the osmotic pressure of counterions.

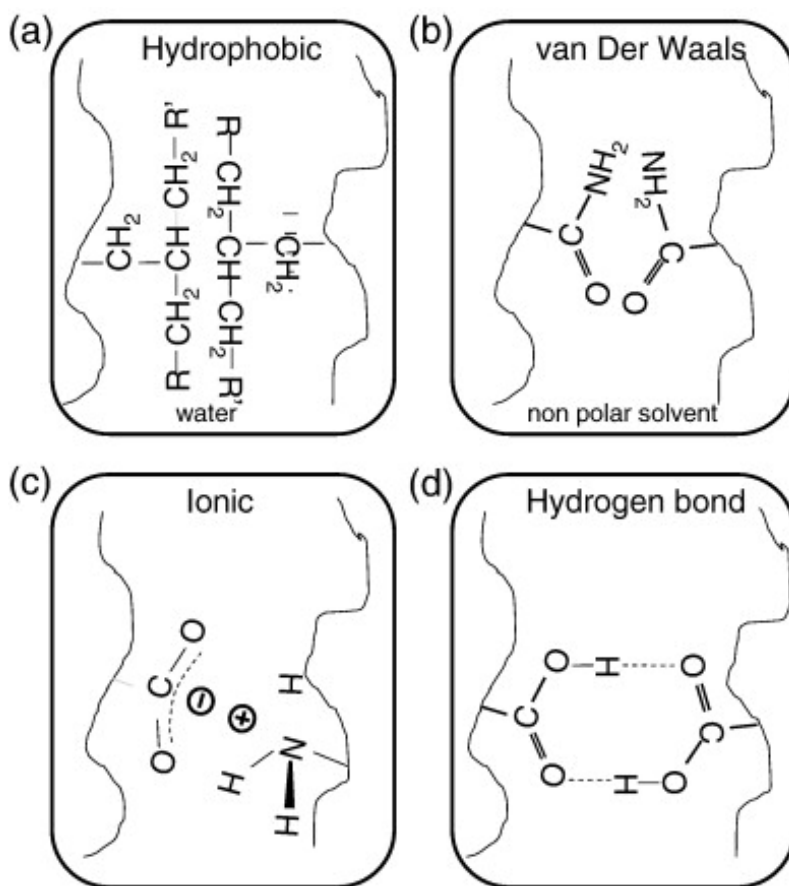


Figure C.1: Fundamental interactions in VES solution (a) For polar solvents, hydrophobic interaction use to dominate, (b) while in the case of non polar solvent Van der Waals is specially relevant, (c) electrostatic and (d) hydrogen bonds.

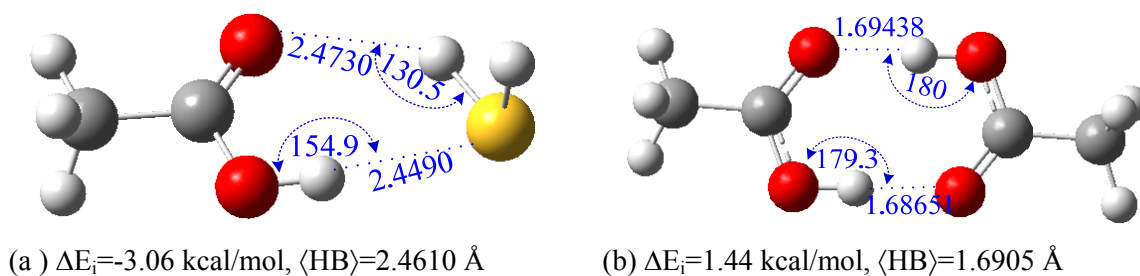


Figure C.2: Optimized molecular structure for (a) $\text{AA}(\text{H}_3\text{O})^+$ in gas-phase, (b) dimer $(\text{AA})_2$ in water solvent, PCM model. All calculated using B3LYP/6-311++G**, and color code is: red for O, dark gray for C, light gray for H and yellow for S.

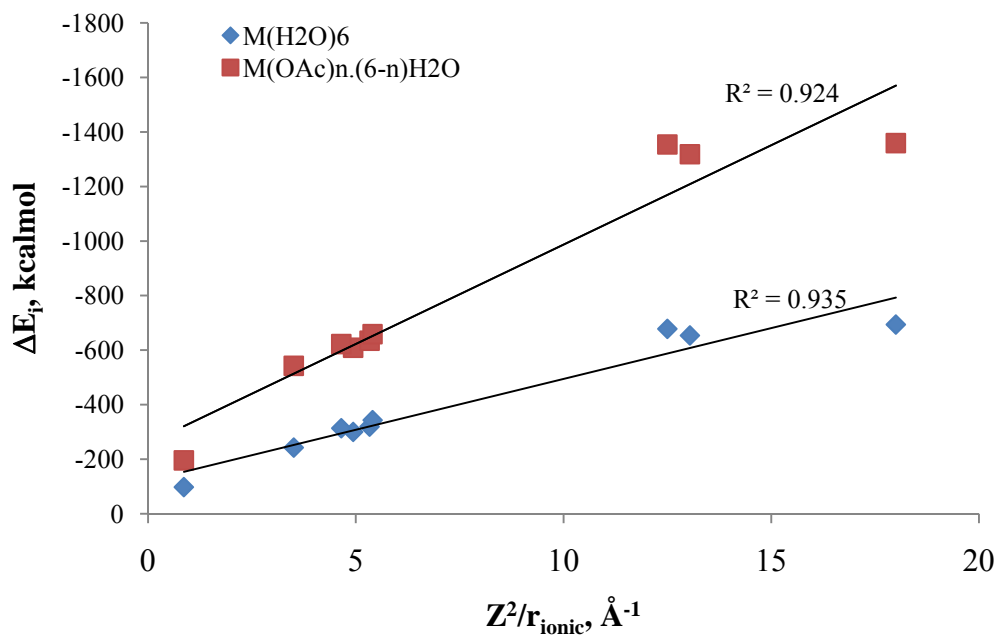


Figure C.3: Relation between binding energy of metal acetate, metal hydrate and square valency divided by ionic radius of the cation.

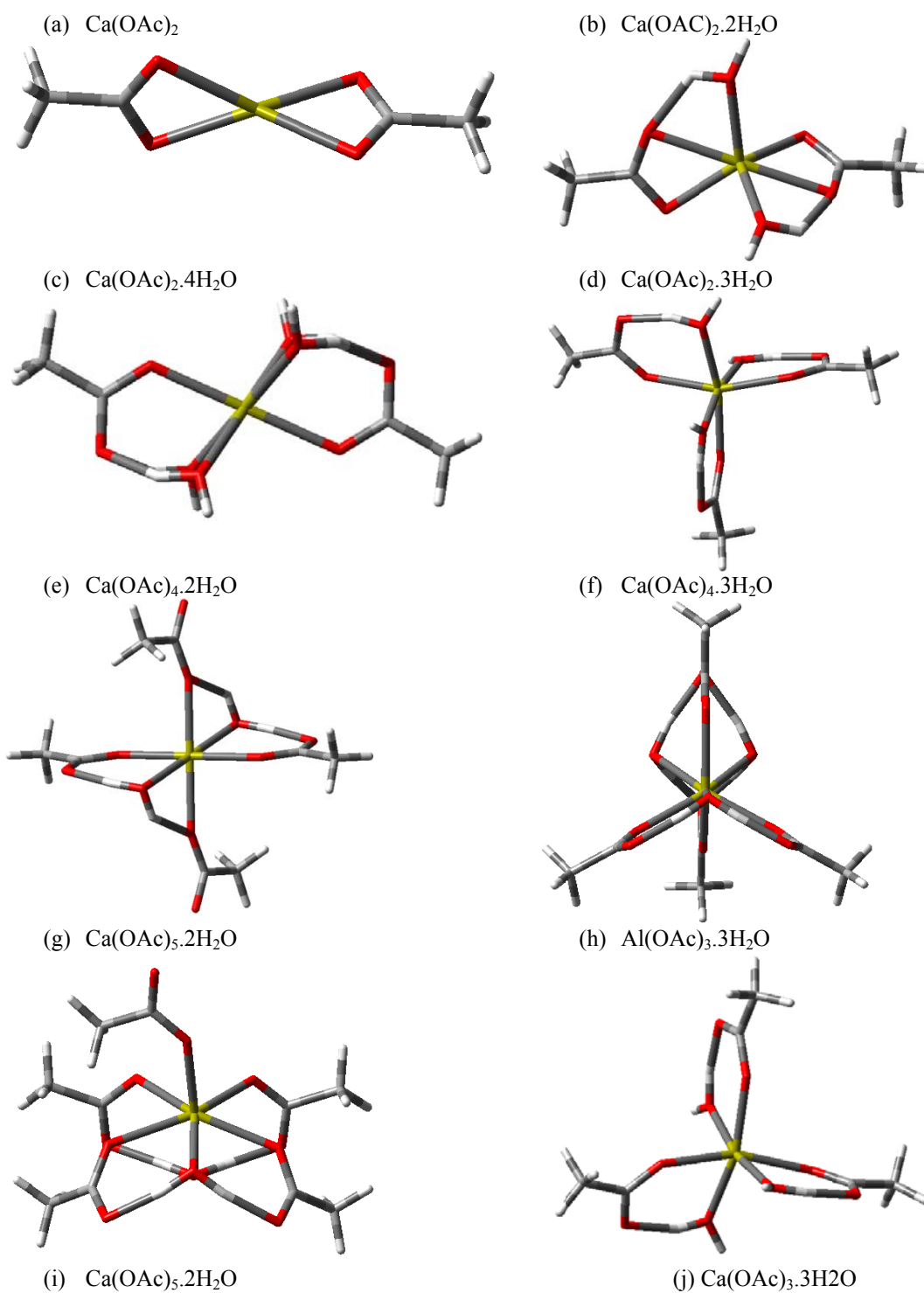


Figure C.4: 3D optimized molecular structure with Ca–O and hydrogen bond (OH–O) are connected for All calculated using B3LYP/6-311++G**, and color code is: red for O, dark gray for C, light gray for H and yellow for Ca, Al.

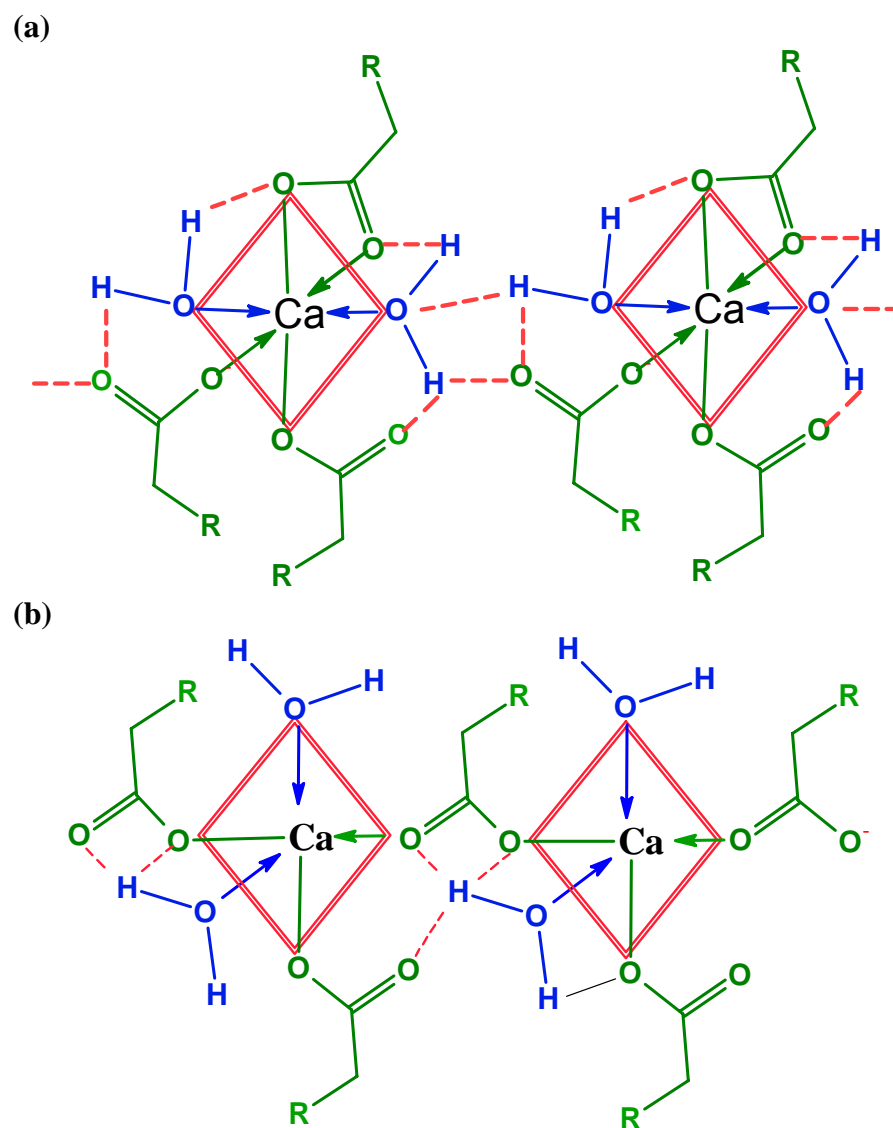


Figure C.5: Proposed schematic structure for $\text{Ca}(\text{AA})_3 \cdot 2\text{H}_2\text{O}$, $[\text{R}=(\text{CH}_3\text{CH}_2)_n]$.

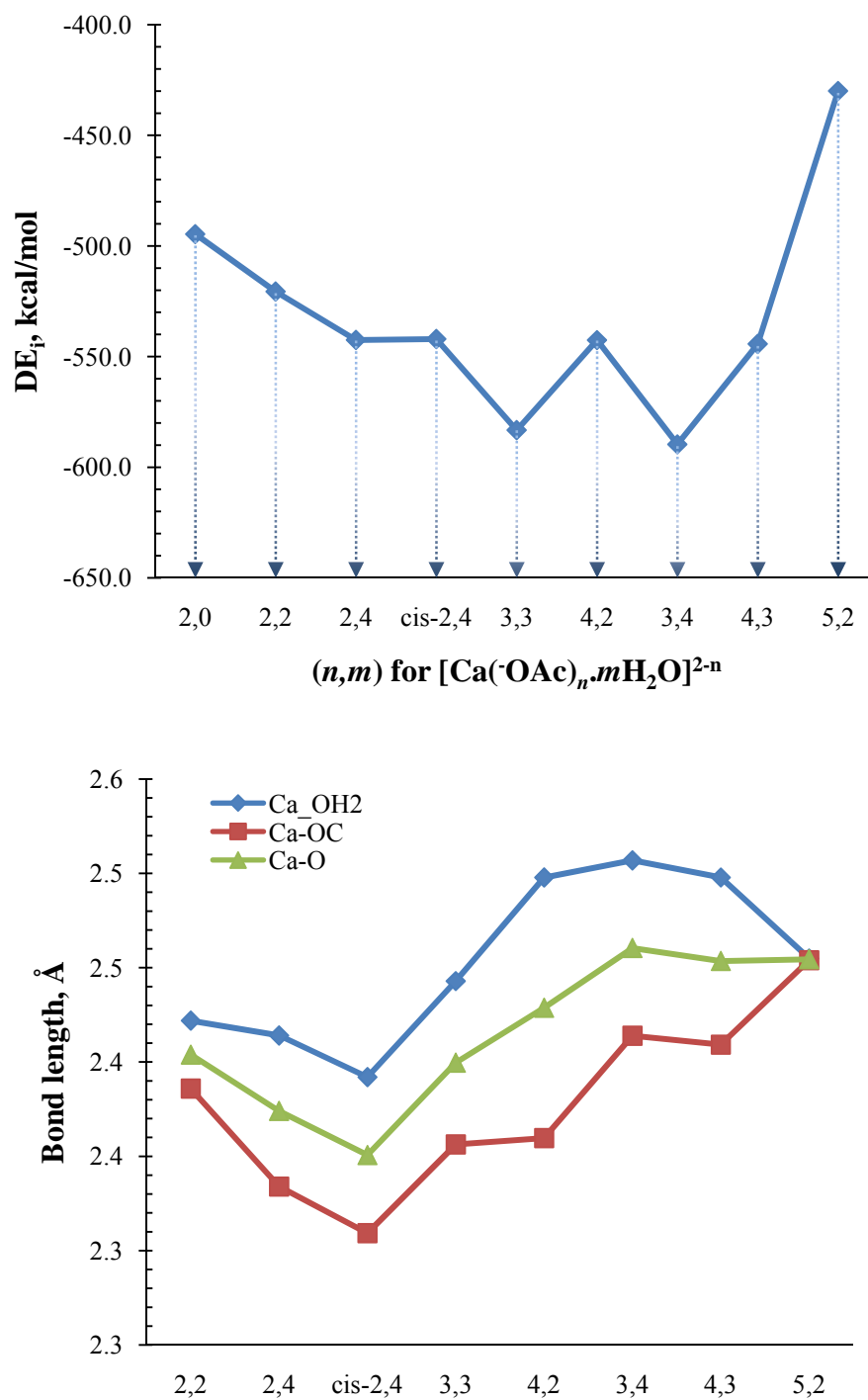


Figure C.6: Effect of coordination number, water molecules, n , and number of acetate HGs, m , on the binding energy (top) and bond length (bottom) for calcium acetate complex, $[\text{Ca}(\text{OAc})_n \cdot m\text{H}_2\text{O}]^{2-n}$.

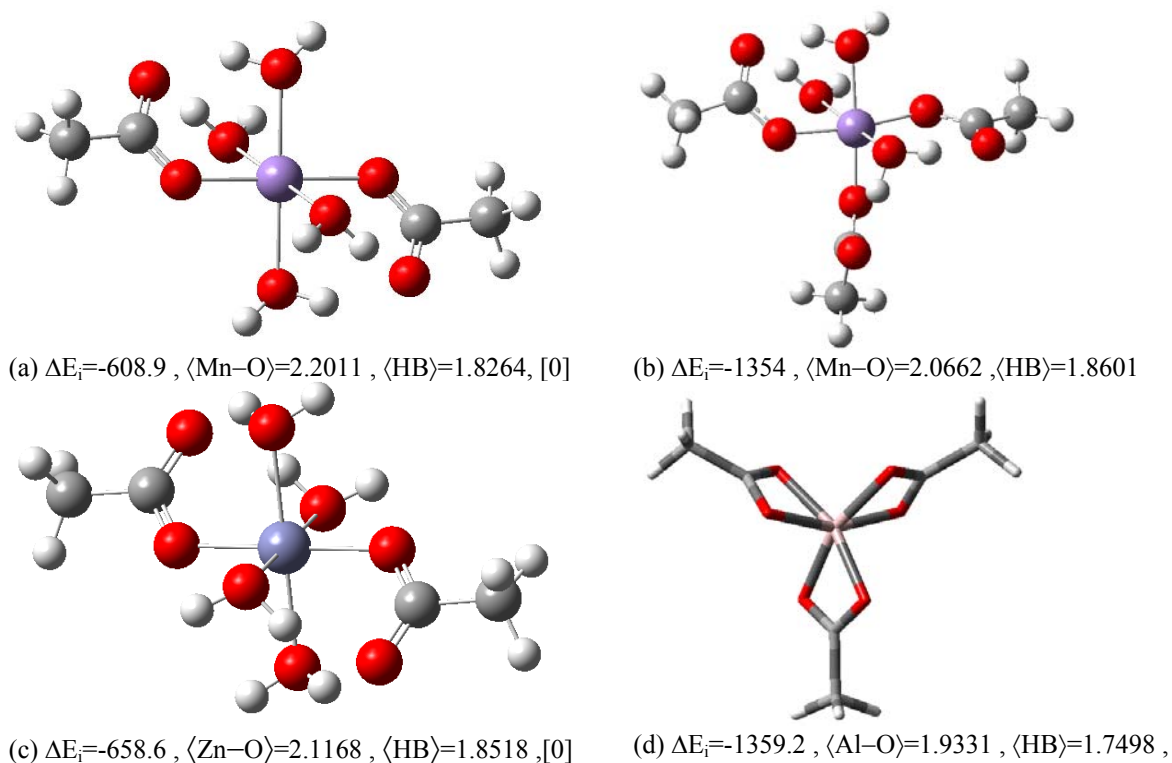


Figure C.7: Optimized geometry of metal acetate at B3LYP/6-311++g**(H,O,C,Al)/SDD(Mn,Zn). (a) $\text{Mn}(\text{OAc})_2 \cdot 4\text{H}_2\text{O}$, (b) $\text{Mn}(\text{OAc})_3 \cdot 3\text{H}_2\text{O}$, (d) $\text{Zn}(\text{OAc})_2 \cdot 4\text{H}_2\text{O}$, and (e) $\text{Al}(\text{OAc})_3$. Shown below each structure, binding energy (kcal/mol), bond length (\AA), and number of imaginary frequency in square brackets.

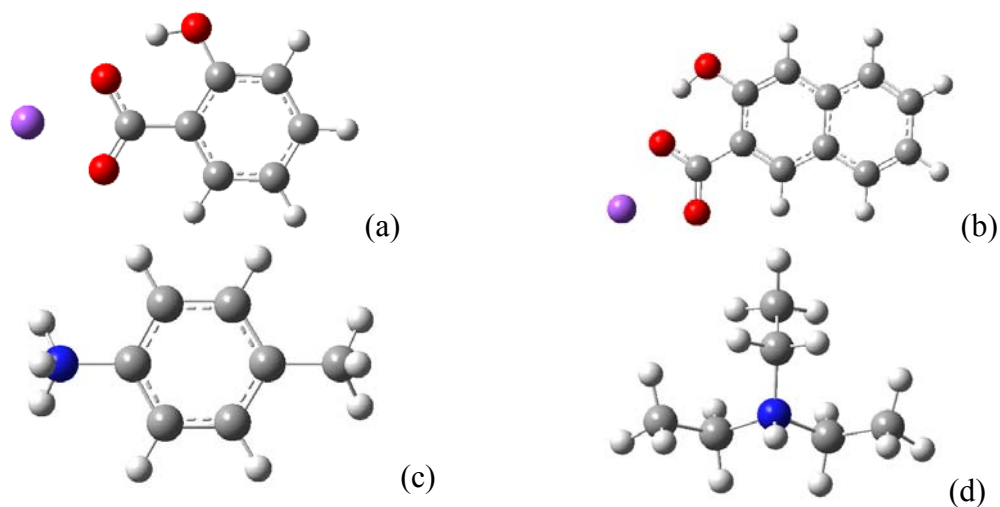
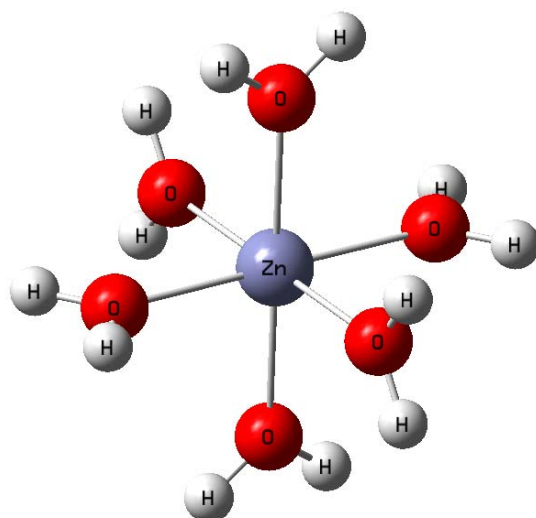
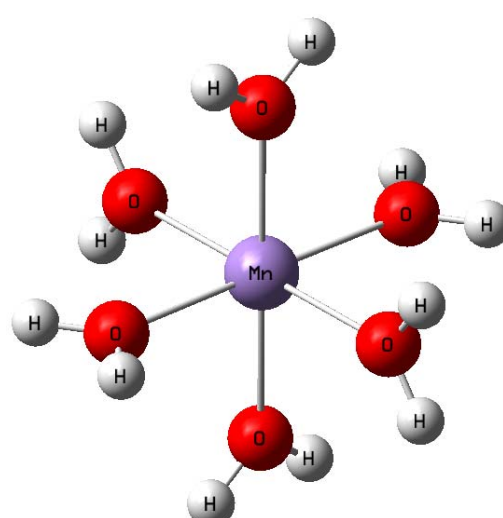


Figure C.8: Optimized structure of organic salts at B3LYP/6-311++g**. (a) NaSal, (b) NaHNC, (c) PTHC, and (d) Et_3NHCl



Optimized $[\text{Zn}(\text{H}_2\text{O})_6]^{2+}$ at B3LYP/genecp			
O	-1.148181	-1.009661	-1.468193
H	-1.783109	-0.607938	-2.077149
O	-0.912559	1.842208	-0.552631
H	-1.722978	2.209214	-0.173255
O	1.146997	1.013107	1.467082
H	1.779808	0.608439	2.0763
O	0.910712	-1.839839	0.550135
H	1.725208	-2.201869	0.174843
O	1.559999	0.32605	-1.402781
H	1.569195	0.062643	-2.333313
O	-1.553269	-0.338501	1.40772
H	-2.380784	-0.8059	1.228631
H	0.59623	-2.461816	1.220605
H	-0.601012	2.460093	-1.228292
H	-1.110422	-1.955592	-1.666107
H	2.383235	0.801612	-1.225456
H	-1.562455	-0.073622	2.337826
H	1.112051	1.958852	1.666406
Zn	-0.001152	0.001966	-0.00039



Optimized $[\text{Mn}(\text{H}_2\text{O})_6]^{2+}$ at B3LYP/genecp			
O	-1.368356	-0.822705	-1.534374
H	-1.959464	-0.322672	-2.114582
O	-0.67892	2.061278	-0.499498
H	-1.402716	2.545315	-0.077714
O	1.36686	0.828215	1.533102
H	1.95443	0.325477	2.114585
O	0.676904	-2.057411	0.496261
H	1.410006	-2.534461	0.082769
O	1.646476	0.154182	-1.479093
H	1.614747	-0.07817	-2.417747
O	-1.640439	-0.17041	1.484518
H	-2.534309	-0.497135	1.311061
H	0.301375	-2.650817	1.161718
H	-0.310885	2.648655	-1.174478
H	-1.482011	-1.75645	-1.760798
H	2.537449	0.489291	-1.306754
H	-1.60582	0.05547	2.424651
H	1.485088	1.761473	1.759192
Mn	-0.001123	0.002753	-0.000369

Table C.1: Geometrical parameters of optimized structure: $[\text{M}(\text{H}_2\text{O})_6]$ at B3LYP

M	(Charge, Multi)	Basis set	# img freq	ΔE_i (kcal/mol)	M–O (Å)	$\angle \text{OMO}$ (°)
Al	(3,1)	6-311++g**	0	-693.481		
Zn	(2,1)	Mixed*	0	-343.061	2.1234	
Mn	(2,6)	Mixed*	0	-299.758	2.2193	
Mn	(3,5)	Mixed*	0	-677.645	2.0472	

* 6-311++g** for H, O atoms and SDD for Mn, Zn atoms.

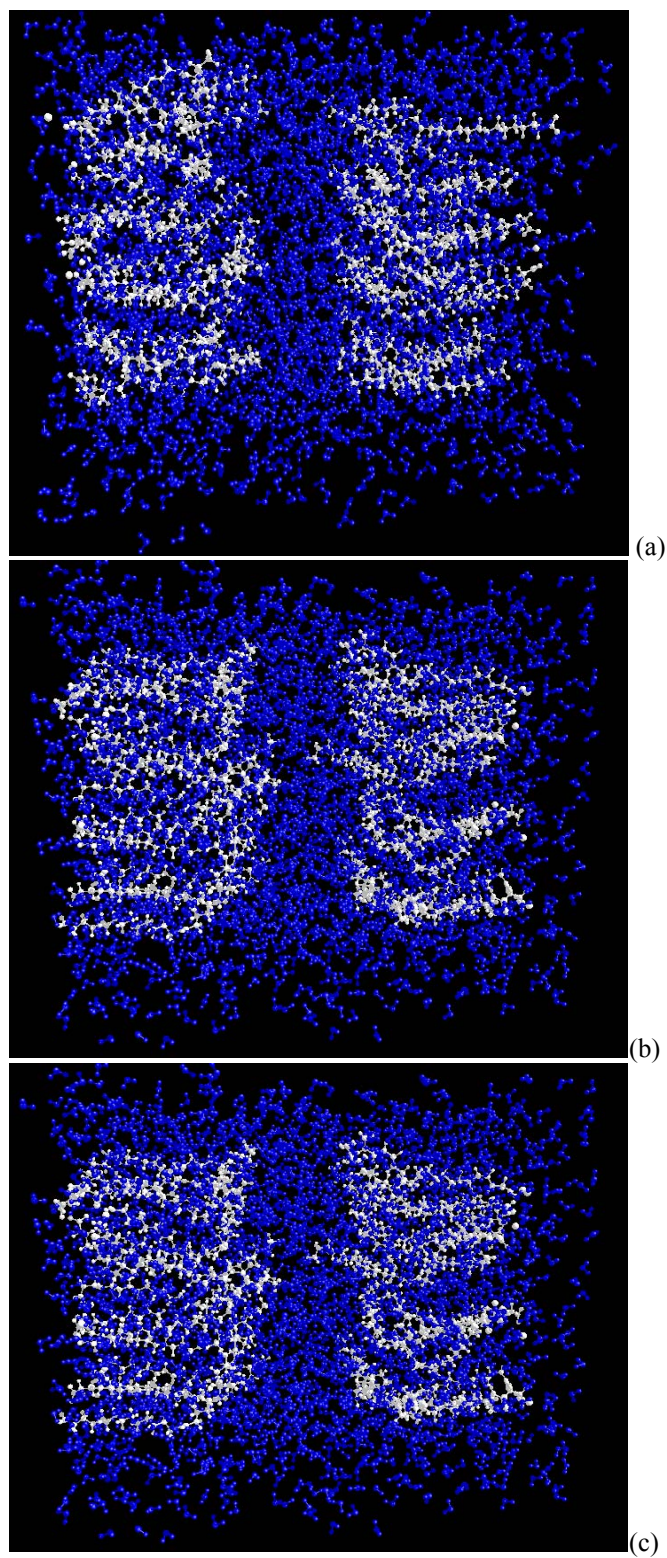


Figure C.9: MD simulation for 1 ns of C22(OAc) with (a) 5, (b) 10 and (c) 15 wt%.

Table C.2: Thermodynamic properties of Acetate (OAc) HG complexation with metal ions calculated at B3LYP/6-311++G**. Binding energy is calculated by:

$$\Delta E_i = [M(OAc)_n \cdot mH_2O] - [nOAc + M^{x+} + mH_2O]$$

M	n,m	# Img	ΔE_i (kcal/mol)	$\langle M-O \rangle$ (Å)	$\angle OMO$ (°)	$\langle HB \rangle$ (Å)
Na	1,0	0	-179.161	2.3407	83.277	1.8150
Na	1,3	0	-195.642	3.4169	75.591	1.6608
Mg	2,4	0	-622.291	2.0473	89.128	1.8377
Zn	2,4	0	-658.601	2.0266	89.446	1.8518
Mn(II)	2,4	0	-608.905	2.1257	88.587	1.8264
Mn(III)	3,3	1	-1354.108	1.9246	89.925	1.8601
Fe(II)	2,4	1	-634.545	2.0441	89.158	1.8693
Fe(III)	3,3	0	-1318.304	2.0210	89.147	1.7667
Al	3,3	0	-1359.195	1.8738	90.248	1.7498

Table C.3: Thermodynamic properties of Acetate (OAc) HG complexation with metal ions calculated at B3LYP/6-311++G**. Binding energy is calculated by:

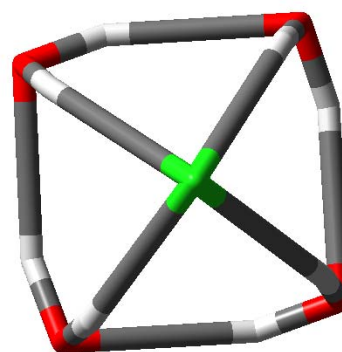
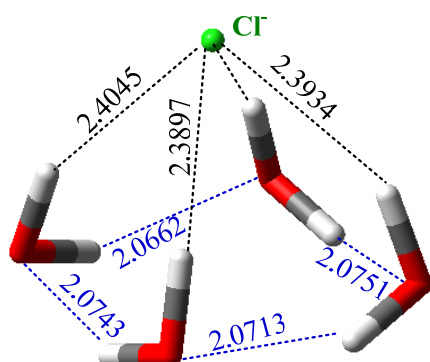
$$\Delta E_i = [Ca(OAc)_n \cdot mH_2O] - [nOAc + Ca^{2+} + mH_2O]$$

CN	n,m	ΔE_i (kcal/mol)	$\langle M-O \rangle$ (Å)	$\angle OMO$ (°)	$\langle HB \rangle$ (Å)
2	2,0	-494.624	2.3029	98.819	0.0000
4	2,2	-520.619	2.3859	73.619	2.0019
4	4,0	-507.143	2.5661	88.727	0.0000
6	3,0	-554.228	2.4217	79.791	0.0000
6	2,4	-542.507	2.3340	86.268	1.7804
6	<i>cis</i> -2,4	-542.054	2.3093	80.156	1.6523
6	3,3	-583.238	2.3564	78.453	1.6737
6	4,2	-542.534	2.3597	79.656	1.7667
7	3,4	-589.651	2.4139	74.722	1.9142
7	4,3	-544.289	2.4092	83.315	1.7341
7	5,2	-429.932	2.4540	79.725	1.5846

APPENDIX D

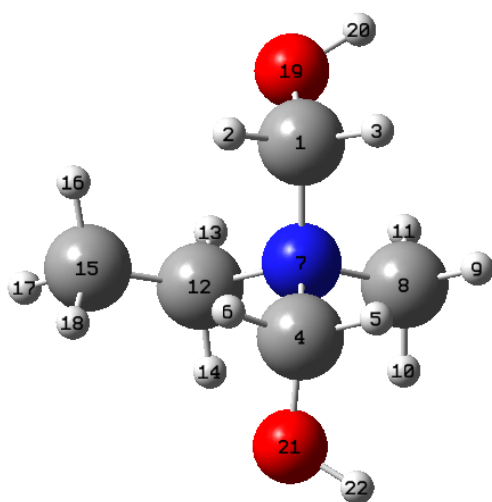
SUPPORTING MATERIALS FOR CHAPTER VII

Theoretical Study of Cationic and Gemini Surfactants in Acid Solution

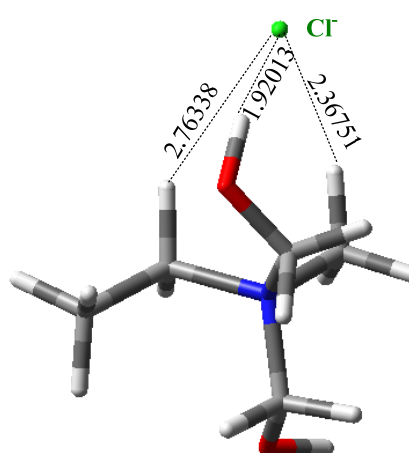


(a) $\Delta E_i = -73.8$ kcal/mol, $\langle \text{HB} \rangle = 2.0717$ Å (b) Top view with all bonds connected

Figure D.1: Optimized molecular structure of $[\text{Cl}(\text{H}_2\text{O})_4]^+$ at B3LYP/6-311++g**(H,O)/SDD(Cl). (a) $[\text{Cl}(\text{H}_2\text{O})_4]^+$, and (b) top view. Shown in the figure binding energy, kcal/mol, average hydrogen bond between water molecules. The average $\langle \text{Cl}-\text{H} \rangle = 2.3929$ Å. color code: green for Cl, red for O, light gray for H.



(a)



(b) $\Delta E_i = -111.6$ kcal/mol, $\text{Cl}-\text{N} = 3.69260$ Å

Figure D.2: Optimized structure in gas-phase of (a) HMMAEA, and (b) HMMEA-Cl (S3).

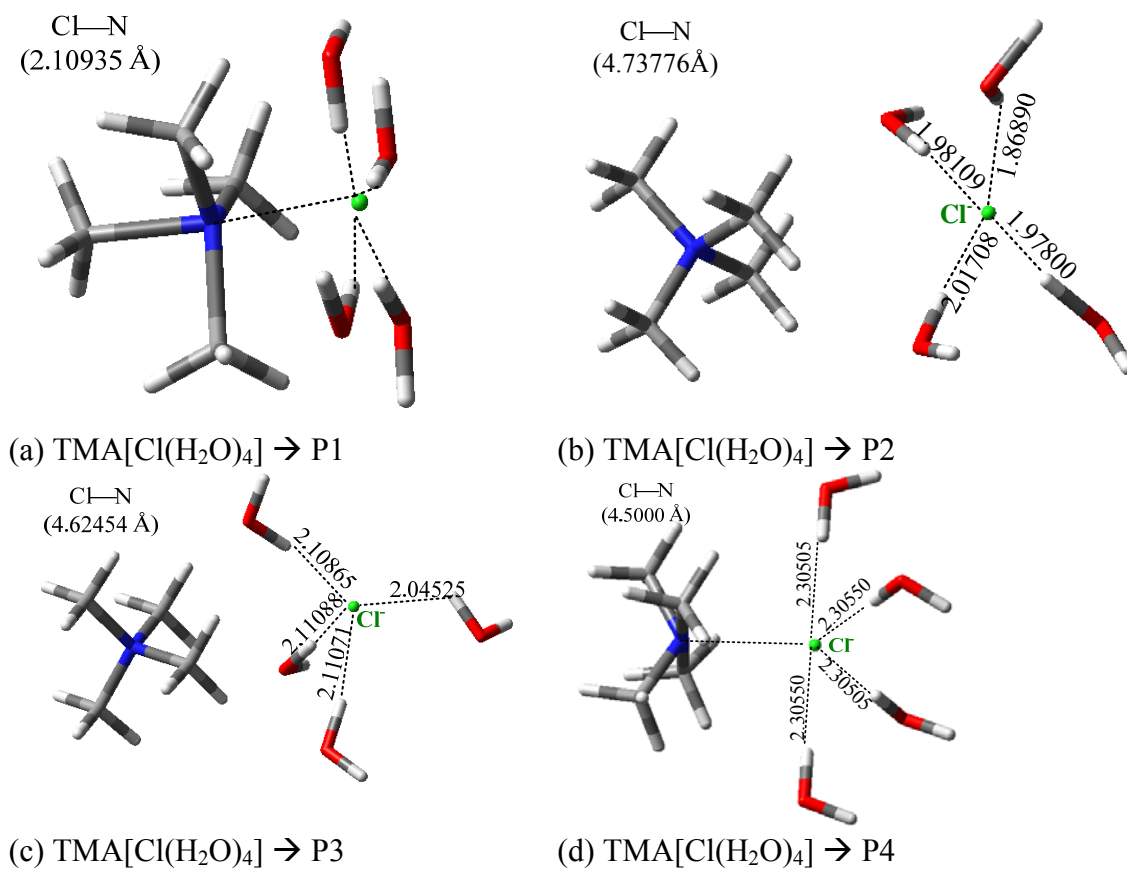


Figure D.3: Initial structures for interaction between TMA⁺ and [Cl(H₂O)₄][−] with final optimized geometries are shown in Figure 7.2. Shown in the picture bond distances, Å. color code: red for O, green for Cl, dark gray for C and light gray for H.

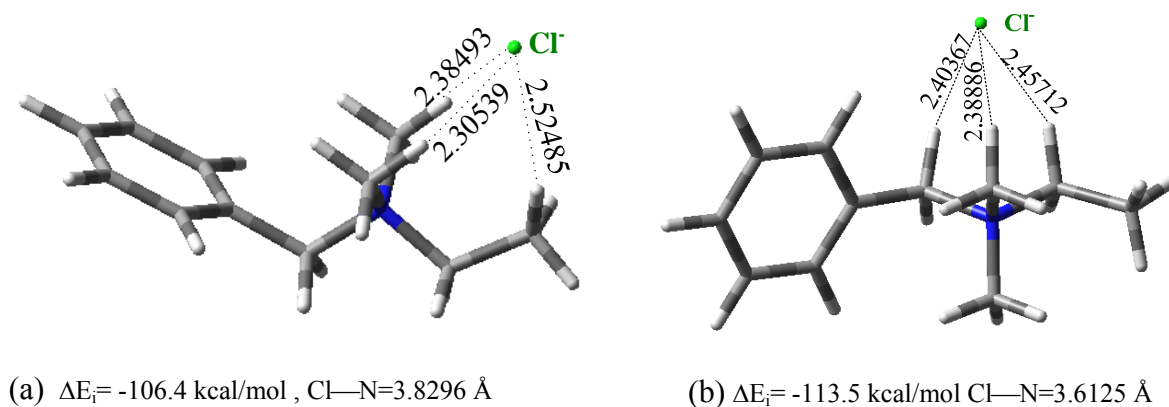
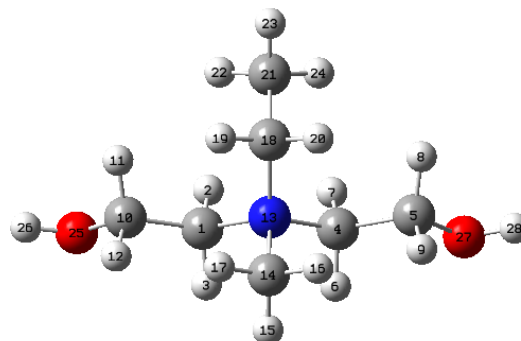
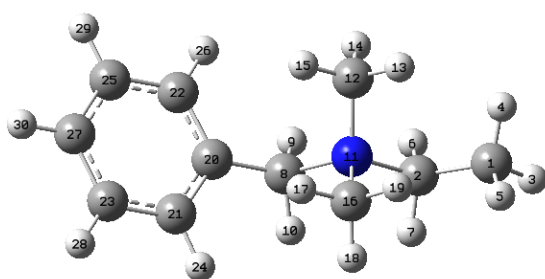


Figure D.4: Optimized structure in gas-phase of (a) BdMEA—Cl (S1), and (b) BdMEA—Cl (S2).



BdMEA at B3LYP/6-311++g** (gas-phase)				EhhMEA at B3LYP/6-311++g** (gas-phase)			
C	4.098801	0.000316	0.118061	C	-1.215334	-0.475788	-0.501068
C	2.83229	-0.000368	-0.724862	H	-1.121563	0.097844	-1.421171
H	4.945333	-0.000543	-0.572591	H	-1.144916	-1.533165	-0.7578
H	4.197461	0.890349	0.740514	C	1.21785	-0.47539	-0.502481
H	4.197269	-0.888411	0.742416	C	2.591027	-0.147508	0.088401
H	2.797672	0.881425	-1.366411	H	1.174411	-1.543536	-0.717073
H	2.797892	-0.882867	-1.365446	H	1.098458	0.058895	-1.443217
C	0.381321	-0.000147	-1.032233	H	2.722234	0.933227	0.215714
H	0.579055	0.88427	-1.638331	H	2.742868	-0.633508	1.059512
H	0.579042	-0.88459	-1.638294	C	-2.589803	-0.204633	0.114635
N	1.506825	-0.000116	0.043399	H	-2.721867	0.858682	0.347099
C	1.39863	1.224625	0.906469	H	-2.743613	-0.784328	1.032187
H	2.17632	1.19557	1.665341	N	0.001475	-0.155663	0.359088
H	1.51953	2.10969	0.283119	C	0.002742	-1.038774	1.581905
H	0.420876	1.234148	1.381725	H	-0.011324	-2.080025	1.264234
C	1.398357	-1.224618	0.906797	H	0.896184	-0.840712	2.16804
H	0.420855	-1.23345	1.382575	H	-0.875577	-0.820918	2.183754
H	1.518415	-2.109873	0.283564	C	0.002603	1.304841	0.823067
H	2.176455	-1.195872	1.665263	H	-0.866711	1.411776	1.471378
C	-1.03038	-0.000071	-0.517136	H	0.886727	1.415537	1.450524
C	-1.711813	-1.207235	-0.309876	C	-0.014068	2.344701	-0.285313
C	-1.711629	1.207212	-0.309945	H	-0.915418	2.299347	-0.898077
C	-3.032801	-1.207137	0.129248	H	0.00256	3.328965	0.188467
H	-1.219788	-2.152752	-0.513915	H	0.859118	2.288116	-0.937113
C	-3.032618	1.207349	0.129175	O	-3.47438	-0.619889	-0.90907
H	-1.219445	2.152634	-0.51404	H	-4.387646	-0.490305	-0.631704
C	-3.691917	0.000163	0.356149	O	3.478835	-0.661548	-0.886337
H	-3.551011	-2.146619	0.279508	H	4.389998	-0.469439	-0.639995
H	-3.550687	2.146919	0.279371				
H	-4.722461	0.000252	0.690763				

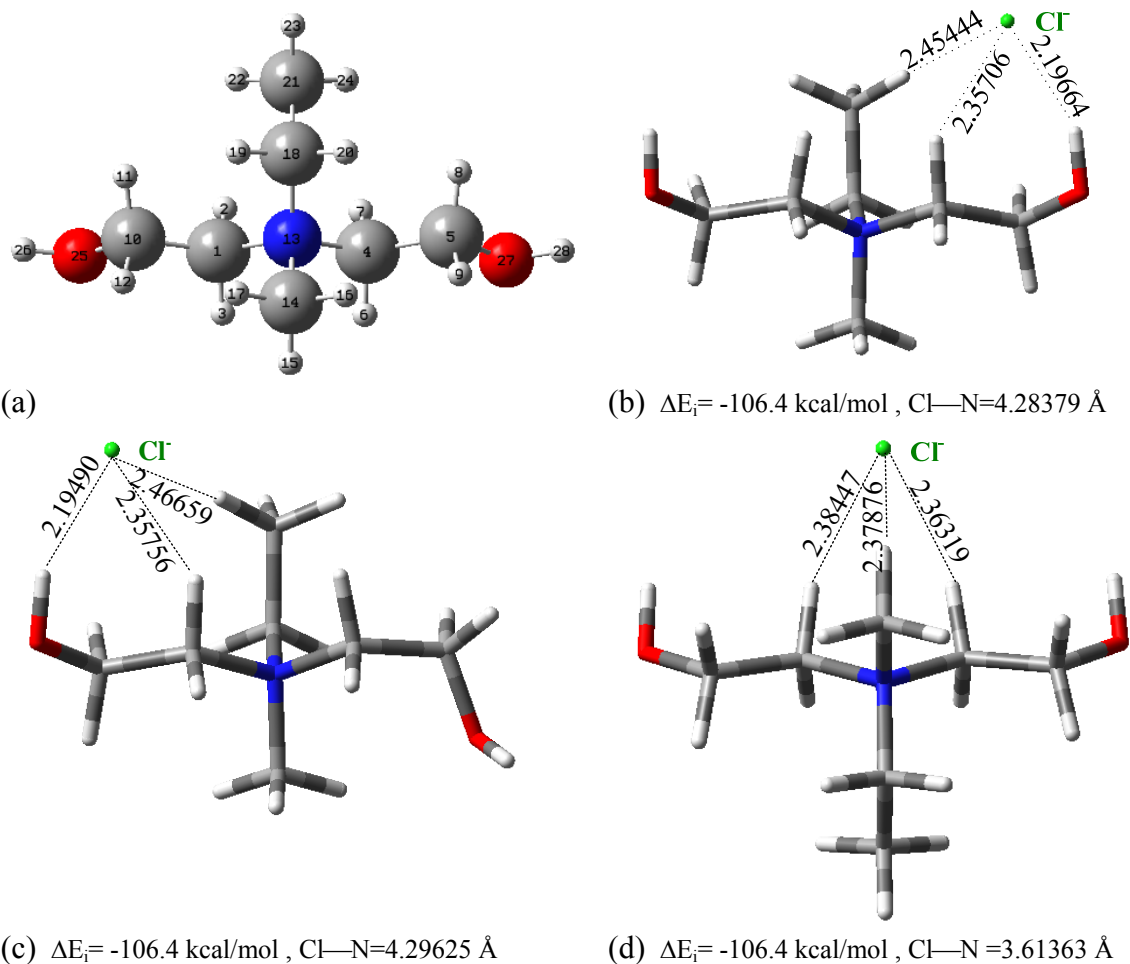


Figure D.5: Optimized structure in gas-phase of (a) EhHMEA (b) EhHMEA—Cl (S1), (c) EhHMEA—Cl (S2), and (d) EhHMEA—Cl (S3).

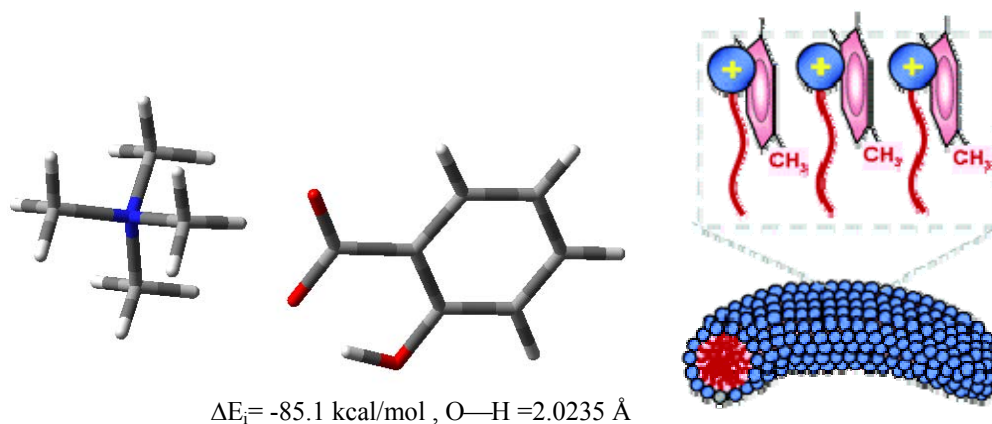


Figure D.6: Optimized structure of TMA with organic salt (Sal⁻) in gas-phase.

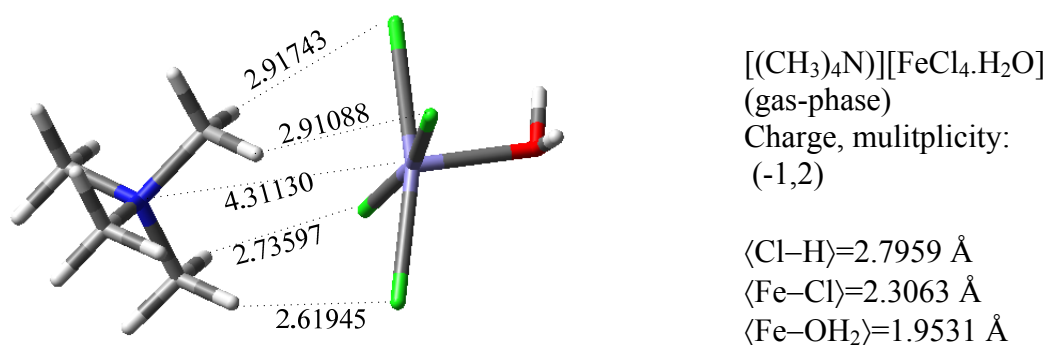
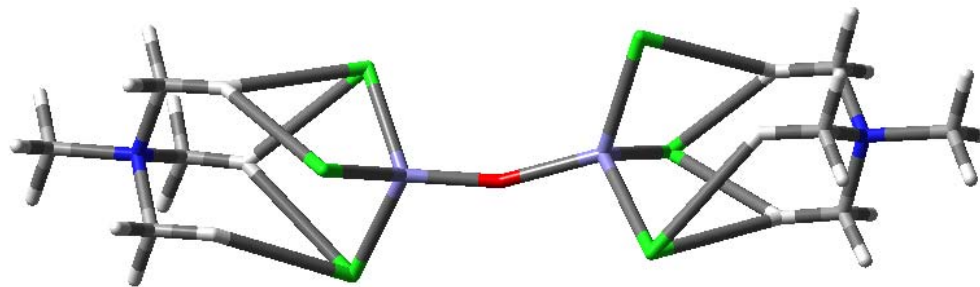


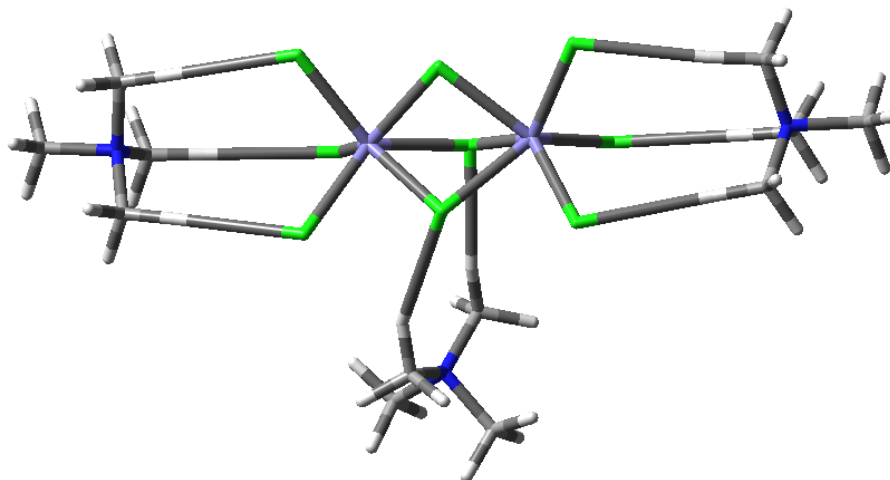
Figure D.7: Optimized structure of TMA⁺ with [FeCl₄]⁻ in gas-phase

Table D. 1: Binding energy and structural properties of cationic HGs with counterions calculated at B3LYP/6-311++g**(N,C,H)/SDD(Cl)

HG	Phase	Counterion	ΔE_i (kcal/mol)	$\langle \text{I-N} \rangle$ (Å)	$\langle \text{I-H} \rangle$ (Å)
TMA	gas-phase	Cl	-105.653		
TMA	gas-phase	Sal-	-85.061	—	2.0235
TMEA (S1)	gas-phase	Cl	-118.813	4.6216	1.8683
TMEA (S2)	gas-phase	Cl	-114.826	3.5744	2.3760
TMEA (S1)	water (PCM)	Cl	-13.111	4.2887	3.1151
TMEA (S2)	water (PCM)	Cl	-10.356	4.2296	3.0818
HMMEA (S1)	gas-phase	Cl	-121.481	4.7877	1.8379
HMMEA (S2)	gas-phase	Cl	-124.513	3.6926	2.3603
HMMEA (S3)	gas-phase	Cl	-111.599	3.78364	2.5800
HMMEA (S1)	water (PCM)	Cl	-2.254	4.24916	3.0835
HMMEA (S2)	water (PCM)	Cl	-8.931	4.25374	3.0921
EhhMEA (S1)	gas-phase	Cl	-113.853	4.28379	2.3360
EhhMEA (S2)	gas-phase	Cl	-115.770	4.29625	2.3397
EhhMEA (S3)	gas-phase	Cl	-115.891	4.29625	2.3755
BdMEA (S1)	gas-phase	Cl	-106.363	3.8296	2.4051
BdMEA (S2)	gas-phase	Cl	-113.514	3.6125	2.4166
bAETMedA	gas-phase	Cl	-323.028	3.6289	2.5616
dETMedA	gas-phase	Cl	-309.038	3.7517	2.4946

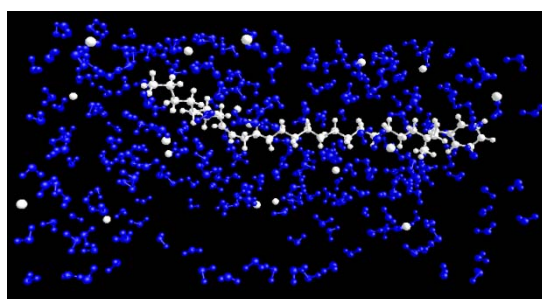


(a) $(\text{TAM})_2-(\text{Fe}_2\text{Cl}_6\text{O})$

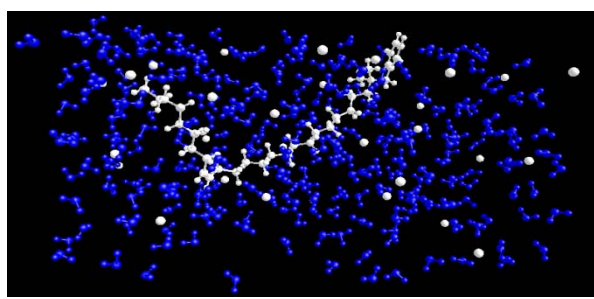


(b) $(\text{TAM})_3-(\text{Fe}_2\text{Cl}_9)$

Figure D.8: Optimized structures of TMA complexes with (a) $\text{Fe}_2\text{Cl}_6\text{O}$, and (b) Fe_2Cl_9 . Shown in the figure all bonds $\text{Cl}-\text{H} < 3.0 \text{ \AA}$, are connected.



C22_BdMEA_266(H₂O)_20Cl (11.9 wt%)

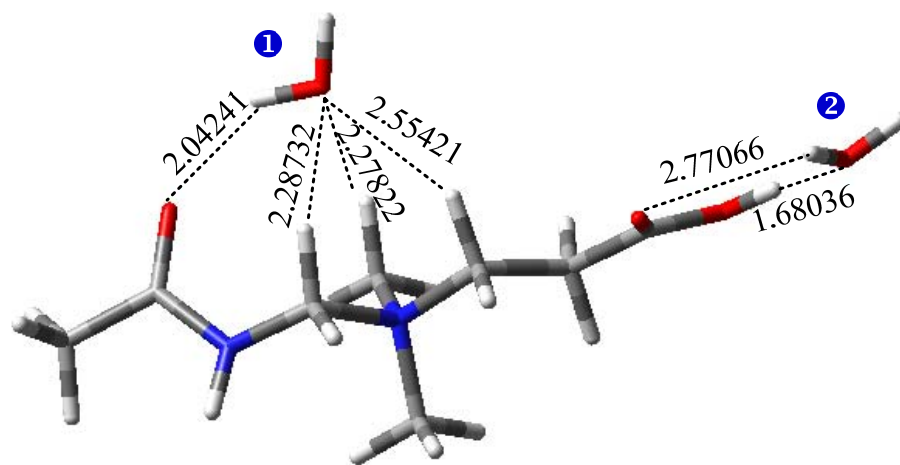


C22_BdMEA_264(H₂O)_30Cl (16.9 wt%)

Figure D.9: MD simulation of C22 BdMEA in water solution at various Cl concentrations.

APPENDIX E
SUPPORTING MATERIALS FOR CHAPTER VIII

**Geometry Optimization and Molecular Simulation of Betaine and Amidoamine
Oxide Surfactants**



$$\Delta E_i = -20.84 \text{ kcal/mol}, \langle \text{HB} \rangle_1 = 2.2905 \text{ \AA}, \langle \text{HB} \rangle_2 = 2.2255 \text{ \AA}, \angle \text{CHO} = 145.5^\circ$$

Figure E.1: Optimized structure for AAMCDEEA with two water molecules calculated at B3LYP/6-311++g**.

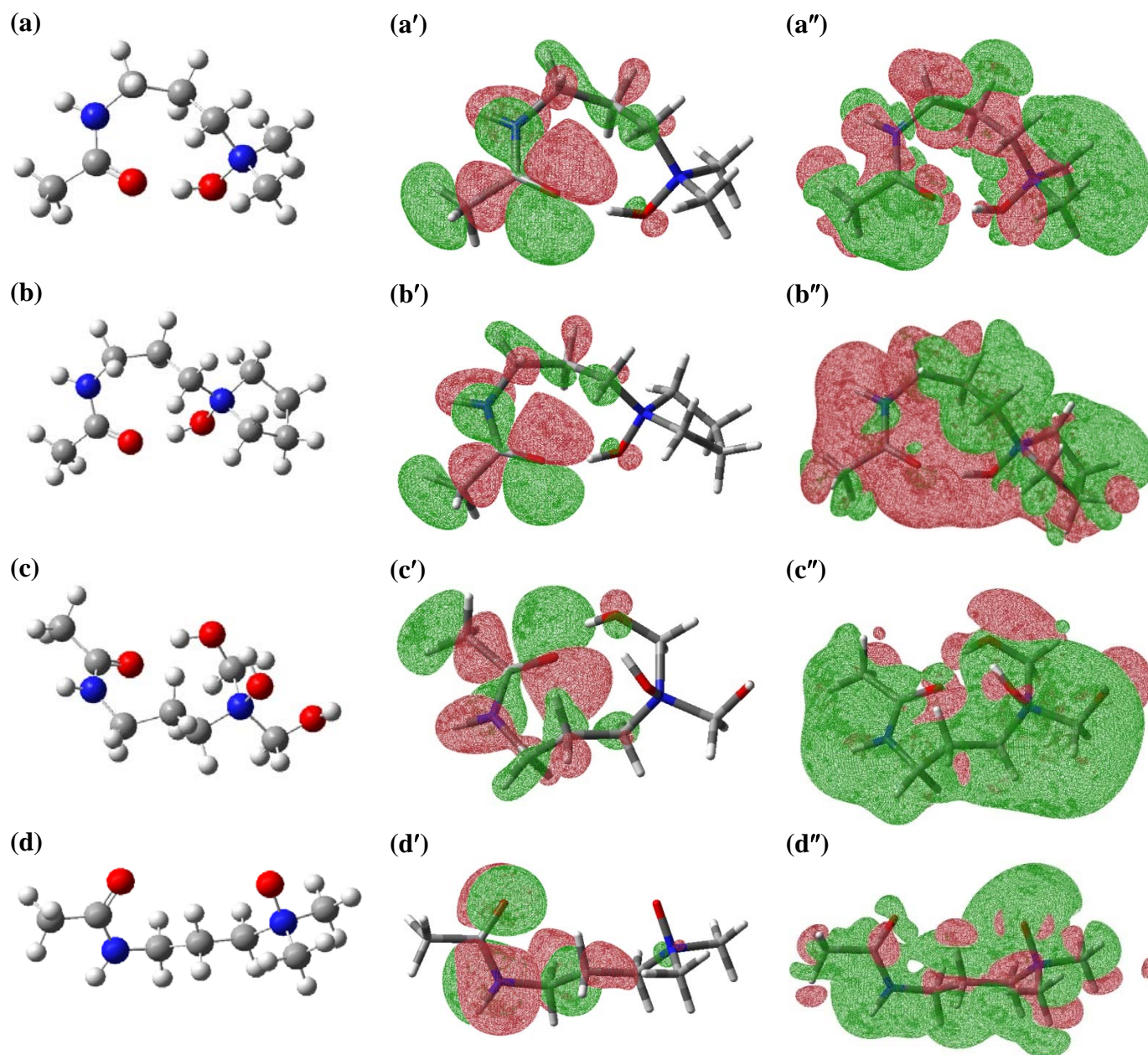
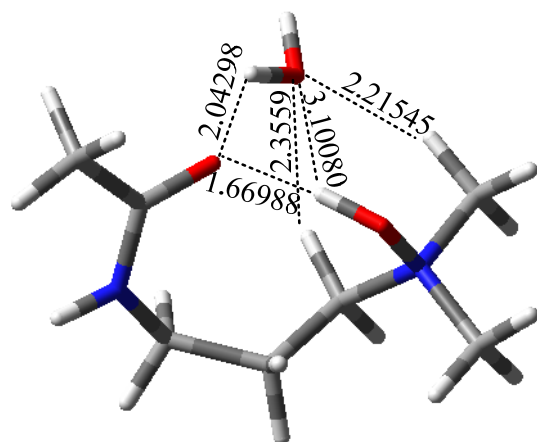
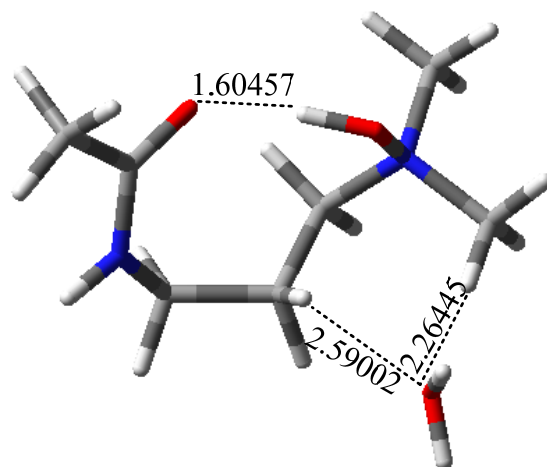


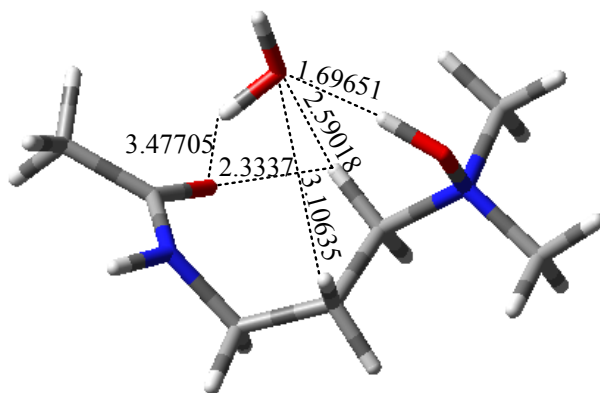
Figure E.2: Optimized geometrical structure of selected *amidoamine-oxide* head groups (HGs) with localized HOMO and LUMO molecular orbitals in the second and third column, respectively. (a) APhdMA, (b) APhP, (c) AphMA, and (d) dMNPA. Color code: red for O, blue for N, dark gray for C and light grey for H.



$\Delta E_i = -7.90$, $\langle \text{HB} \rangle = 2.0710 \text{ \AA}$, $\angle \text{CHO} = 155.0^\circ$

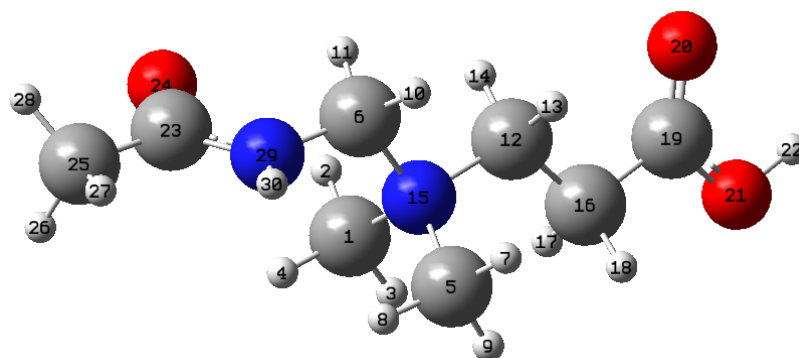


$\Delta E_i = -5.30$, $\langle \text{HB} \rangle = 2.4272 \text{ \AA}$, $\angle \text{CHO} = 152.6.0^\circ$



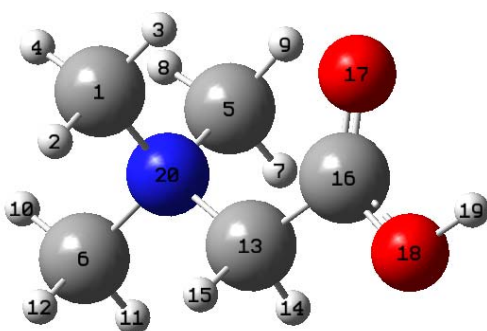
$\Delta E_i = -4.46$, $\langle \text{HB} \rangle = 2.1433 \text{ \AA}$, $\angle \text{CHO} = 118.2^\circ$

Figure E.3: Optimized structure of Amidoamine Oxide with water molecules.



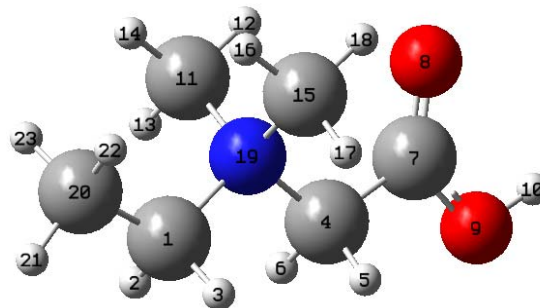
N-[(acetylamino)methyl]-2-carboxy-*N,N*-dimethylethanaminium
(AAMCDEEA) optimized geometry at B3LYP/6-311++g** (PCM)

C	-0.441591	0.30321	1.432692
H	-0.458926	-0.762484	1.653116
H	0.307432	0.809986	2.037618
H	-1.417338	0.743005	1.624308
C	-0.086953	1.958064	-0.348737
C	-1.172992	-0.214687	-0.904978
H	0.221326	2.082005	-1.387089
H	-1.087515	2.360996	-0.20076
H	0.60754	2.466826	0.316573
H	-0.862038	-0.023388	-1.932873
H	-1.095258	-1.275087	-0.665867
C	1.212092	-0.176626	-0.373575
H	1.31706	-0.094621	-1.457441
H	1.093413	-1.231943	-0.120041
N	-0.108655	0.49245	-0.020429
C	2.435997	0.405593	0.323759
H	2.355319	0.370955	1.414545
H	2.617154	1.449572	0.050384
C	3.680755	-0.374368	-0.054554
O	3.703583	-1.319319	-0.812954
O	4.757058	0.117793	0.562621
H	5.55842	-0.412343	0.304909
C	-3.408015	-0.495694	0.046401
O	-3.06151	-1.48208	0.682075
C	-4.829565	0.009589	0.042923
H	-5.055981	0.413004	1.034079
H	-5.007034	0.78584	-0.702577
H	-5.500356	-0.832672	-0.13466
N	-2.501685	0.242568	-0.689068
H	-2.852257	0.983584	-1.305269



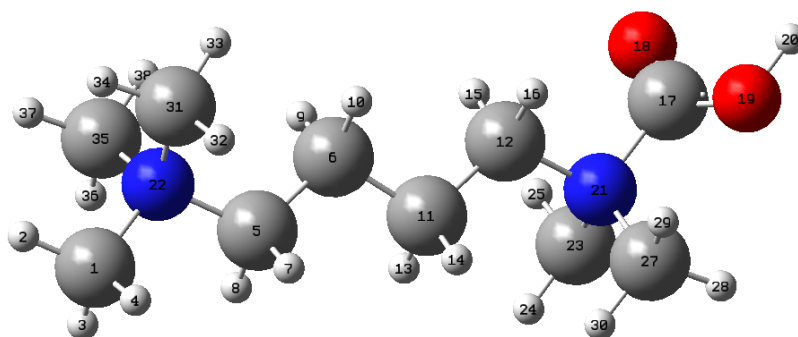
carboxy-*N,N,N*-trimethylmethanaminium
(**CTMMA**) optimized geomtery at
B3LYP/6-311++g** (PCM)

C	-1.159886	0.803988	1.238004
H	-1.080353	0.157727	2.111935
H	-0.370235	1.54911	1.235768
H	-2.137992	1.282989	1.212758
C	-1.153184	0.807834	-1.236197
C	-2.149799	-1.062534	-0.005196
H	-1.0256	0.170736	-2.111255
H	-2.147954	1.251631	-1.236943
H	-0.389834	1.579172	-1.207319
H	-3.095658	-0.522795	0.011109
H	-2.073655	-1.665493	-0.909532
H	-2.058314	-1.69238	0.879145
C	0.266271	-0.826003	0.003846
H	0.269181	-1.472882	-0.878517
H	0.269219	-1.466559	0.890869
C	1.54412	0.004579	0.00064
O	1.608858	1.211342	0.000363
O	2.581534	-0.821967	-0.000674
H	3.430766	-0.298055	-0.00359
N	-1.028264	-0.050769	0.000212



N-(carboxymethyl)-*N,N* dimethylethanaminium
(**CMDMEA**) optimized geomtery at
B3LYP/6-311++g** (PCM)

C	1.816018	-0.923691	-0.000106
H	1.677947	-1.548817	0.883465
H	1.677789	-1.548665	-0.88376
C	-0.61684	-0.806848	-0.000006
H	-0.580226	-1.450839	-0.8802
H	-0.580323	-1.450871	0.880169
C	-1.951619	-0.060757	-0.000064
O	-2.101442	1.13137	-0.000112
O	-2.929198	-0.967185	-0.000026
H	-3.791218	-0.517704	-0.000063
C	0.666743	0.922668	1.238019
H	-0.201172	1.575132	1.235623
H	0.661835	0.276952	2.115451
H	1.577223	1.514769	1.216684
C	0.666672	0.923015	-1.237624
H	1.577135	1.515139	-1.21615
H	0.661759	0.277545	-2.115235
H	-0.201262	1.575453	-1.235018
N	0.624912	0.055333	0.000077
C	3.198581	-0.291521	-0.000182
H	3.922329	-1.110002	-0.000331
H	3.395705	0.307033	-0.890034
H	3.395884	0.306866	0.889743



N-carboxy-*N,N,N',N',N'*-pentamethylbutane-1,4-diaminium
(CMPMBdA) optimized geomtery at B3LYP/6-311++g** (PCM)

C	-4.864346	0.967136	-0.028442
H	-5.836284	0.475388	-0.049852
H	-4.76009	1.557236	0.881339
H	-4.743126	1.601509	-0.905719
C	-2.441217	0.624337	0.004539
C	-1.212701	-0.279498	-0.045665
H	-2.44342	1.315526	-0.84242
H	-2.454068	1.210195	0.927613
H	-1.223959	-1.006567	0.771484
H	-1.178467	-0.835581	-0.987293
C	0.056372	0.586856	0.074277
C	1.281338	-0.311209	-0.06008
H	0.046679	1.099884	1.040664
H	0.04551	1.3482	-0.710684
H	1.265248	-1.115885	0.67688
H	1.329374	-0.750182	-1.061246
C	3.687813	-0.690574	-0.098229
O	3.782199	-1.59133	0.675797
O	4.338532	-0.442665	-1.197183
H	5.016083	-1.166413	-1.370482
N	2.633505	0.399094	0.143829
N	-3.790077	-0.090208	-0.044047
C	2.799214	0.866565	1.573702
H	2.069998	1.649979	1.765442
H	2.644195	0.020282	2.237847
H	3.808444	1.262094	1.687744
C	2.782509	1.575199	-0.789594
H	3.791098	1.970921	-0.69296
H	2.5996	1.248241	-1.810214
H	2.058514	2.330715	-0.493177
C	-3.932105	-0.902251	-1.302861
H	-3.752957	-0.252777	-2.159378
H	-3.215187	-1.7203	-1.290308
H	-4.945065	-1.301945	-1.339741
C	-3.976189	-0.980793	1.154744
H	-3.846721	-0.383089	2.056661
H	-4.983119	-1.395587	1.120191
H	-3.246252	-1.786701	1.125866

VITA

Abdullah Sultan was born in 1980 in the beautiful city of Abha, Saudi Arabia, to his parents Saad bin Sultan and Sandalah Al-Abbas. He was raised along with his younger four sisters and two brothers. After early education in his home town, he obtained his high school degree in 1997, ranked 9th in the region of Asir and among the top 1% on the nation. Later, he went on to pursue his undergraduate studies in chemical engineering at King Fahd University of Petroleum & Minerals (KFUPM), Dhahran, Saudi Arabia. During his 2nd year at KFUPM, he became interested in cosmology and space which was to become his lifelong passion. He was nominated by KFUPM to join Foster Wheeler-Italiana, Milan, for summer training in 2001 and assigned to be part of the team working on the “CCR reforming and isomerization unit project” for the Turkish Petroleum Refineries Corporations, TUPRAS, Izmir. In his final year at KFUPM, he worked on the “Process design of dehydrogenation of isobutane to isobutene for MTBE production” and won the best senior project design and was the KFUPM nominee for the SABIC prize. He was ranked 4th of more than 900 students from six different colleges upon his graduation. After graduating with a B.Sc. in chemical engineering in 2002, he went on to pursue his M.Sc. degree in the Chemical Engineering Department at KFUPM. He worked on “rheological and thermal characterizations of newly developed polymeric membrane for fuel cell applications” under the supervision of Dr. J. M. Zaidi and Dr. I. A. Hussin. He published three papers and two conference proceedings. After obtaining his M.Sc. degree in Chemical Engineering in 2005, he joined the research group of Prof. A. Dan Hill in 2006, where he carried out the work presented in this dissertation. He graduated with a Ph.D. in petroleum engineering from Texas A&M University in August 2009.

Mr. Sultan may be reached at the Department of Petroleum Engineering, King Fahd University of Petroleum & Minerals, P.O.Box 5049, Dhahran 31261, Saudi Arabia. His email is: asultan101@mail.com or sultanas@kfupm.edu.sa